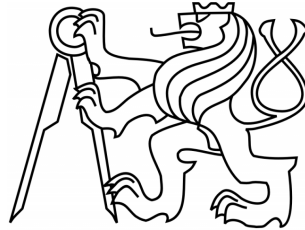


CZECH TECHNICAL UNIVERSITY IN PRAGUE
FACULTY OF NUCLEAR SCIENCES AND PHYSICAL ENGINEERING

Department of Physics



DOCTORAL THESIS

**Tunable laser plasma based X-ray
source from relativistic electrons**

Prague 2018

Karel Boháček

Declaration

This dissertation is the result of my own work, except where explicit reference is made to the work of others, and has not been submitted for another qualification to this or any other university.

In Prague, 29th November 2018

Karel Boháček

Acknowledgement

I would like to thank my wife Nesrine, who never stops believing in me and always motivates me to achieve my goals, and our daughter Zahra who is a constant source of happiness and joy in our life. I would not be able to finish the thesis without you.

I am grateful to my supervisors, Vojtěch Petráček and Michaela Kozlová, for always encouraging me and guiding me during the years of my studies. I also want to thank the leader of the experimental group RP2 at ELI Beamlines, Jaroslav Nejd, for often advising me using his experience and humanity. And I would like to acknowledge all my colleagues from ELI Beamlines and PALS Research Centre since their help at our experiments was always invaluable.

Autor: Ing. Karel Boháček,
České vysoké učení technické v Praze,
Fakulta jaderná a fyzikálně inženýrská,
Katedra fyziky

Název práce: **Laditelný plasmový zdroj vysokoenergetického záření pomocí laserem urychlených relativistických elektronů**

Studijní program: Aplikace přírodních věd

Obor: Jaderné inženýrství

Školitel: doc. RNDr. Vojtěch Petráček, CSc.,
České vysoké učení technické v Praze,
Fakulta jaderná a fyzikálně inženýrská,
Katedra fyziky

Školitel specialista: Ing. Michaela Kozlová, Ph.D.,
ELI Beamlines,
Fyzikální ústav AV ČR, v. v. i.,

Akademický rok: 2018/2019

Počet stran: 150

Klíčová slova: betatron, urychlování elektronů, femtosekundové laserové impulzy, inverzní Comptonův rozptyl, interakce laseru s plasmatem, zdroj rentgenového záření

Author: Ing. Karel Boháček,
Czech Technical University in Prague,
Faculty of Nuclear Sciences and Physical Engineering,
Department of Physics

Title of Dissertation: **Tunable laser plasma based X-ray source from relativistic electrons**

Degree Programme: Application of Natural Sciences

Field of Study: Nuclear Engineering

Supervisor: doc. RNDr. Vojtěch Petráček, CSc.,
Czech Technical University in Prague,
Faculty of Nuclear Sciences and Physical Engineering,
Department of Physics

Supervisor Specialist: Ing. Michaela Kozlová, Ph.D.,
ELI Beamlines,
Institute of Physics CAS

Academic Year: 2018/2019

Number of Pages: 150

Keywords: betatron source, electron acceleration, femtosecond laser pulse, inverse Compton scattering, laser-plasma interaction, tunability, X-ray source

Abstrakt

Interakce femtosekundových laserových impulzů s podkritickým plazmatem se ukázala být slibnou metodou produkce ionizujících částic a záření. Díky tomu, že svazky relativistických elektronů urychlených brázdovým polem laseru mohou sloužit jako zdroje kolimovaného femtosekundového rentgenového záření z bodového zdroje, jsou zdroje sekundárních fotonů tohoto typu nyní ve velkém zájmu ve vědeckých institucích, které využívají laserové systémy o vysokém výkonu a s krátkými impulzy. Stabilní zdroj rentgenového záření tohoto typu založený na několikaterawattovém laserovém systému by díky své dostupnosti v mnoha laboratořích po celém světě otevřel široké spektrum možností pro využití v biologii, chemii, medicíně nebo výzkumu materiálů.

V této práci je zkoumáno, zda je možné stabilně urychlovat elektronové svazky a produkovat betatronové rentgenové záření za pomoci optimalizace vlastností nadzvukového plynového výtrysku pro použití s femtosekundovým několikaterawattovým laserem, jehož parametry jsou na hranici pro dosažení režimu bubliny. Syntetický vzduch je vyzkoušen jako urychlující médium a získané urychlené elektronové svazky jsou porovnány s těmi, které lze obdržet za pomoci běžně používaných typů plyných terčů. Jsou prezentovány experimentální výsledky získané za pomoci navržených diagnostických systémů, a to zejména urychlené elektronové svazky a produkované ultrakrátké rentgenové záření.

Kromě toho je zde také věnována pozornost těmto typům zdrojů sekundárních fotonů založených na velkých petawattových laserech, jako je tomu v případě ELI Beamlines. U těchto systémů se předpokládá, že urychlené elektrony a produkované sekundární rentgenové impulzy budou mít mnohem lepší vlastnosti, zejména co se týče dosažené energie, energetického rozptylu a stability. Na těchto zařízeních však stále zbývá vyřešit, jak zajistit provoz s vysokou frekvencí opakování výstřelů a jak produkovat kvazi-monoenergetické rentgenové impulzy, které by byly laditelné. V této práci bude navrženo experimentální uspořádání betatronového a comptonovského zdroje na ELI Beamlines, který bude s takovou frekvencí opakování fungovat. Zároveň bude představena metoda produkce kvazi-monoenergetických rentgenových impulzů z laditelného zdroje comptonovského záření a budou diskutovány výsledky dosažené pomocí této metody.

Abstract

Femtosecond laser pulses interacting with underdense plasma were shown to be a promising technique of ionizing particle generation. Relativistic electron beams accelerated by laser wakefield have the ability to serve as sources of collimated, point-like and femtosecond X-ray radiation. These secondary photon sources are now of a great interest at short-pulse high-power laser facilities. Such X-ray source based on a few-terawatt laser system would open broad possibilities for applications in biology, chemistry, and medical and material research due to the availability of these laser systems in many laboratories around the world.

It is investigated whether the stable electron beam acceleration and betatron X-ray pulse generation can be achieved by optimizing the properties of the supersonic gas jet target for femtosecond few-terawatt laser operated near the laser intensity threshold for the bubble regime. Synthetic air is tested as the accelerating medium, and obtained accelerated electron beams are compared with those generated with commonly used targets. Experimental results obtained with a set of designed diagnostics are presented, including the accelerated electron beams and generated ultrashort X-ray radiation.

Moreover, at large-scale facilities with PW-class lasers, such as ELI Beamlines in the Czech Republic, although the parameters of accelerated electrons and generated secondary X-ray pulses are expected to be much improved in terms of energy, energy spread and stability, other challenges require further research. Among issues remaining to be solved are high-repetition rate operation and generation of quasi-monoenergetic X-ray pulse tunable in energy. In this work, an experimental setup of the betatron and Compton source at ELI Beamlines is designed and presented and a method of generating X-ray and gamma radiation from inverse Compton scattering with the high-repetition rate is proposed. Furthermore, a technique for generation of quasi-monoenergetic X-ray pulses from the tunable Compton source is investigated and the results are discussed.

Contents

Introduction	4
1 Laser wakefield acceleration	6
1.1 Laser-electron interaction	6
1.1.1 Laser interaction with single electron	6
1.1.2 Ponderomotive force	8
1.2 Laser-plasma interaction	9
1.2.1 Ionization of matter	9
1.2.2 Nonlinear relativistic effects	10
1.2.3 Laser pulse self-focusing and self-guiding	11
1.2.4 Laser pulse self-compression	12
1.2.5 Plasma waves	12
1.2.6 Bubble regime	13
1.2.7 Wave breaking	14
1.3 Electron trapping	15
1.4 Electron injection	16
1.4.1 Self-injection	17
1.4.2 Ionization injection	17
1.4.3 Plasma density ramp injection	18
1.4.4 Optical injection	18
2 Radiation from relativistic electrons	20
2.1 Fundamental radiation properties	20
2.2 Synchrotron radiation	21
2.2.1 Bending magnets	21
2.2.2 Undulator and wiggler	24
2.3 Betatron radiation	28
2.4 Inverse Compton scattering	31
2.5 Applications of betatron and Compton radiation	35
2.5.1 X-ray Phase Contrast Imaging and microtomography	35
2.5.2 Femtosecond X-ray Absorption Spectroscopy	37
2.5.3 Time-resolved imaging of shock-compressed matter	39
2.5.4 Opacity measurement of dense plasma	40
2.5.5 Time-Resolved X-ray Solution Scattering (TRXSS)	40
2.5.6 Femtosecond Time-Resolved X-ray Diffraction	41
2.5.7 In-operando studies of electrochemical batteries	41
2.5.8 Femtosecond X-ray damage threshold measurement in bio-crystals	41
2.5.9 Nuclear resonance fluorescence	42
2.5.10 Medical radioisotopes production	42

3	Experimental results and discussions	46
3.1	Experimental setup at PALS laboratory	46
3.1.1	Target	47
3.1.2	Focal spot and laser pointing monitor	47
3.1.3	Plasma diagnostics	48
3.1.4	Particle diagnostics	50
3.1.5	Plasma mirror for the Compton source with high repetition rate	63
3.2	Obtained experimental results with a few-terawatt laser	66
3.2.1	Accelerated electron beams	67
3.2.2	Generated betatron radiation	73
3.2.3	X-ray spectrum from Ross filter based spectrometer	75
4	Betatron and Compton sources at ELI Beamlines	82
4.1	ELI Beamlines facility	82
4.2	Conceptual design of the betatron and Compton source at ELI Beamlines	83
4.3	Modular magnetic spectrometer for high-energy electrons	88
4.4	Electron spectrometer for tunable Compton source	91
4.4.1	Electron focusing with dipole magnet	91
4.4.2	Dipole magnet for electron selection for Compton source	99
	Conclusion	108
	A Practical unit formulas	110
	B Ross filter analysis code	114
	References	140

Physical constants

$c = 299792458$ m/s	...	speed of light in vacuum
$e = 1.602 \times 10^{-19}$ C	...	elementary charge
$m_e = 9.109 \times 10^{-31}$ kg	...	electron rest mass
$\varepsilon_0 = 8.854 \times 10^{-12}$ F/m	...	vacuum permittivity
$\mu_0 = 4\pi \times 10^{-7}$ N/A ²	...	vacuum permeability
$h = 6.626 \times 10^{-34}$ J · s	...	Planck constant
$\hbar = h/(2\pi) = 1.055 \times 10^{-34}$ J · s	...	reduced Planck constant

Introduction

State-of-the-art X-ray sources, such as Free-Electron Lasers (FEL) and synchrotrons, have increased in dimensions up to kilometers due to the size of conventional radiofrequency electron accelerators which they are based on [1]. The large dimensions are limiting not only due to space and cost requirements but consequently because of limited user access to scarce facilities. Despite these limitations, synchrotron radiation is nowadays widely used for medical purposes [2] and FELs are the brightest sources of X-rays to date [3]. Moreover, the size is necessary to avoid the fundamental limit on the maximum accelerating field, which is restricted by the RF breakdown of the accelerator cavity that typically occurs at hundreds of MV/m [4]. Additionally, the maximum photon energy obtained from these sources is a few hundred keV at best.

These limits, however, can be overcome by employing laser-plasma accelerators using new techniques of X-ray pulse generation instead of the conventional radiofrequency accelerators with undulators and wigglers. The electric field of plasma waves induced by the high-power laser pulses can reach up to hundreds of GV/m due to the space charge separation [5], and it is thus possible to use the technique to accelerate electrons up to energies in the GeV range [6] with an electron bunch duration of a few femtoseconds [7]. Furthermore, the new generation of laser-plasma accelerators can be much smaller in dimensions due to the latest improvements to laser technology, such as mode-locking techniques [8] and chirped-pulse amplification [9] – a method of laser amplification recently awarded by a Nobel Prize in physics to Donna Strickland and Gerard Mourou [10]. In addition, the maximum X-ray photon energy of a source based on inverse Compton scattering can be much higher (even tens of MeV) than from the conventional sources due to the nature of the process. As the high-power terawatt lasers have become affordable, construction of inexpensive X-ray sources based on laser-plasma accelerators is now possible.

The main obstacle in this effort is acceleration of monoenergetic electron beams in plasma with a sufficient shot-to-shot energy stability, which requires taming the experimental conditions in the plasma. Such monoenergetic electrons can subsequently generate X-ray beams either directly in the acceleration process through betatron oscillations in the bubble regime or via inverse Compton scattering of the accelerated electron beam in a secondary laser pulse. Moreover, the laser plasma based X-ray source promises versatility in terms of the tunable energy of electrons and X-rays, which is unparalleled by the other sources, extending from THz radiation to the MeV range.

The goal of this dissertation is twofold: (I) to design a stable betatron and Compton X-ray source using a few-terawatt, femtosecond Ti:sapphire laser system (600 mJ, 50 fs) at PALS Research Centre in Prague, Czech Republic; and (II) to design a betatron and Compton source tunable in energy for a PW-class laser system at ELI Beamlines, where much improved parameters are expected in terms of the stability, the electron and X-ray photon energy and the energy spreads.

Due to the availability of the few-terawatt laser systems in many laboratories around the world, a method of stable laser-plasma electron acceleration and X-ray pulse generation would open broad possibilities for applications of this type of particle source. It is a challenging task to achieve this with the few-terawatt femtosecond laser pulse since the laser intensity is at the threshold of reaching the bubble regime, which enables betatron oscillations. Furthermore, the

bubble regime itself is the most efficient mechanism of the laser-plasma electron acceleration to date, which makes it useful for the Compton source since the X-ray photon spectrum of the source strongly depends on the electrons used for scattering. In both cases, point-like sources of collimated femtosecond X-ray radiation in the keV–MeV range can be obtained [11, 12]. In addition, it is intended to design the experimental setup for a high repetition rate of 10 Hz given by the driving laser at PALS in order to increase the feasibility of the Compton source for applications.

On the other hand, using the PW-class laser system at ELI Beamlines for the betatron and Compton sources requires scaling the parameters of the setup, such as the target dimensions and its density and type, accordingly, and a new set of particle and radiation diagnostics for higher energies must be designed and developed. The higher laser intensity well above the bubble regime threshold should allow creating a cavity completely evacuated of all electrons and generating stable electron beams tunable in energy, which is essential for the tunable Compton source. Under these conditions, a method of optimizing the electron beam for generation of monoenergetic X-ray pulses from the tunable Compton source will be investigated.

Since the energy of the accelerated electrons and the generated X-ray photon energy can be, in principle, tuned in both betatron and Compton sources by changing parameters of the laser pulses, the plasma and the accelerated electron or by modifying the geometry of the setup, it is necessary to show theoretically how the properties of the electron beams and X-ray pulses depend on the parameters of the driving laser and the accelerating medium. Therefore, the first chapter introduces the theory of laser-matter and laser-plasma interactions in order to understand the processes occurring in the laser-plasma accelerator and the behaviour of electrons that serve as the source of X-ray radiation. The ionization of matter with laser pulses will be discussed and fundamental phenomena of the laser-plasma interaction with the most important physical quantities describing the plasma, as well as the crucial nonlinear effects, will be explained. The limits on the electron acceleration using plasma waves are presented, and the bubble regime and its requirements are described since it is the paramount technique behind effective acceleration of electrons in plasma and the betatron X-ray pulse generation.

In the second chapter, the betatron and Compton radiation, being specific types of synchrotron radiation, are explained using theory, which is build around the physics of electron oscillations in magnetic fields known from FELs and synchrotrons. The crucial parameters are derived in the theory and it is identified how their variations provide the tunability of the betatron and Compton sources. Formulas in practical units are derived for the fundamental parameters, which can be of use for experimental physicists in order to quickly and conveniently predict the requirements for the source and its resulting performance.

In the third chapter, experimental conditions for acceleration of stable quasi-monoenergetic electron bunches using the few-terawatt laser pulse will be investigated as they are essential for generation of stable betatron radiation and X-ray pulses from inverse Compton scattering. A major effort of building the stable laser plasma based X-ray source from the beginning on such laser system will be described, including all systems of diagnostics that must be designed, developed and tested as a part of the experimental work on this thesis to monitor the principal parameters responsible for the source performance. In order to build the X-ray source, it is necessary to construct the stable laser-wakefield electron accelerator first, which produces electrons of relativistic energies. Various gas jet targets have to be tested to optimize the electron injection process and provide uniform accelerating conditions in plasma resulting in stable electron beam acceleration. In the second step, a betatron X-ray source generating X-rays in the keV range will be built and its radiation measured and characterized. Last but not least, a method of generation of the Compton radiation at 10 Hz repetition rate poses a challenge that will be investigated.

Furthermore, in chapter 4, the experience from designing the small-scale sources will be

used for design and development of the betatron and Compton source based on the *HAPLS-L3* PW-class laser system at ELI Beamlines. A new electron spectrometer for the higher energy range of up to 1.5 GeV will be designed and developed. The requirements of the dipole magnet are discussed and the final design of the manufactured units is presented. Furthermore, the magnet of the electron spectrometer can be used for focusing of divergent electron beams in the dispersion dimension of the magnet under certain conditions, which lowers uncertainties in the energy measurement of electron beams. The focusing technique is then used as a part of a significant effort of inventing a novel method of monoenergetic X-ray pulse generation from the tunable Compton X-ray source, which is introduced at the end of this chapter.

LASER WAKEFIELD ACCELERATION

Plasma as a state of matter is rare on the Earth under normal conditions. However, it is the most dominant constituent of the universe and as such is of great interest in various fields of science. Plasma can be created in a laboratory in many ways, such as by an electric discharge in gas, or a laser beam propagating through a medium or irradiating its surface. Many fields of modern physics sprouted as a result of the ubiquitous nature of plasma and its properties, e.g. inertial confinement and magnetic confinement fusion, or laser-plasma particle acceleration and laser-based X-ray sources, which are discussed in this thesis.

Laser wakefield acceleration of electrons (LWFA) brings many advantages to the domain of electron acceleration. Not only is the laser-plasma accelerator table-top due to the compact dimensions of the laser systems but the accelerating field is not limited by the cavity breakdown as in the case of conventional RF accelerators. The electric field of plasma waves induced by the high-power laser pulses can reach up to hundreds of GV/m and thus femtosecond electron bunches with an energy of up to a few GeV can be obtained [6].

In this chapter, in order to introduce the LWFA as a modern method of electron acceleration, it must first be described how laser pulses interact with electrons. Moreover, the plasma creation in laser-matter interactions and nonlinear relativistic effects in plasma need to be studied in order to understand the process of plasma wave generation, among which the most important is the bubble regime that allows effective and stable electron acceleration as well as generation of the betatron radiation. Finally, electron trapping in the acceleration phase of the plasma wave and means of electron injection are discussed.

1.1 Laser-electron interaction

Before getting into the laser-plasma interaction, it is a necessary to investigate the behaviour of electrons in the presence of a laser field.

1.1.1 Laser interaction with single electron

The motion of an electron in the electric field \vec{E} and magnetic field \vec{B} is described by the equation for the Lorentz force

$$\frac{d\vec{p}}{dt} = -e \left(\vec{E} + \vec{v}_e \times \vec{B} \right) \quad (1.1)$$

where $\vec{p} = \gamma m_e \vec{v}$ is the momentum of electron and $\gamma = 1/\sqrt{1 - \beta^2}$ is the Lorentz gamma factor. The simplest case to consider is the electron motion in a plane monochromatic wave of linearly polarized electromagnetic wave. If we consider the wave propagating along the x axis, the expression for the electric field of laser is

$$\vec{E}(x, t) = E_L \exp[i(k_0 x - \omega_L t)] \vec{e} \quad (1.2)$$

where E_L is the electric laser field amplitude and \vec{e} is the polarization vector (in case of the linear polarization, it is simply \vec{e}_y or \vec{e}_z , for the circular polarization $\vec{e} = (\vec{e}_y + i\vec{e}_z)/\sqrt{2}$). Since the real fields are described by the real parts of these expressions, we obtain a simplified expression

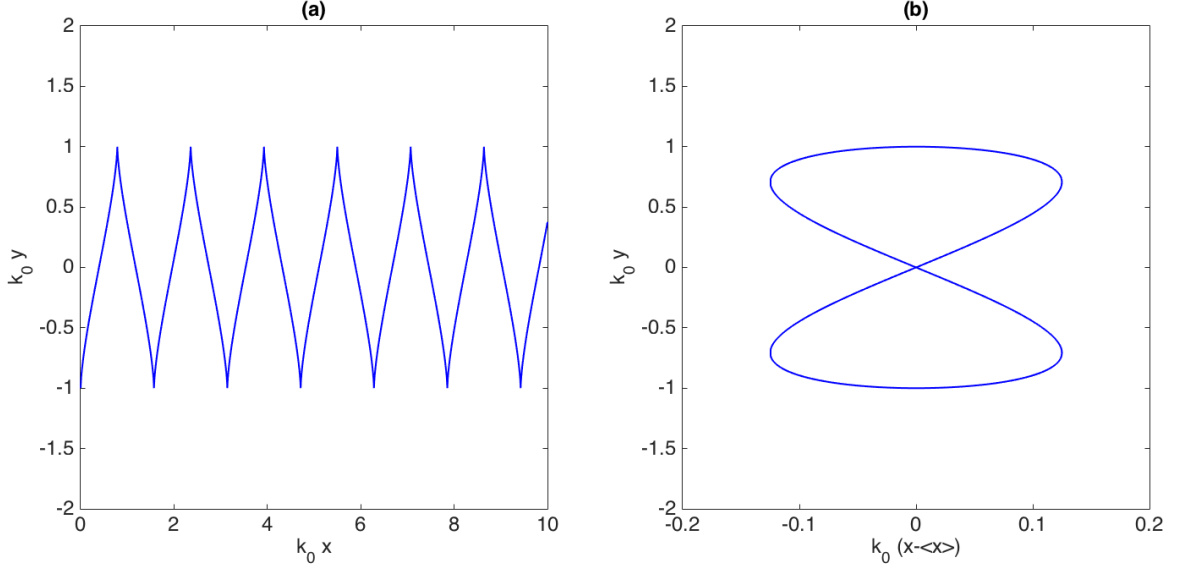


Figure 1.1: Zig-zag trajectory of electron in the electromagnetic field of laser pulse as seen in the laboratory frame (a), and in the frame moving with the average velocity of the electron (b).

for the electric field (for the linear polarization in the y axis) by taking only the real part of Eq. (1.2). This can be written as

$$\vec{E}(x) = E_L \cos(k_0 x - \omega_L t) \vec{e}_y. \quad (1.3)$$

The electric field is often written in terms of electric (scalar) and magnetic (vector) potentials as

$$\vec{E} = -\vec{\nabla}\phi - \frac{\partial \vec{A}}{\partial t}, \quad (1.4)$$

which allows Eq.1.3 to be rewritten as

$$\vec{A}(x) = A_0 \sin(k_0 x - \omega_L t) \vec{e}_y, \quad (1.5)$$

where $A_0 = E_L/\omega_L$. From the third Maxwell's equation, we get the relation between the electric and magnetic field amplitudes $B_L = \frac{1}{c}E_L$, which suggest that the second term on the right side of Eq. 1.1 can be neglected in the nonrelativistic regime when $\beta \ll 1$ and Eq.1.1 can thus be simplified to

$$\frac{d\vec{p}}{dt} \simeq -e\vec{E} = e \frac{\partial \vec{A}}{\partial t}. \quad (1.6)$$

Hence, an electron, which is located in the electric field of the plane electromagnetic wave and which was initially in $z = 0$ and at rest, starts oscillating with the velocity of

$$\beta = -\frac{eA_0}{m_e c} \sin(\omega_L t) \equiv -a_0 \sin(\omega_L t), \quad (1.7)$$

where we defined the *normalized vector potential* (also commonly called *laser strength parameter*) $a_0 = eA_0/m_e c = eE_L/m_e c\omega_L$. Equation (1.7) shows that the electron goes back into rest once outside of the electromagnetic wave ($A_0 = 0$), i.e. once the laser pulse passed by the electron.

For a laser strength of $a_0 > 1$, the velocity of the oscillating electron approaches the speed of light c and the second term in Eq.(1.1) cannot be neglected. As described in [13, 14], in

the relativistic regime, the electron momentum in the electromagnetic plane (and again linearly polarized) wave is given by

$$p_x = \frac{a_0^2}{2} \sin^2(k_0x - \omega_L t) \equiv \frac{a_0^2}{2} \sin^2(k_0\xi), \quad (1.8)$$

$$p_y = a_0 \cos(k_0x - \omega_L t) \equiv a_0 \cos(k_0\xi), \quad (1.9)$$

$$p_z = 0, \quad (1.10)$$

where $\xi = x - ct$ is the coordinate in the reference frame moving with the laser pulse. It is clear from Eq.(1.8) that the longitudinal electron velocity in the direction of the laser propagation is always positive. The magnetic constituent of the Lorentz force $\vec{v} \times \vec{B}$ is responsible for this motion. From integration of Eqs. (1.8) and (1.9), we obtain the electron trajectory given by

$$x = \frac{a_0^2}{8k_0} [2k_0\xi - \sin(2k_0\xi)]. \quad (1.11)$$

$$y = -\frac{a_0}{k_0} \cos(k_0\xi), \quad (1.12)$$

The first of these equations shows that the electron motion consists of not only moving forward but also oscillations with twice the laser frequency in the x direction. In the laboratory frame of reference, the electron motion follows a zig-zag trajectory as shown in Fig.1.1 (a). In the reference frame moving with the average velocity of the electron, the motion follows the familiar eight-shaped trajectory as seen in Fig.1.1 (b).

While this investigation proves the importance of the operation in the relativistic regime, it also shows that interaction of a laser pulse with single electron is not suitable for acceleration as the electron does not gain any energy from the laser pulse but is simply pushed forward in each light cycle and remains at rest once the interaction with laser ends. Through this means, the electron is only moved to a new longitudinal position, rather than accelerated.

1.1.2 Ponderomotive force

In regions of the intensity gradients of the laser pulse, a nonlinear force associated with the second-order electron motion acts on electrons. This force is called *ponderomotive force* [15, 16] and can be derived by introducing a small perturbation $\vec{p} = \vec{p}_q + \delta\vec{p}$ (where $\delta\vec{p} \ll \vec{p}_q$) into Eq. 1.1. First, it can be shown from Eq. 1.7 that the momentum of the first-order quiver motion of particle is $\vec{p}_q = m_e c \vec{a}$, then the net second-order motion averaged over one optical laser cycle is given by

$$\begin{aligned} \left\langle \frac{d\delta\vec{p}}{dt} \right\rangle &= -m_e \left\langle [(\vec{v}_q \cdot \vec{\nabla})\vec{v}_q + c\vec{v}_q \times (\vec{\nabla} \times \vec{a})] \right\rangle = \\ &= -m_e c^2 \left\langle [(\vec{a} \cdot \vec{\nabla})\vec{a} + c\vec{a} \times (\vec{\nabla} \times \vec{a})] \right\rangle = \\ &= -m_e c^2 \vec{\nabla} \left\langle \frac{a^2}{2} \right\rangle = -m_e c^2 \vec{\nabla} \frac{a_0^2}{4} \equiv \vec{F}_p, \end{aligned} \quad (1.13)$$

where F_p is the ponderomotive force. However, it does not affect only electrons but ions as well. In the nonrelativistic regime, the force can be generalized to [15]

$$\vec{F}_p = -\frac{q^2}{2\omega_L^2 m} \vec{\nabla} \langle E^2 \rangle, \quad (1.14)$$

where m is the mass of particle (i.e. electron, ion), and q is the particle charge. In the relativistic regime, it is simply a matter of substitution of $m \rightarrow \gamma m$. Nevertheless, as the particle mass was also averaged over the optical laser cycle, we get

$$\vec{F}_p = -\frac{q^2}{2\omega_L^2 m \langle \gamma \rangle} \vec{\nabla} \langle E^2 \rangle = -\frac{q^2}{2m \langle \gamma \rangle} \vec{\nabla} \langle A^2 \rangle, \quad (1.15)$$

where $\langle \gamma \rangle$ is the relativistic Lorentz factor averaged over one optical laser cycle.

The ponderomotive force is basically the radiation pressure of laser intensity, which means the force pushes charged particles out of the high-intensity regions. Equation 1.14 indicates the force is inversely proportional to the mass of the particle. Therefore, ions can be considered motionless on the time scale of femtosecond laser pulse duration due to their high mass, while much lighter electrons are displaced (both longitudinally and transversely) by the laser pulse and start oscillating in plasma waves [16]. Moreover, the force is independent of the electric charge sign, and thus pushes both electrons and ions in the same direction. And finally, the direction of the force is towards regions of lower laser intensity because of the negative sign in front of the gradient in Eq. 1.14. For this reason, the force also does not depend on the polarization of the electromagnetic wave.

1.2 Laser-plasma interaction

1.2.1 Ionization of matter

Plasma can be created by laser at relatively low pulse intensities of 10^{10} W/cm² and higher [17]. Keldysh parameter Γ defined as [18]

$$\Gamma = \sqrt{\frac{I_p}{2U_p}}, \quad (1.16)$$

where I_p is the ionization potential and U_p is the quiver energy of a free electron in an electromagnetic field. This type of electron energy is called ponderomotive energy and is defined as

$$U_p = \frac{e^2 E_0^2}{4m_e \omega_L^2} = \frac{e^2}{8\pi^2 \epsilon_0 m_e c^3} I \lambda_L^2. \quad (1.17)$$

In this equation, an expression for the laser intensity given as the time-averaged value of the Poynting vector in a certain point is used

$$I = \langle S(t) \rangle = \frac{1}{2} \epsilon_0 c E_0^2 = \frac{1}{2} \frac{E_0^2}{\mu_0 c}, \quad (1.18)$$

where E_0 is the amplitude of the electric field.

For the Keldysh parameter $\Gamma > 1$, the *multiphoton ionization* occurs [19]. For near infrared lasers, such as Ti:Sapphire lasers with a central pulse wavelength of 800 nm, which are typically used for electron acceleration, the multiphoton ionization takes place at laser pulse intensities of $10^{11} - 10^{13}$ W/cm². Under these conditions, the laser field is not strong enough to affect electron potentials of neutral atoms. The type of ionization can be described as an absorption of more than one photon which results in release of an electron from its bound state.

As the value of the Keldysh parameter decreases to $\Gamma < 1$, the *tunnel ionization* [20] and *Coulomb barrier suppression ionization* [21] dominate. For the near infrared lasers, the tunnel ionization occurs for intensities of approximately $10^{14} - 10^{15}$ W/cm². The laser electric field distorts the Coulomb potential of atoms, allowing electrons to tunnel through the suppressed

barrier of the atomic potential. In this case, however, no electron ground state appears above the barrier. The probability of electron tunnelling through the barrier increases as the laser intensity increases and due to this the height and width of the potential barrier decreases.

When the laser intensity is increased further, the Coulomb atomic potential is affected so much that an electron ground state gets above the Coulomb barrier and the electron becomes free. The Coulomb barrier suppression ionization dominates for very high intensities over all other ionization mechanisms. In fact, for ultrashort pulses, the tunnelling does not occur and the ionization due to the Coulomb barrier suppression takes place when the laser intensity is increased above the level for the multiphoton ionization.

The number of photons with an energy $E_L = \hbar\omega_L$ required to ionize an atom with an ionization potential I_p is given by [22]

$$N_\gamma = 1 + \left\lceil \frac{I_p}{E_L} \right\rceil. \quad (1.19)$$

1.2.2 Nonlinear relativistic effects

When an external force causes displacement of electrons in plasma, they start oscillating with a plasma frequency ω_p , which is a fundamental plasma parameter, given by [23]

$$\omega_p^2 = \omega_e^2 + \omega_i^2, \quad (1.20)$$

where ω_e is the electron plasma (Langmuir) frequency that only depends on the electron number density n_e and is given by

$$\omega_e^2 = \frac{n_e e^2}{\varepsilon_0 m_e} \quad (1.21)$$

and ω_i is the ion plasma frequency defined as

$$\omega_i^2 = \frac{n_i Z^2 e^2}{\varepsilon_0 m_i} \quad (1.22)$$

for the ion plasma density n_i , the ion charge Z and the ion mass m_i . Due to the higher mass of ions, the ion frequency is negligible and the Langmuir frequency is typically referred to as the frequency of plasma. The electron plasma frequency can be expressed in practical units as

$$\omega_e [\text{Hz}] = 5.64 \times 10^4 \sqrt{n_e [\text{cm}^{-3}]}. \quad (1.23)$$

Since the plasma frequency does not depend on the wavenumber k , the phase velocity is given by $v_\phi = \omega_p/k$ and the group velocity $v_g = \partial\omega_p/\partial k = 0$. The wavelength of the plasma wave can be expressed as

$$\lambda_p = \frac{2\pi v_\phi}{\omega_e}, \quad (1.24)$$

which, in practical units, gives a formula

$$\lambda_p [\mu\text{m}] = \frac{3.34 \times 10^{10}}{\sqrt{n_e [\text{cm}^{-3}]}}. \quad (1.25)$$

The laser pulse is an electromagnetic radiation with a frequency ω_L and as such can either propagate in plasma or be reflected. For $\omega_p < \omega_L$, the period of the laser pulse is shorter than the response time of the plasma, and thus the laser pulse can propagate through. In contrast, for $\omega_p > \omega_L$, plasma electrons can respond quick enough to the laser oscillations and reflect the laser pulse. The limiting value $\omega_p = \omega_L$ allows us to calculate the *critical density* using Eq. 1.21, which is given by

$$n_c = \frac{\varepsilon_0 m_e \omega_L^2}{e^2}. \quad (1.26)$$

Using the density terminology, the two types of plasma are referred to as the *underdense plasma*, which has a density $n_e < n_c$ and in which the laser can propagate, and the *overdense plasma*, which reflects the laser pulse due to its density $n_e > n_c$. Therefore, the critical density is a parameter related to the specific laser beam and it can be easily calculated using the laser pulse wavelength λ_L and a practical unit formula obtained from Eq. 1.26 as

$$n_c[\text{cm}^{-3}] = \frac{1.1 \times 10^{21}}{\lambda_L^2[\mu\text{m}]}. \quad (1.27)$$

The interaction length of a laser beam with plasma is basically limited by the Rayleigh length given by [24]

$$Z_R = \frac{1}{M^2} \frac{\pi w_0^2}{\lambda_L}, \quad (1.28)$$

where w_0 is the radius of the laser focal spot and M^2 is the beam quality factor describing the degree of difference from Gaussian beam (i.e. $M^2 = 1$ for Gaussian laser beams).

When an intense laser pulse with $a_0 > 1$ interacts with plasma and forces electrons to oscillate with relativistic velocities in its field, the refractive index of plasma changes due to the relativistic increase of the electron mass

$$\eta = \sqrt{1 - \frac{\omega_p^2}{\gamma \omega_L^2}}. \quad (1.29)$$

In such cases, relativistic effects in plasma, such as laser self-focusing [25, 26, 27, 28, 29], self-guiding [25, 26, 27, 28, 29], self-compression [30, 31] and self-phase modulation [30, 32, 33] take place.

1.2.3 Laser pulse self-focusing and self-guiding

It was first considered by Litvak in 1970 and Max et al. in 1974 [34, 35] that self-focusing of laser beams in plasma might occur for high-power laser pulses. In such cases, natural diffraction of laser pulse is reduced, balanced or overcome due to relativistic effects. It depends mainly on the laser pulse power, which of these particular situations occur. The critical power for collimated laser beam with a Gaussian profile, is given by

$$P_c = 8\pi\epsilon_0 \frac{m_e^2 c^5 \omega_L^2}{e^2 \omega_e^2}. \quad (1.30)$$

For laser powers $P < P_c$, the natural divergence of the laser beam is reduced by the effect of self-focusing but the focal spot still diffracts. As the laser power reaches the value $P = P_c$, the laser divergence is balanced, and the laser pulse self-guiding appears, which allows the laser pulse to be guided over distances much larger than the Rayleigh length Z_R given by Eq. 1.28 [25]. For $P > P_c$, the condition for self-focusing is reached, and thus the plasma acts as a positive lens and the laser spot size focuses.

The formula from Eq. 1.30 can be conveniently expressed in practical units as

$$P_c[\text{GW}] = 17.4 \left(\frac{\omega_L}{\omega_e} \right)^2 = 17.4 \frac{n_c}{n_e}. \quad (1.31)$$

This, however, neglects the electron density response, which further affects the refractive index. If the effect of the ponderomotive force, expelling electrons from the laser axis and thus causing a decrease of the electron density, cannot be neglected, the focusing effect is increased and the threshold for relativistic self-focusing is reduced to [25, 36, 37, 38, 39]

$$P_c[\text{GW}] = 16.2 \frac{n_c}{n_e}. \quad (1.32)$$

The decrease of the electron density due to the ponderomotive force causing laser pulse focusing is referred to as *ponderomotive guiding* or *ponderomotive self-channeling*.

The effect of relativistic self-focusing occurs due to the laser beam intensity profile having its maximum on the laser axis, i.e. $a_0(0) > a_0(r)$. Therefore, the plasma refractive index develops a radial dependence

$$\eta = \sqrt{1 - \frac{n_e(r)}{\gamma(r)n_c}}, \quad (1.33)$$

where

$$\gamma(r) = \sqrt{1 + \frac{a_0^2(r)}{2}} \quad (1.34)$$

for linearly polarized laser beams, or

$$\gamma(r) = \sqrt{1 + a_0^2(r)} \quad (1.35)$$

for circularly polarized laser beams. From formulae (1.33)–(1.35), it is obvious the maximum of the refractive index is on the laser axis. Hence, the diverging laser beams is refracted and more so, for $P > P_c$, can create secondary foci. The phenomena of relativistic and ponderomotive guiding were both observed experimentally [26, 40, 41, 42, 43, 44, 45, 46]. The biggest advantage of these mechanisms is that they do not require any preformed guiding structures in order to take place as only a single laser pulse of sufficient power is needed. In addition, in order to keep stable self-guiding, the laser pulse length must be larger than the plasma wavelength ($c\tau_L > \lambda_p$) [47]. For its simplicity and the ability to reach higher intensity than using conventional methods, such as mirrors and lenses, both guiding methods are attractive for laser-plasma particle acceleration. Equation 1.32 shows that the critical power P_c can be effectively lowered by increasing the plasma density n_e , which results in stronger self-focusing. The laser pulse reaches a higher normalized vector potential due to self-focusing given by [48]

$$a_{SF} = 2 \left(\frac{P}{P_c} \right)^{1/3} \quad (1.36)$$

with the focal spot radius

$$R_{SF} = \frac{\lambda_L}{\pi} \left(a_{SF} \frac{n_c}{n_e} \right)^{1/2}. \quad (1.37)$$

1.2.4 Laser pulse self-compression

Furthermore, the relativistic increase in the electron mass, which causes the changes of the refractive index, may result in the laser pulse to undergo *relativistic self-compression*. A nonlinear dependence of the longitudinal phase velocity on the refractive index ($v_\phi = c/\eta$) causes a frequency chirp that compresses the laser pulse. This creates a longitudinal chirp of the group velocity of the laser beam, where different parts of the laser pulse propagate with different velocities: the laser front (lower frequencies) propagates with lower velocity, while the rear of the pulse (higher frequencies) moves faster. This effect can cause steepening of the rising edge of the laser pulse, and thus enhancing the ponderomotive force.

1.2.5 Plasma waves

When the ponderomotive force expels plasma electrons out of the region of a short intense laser pulse propagation, plasma ions remain almost unaffected as their mass is too large to react quick enough to the laser field. As a result, a strong Coulomb potential appears due to charge

separation and pulls electrons back to the evacuated regions in the wake of the laser pulse. The electrons overshoot the point of balance and start oscillations, creating a wave-like structure travelling behind the laser pulse.

The phase velocity v_ϕ of these waves is determined by the exciting force and is approximately equal to the group velocity v_g of the laser pulse and is near the speed of light in vacuum [5]

$$v_\phi = v_g = c\sqrt{1 - \frac{\omega_p^2}{\omega_L^2}} = c\sqrt{1 - \frac{n_e}{n_c}}. \quad (1.38)$$

Plasma waves can be effectively created when the laser pulse duration τ_L is of the order of the plasma wave period $\tau_p = 2\pi/\omega_p$, which corresponds to the plasma electron density [49]

$$n_e[\text{cm}^{-3}] \simeq \frac{1.6 \times 10^{21}}{\tau_L^2[\text{fs}]}. \quad (1.39)$$

The transverse laser field is thus converted into the longitudinal electric field within the plasma. This longitudinal electric field can reach extremely high values with excess of [5, 50]

$$E_0 = \frac{m_e \omega_e c}{e}, \quad (1.40)$$

which can be expressed in practical units as

$$E_0[\text{V/cm}] \simeq 0.96\sqrt{n_e[\text{cm}^{-3}]}. \quad (1.41)$$

Equation (1.41) is referred to as the cold nonrelativistic wave breaking field [51]. As the plasma wave amplitude increases, the shape of the wave changes from sinusoidal in linear regime to a steeper shape in nonlinear regime (see Fig. 1.2). The maximum electric field of the nonlinear waves is given by [5, 52, 53, 54, 55, 56, 57] (for linear polarization of laser pulses)

$$E_{max} = \frac{a_0^2}{2} \frac{E_0}{\sqrt{1 + a_0^2/2}}, \quad (1.42)$$

where E_0 is the electric field of a linear plasma wave given by Eq. 1.41. This longitudinal electric field can become very high, up to hundreds of GV/m for a laser strength parameter $a_0 = 2$ and a plasma density 10^{19} cm^{-3} .

1.2.6 Bubble regime

A laser pulse of a sufficient intensity is capable of expelling majority of the plasma electrons from the regions of its propagation as was first proposed by Pukhov and Meyer-ter Vehn [58]. The resulting ion cavity, which is completely free (or mostly free) of electrons has, in general, an ellipsoidal shape and resembles a bubble. Therefore, we are usually talking about so-called *bubble regime*, although in some literature it is referred to as a *cavitated* or *blowout regime*. Furthermore, not only must the laser pulse have the sufficient intensity but it must be focused into an appropriately chosen spot size and must contain enough energy in order to maintain the stability of the cavity structure and its propagation over several Rayleigh lengths.

The bubble, which propagates on these lengths with only minimum fluctuations in the spot size, is formed by the balance between the transverse ponderomotive force of the laser pulse and the Coulomb force of the ion cavity. Using the balance between the two forces and the fact that the bubble radius scales with the laser spot size, we obtain a matching condition [59]

$$w_0 = \frac{2}{k_p} \sqrt{a_0}, \quad (1.43)$$

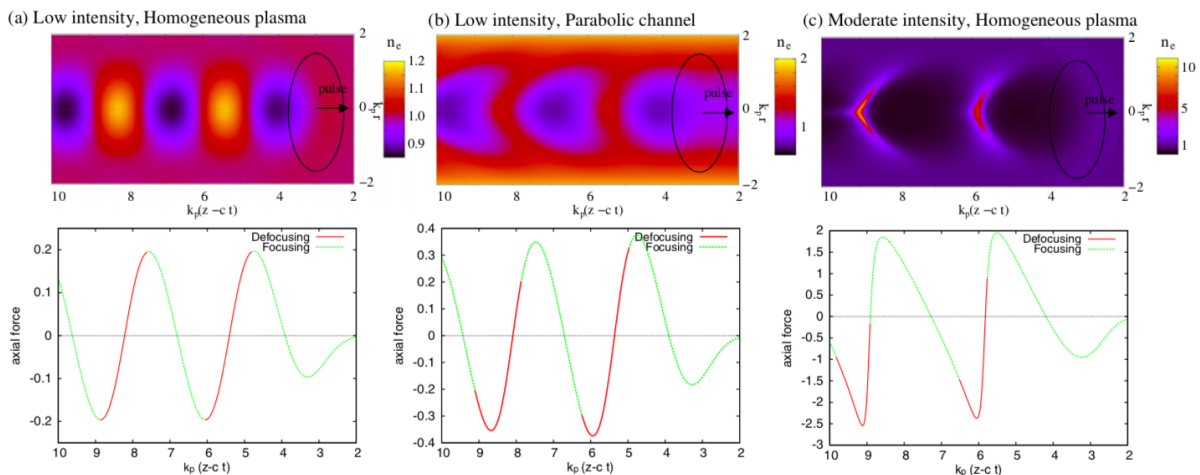


Figure 1.2: Spatial distribution of the electron plasma density (top), and longitudinal force, consisting of the ponderomotive force and the wakefield, on electrons (bottom) for different plasma conditions and laser intensities: (a) Low intensity laser pulse ($a_0 = 0.5$) in a homogeneous plasma, (b) low intensity laser pulse ($a_0 = 0.5$) in a parabolic plasma channel, and (c) moderate intensity laser pulse ($a_0 = 2$) in a homogeneous plasma. Reprinted from [49].

where $k_p = 2\pi/\lambda_p$ is the wavenumber of the plasma wave. The bubble appears for $a_0 > 2$ [60] and becomes spherically shaped and completely void of electrons for $a_0 \geq 4$ [61]. Its radius is given by $r_B \simeq w_0 = 2/k_p\sqrt{a_0}$, and can be expressed as $r_B \approx \lambda_p/2$ [28, 58, 59, 61, 62, 63, 64].

The electric field within the bubble is ideal for accelerating electrons since the longitudinal acceleration field is not radially dependent and the driving laser is propagating separately from the accelerated electrons, which helps minimize the energy spread of the accelerated electron bunch. Schematics of the process is shown in Fig. 1.3.

Since the ponderomotive force is proportional to the inverse gradient of the square of the laser intensity, plasma waves get excited when the front of the driving laser pulse is incoming as well as when the driving pulse is leaving. Thus, a resonant condition for plasma wave excitation as a function of the laser pulse length (FWHM) can be found. The incoming laser pulse expels electrons via the ponderomotive force from the high laser intensity regions, and after a half of the plasma period as the electrons are passing over their mean position, they receive a second "kick" from the ponderomotive force of the leaving laser pulse. Therefore, a short pulse with a relatively small energy can excite large amplitude plasma waves. The laser pulse length $L_{FWHM} = c\tau_L$ has an influence on the way plasma waves are excited. The plasma waves can be, of course, excited even with slightly longer pulses. It is however most efficient when the resonance is reached. The resonant condition necessarily depends on the envelope shape of the laser pulse as well. It is $L_{FWHM} \approx 0.5\lambda_p$ for a square pulse, $L_{FWHM} \approx 0.37\lambda_p$ for a Gaussian pulse and $L_{FWHM} \approx 0.42\lambda_p$ for a sine pulse [5].

1.2.7 Wave breaking

However, the plasma wave amplitude cannot grow to infinity and is limited. At a certain point, electrons in plasma undergo so large oscillations that the returning Coulomb force is not able to maintain the wave structure and the plasma wave electrons cannot follow the regular trajectory of their oscillations. They become dephased and the wave breaks. Therefore, we are talking about so-called *wave breaking*. The wave breaking limit in cold plasma is a limit on the

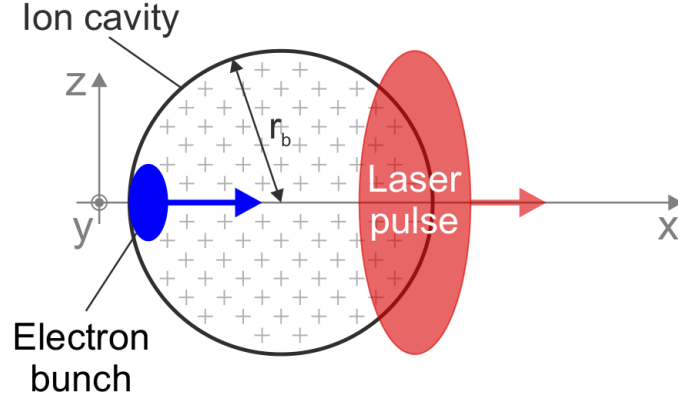


Figure 1.3: Schematics of laser wakefield acceleration in the bubble regime. Electrons that are injected and trapped in the ion cavity are subsequently accelerated along the x -axis towards the center of the bubble, which moves behind the laser pulse.

electric field, which can be expressed as

$$E_{\text{WB}}[\text{V/cm}] = E_0 \sqrt{2(\gamma_\phi - 1)}, \quad (1.44)$$

where $\gamma_\phi = \left(1 - v_\phi^2/c^2\right)^{-1/2}$ is the relativistic Lorentz gamma factor corresponding to the electron phase velocity v_ϕ . If we consider thermal effects, the wave breaking limit is reduced (compared to Eq. 1.44) [65, 66].

1.3 Electron trapping

An electron successfully gains an energy from a plasma wave when it is situated in an acceleration phase region, which is an interval $-\pi < \phi < 0$, where $\phi = k_p \xi = k_p(z - v_p t)$ is the phase of the 1D plasma wave. In order to better understand the electron acceleration in plasma, we can study electron orbits in phase space (\tilde{p}, ϕ) , where \tilde{p} is the normalized electron momentum. If the electron does not have a sufficient initial velocity, it will merely slip through the acceleration phase of the plasma wave. In this case, the electron does not gain sufficient energy, its velocity v_ϕ stays smaller than the phase velocity of the plasma wave v_p at the end of the acceleration phase $\phi \rightarrow -\pi$ and the *untrapped* electron slips backwards through the plasma wave. However, if the electron has a sufficient initial velocity as the electron gets to the end of the acceleration phase region $\phi \rightarrow -\pi$, its velocity v_e is already greater than the plasma wave phase velocity v_p . In this case, it follows a closed orbit in the $-\pi < \phi < \pi$ phase region and the electron is *trapped*. The curve separating the trapped and untrapped orbits in the phase space is called *separatrix* and it corresponds to the electron orbit with the threshold energy, which is needed for trapping. The trapped electron orbits in phase space (\tilde{p}, ϕ) are shown in Fig. 1.4.

The accelerated electron eventually outruns the plasma wave and starts decelerating by giving its energy back to the plasma wave. This is called *dephasing* and it limits the energy gain of electrons accelerated by the plasma wave. We define the dephasing length L_d as the length that the electron travels before it slips in the phase by a half of the period with respect to the plasma wave [48], which can be expressed for the bubble regime as [59]

$$L_d = \frac{2}{3} \frac{\omega_L^2}{\omega_p^2} r_B, \quad (1.45)$$

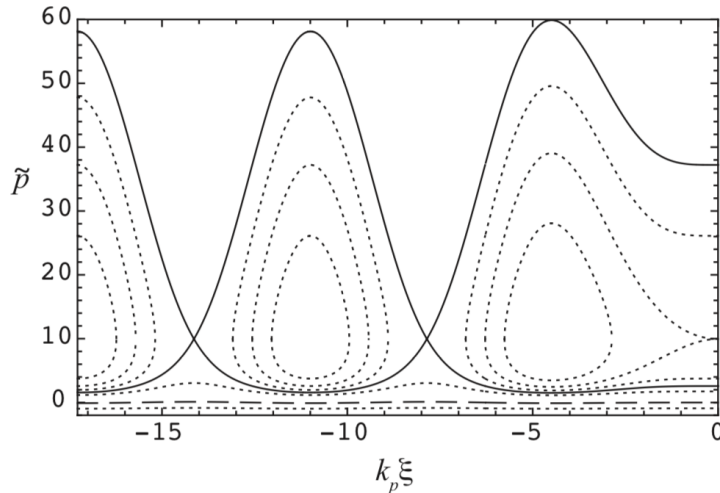


Figure 1.4: Closed electron orbits in phase space (\tilde{p}, ϕ) belonging to the trapped electrons are shown as dashed lines. The separatrix is shown as the solid line. A plasma wave excited by a laser pulse with a half-sine envelope of length $\lambda_p/2$ is assumed. Reprinted from [5].

where r_B is the bubble radius and where we assume $\omega_L^2/\omega_p^2 = n_{\text{crit}}/n_e \gg 1$. This can be rewritten in practical units as [67]

$$L_d = 0.3\lambda_L (n_{\text{crit}}/n_e)^{4/3} P[\text{TW}]^{1/6}. \quad (1.46)$$

The maximum energy that an electron can gain after a dephasing length is [59]

$$\Delta E = \frac{2}{3} m_e c^2 \left(\frac{\omega_L^2}{\omega_p^2} \right) a_0, \quad (1.47)$$

which can be rewritten again in practical units as

$$\Delta E[\text{GeV}] \simeq 1.7 \left(\frac{P[\text{TW}]}{100} \right)^{1/3} \left(\frac{10^{18}}{n_e[\text{cm}^{-3}]} \right)^{2/3} \left(\frac{0.8}{\lambda_L[\mu\text{m}]} \right)^{4/3}. \quad (1.48)$$

1.4 Electron injection

Conventional RF accelerators require an electron source, such as an electron gun or a photocathode, which generates electrons and injects them into the accelerator. The electron bunch is synchronized with the RF wave, so it gains energy when it is located in the acceleration phase [68]. These requirements hold for the laser-plasma accelerators as well. However, the common injectors cannot be used since they generate electron bunches longer than the plasma wavelength (picoseconds) which would result in an uneven acceleration of electrons from the bunch and thus a large relative energy spread. Moreover, it is difficult to provide a precise synchronization between the injector and the laser-plasma accelerator.

Fortunately, there is a feasible option of injecting electrons into the accelerating electric field of the plasma wave in a controlled way directly from the intrinsic plasma electrons. Electrons can be injected into the wakefield using *self-injection* through wave-breaking, *ionization injection*, *plasma density transition injection* and *optical injection*.

1.4.1 Self-injection

If the amplitude of the plasma wave is sufficiently high, a number of electrons cannot follow the regular trajectories of their oscillations and become dephased. Some of the electrons can be trapped in the electric field of the plasma wave and accelerated [69, 70, 71, 72]. The self-injection of electrons is a simple mechanism since only a single laser pulse is required both for the wakefield creation and the electron injection [41, 73, 74, 75, 76]. Furthermore, no precise spatial or temporal synchronization is required.

The electron bunch charge that can be obtained using self-injection mechanism is limited because the injection stops when the charge density of the bunch is in the same order of magnitude as the charge density of the plasma wave. The self-injection threshold is at the value $\alpha P/P_c$ where α is a fraction of laser power contained within the focal spot (FWHM) since only the area of the focal spot is self-focused or self-guided unlike the tails of the laser beam profile [77, 78]. Due to the dependence on the ratio of the laser power to the critical power, the self-focusing threshold can be expressed in terms of a minimum plasma density above which self-injection occurs.

Electrons are self-injected when the conditions for wave-breaking are satisfied. It happens when the plasma electric field exceeds the critical electric field, which can be expressed in a practical unit formula derived from Eqs. 1.41 and 1.44 as

$$E_{\text{WB}} = 0.96\sqrt{2(\gamma_p - 1)n_e[\text{cm}^{-3}]} \quad (1.49)$$

This formula is valid for a 1D cold plasma and describes a limit for longitudinal wave breaking. The actual limit is lower for a 3D or hot plasma. Despite its simplicity, the self-injection is a continuous process that occurs along the laser propagation trajectory through the plasma as long as the conditions for wave-breaking are satisfied. Therefore, electrons can be injected into the wakefield in various locations along the laser pulse propagation in the plasma. Each such injected electron bunch is accelerated differently and, as a result, electron spectrum with a large energy spread is obtained.

Transverse wave breaking, which occurs perpendicularly to the laser propagation, is possible as well. Moreover, if the wavelength of the plasma wakefield is equal to or greater than the laser pulse width, transverse wave breaking dominates over the longitudinal wave breaking since it requires a lower amplitude of plasma waves [58, 73, 79]. It predominantly occurs in the bubble regime when the radius of the wake wave approaches the electron displacement in the wave [79, 80, 81, 82, 83, 84]. Electrons from the edges of the bubble can be trapped at the rear of the bubble when transverse wave breaking occurs due to the electron density at the wall of the bubble reaching the wave breaking threshold. The process continues until the charge density of trapped electrons is comparable with the charge density of the bubble wall at its rear. Since the transverse injection is a short process and the region where the electrons are injected is well localized, the mechanism can result in generation of monoenergetic electron beams [69, 71, 72]. However, the injected electrons get a large transverse momentum as they follow a trajectory from the edge of the bubble toward its rear, which results in transverse oscillations within the bubble.

1.4.2 Ionization injection

For the reason that the process of self-injection can be difficult to control, alternative injection mechanisms were discovered. When a small admixture of a high- Z gas, such as nitrogen or argon, is used in the target in combination with a typically used light gas like hydrogen or helium, the ionization injection is possible. If a commonly used laser pulse intensity in the order of magnitude of 10^{18} – 10^{19} W/cm² is used, the light gas is completely ionized by the pre-pulse or the rising

edge of the driving laser pulse. The resulting ions and electrons from the light gas create the plasma together with electrons from L-shells and M-shells of the heavier atoms, which become ionized as well. However, the high-Z gas does not become fully ionized by the laser pulse of this intensity since the required intensity to ionize K-shells of the heavier elements is more than 10^{19} W/cm² (e.g. for nitrogen or oxygen) and can be as high as 10^{21} W/cm² (e.g. for argon) [85, 86]. Fortunately, such laser intensities can be achieved due to self-focusing of the laser beam. When it happens, the electrons from K-shells are subsequently injected. The ionization injection can thus be well localized in time and space because of its connection to the self-focusing effect.

It can be advantageous to use a circularly polarized laser pulse for its lower electric field in comparison to linearly polarized pulses of the same intensity. Therefore, the ionization occurs closer to the maximum of the laser intensity, the ionization phase is shifted closer to the maximum of the laser pulse intensity and the injected electron bunch has a lower energy spread [87]. It is also favorable to keep the laser pulse power below the self-injection threshold.

1.4.3 Plasma density ramp injection

Another way how to stabilize the injection mechanism is to trigger the self-injection by a sharp density ramp. The wave breaking occurs on the density gradient (from high to low density) which has a well defined location. Electrons in regions with the higher density oscillate faster than in low density regions. On the density transition, the frequency changes abruptly. The sudden change of the electron plasma frequency causes dephasing of a large number of the plasma electrons into the acceleration phase of the wakefield.

A dark-current-free electron beam, which is phase-locked with the accelerating phase of the wakefield and which has a small relative energy spread, can be injected. Same as the injection schemes described above, the injection on the density ramp does not require any temporal or spatial synchronization. The density ramp can be produced by a shock wave created by a knife edge in the supersonic gas jet [88], or a wire that creates a double density ramp [89]. It can also be produced by two gas jets, one of which operates with a higher backing pressure or uses a heavier gas and the other one with a lower backing pressure or a lighter gas [90]. Another option is to create a specially shaped gas jet nozzle that creates a shock wave or a pressure transition.

1.4.4 Optical injection

The simplest way to achieve optical injection is to use two laser pulses, one of which creates the wakefield in the regular laser wakefield mechanism, and the other, less powerful laser pulse interacts with the produced wakefield after the primary (driving) laser pulse. The ponderomotive force caused by the secondary (injecting) laser pulse pushes a fraction of electrons from the plasma wave and rephases them into the acceleration phase of the wakefield [67]. Another possibility is to use two injection laser pulses with slightly different frequencies $\omega_1 - \omega_2 \gg \omega_p$. Both the laser pulses are identically polarized and their polarization is perpendicular to the polarization of the driving laser pulse. The interference of the injecting laser pulses creates a resonance plasma wave that injects electrons into the acceleration phase of the wakefield. The optical injection mechanisms allow energy tuning by changing the focus position of the injection pulse or by colliding two circularly polarized laser pulses.

RADIATION FROM RELATIVISTIC ELECTRONS

Given the relatively compact size of LWFA sources, it has been of great interest to create table-top sources of X-ray radiation based on LWFA, which would generate X-rays with a duration of a few femtoseconds, a high brightness and tunable in energy (from soft X-rays to gamma rays). The most promising among the sources are a betatron source due to its simplicity, which is not significantly more complex than an LWFA source, and an X-ray source based on inverse Compton scattering due to high energy of the generated X-rays and its tunability [14]. In order to describe the properties of the betatron and Compton radiation, a standard theory of electron radiation in bending magnets, undulators and wigglers needs to be established.

2.1 Fundamental radiation properties

It is well known that accelerated motion of charged particles causes emission of electromagnetic radiation. The reason why it happens is the finite speed of light. A charged particle in the vacuum is the source of radial electric field with infinite range. While the charged particle is at rest or in uniform motion, the electric field lines are at rest or in uniform motion with the particle as well. When the particle is accelerated, however, the field lines are accelerated too. Since the signal of acceleration travels away from the particle at the finite speed of light, the field lines, which are close to the particle, point radially toward it, but the field lines far from the particle still point to the original location where the particle would be had it not been accelerated. The electromagnetic radiation are the distorted field lines between these two regions, travelling away from the source with the speed of light.

The radiation field thus depends on the position of the charged particle at the retarded time, when it was emitted. The solution to retarded potentials of point charges in the electromagnetic theory was found by Liénard and independently by Wiechert. The Liénard-Wiechert potentials answer the question how the scalar and vector potential of electromagnetic fields at the location of observation depend on the region of emitting charges at the time of emission. The radiation emitted by electron is, in general, obtained from the Liénard-Wiechert field. For an observer far from the electron (i.e. vector of the direction of observation is constant), the energy radiated within a solid angle $d\Omega$ centered on the direction of observation \vec{n} and within a spectral band $d\omega$ centered on the frequency ω is given by the expression [91]:

$$\frac{d^2W}{d\omega d\Omega} = \frac{e^2}{4\pi\epsilon_0} \frac{1}{4\pi^2c} \times \left| \int_{-\infty}^{+\infty} e^{i\omega(t - \frac{\vec{n} \cdot \vec{r}(t)}{c})} \frac{\vec{n} \times [(\vec{n} - \vec{\beta}) \times \dot{\vec{\beta}}]}{(1 - \vec{\beta} \cdot \vec{n})^2} dt \right|^2, \quad (2.1)$$

where $\vec{\beta} = \vec{v}_e/c$ is the dimensionless velocity of the electron, $\dot{\vec{\beta}}$ is similarly normalized acceleration of the electron and $\vec{r}(t)$ is the position of the electron at time t . Important general features of the emission of radiation can be deduced from expression for the radiated energy (Eq. 2.1). First of all, the expression equals zero for $\dot{\vec{\beta}} = \vec{0}$, hence no radiation is emitted by the electron, showing that the radiation originates in the acceleration of the particle.

Second, the term $1/(1-\vec{\beta}\cdot\vec{n})^2$ in the integrand suggests that the radiated energy is maximum when $\vec{\beta}\cdot\vec{n} \rightarrow 1$. This is valid for $\beta \simeq 1$ and $\vec{\beta} \parallel \vec{n}$, which means the energy radiated by relativistic electrons is orders of magnitude higher than by non-relativistic electrons, and the radiation will be emitted along the direction of the electron velocity. It is a consequence of the Lorentz transformation from the electron rest frame, where it emits an isotropic radiation, to the laboratory frame, where the radiation will be collimated in a small cone of opening angle $\theta = 1/\gamma$ around the electron velocity direction.

Third, the term $(\vec{n} - \vec{\beta}) \times \dot{\vec{\beta}}$ in the integrand in combination with the relations $\dot{\vec{\beta}}_{\parallel} \propto \vec{F}_{\parallel}/\gamma^3$ and $\dot{\vec{\beta}}_{\perp} \propto \vec{F}_{\perp}/\gamma$ between the acceleration and the external force applied to the electron in the longitudinal or transverse direction with respect to the electron velocity $\vec{\beta}$ imply that applying a transverse force ($\vec{F} \perp \vec{\beta}$) is more efficient than a longitudinal force. The radiation power P is proportional to the applied longitudinal or transverse force as $P \propto F_{\parallel}^2$ and $P \propto \gamma^2 F_{\perp}^2$, respectively, as derived in [92]. As can be seen from these expressions, the radiation power for acceleration along the particle propagation is independent of the particle energy ($\vec{F} \parallel \vec{\beta}$). However, when the same accelerating force is applied transversely ($\vec{F} \perp \vec{\beta}$), the radiation power is much higher due to the factor γ^2 . Therefore, a transverse acceleration force is much more efficient for obtaining high radiation power from relativistic electrons ($\gamma \gg 1$).

And last but not least, it is possible to approximate the phase term $e^{i\omega(t-\vec{n}\cdot\vec{r}(t)/c)}$ by $e^{i\omega(1-\beta)t}$. The result of the integral is zero unless the rest of the integrand (without the exponential) oscillates approximately at the frequency of the phase term $\omega(1-\beta)$. The velocity of the electron β oscillates with the frequency ω_e and for this reason it is required that $\omega_e \sim \omega(1-\beta)$ to obtain a non-zero result. Radiation of the frequency $\omega = \omega_e/(1-\beta) \simeq 2\gamma^2\omega_e$ is produced by the electron. Therefore, it is possible to generate X-ray beams by forcing a relativistic electron beam to oscillate at a frequency much lower than the X-ray frequency. The observed wavelength λ is relativistically contracted due to the Lorentz transformation and the Doppler shift and is given by

$$\lambda = \frac{\lambda_u}{2\gamma^2}, \quad (2.2)$$

where λ_u is the spatial period of the oscillations.

2.2 Synchrotron radiation

An efficient way to satisfy the conditions for radiation emission and cause the accelerated motion of electrons is to use magnetic field perpendicular to the electron propagation. The result is so-called *synchrotron radiation* and it is called this way for historic reasons since the radiation was found on synchrotrons. In principle, structures of magnets can be divided into three categories based on how they generate synchrotron radiation: bending magnets, undulators and wigglers. Each of these systems generates radiation from electrons that is unique in its qualities but can be described by a similar set of parameters.

The synchrotron radiation was first discovered on the early synchrotrons and storage rings as an energy loss of accelerated electrons due to the circular electron trajectories in the bending magnets. Eventually, following generations of synchrotrons were dedicated to generation of synchrotron radiation, going as far as omitting the circular shape of the accelerator since modern synchrotrons consist of many sections consisting of undulators and wigglers.

2.2.1 Bending magnets

Bending magnets force electrons to follow a circular trajectory, which results in emitting radiation due to radially accelerated motion through a broad angular pattern in the electron

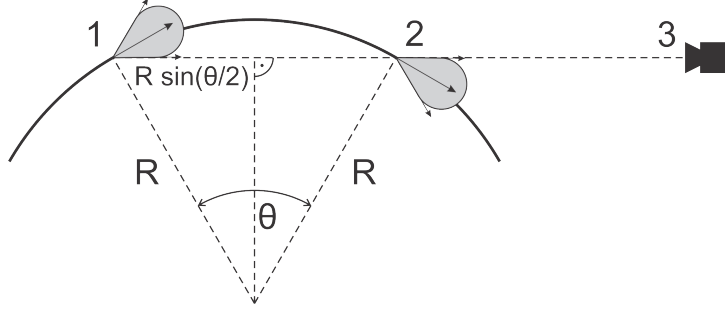


Figure 2.1: A schematic of radiation in the bending magnet resembling a sweeping searchlight. The photons start being emitted in the direction of the detector when the electron reaches point 1 and stop being emitted in its direction when the electron reaches point 2. The duration of the detected pulse is the difference of the duration τ_2 , which the electron needs to pass from point 1 to point 2, and the duration τ_1 , which the photons emitted from point 1 need to reach the detector.

frame of reference. Upon Lorentz transformation to the observer's frame of reference, the angular patterns become compressed when the electron motion is highly relativistic. For large emission angles in the electron frame, the radiation is compressed into a narrow forward radiation cone with an opening angle [91, 93]

$$\theta = \frac{1}{\gamma}. \quad (2.3)$$

For an observer far from the source, the electrons radiating in energy resembles a sweeping searchlight. Based on an application of Heisenberg's uncertainty principle and the duration of the observed signal, the energy range of the emitted radiation can be estimated. The photon wavelengths and energies can be estimated using Heisenberg's uncertainty principle, $\Delta E \cdot \Delta \tau \geq \hbar/2$, where $\Delta \tau$ is the rms (1σ) time duration of detecting radiation and ΔE is the uncertainty in detected photon energies (rms spread). The pulse duration $2\Delta\tau$ (full width) of the detected radiation emitted by a short electron bunch travelling around a circle of radius R can be estimated as follows. A detector of radiation placed at point 2 (as shown in Fig. 2.1) or at point 3 further to the right becomes in the path of the emitted photons when electrons arrive at point 1, which is within one half of the angle θ from the detector level. The photons from this point will be detected by the detector after a transit time τ_1 . The detected signal will continue until the electron bunch reach point 2, in which the last photons are emitted within the half of the angle θ and still reach the detector. The electron bunch reaches point 2 after a transit time around the circular bend τ_2 . The pulse duration (full width $2\Delta\tau$) is thus the difference of these transit times.

$$2\Delta\tau = \tau_2 - \tau_1 = \left(\frac{L_{arc}}{v_e} + \frac{L_{det}}{c} \right) - \frac{L_\gamma + L_{det}}{c} = \frac{L_{arc}}{v_e} - \frac{L_\gamma}{c} \quad (2.4)$$

After substituting $L_{arc} = R \cdot \theta$ and $L_\gamma = 2R \sin(\theta/2)$, we obtain

$$2\Delta\tau = \frac{R \cdot \theta}{v_e} - \frac{2R \sin(\theta/2)}{c}. \quad (2.5)$$

Making an approximation $\sin \theta \simeq \theta$, which is valid for small angles, gives

$$2\Delta\tau \simeq \frac{R \cdot \theta}{v_e} - \frac{R \cdot \theta}{c} = \frac{R}{\gamma v_e} - \frac{R}{\gamma c} = \frac{R}{\gamma} \left(\frac{1}{v_e} - \frac{1}{c} \right). \quad (2.6)$$

Further substituting $v_e = \beta c$, we get

$$2\Delta\tau = \frac{R}{\gamma\beta c} (1 - \beta), \quad (2.7)$$

which can be simplified using

$$\gamma^2 = \frac{1}{1 - \beta^2} = \frac{1}{(1 - \beta)(1 + \beta)} \quad (2.8)$$

and using relativistic limit $\beta \rightarrow 1$

$$1 - \beta \simeq \frac{1}{2\gamma^2}, \quad (2.9)$$

the expression for the pulse duration is

$$2\Delta\tau \simeq \frac{R}{2\gamma^3 c}. \quad (2.10)$$

Formula from Eq. 2.10 can be used to estimate a photon energy (rms) spread using Heisenberg's uncertainty ($\Delta E \cdot \Delta\tau \geq \hbar/2$) as

$$\Delta E \geq \frac{2\hbar c \gamma^3}{R} \quad (2.11)$$

It can be modified by replacing the radius of electron trajectory R with an expression involving the Lorentz gamma factor γ and the magnetic field B . The electrons propagating through a perpendicular magnetic field B are deviated by the magnetic part of the Lorentz force (Eq. 1.1)

$$\vec{F} = -\vec{v} \times \vec{B} \quad (2.12)$$

and from the balance between the centrifugal force and the centripetal force (which is the magnetic part of the Lorentz force in this case) the expression for the radius of electron in a uniform magnetic field can be derived as

$$R = \frac{\gamma m_e v_e}{eB} \simeq \frac{\gamma m_e c}{eB}, \quad (2.13)$$

where we used the ultrarelativistic limit $v_e \rightarrow c$ again. Combining the expression for the radius R with Eq. 2.11, we obtain

$$\Delta E \geq \frac{2e\hbar B \gamma^2}{m_e}. \quad (2.14)$$

It can be rewritten in practical units as

$$\Delta E[\text{keV}] = 8.867 \times 10^{-7} B[\text{T}] (E_e[\text{MeV}])^2. \quad (2.15)$$

This result, however is somewhat artificial as we assumed that all electrons are radiated within the angle $\theta \simeq 1/\gamma$ rather than within a certain angular distribution. With a proper, rather tedious description, it can be found that the resulting on-axis photon flux is described by the modified Bessel functions of the second kind [91, 94, 95]. It is useful to define a *critical photon energy*

$$E_c = \frac{3e\hbar B \gamma^2}{2m_e}, \quad (2.16)$$

which is defined as an energy value, for which half of the radiated power is in lower energy photons and half is in higher energy photons. Therefore, using the fact that the photon energy distribution of synchrotron radiation is described by a known function, we defined one primary parameter to describe the photon energy spectrum. It is possible to rewrite Eq. 2.16 in practical units similar to the approach we used to obtain Eq. 2.15. Hence, the critical photon energy can be estimated by

$$E_c[\text{keV}] = 6.650 \times 10^{-7} B[\text{T}] (E_e[\text{MeV}])^2. \quad (2.17)$$

E/E_c	$H_2(E/E_c)$
0.0001	6.271×10^{-3}
0.0010	2.910×10^{-2}
0.0100	1.348×10^{-1}
0.1000	6.025×10^{-1}
0.3000	1.111×10^0
0.5000	1.356×10^0
0.7000	1.458×10^0
1.0000	1.454×10^0
1.5000	1.250×10^0
2.0000	9.780×10^{-1}
3.0000	5.195×10^{-1}
4.0000	2.493×10^{-1}
5.0000	1.131×10^{-1}
7.0000	2.107×10^{-2}
10.000	1.478×10^{-3}

Table 2.1: Values of the modified Bessel function of the second kind $H_2(E/E_c)$ with respect to the energy ratio E/E_c calculated in [96].

Using Eq. 2.17, we can estimate that an electron with an energy $E_e = 100$ MeV in a magnetic field of $B = 1$ T emits photons with a critical energy of $E_c = 6.7$ eV. It would require electrons with an energy of at least 1.2 GeV in the same magnetic field to obtain radiation with a critical energy of 1 keV.

For better description of the bending magnet radiation, it is useful to refer to Tab. 2.1, which shows values of the modified Bessel function of the second kind with respect to the ratio E/E_c .

Since the electrons are accelerated in one plane (horizontal in case of bending magnets on a synchrotron), the generated radiation is linearly polarized in this plane.

2.2.2 Undulator and wiggler

If we consider an electron moving through a periodic magnetic structure and executing transverse harmonic oscillations, we can distinguish between two regimes of emitting radiation. In the *undulator* regime, an ultrarelativistic electron undergoes oscillations of a small amplitude (undulations) in a magnetic structure creating a moderate field, and radiates energy. The maximum angle of the trajectory ψ is smaller than half of the opening angle of the radiation cone $\theta = 1/\gamma$ and the electron radiates in the same direction during the whole trajectory. In the *wiggler* regime, an electron rapidly oscillates in a periodic system with a strong magnetic field and the maximum angle of the trajectory is larger than the half of the opening angle (i.e. $\psi \gg \theta/2 = 1/2\gamma$). Thus, different trajectory sections radiate in different directions. A dimensionless parameter $K = \gamma\psi$ can be defined, which separates the undulator regime ($K < 1$) and the wiggler regimes ($K > 1$). The qualitative and quantitative properties of the generated radiation significantly differ in terms of the energy spectrum, the radiated energy, the divergence and the number of emitted photons.

The properties of the radiation can be derived using simple arguments. If the magnet period is λ_u , the electron in its rest frame experiences the magnet structure moving toward it, which results in a relativistically (Lorentz) contracted period

$$\tilde{\lambda} = \frac{\lambda_u}{\gamma}. \quad (2.18)$$

Due to the periodic structure of dipole magnets, the electron performs short oscillations and emits photons. The electron radiates as a classical dipole in its rest frame. In this frame of reference, the frequency of emitted photons is simply

$$\tilde{f} = \frac{c}{\tilde{\lambda}} = \frac{\gamma c}{\lambda_u}. \quad (2.19)$$

In the laboratory frame, the frequency is Doppler shifted with a maximum on the axis, which is obtained using the relativistic Doppler formula

$$f = \frac{\tilde{f}}{\gamma(1 - \beta \cos \theta)} = \frac{c}{\lambda_u(1 - \beta \cos \theta)}, \quad (2.20)$$

where θ is the angle of the radiation from the axis. For the radiation on axis ($\theta = 0$) in the laboratory frame and ultrarelativistic electrons ($\beta \simeq 1$, which gives $1 - \beta \simeq 1/2\gamma^2$), the frequency of emitted radiation is

$$f = \frac{c}{\lambda_u(1 - \beta)} = \frac{2\gamma^2 c}{\lambda_u}, \quad (2.21)$$

which corresponds to the wavelength observed on axis

$$\lambda = \frac{c}{f} = \frac{\lambda_u}{2\gamma^2} \quad (2.22)$$

In order to obtain the wavelength observed at a small angle off axis ($\theta \neq 0$), the expression for the relativistic Doppler frequency formula (Eq. 2.20) can be modified using the Taylor expansion $\cos \theta = 1 - \theta^2/2 + \dots$, which is valid for small angles, as

$$f = \frac{c}{\lambda_u \left[1 - \beta \left(1 - \frac{\theta^2}{2} + \dots\right)\right]} = \frac{c}{\lambda_u \left[1 - \beta + \frac{\beta\theta^2}{2} - \dots\right]} = \frac{c}{\lambda_u (1 - \beta) \left[1 + \frac{\beta\theta^2}{2(1-\beta)}\right] - \dots}. \quad (2.23)$$

This expression can be simplified again for ultrarelativistic electrons ($\beta \simeq 1$ and $1 - \beta \simeq 1/2\gamma^2$) and written in terms of energy of the observed radiation as

$$E_\gamma = \hbar\omega_\gamma = hf = \frac{2hc\gamma^2}{\lambda_u \left[1 + \frac{2\gamma^2\theta^2}{2} - \dots\right]} \simeq \frac{2hc\gamma^2}{\lambda_u [1 + \gamma^2\theta^2]}, \quad (2.24)$$

which is sometimes more convenient to express as an observed radiation wavelength

$$\lambda \simeq \frac{c}{f} = \frac{\lambda_u}{2\gamma^2} (1 + \gamma^2\theta^2). \quad (2.25)$$

Therefore, the maximum energy is obtained on axis and is given by

$$E_{\gamma,\max} = \frac{2hc\gamma^2}{\lambda_u}, \quad (2.26)$$

which can be expressed in practical units as

$$E_{\gamma,\max}[\text{keV}] = 9.5 \times 10^{-7} \frac{(E_e[\text{MeV}])^2}{\lambda_u[\text{cm}]}. \quad (2.27)$$

It can be easily calculated that electrons with an energy of $E_e = 100$ MeV in an undulator with the magnet period $\lambda_u = 1$ cm generate radiation with the maximum energy $E_{\gamma,\max} = 9.5$ eV. Similarly to the bending magnet case, it requires electrons with an energy of more than 1 GeV in this magnet structure to generate radiation of $E_{\gamma,\max} = 1$ keV.

Furthermore, the equation 2.25 shows that the photon energy in the laboratory frame of reference depends on the angle of the emission. In order to determine the spectral width within the radiation cone, a difference between two angles can be calculated. If the wavelength λ is on axis ($\theta = 0$) and wavelength $\lambda + \Delta\lambda$ is off axis at an angle θ , then the ratio of the two, describing how the wavelength increases as a function of the angle, is expressed as

$$\frac{\Delta\lambda}{\lambda} \simeq \gamma^2 \theta^2. \quad (2.28)$$

Equation 2.28 suggests that the ratio between the either half of the angle $\theta = 1/\gamma$ and the maximum is $1/4$. Therefore, the cone containing half of the intensity encloses a relative spectral bandwidth of about 25 %. If a narrower spectrum is needed, typically a monochromator of some kind must be used. In case of the undulator radiation generated from an ultrashort electron bunch, it is possible to use a pinhole as a collimator to reduce the bandwidth since the wavelengths are angle-dependent and obtain a relative spectral bandwidth as narrow as $1/N$ (so-called "natural" bandwidth), where N is the number of oscillations. The angle θ_{cen} , in which the natural bandwidth $1/N$ occurs, can be calculated using a condition $\Delta\lambda/\lambda = 1/N$, which gives an expression

$$\theta_{\text{cen}} = \frac{1}{\gamma\sqrt{N}}. \quad (2.29)$$

The angle θ_{cen} is commonly referred to as *central* radiation cone. Since the maximum angle of the electron trajectory in the undulator is relatively small and it is considered that the energy of the electron stays constant due to a negligible effect of the radiated energy on the total electron energy, the longitudinal momentum is considered constant as well ($\gamma_z \simeq \gamma$). In the wiggler regime, however, where the electron trajectory can be significantly deviated from the axis, the longitudinal momentum cannot be considered constant anymore. Solution of equations of motion gives a relation between the transverse momentum p_z and the axial position x [93]

$$p_z = \gamma m_e v_z = \frac{eB\lambda_u}{2\pi} \sin\left(\frac{2\pi x}{\lambda_u}\right) \quad (2.30)$$

The dimensionless parameter K mentioned in the beginning of this section, which is sometimes called *undulator parameter*, is thus defined as

$$K = \frac{eB\lambda_u}{2\pi m_e c}, \quad (2.31)$$

which simplifies Eq. 2.30 to

$$p_z = \gamma m_e v_z = \frac{Kc}{\gamma} \sin\left(\frac{2\pi x}{\lambda_u}\right). \quad (2.32)$$

Eq. 2.32 shows that the amplitude of the oscillations is proportional to the parameter K . For this reason, the parameter is sometimes referred to as *deflection parameter*. The angle between the propagation axis x and the dimension of transverse oscillations z is (with an approximation $v_x \simeq c$)

$$\tan \theta_e = \frac{v_z}{v_x} \simeq \frac{K}{\gamma} \sin\left(\frac{2\pi x}{\lambda_u}\right). \quad (2.33)$$

Therefore the maximum angle of the trajectory is

$$\theta_{e,\text{max}} \simeq \frac{K}{\gamma}. \quad (2.34)$$

This is the source of differences between the undulator and wiggler. The characteristic angle of radiation emission is $\theta = 1/\gamma$. While for the undulator where $K < 1$ the maximum angle of

the electron trajectory is within the radiation cone, which results in the narrow angle-dependent spectral bandwidth. For the wiggler where $K > 1$, the maximum angle of the electron trajectory can be much larger and, thus, the properties of the generated radiation are different.

In the undulator regime, we could effectively consider that the relativistic factor γ does not change in the axial dimension since the excursions of the electron are small. This simplification is no longer valid in the wiggler regime. The effective axial relativistic factor defined as [93]

$$\gamma_z = \frac{\gamma}{\sqrt{1 + \frac{K^2}{2}}}. \quad (2.35)$$

must be taken into account. Modifying the undulator equation for the photon wavelength in the laboratory frame of reference by using γ_z instead of γ gives

$$\lambda = \frac{\lambda_u}{2\gamma_z^2} (1 + \gamma_z^2 \theta^2). \quad (2.36)$$

After substituting Eq. 2.35 in the previous formula, the general undulator equation is obtained as

$$\lambda = \frac{\lambda_u}{2\gamma^2} \left(1 + \frac{K^2}{2} + \gamma^2 \theta^2 \right). \quad (2.37)$$

Eq. 2.37 shows why the approximation without the term $K^2/2$ in Eq. 2.25 was possible in the undulator regime where $K < 1$ as the term is negligible for these values of K .

Furthermore, due to the transverse oscillations as $K \rightarrow 1$, higher harmonics at energies nE_1 are generated in addition to the fundamental wavelength given by Eq. 2.37 and their wavelengths can be immediately written as

$$\lambda_n = \frac{\lambda_u}{2\gamma^2 n} \left(1 + \frac{K^2}{2} + \gamma^2 \theta^2 \right) \quad (2.38)$$

When we consider a finite number of oscillation periods N again, properties of Fourier transform dictate that an n -th harmonic has an improved relative spectral bandwidth given by

$$\left(\frac{\Delta\lambda}{\lambda} \right)_n = \frac{1}{nN}, \quad (2.39)$$

where N is the number of magnetic periods. Due to the dependence of the wavelength λ_n on the angle of observation θ , each harmonic is broadened as we integrate over a finite radiation cone. When we take into account and integrate over the total angular distribution, the radiation spectrum becomes continuous but extends to the critical energy E_c , which is inversely proportional to the duration of the photon pulse $2\Delta\tau$ that reaches the observer as described in Eq. 2.10. This gives us

$$E_c \sim \frac{1}{2\Delta\tau} \simeq \frac{2\gamma^3 c}{R}, \quad (2.40)$$

where R is the radius of the circular trajectory in the magnetic field. In fact, in case of a sinusoidal trajectory, the critical energy is the same as for the bending magnet radiation (Eq. 2.16) in previous section, which can be expressed using the undulator parameter K as

$$E_c = \frac{3e\hbar B\gamma^2}{2m_e} = 3\pi \frac{\hbar c\gamma^2}{\lambda_u} K. \quad (2.41)$$

The duration of the radiation of one electron in an undulator or wiggler can be simply calculated from the number of oscillation periods N and the wavelength λ as

$$\tau = \frac{N\lambda}{c} \quad (2.42)$$

and the divergence is simply $\theta = 1/\gamma$ for undulator ($K \ll 1$) but $\theta = K/\gamma$ for wiggler (as was shown in Eq. 2.34).

Using a formula for the radiated power by an electron $P(t) = (e^2/6\pi\epsilon_0c)\gamma^2[(d\hat{p}/dt)^2 - (d\gamma/dt)^2]$ [60], where \hat{p} is the electron momentum normalized to $m_e c$, the averaged radiated power $\langle P \rangle_\gamma$ for both undulator and wiggler case can be derived and the resulting expression is [60]

$$\langle P \rangle_\gamma = \frac{\pi e^2 c \gamma^2 K^2}{3\epsilon_0 \lambda_u} \quad (2.43)$$

and the total energy radiated per one oscillation period is thus

$$I_\gamma = \frac{\bar{P}_\gamma \lambda_u}{c} = \frac{\pi e^2 \gamma^2 K^2}{3\epsilon_0 \lambda_u}. \quad (2.44)$$

These expressions can be used to obtain the number of emitted photons $N_\gamma = I_\gamma / \langle E_\gamma \rangle$. In the undulator case ($K < 1$), the mean photon energy is simply $\langle E_\gamma \rangle = E_{\gamma, \max}/2 = hc\gamma^2/\lambda_u$, which gives the number of emitted photons per electron per oscillation

$$N_\gamma = \frac{I_\gamma}{\langle E_\gamma \rangle} = \frac{e^2 K^2}{6\epsilon_0 \hbar c} = \frac{e^2}{4\pi\epsilon_0 \hbar c} \frac{3\pi K^2}{3} = \frac{2\pi}{3} \alpha_e K^2, \quad (2.45)$$

where α_e is the fine structure constant. In the wiggler case ($K > 1$), the synchrotron-like spectrum with the critical energy E_c has the mean photon energy $\langle E_\gamma \rangle = \frac{8}{15\sqrt{3}} E_c$, which gives the number of emitted photons per electron per oscillation

$$N_\gamma = \frac{I_\gamma}{\langle E_\gamma \rangle} = \frac{5\sqrt{3}}{8} \frac{e^2 K}{3\epsilon_0 \hbar c} = \frac{5\sqrt{3}\pi}{6} \alpha_e K. \quad (2.46)$$

Until now, it was discussed how one electron emits the synchrotron radiation in terms of quantities which are independent of the total electron number in the oscillating bunch. In case of an electron bunch consisting of N_e electrons, the shape of the radiation spectrum remains unchanged and the divergence is given by $\theta = 1/\gamma$ for an undulator and $\theta = K/\gamma$ for a wiggler. The temporal profile can be obtained simply by convoluting the temporal profile of the electron bunch with the radiation profile from a single electron. Given the duration of the electron bunch from a laser-plasma accelerator is typically in the fs range and the radiation length from one electron is $l = N\lambda$, where $\lambda = hc/E_\gamma$ is the wavelength from X-ray range (e.g. 1 keV and higher, which corresponds to a duration in the attosecond range, the duration of the X-ray radiation generated by the electron bunch is approximately equal to the electron bunch duration ($\tau_\gamma = \tau_e$).

Furthermore, motion and energy of an electron from the bunch can be modified due to the radiation from other electrons in the bunch, which results in microbunching of the electron distribution. Through this process, the coherent radiation is generated at a free electron lasers (FEL).

2.3 Betatron radiation

The bubble regime, described in Section 1.2.6, in which an ion cavity is created in the wake of the laser pulse, not only allows acceleration of electrons to relativistic energies, but can also generate femtosecond pulses of X-rays. As was previously described, electrons trapped at the back of the bubble are accelerated by the longitudinal electric field. In addition, the electrons that are injected off the laser propagation axis are forced by the transverse electric field to rapidly oscillate around the axis as shown in Fig. 2.2. The frequency of the motion can be derived using Gauss's law

$$\vec{\nabla} \cdot \vec{E} = \frac{\rho_e}{\epsilon_0}, \quad (2.47)$$

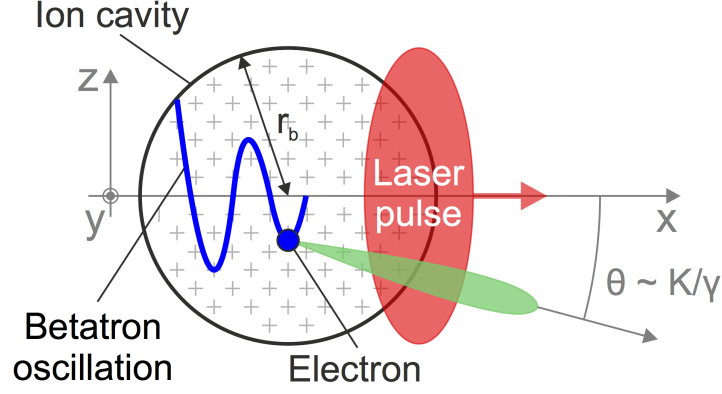


Figure 2.2: Schematics of the betatron radiation. Electrons inside the ion cavity are accelerated by the longitudinal electric field and at the same time they are forced by the transversal electric field to wiggle around the propagation axis.

where ϱ_e is the electron charge density and ε_0 is the vacuum permittivity. In this case, Eq. 2.47 can be written as

$$\frac{1}{r} \frac{\partial}{\partial r} (r E_{\perp}) = \frac{\varrho_e}{\varepsilon_0}, \quad (2.48)$$

which results in the expression for the transverse field

$$E_{\perp} = \frac{\varrho_e r}{2\varepsilon_0} = \frac{en_e r}{2\varepsilon_0}, \quad (2.49)$$

where the relation $\varrho_e = en_e$ with the electron number density n_e is used. The electron motion in this electric field is given by the Lorentz force equation (Eq. 1.1)

$$\frac{dp}{dt} = -eE_{\perp} = -\frac{e\varrho_e r}{2\varepsilon_0} = -\frac{e^2 n_e r}{2\varepsilon_0}. \quad (2.50)$$

Using $p = \gamma m_e v$, we get

$$\frac{dv_{\perp}}{dt} = -\frac{e^2 n_e r}{2\varepsilon_0 \gamma m_e} = -\frac{\omega_p^2}{2\gamma} r = -\omega_{\beta}^2 r, \quad (2.51)$$

where $\omega_{\beta} = \omega_p / \sqrt{2\gamma}$ is the betatron frequency. Therefore the wavelength of the betatron oscillations is given by $\lambda_{\beta} = \lambda_p \sqrt{2\gamma}$. This electron motion results in the emission of a synchrotron-like radiation called *betatron radiation*.

Therefore, the transverse velocity of electron oscillates as

$$v_{\perp} = \omega_{\beta} r_{\beta} \cos(\omega_{\beta} t) = k_{\beta} c r_{\beta} \cos(k_{\beta} c t), \quad (2.52)$$

where r_{β} is the amplitude of the oscillations, and the expression $\omega_{\beta} = k_{\beta} c$ was used.

The betatron strength parameter is equal to the maximum normalized electron transverse momentum and can thus be obtained as

$$K = \gamma k_{\beta} r_{\beta} = k_p r_{\beta} \sqrt{\gamma/2}. \quad (2.53)$$

The amplitude of the oscillations r_{β} is the radius of the betatron motion. It is analogous to the strength parameter of an undulator on a synchrotron as described in the previous section. The betatron strength parameter can be expressed in practical units as

$$K = 1.33 \times 10^{-10} \sqrt{\gamma n_e [\text{cm}^{-3}]} r_{\beta} [\mu\text{m}], \quad (2.54)$$

The bubble propagating through plasma behind the laser pulse thus acts as a microscopic undulator or wiggler with the period wavelength $\lambda_u = \lambda_\beta$ and the strength parameter K . As in the theory of synchrotron radiation, if $K < 1$, the amplitude of the betatron radiation is small, the ion cavity acts as an undulator and the radiation is collimated within an opening angle $\theta = 1/\gamma$. For $K > 1$, the cavity acts as a wiggler and the radiation is emitted within an opening angle $\theta = K/\gamma$ [93]. The duration of the betatron X-ray pulse is of the same order as the electron bunch duration [7].

The strength parameter K differs for electrons within the bunch because the radius of the betatron motion can vary. At the same time as electrons radiate their energy in form of photons, the mean energy of the electron bunch decreases and the energy spread increases [97].

The electron trajectory in its average rest frame is a figure-eight motion. However, in the laboratory frame, the radiation emitted in this motion appears as a collimated beam of X-rays due to the Lorentz transformation and Doppler upshift of the frequency.

The spectrum of the radiation depends on the strength parameter K . For the undulator regime ($K < 1$), the radiation is emitted at the fundamental photon energy E_γ with a narrow bandwidth in the forward direction. According to the theory set in the previous section, the energy of the radiation on axis ($\theta = 0$) is given by

$$E_\gamma = \frac{2hc\gamma^2}{\lambda_u \left[1 + \frac{K^2}{2}\right]} = 2\gamma^2 \frac{\hbar\omega_\beta}{1 + \frac{K^2}{2}} \quad \text{for } K < 1. \quad (2.55)$$

For the wiggler regime, the spectrum contains many harmonics of the fundamental energy and the critical energy of the produced betatron radiation can be calculated using the critical energy of the synchrotron radiation as

$$E_c = \frac{3e\hbar B\gamma^2}{2m_e} = \frac{3}{2}\gamma^2 \hbar\omega_\beta K \quad \text{for } K > 1, \quad (2.56)$$

where the expressions for the strength parameter K was used (Eq. 2.31) and for the betatron frequency $\omega_\beta = \omega_p/\sqrt{2\gamma}$ were utilized. The formulae for the photon energy can be expressed in practical units as

$$\begin{aligned} E_\gamma[\text{keV}] &= 5.25 \times 10^{-14} \gamma^{3/2} \sqrt{n_e[\text{cm}^{-3}]} \quad \text{for } K < 1 \\ E_c[\text{keV}] &= 5.24 \times 10^{-24} \gamma^2 r_\beta[\mu\text{m}] n_e[\text{cm}^{-3}] \quad \text{for } K > 1. \end{aligned} \quad (2.57)$$

Furthermore, the number of photons emitted per period per electron can be estimated as

$$\begin{aligned} N_\gamma &= \frac{2\pi}{3} \alpha_e K^2 \quad \text{for } K < 1, \\ N_\gamma &= \frac{5\sqrt{3}\pi}{6} \alpha_e K \quad \text{for } K > 1, \end{aligned} \quad (2.58)$$

where $\alpha_e = e^2/4\pi\epsilon\hbar c$ is the fine structure constant. These quantities can be written in practical units as

$$\begin{aligned} N_\gamma &= 1.53 \times 10^{-2} K^2 \quad \text{for } K < 1, \\ N_\gamma &= 3.31 \times 10^{-2} K \quad \text{for } K > 1. \end{aligned} \quad (2.59)$$

From the equations above, typical parameters of the generated X-ray pulses can be estimated. For electrons with an energy of 100 MeV ($\gamma \simeq 200$) wiggling in the ion cavity in a plasma of the density $n_e = 1 \times 10^{19} \text{ cm}^{-3}$ and a typical radius of betatron oscillations $r_\beta = 1 \mu\text{m}$, the strength parameter is $K \simeq 6$ (which means betatron sources typically operate in the wiggler regime) and the critical energy is expected to be $E_{\text{crit}} = 2.1 \text{ keV}$. When we consider an electron bunch charge of $Q = 10 \text{ pC}$ and electrons typically radiating at the maximum energy only for 3 betatron periods, the total number of generated photons is $N_\gamma \simeq 4 \times 10^7$ and they are emitted into a cone with an opening angle $\theta = 30 \text{ mrad}$.

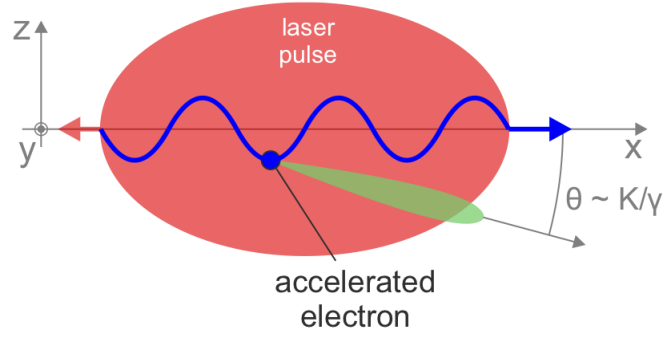


Figure 2.3: Schematics of the Compton radiation. Electrons passing through a laser pulse are forced to strongly oscillate by the electric field of the laser.

2.4 Inverse Compton scattering

Radiation of even higher energies can be generated by scattering a laser pulse on high energy electrons. Regular Compton scattering is a widely known process in which an X-ray photon is scattered on a motionless electron and the photon transfers a part of its energy and momentum to the electron, resulting in the energy after scattering [98]

$$E'_\gamma = \frac{E_\gamma}{1 + \frac{E_\gamma}{m_e c^2} (1 - \cos \theta)}, \quad (2.60)$$

where E_γ is the incident photon energy and θ is the scattering angle. Similarly, inverse Compton scattering is a process of a low energy photon scattered on a high-energy electron. The energy of the scattered photon is then given by [14]

$$E'_\gamma = \frac{E_\gamma (1 + \beta \cos \alpha)}{1 - \beta \cos \theta + \frac{E_\gamma}{E_e} (1 + \cos (\alpha + \theta))}, \quad (2.61)$$

where E_e is the incident electron energy, $\beta = v_e/c$ is the dimensionless electron velocity, α is the collision angle ($\alpha = 0$ for a head-on collision).

Using this process, the X-ray range can be reached even with few MeV electrons. In the average rest frame of the electron, the frequency of incident photons is $\tilde{\omega}_\gamma = 2\gamma\omega_\gamma$ due to the Doppler shift and the interaction in this frame can be described as Thomson scattering, the low-energy limit of Compton scattering when $E_\gamma \ll m_e c^2$. The maximum frequency of scattered photons is $\tilde{\omega}'_\gamma \simeq \tilde{\omega}_\gamma$ (for the undulator regime and the linear Compton scattering which occurs at low intensity of the laser pulse) or $\tilde{\omega}'_\gamma \simeq n\tilde{\omega}_\gamma$ (for the wiggler regime and the nonlinear Compton scattering which occurs at high laser intensity). In the laboratory frame, the frequency of the scattered photons is Doppler shifted again and photons with a frequency up to $\omega'_\gamma = 4\gamma^2\omega_\gamma$ or its harmonics are observed.

The laser pulse in this scheme can be seen as an undulator or wiggler with a spatial period given by the laser wavelength as

$$\lambda_u = \lambda_L/2 \quad (2.62)$$

and a strength parameter

$$K = a_0 = 0.855 \sqrt{I [10^{18} \text{ W/cm}^2] \lambda_L^2 [\mu\text{m}]}. \quad (2.63)$$

As in previous sections, for $K < 1$, the electromagnetic wave acts as an undulator and in the average rest frame of the electron, Compton scattering occurs in the linear regime and the emitted radiation is Doppler shifted in the laboratory frame. For $K > 1$, the electromagnetic wave acts as a wiggler, nonlinear Compton scattering occurs in the average rest frame of the electron and the spectrum contains many harmonics of the fundamental energy. The photon energies near axis can be calculated as

$$E_\gamma = \frac{4\gamma^2 hc}{\lambda_L} (1 + K^2/2) = 4\gamma^2 \frac{\hbar\omega_L}{1 + \frac{K^2}{2}} \quad \text{for } K < 1,$$

$$E_c = 3\gamma^2 \hbar\omega_L K \quad \text{for } K > 1,$$
(2.64)

which can be expressed in practical units as

$$E_\gamma[\text{keV}] = 4.96 \times 10^{-3} \frac{\gamma^2}{\lambda_L[\mu\text{m}]} \quad \text{for } K < 1$$

$$E_c[\text{keV}] = 3.18 \times 10^{-3} \gamma^2 \sqrt{I[10^{18} \text{ W/cm}^2]} \quad \text{for } K > 1.$$
(2.65)

The generated radiation is, as in the case of the betatron radiation, scattered within a cone of opening angle $\theta = 1/\gamma$ for the undulator case, and $\theta = K/\gamma$ for a wiggler; the duration is approximately equal to the duration of the electron bunch [14] and the number of produced photons is given by Eq. 2.58 as in the case of the betatron radiation, i.e.

$$N_\gamma = 1.53 \times 10^{-2} K^2 \quad \text{for } K < 1,$$

$$N_\gamma = 3.31 \times 10^{-2} K \quad \text{for } K > 1.$$
(2.66)

As can be seen from Eq. 2.61, the energy of the produced radiation in the undulator regime can be tuned by changing the energy of the incident electrons or by changing the collision angle α . The dependence of the maximum energy of generated X-rays on these parameters is depicted in Figs. 2.4 and 2.5. Moreover, as can be seen from Eq. 2.64, the critical energy of the radiation generated in the wiggler regime can be changed by varying the strength parameter $K = a_0$. Therefore, it can be done by changing the intensity of the scattering laser pulse. However, this energy tuning is also altering the number of generated photons, which is proportional to K as well.

So-called *all-optical Compton X-ray source* can be built (as opposed to the source based on a conventional electron accelerator and a laser system), which utilizes electrons accelerated in laser-plasma sources as described above, and a secondary, counter-propagating laser pulse. The brightness of such all-optical Compton source is about four orders of magnitude higher over Compton sources based on conventional accelerators [99, 100, 101]. In principle there are two potential schemes how to obtain a source of this type.

The first scheme uses a plasma mirror which reflects the driving laser pulse used for LWFA and thus the primary laser pulse is also used as the counter-propagating pulse for inverse Compton scattering [101] as shown in Fig. 2.6. A solid foil positioned close to the end of the plasma can serve as the plasma mirror [102]. It is ionized and the laser pulse is back-reflected by the created overdense plasma. This scheme is simple to set up and provides the spatial and temporal synchronization inherently. However, the option to tune the energy of generated X-rays using variations of the collision angle is not possible as the plasma mirror must be placed perpendicularly to the axis and thus only head-on collisions are possible.

The second scheme requires a secondary laser pulse that is focused onto the rear end of the plasma [103, 104, 105] as depicted in Fig. 2.7. Using the second focused laser pulse for

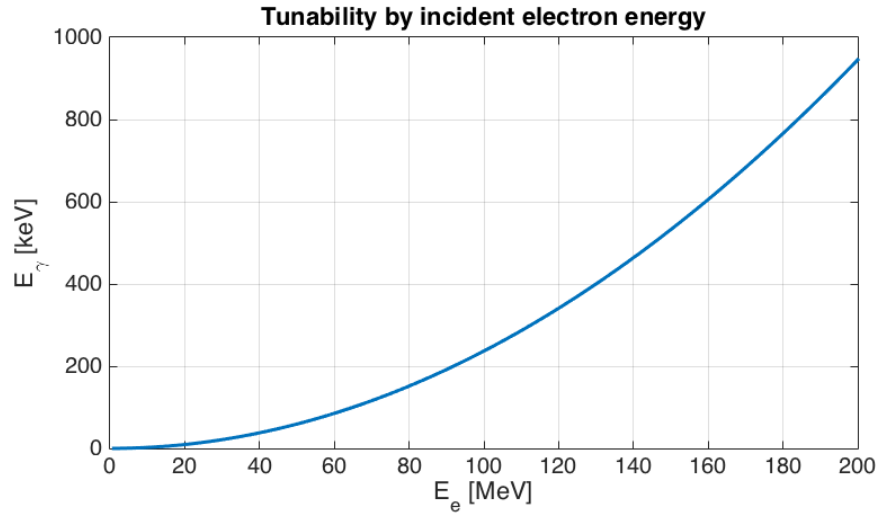


Figure 2.4: The dependence of the maximum energy of generated X-rays (i.e. corresponding to the scattering angle $\theta = 0$) on the incident electron energy E_e for the head-on collision ($\alpha = 0$). Variation of this parameter allows to finely tune the energy of the generated X-ray pulses.

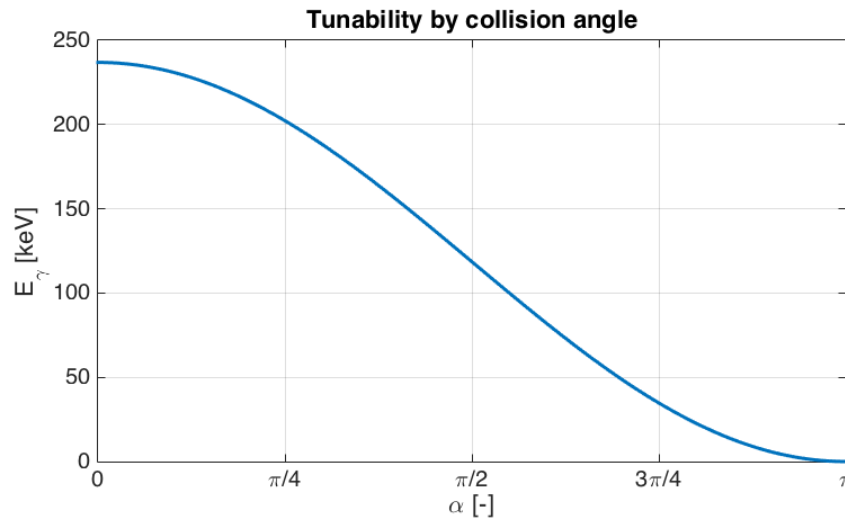


Figure 2.5: The dependence of the maximum energy of generated X-rays (i.e. corresponding to the scattering angle $\theta = 0$) on the collision angle α for the incident electron energy $E_e = 100$ MeV. Variation of this parameter allows to finely tune the energy of the generated X-ray pulses.

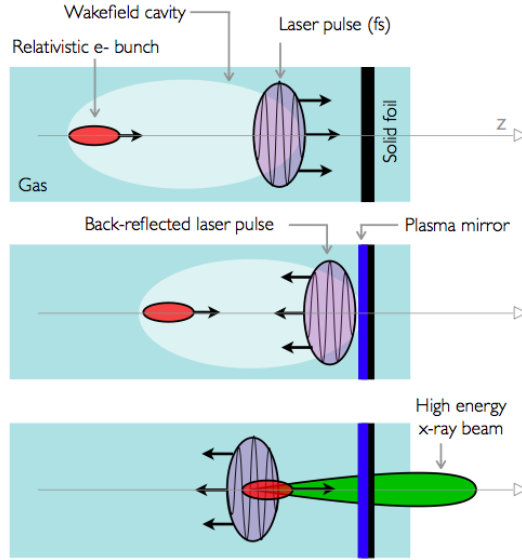


Figure 2.6: Schematics of inverse Compton backscattering. The laser pulse used for driving the laser-plasma electron accelerator is reflected using a plasma mirror created from a solid foil and inverse Compton scattering of the laser pulse and accelerated electrons occurs. Reprinted from [101].

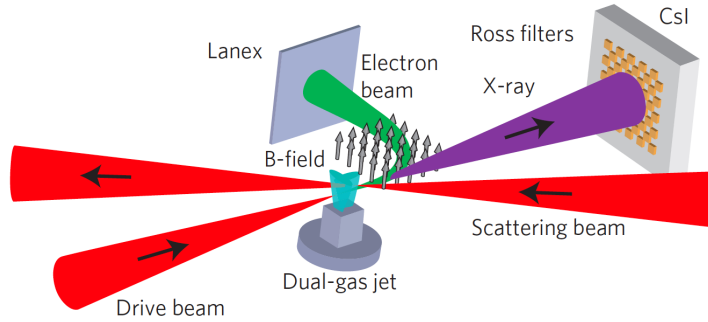


Figure 2.7: Schematics of two-laser pulse scheme for inverse Compton scattering. The primary laser pulse is driving the laser-plasma electron accelerator and the secondary laser pulse is focused at the end of the plasma for inverse Compton scattering on the accelerated electrons. Reprinted from [106].

scattering may provide a higher intensity of the incident photons when compared to the previously described method of plasma mirror and at the same time avoids creating bremsstrahlung background generated by accelerated electrons hitting the foil. Moreover, the propagation axis of the secondary laser beam can be placed at any angle, which results in an additional way of tuning the photon energy of the Compton source. A disadvantage of this mechanism is a difficult synchronization both in time (a sub-picosecond laser pulse scattering off a femtosecond electron bunch) and in space (the size of the focal spot of the laser beam as well as the electron bunch size are typically in the order of a few microns).

The energy of X-ray pulses can reach up to the MeV range [103] when ultra-relativistic electron bunches and a sufficient laser pulse intensity are employed. When we consider a counter-propagating laser pulse with a strength parameter of $a_0 = 0.5$ and (as before) a monoenergetic electron bunch with an energy of 100 MeV and a charge of 10 pC, it can be calculated that the number of scattered photons is in the order of 10^7 and they have an energy $E \simeq 250$ keV within an angle of 5 mrad, considering that the laser pulse contains about ten optical cycles.

This means the radiation obtained from inverse Compton scattering has an energy that is two orders of magnitude higher than the betatron radiation at approximately the same number of photons, while the photons are produced within a cone with opening angle of 5 mrad, which is narrower by a factor of 10.

The femtosecond X-ray pulses generated by the all-optical inverse Compton scattering source enable novel applications in advanced biomedical imaging [107, 108], K-edge imaging [109], phase-contrast imaging [110, 111, 112], dynamic diffraction studies of laser-pumped materials and time-resolved molecular dynamics [113, 114], nuclear physics research [115, 116, 117], ultrafast nuclear science [118, 119], radiography and radiotherapy [120, 121, 122], or construction of gamma-gamma colliders [123, 124].

2.5 Applications of betatron and Compton radiation

The betatron and Compton sources generate X-ray radiation of unique properties while being tunable in energy, which opens broad possibilities of applications for these sources. The betatron source provides X-ray radiation with a broadband continuous spectrum with the critical energy of up to hundreds of keV, a narrow divergence (less than ten mrad), a micron source size, a femtosecond pulse duration and a perfect synchronization with the laser that drives the source. The Compton source provides X-ray radiation with similar properties but in addition it can generate quasi-monochromatic radiation in the undulator regime and much higher energy since the photons are double Doppler-shifted. While it is possible to find radiation sources with some similar properties of those mentioned above, it is the combination of these parameters and the tunability of the betatron/Compton source that make it unique and feasible for user applications.

In this chapter, betatron and Compton source applications are explored, their performance is compared to other sources and necessary improvements on the sources, which can revolutionize the medicine and industry, are stated.

2.5.1 X-ray Phase Contrast Imaging and microtomography

In comparison to conventional X-ray radiography, X-ray Phase Contrast Imaging (XPCI) offers superior image quality. Objects, which are quasi-transparent for X-rays, such as soft tissues, and which have homogeneous absorption profile, are invisible using absorption based radiography [125, 126, 127]. XPCI takes advantage of the modifications of the phase of X-ray beam rather than simply recording its amplitude with common X-ray radiography techniques. In XPCI, the image contrast is achieved by phase shifts in X-rays passing through the sample. The cross-section of the X-ray phase shift interaction is a few orders of magnitude higher than the cross section for absorption [127], which allows highly sensitive imaging of a sample with gradient or relatively homogeneous absorption coefficients. Therefore, XPCI is more sensitive to small density variations and offers better contrast for various biological samples than conventional radiography of objects transparent for X-rays.

XPCI has been achieved using several techniques developed in past years. They are based on interferometry [126], gratings [131], free space propagation [132] and tested with various X-ray sources. Standard X-ray tubes and laser-based K-alpha sources were used [133, 134, 135] as well as X-pinch radiation [136]. Accelerator-based synchrotron sources and X-ray free-electron lasers (XFELs) are routinely used to perform the XPCI. While these sources allow the production of X-rays at remarkable brightness, they have never been available for a wide user community due to their immense costs and size.

With a micron source size [135, 137], a high peak spectral brightness [128, 132, 138, 139], laser driven betatron source combines properties that are of great interest for XPCI and microtomography. Although monochromatic X-ray sources are commonly used for XPCI, it is also

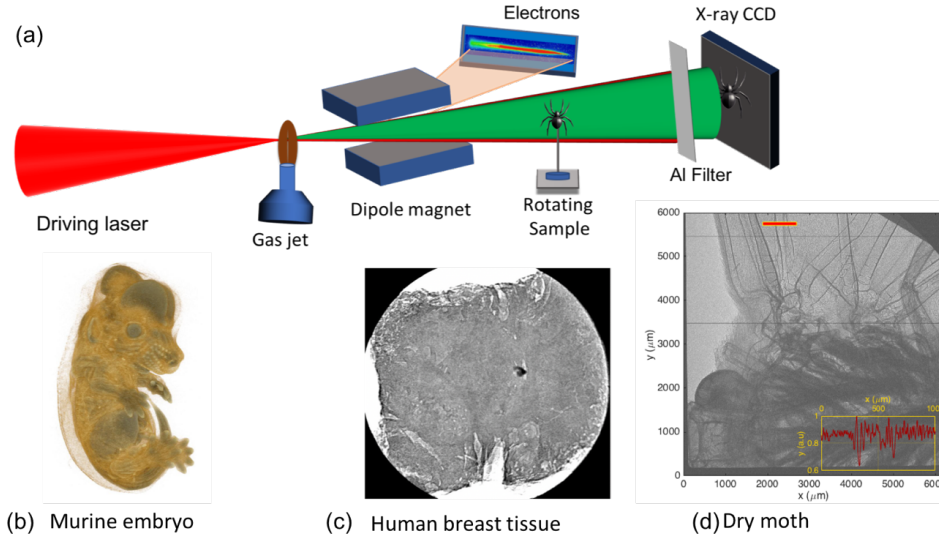


Figure 2.8: (a) Schematic drawing of experiment for propagation-based x-ray phase contrast microtomography. The laser pulse (red) is focused onto the gas jet and drives electron acceleration and betatron x-ray generation. Dipole magnets of the electron spectrometer deflect the accelerated electrons (yellow) away from the laser axis onto a scintillating screen. The x-ray beam (green) transmitted through the foil is recorded by a CCD. (b) A tomography image of a murine embryo [128]. (c)-(d) Phase contrast images of clinically relevant human breast tissue [129] and a dry moth specimen using betatron x-ray sources [130]. Reprinted from [128, 129, 130].

possible to employ polychromatic sources with high spatial coherence [140] such as the broadband betatron X-ray source, the spatial coherence of which is sufficiently high (tens of microns) to make propagation-based phase contrast imaging possible.

In this technique, the distances of the object from the source and the detector meet the requirements for the near-field Fresnel diffraction regime [141], which does not require complex and expensive X-ray optics. The few femtosecond pulse durations of the betatron potentially provide a few orders of magnitude better temporal resolution than commonly available sources. Both the source flux and fluctuations of the source could be further improved using ionization-induced injection in gas mixtures. The improved technique of electron injection in the laser-wakefield acceleration enhance the photon flux of the betatron sources. Recent experimental results reported the betatron photon flux can reach up to 10^{10} photons per shot [132, 138, 139, 142].

X-ray photon energies in the range of 10–30 keV are used for soft tissue absorption radiography (e.g. mammography) and 50–150 keV for hard tissue (bone) radiography. With a PW-class laser, it is possible to generate betatron radiation in the energy range of up to hundreds of keV. Combining with a high repetition rate and the number of photons of 10^{10} per shot, the betatron source can provide a high photon flux (10^{11} per second) that will be an ideal X-ray source required for XPCI covering various thickness biological samples. Proof-of-principle experiments on XPCI and microtomography of biological samples have been performed recently using betatron radiation at different laser facilities [111, 112, 143].

One of the possible medical applications of XPCI is searching for and localising breast cancer. In addition, XPCI with betatron radiation can be used for ultrafast X-ray imaging with femtosecond temporal resolution [138] since betatron radiation can provide the best temporal resolution ever achieved. X-rays radiated by relativistic electrons driven by well-controlled high-power lasers offer a promising route to a proliferation of this powerful imaging technology.

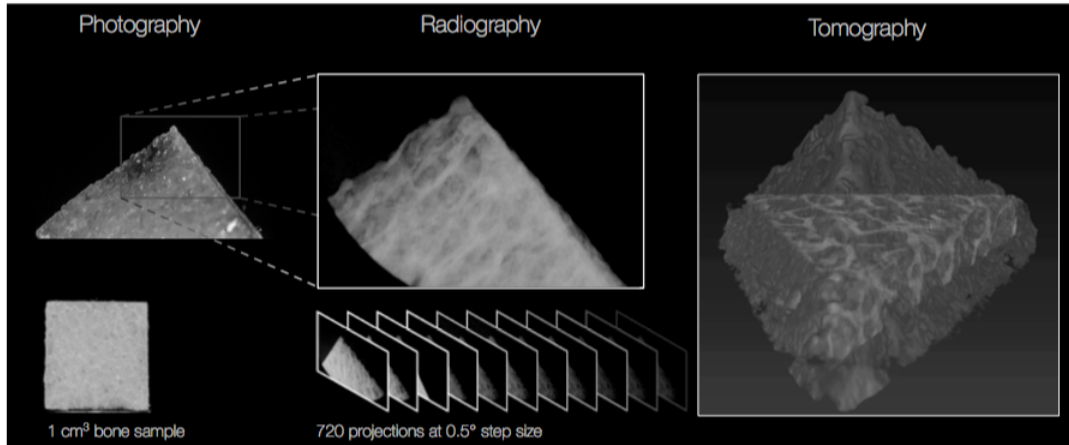


Figure 2.9: Tomography of cancellous bone sample using LWFA-driven betatron x-ray source, taken from [132].

Furthermore, a higher repetition rate allows motion freezing and time lapse imaging, and allows real-time visualization of internal physiological mechanisms in biological phenomena (e.g. the respiration and circulatory system, the beating of a heart, etc).

A second potential application of betatron radiation source is as a source for the X-ray phase contrast microtomography. With a small source size, beam-like source that operates at high repetition rate, betatron source is ideal to perform the microtomography. Proof-of-principle experiments on microtomography of human bone have been recently performed using betatron source [128, 132]. The photon flux over 10^9 photons per shot is sufficient for single-shot acquisition of projections, and tomographies can be generated using iterative reconstruction algorithms. Furthermore, being able to acquire tomographs of dense objects within minutes would be a major step towards real-life applications of laser-driven X-ray sources.

2.5.2 Femtosecond X-ray Absorption Spectroscopy

X-ray Absorption Spectroscopy (XAS) is a powerful tool as it can simultaneously reveal both electronic and atomic structures, and thus unravel their non-equilibrium dynamic interplay which is at the origin of most of the ultrafast mechanisms. The oxidation state of the absorbing element is revealed by a "chemical shift", meaning a translation of the absorption edge feature in energy. Geometric structure is studied by analyzing the extended X-ray absorption fine structure (EXAFS), which appears as oscillatory features in X-ray absorption over a few hundreds eV reach above an absorption edge. The X-ray Absorption Near-Edge Structure (XANES) and Extended X-ray Absorption Fine Structure (EXAFS) exploit wide range of applications in chemistry, gas-phase systems, materials science or in the study of complex biological samples. These absorption spectra can provide not only basic parameter diagnostics, but also information about the ionic correlation and internal structure on the matter. Time-resolved XAS can also be used to study the pathways of photoactivity in these systems.

X-ray absorption spectroscopy has been extensively developed at synchrotrons, with X-ray energy in the range 1–30 keV, but the temporal resolution of the observed phenomena is limited by the duration of the synchrotron pulses (~ 10 ps). For most processes governed by atomic motion (eg. structural changes and phase transitions), the timescale of interest corresponds to one vibrational period, which is about 100 fs. In laser facilities, XAS have been developed on OMEGA to diagnose iron up to 560 GPa [144], and at LULI-2000 to diagnose metal-nonmetal transitions [145] and to investigate the electron structure of highly compressed Al [146] but the

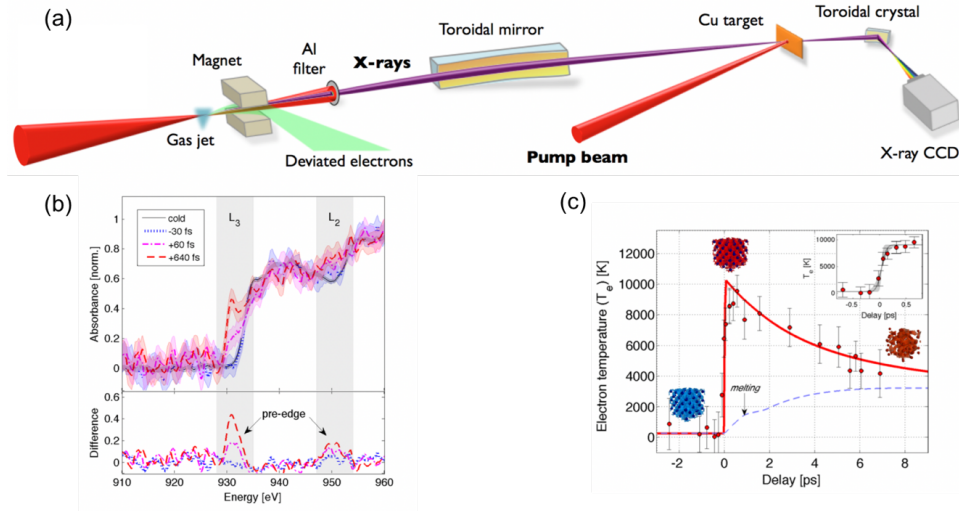


Figure 2.10: Experimental setup to study femtosecond x-ray absorption spectroscopy using laser-driven betatron x-ray source. (a) experimental setup showing the full scheme of pump-probe technique (b) Time resolved Cu XAS data near Cu L-edge (c) Time evolution of the electron temperature. Reprinted from [149].

temporal resolution of these measurement is still poor. XANES experiments using the XFEL beam as a probe for shocked-compressed matter were performed at LCLS near the Molybdenum LIII edge (2.52 keV) [147], and the iron K-edge [148]. However, the stochastic nature of the LCLS SASE FEL spectrum makes this type of measurement extremely challenging, and since LCLS is used as a probe, it cannot be used as the pump, even in the two-color scheme, where pulses cannot be separated by over 150 fs.

The LWFA-driven betatron radiation is a suitable candidate for laboratory-based time-resolved X-ray absorption spectroscopy (EXAFS and XANES) applications due to their unique features: ultrashort pulse durations (\sim fs), a continuous spectrum from soft to hard X-ray energy range, intrinsic all optical and jitter-free synchronization with the driving laser pulse, a sufficient photon flux, and long-term stability. Currently, state-of-the-art betatron radiation sources produce up to 10^{10} photons (in the whole spectrum) and numbers of $10^5 - 10^6$ photons/eV have been reported [132, 139, 142]. Recently, experimental result from LOA [149] reported, for the first time, femtosecond time resolved X-ray absorption spectroscopy of heated Cu foil using a LWFA-driven betatron X-ray source. The X-ray absorption spectra are registered near the Cu L-edge (0.95 keV) with femtosecond temporal resolution. Such femtosecond time-resolved X-ray absorption spectra of heated matter at well-defined density and temperature conditions, giving access to its electron temperature, ion temperature, and charge state as the sample relaxes back to equilibrium. A stable broadband betatron source will be extremely useful to study the warm dense matter (WDM).

In chemistry, the time-resolved X-ray absorption spectra are measured shortly after photoexcitation of the sample, is ideal for determining the oxidation state and structure of intermediate photoproducts in the photoreduction of the sample. Time resolved XAS of aqueous solution Ferrioxalate complexes, which are exist in natural waters including aerosols, have been reported recently using plasma-based x-ray sources [150], the time resolution will be enhanced using the betatron x-ray source.

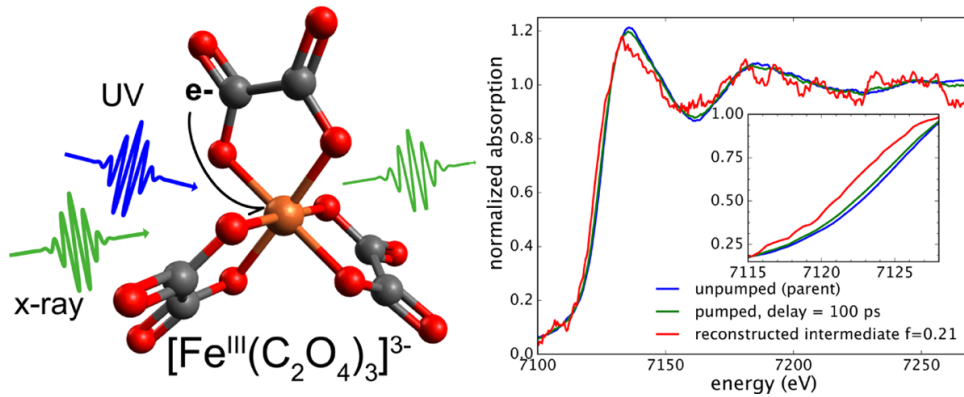


Figure 2.11: Molecular structure of Ferrioxalate complexes and its time resolved x-ray absorption spectra, taken from [150].

2.5.3 Time-resolved imaging of shock-compressed matter

The femtosecond duration of betatron radiation makes it an ideal candidate for performing time resolved imaging of rapidly evolving phenomena, and the pulses are naturally well synchronised to high energy laser pulses for pump-probe experiments. Understanding the behaviour of materials in extreme states of temperature and pressure is fundamental to multiple fields of physics, from condensed matter to meteorite impacts on planetary atmosphere, or material failure mechanisms. The only way to access states at very high energy densities in the laboratory are dynamic compression experiments, where a shock wave is driven into a material by a pulsed laser. Shock in the material (solid or foam) can be generated by a pump laser or a relatively higher energy and longer pulse laser beam can be used to create strong shocks in materials and extreme states reaching high temperatures and densities at equilibrium relevant to planetary interiors and melting of solids.

Both the shock front and the post-shock are extremely dense regimes with the electron densities ranging from 10^{21} – 10^{26} cm^{-3} . A commonly used device to measure the shock velocity in high energy density matter is VISAR based on the optical laser that does not provide detailed information about the shock front structure. The current X-ray sources used for imaging of the shock do not provide a high temporal resolution that is required to image these laser-driven shocks and other fast phenomena as the radiation from synchrotron is limited to a temporal resolution of ~ 100 ps [151]. The critical aspect of radiographing laser-driven shocks in High Energy Density (HED) is to have: (A) High energy photons to penetrate highly dense plasmas, and (B) enough photons to overcome the plasma self-emission. The LWFA driven X-ray sources provides very high peak brightness, about six orders of magnitude higher than conventional X-ray backlighter sources due to their shorter duration (femtosecond vs. nanosecond), and are thus extremely beneficial to image the high dense shock structure. Also, due to micron-scale source size, the LWFA driven X-ray source possess significant spatial coherence that allows obtaining the phase contrast image of the shock front.

The intrinsic temporal resolution of betatron radiation is about 10 fs [152], indicating that significantly faster processes could be probed in future without compromising spatial resolution. This suggests that future compact betatron imaging beamlines could be useful in the imaging and diagnosis of high-energy density physics experiments.

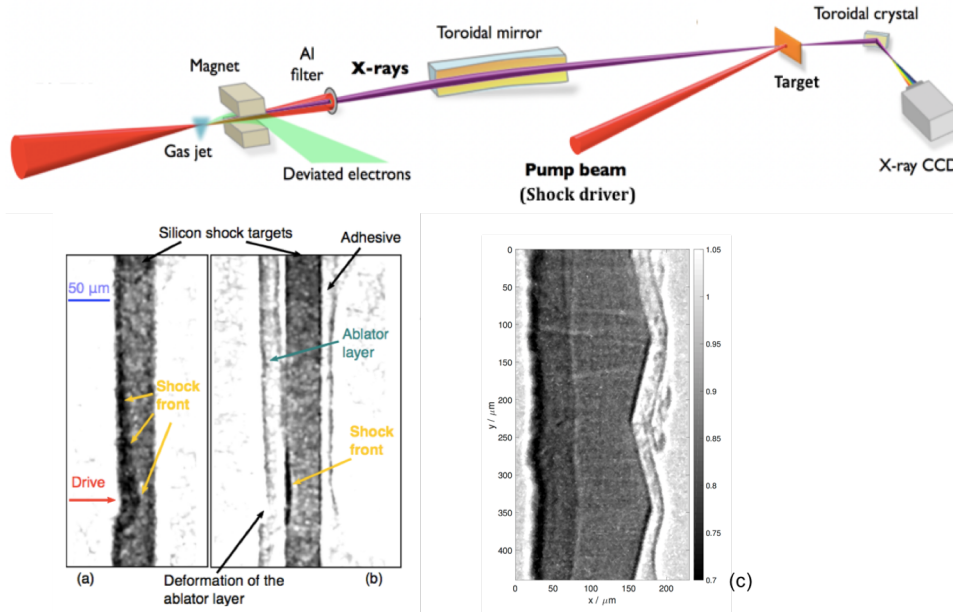


Figure 2.12: Schematic setup phase contrast imaging of laser produced shock wave (top). (bottom) High contrast and high resolution HED shock images on Silicon using LWFA driven betatron radiation, reprinted from [142].

2.5.4 Opacity measurement of dense plasma

In High-Energy Density physics (HED), opacity plays a crucial role to understand the rate at which radiation is absorbed by matter. It plays among the most important issues in HED science because it aspects nearly every HED experiment involving radiation. Numerical modelling shows that the rate of ionization is in the order of a few tens of femtoseconds, this means that ideally the hard X-ray source for an opacity measurement experiment should be a few tens of femtoseconds in duration to provide time-resolved information [153]. The ionization state of a hot (> 100 eV) and dense plasma can be determined by measuring its emission spectrum. This could be achieved by analysing the transmission of ultrafast betatron X-rays through the sample at different delays between the pump and the probe and at energies corresponding to a given electronic shell absorption lines [154]. The LWFA driven betatron source would be an ideal source to perform opacity experiment, the photon flux and temporal resolution required are very much sufficient, in Warm Dense Matter (WDM) to benchmark the opacity model that are essential for HED science.

2.5.5 Time-Resolved X-ray Solution Scattering (TRXSS)

X-ray solution scattering is a technique widely used in characterizing biomolecules, soft matter and chemicals in their native state. The technique is being practiced with synchrotron radiation which at best can provide sub-100 ps resolution. In order to trace the extremely short-lived structural changes in photo-activated molecules and chemical reactions, X-ray sources with femtosecond pulse duration are required. This is where the novel ultrafast X-ray sources such as X-ray free electron lasers (XFELs) and laser-driven X-ray sources such as the betatron X-ray source will become particularly useful. While the laboratory ultrafast X-ray sources are still in the developmental phase, the large-scale X-ray free electron lasers have already come into operation. Several groundbreaking experiments has been performed using such sources. For

instance, the ultrafast bond formation dynamics in the chemical reactions has been studied at Japanese XFEL using time-resolved X-ray solution scattering [153]. Similarly, the ultrafast protein quakes have been reported by [155] using the time-resolved wide-angle solution scattering. These examples depict that the ultrashort X-ray is required to follow the ultrafast reaction and molecular dynamics. However, majority of such experiments are reported with X-ray free electron lasers, which are not accessible to large number of users. Having in-house sources, such as the betatron source, would facilitate large number of users and complement other existing large-scale facilities in building new understanding in fundamental biology and chemistry.

2.5.6 Femtosecond Time-Resolved X-ray Diffraction

Light induced phase transition is an important phenomenon observed in materials. These changes usually occur in very short timescales which are quite interesting for applications, such as ultrafast optical switches. In order to follow the phase changes and learn about all the intermediate transitional states, we need techniques based on hard X-rays which can provide a temporal resolution in the order of femtoseconds. Hence, sources such as XFELs and laser-driven X-ray sources can make huge impact in this line of research. Betatron radiation which can deliver about $10^5 - 10^6$ photons after mono-chromatization can be a suitable probe to making atomic-scale movies of such phase transitions. A seminal work done in this line of research was done by [156].

A similar work on VO_2 crystals has been done using Japanese XFEL which reports the transition of the insulator phase to a metallic phase being occurred at a few hundreds of femtosecond [157]. However, an elaborated study of such phase transition and its correlation with the charge and spin dynamics is yet to be performed. In-house femtosecond sources such as the betatron source will come into play in providing such experiments revealing all possible mechanism in the metal-insulator phase transition.

In addition, the LWFA betatron X-ray source would be an ideal candidate for the time-resolved ultrafast Laue X-ray diffraction which uses a broadband X-ray source because the Bragg condition can be satisfied in multiple crystallographic planes in a single shot. Each plane results in a characteristic Laue spot, giving rise to a complex diffraction pattern of the bio-crystals.

2.5.7 In-operando studies of electrochemical batteries

There is a huge interest of scientific community to develop a new type of energy materials and to improve the existing ones. Li-ion batteries are one of the variants of the existing commercial energy materials. Understanding how the structural and chemical changes occur in the batteries during operation can lead to the improvement of the energy storage in these materials [158]. This would be particularly important in realizing battery-driven next generation automobiles.

The technique used in structural characterization is X-ray tomography while the chemical environments in batteries are probed using X-ray absorption fine structure (XAFS). With the availability of broadband X-ray sources, such as the betatron source, the characterization of battery exploiting such source would be a promising research direction. Additionally, the ultrashort pulse from the betatron source can also help in tracing the short-lived phenomenon in batteries such as charge transfer.

2.5.8 Femtosecond X-ray damage threshold measurement in bio-crystals

Femtosecond X-ray pulses would facilitate a new regime with respect to the X-ray exposure that can be tolerated by biological samples. However, the photon-matter interactions cause heavy ionization and subsequent sample decay. The ionization causes the molecular bonds to break and leads to subsequent changes in the structure. In a crystalline sample the ionization

is spread out among a large number of individual molecules, which reduces the influence on the diffracted signal. The ionization of the crystal leads to both a resolution-dependent reduction in Bragg signal and the addition of uniform diffuse scattering [159]. Despite the X-ray matter interaction being ultrashort in time scales, it may limit the diffractive possibilities. Understanding these processes is thereby paramount to identifying and overcoming present limits of femtosecond crystallography [160]. The effect of radiation damage due to ultrashort, intense X-ray pulses on the bio-crystal and protein is required to be investigated using ultrashort X-ray sources.

2.5.9 Nuclear resonance fluorescence

While soft X-rays interact with the inner-shell electrons of atoms, hard X-rays and gamma-rays interact with the nuclei of atoms and are a powerful tool to probe unique properties of specific isotopes of certain materials. Nuclear Resonance Fluorescence (NRF) is a process, in which a high-energy photon is absorbed by a nucleus, which consequently emits a photon of a slightly lower energy in order to get back to the equilibrium. The energy of the absorbed and emitted photons is not equal due to recoil [161] and typically differs by a few tens of eV, which is larger than the natural linewidth and NRF thus cannot be excited by the emission from the same isotope.

In a similar manner to the K-shell and L-shell fluorescence lines in atoms providing information on properties of the spin and oxidation states of a chemical element, NRF can provide information on properties of nuclei of isotopes, such as spin, parities and excitation energies [162]. NRF can be used for non-destructive evaluation of materials [163, 164], analysis and processing of nuclear waste [165, 166], mining [167] or homeland security [163, 168, 169].

The downside of NRF is the small spectral width of the NRF lines ($\Delta E/E \sim 10^{-6}$). While it is possible to detect NRF lines with broadband gamma-ray sources that use bremsstrahlung radiation, it is more convenient to use a narrow-band gamma-ray source. It has been shown that a Compton source with a conventional accelerator can excite NRF lines. Although it is possible to generate MeV photons using a betatron source, inverse Compton scattering, in which low-energy laser photons (\sim eV) are scattered off high-energy electrons and causing a double Doppler shift in the photon energy, is a more promising option as the requirements to generate gamma-rays are much lower (electrons of approximately 200 MeV are needed to obtain photons in the MeV range from a Compton source, while electrons with an energy of a few GeV are required for the same purpose in a betatron source).

Recently, LWFA-driven Compton scattering source reported 10^7 photons/shot within a 10 % bandwidth at 13 MeV [171], which makes NRF application within the reach of modern Compton sources based on PW-class laser systems.

2.5.10 Medical radioisotopes production

Since the route of the nuclear fission is slowly being abandoned in favor of renewable sources, a major concern of the nuclear medical field emerged - a lack of availability of medical isotopes in the near future. Producing the radioactive isotopes for medical applications is a possible field where LWFA-based photon sources can make a real impact. The radioisotopes used in nuclear medicine are chosen by their cost and availability but do not necessarily represent the best solution. Table-top LWFA-based Compton radiation sources may decrease costs and increase availability of sources with optimum nuclear and chemical properties. Compton scattering is produced when relativistic LWFA electrons are wiggled in the field of a second laser pulse and emit double Doppler-shifted radiation and are more efficient to produce photons beyond 100 keV. The highest photon energy reported to date in a LWFA-driven experiment is 18 MeV [172], similar or even higher photon energy can be easily accessible at PW-class laser facilities (with 2 GeV electrons, photons of up to 90 MeV can be generated). Furthermore, the Compton

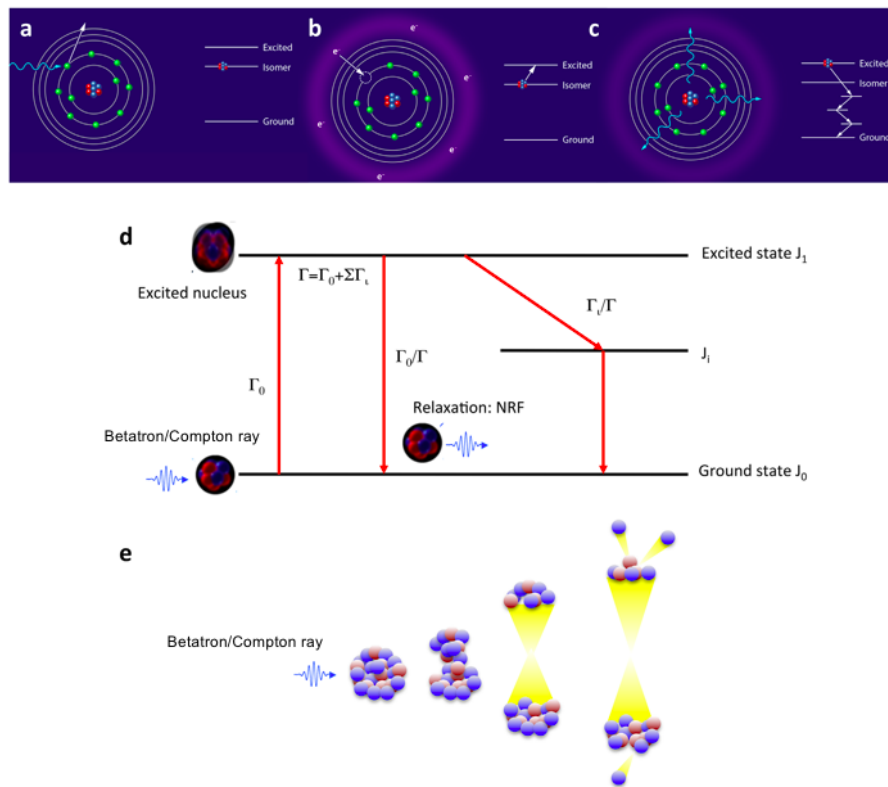


Figure 2.13: Scheme illustrating the nuclear processes that could be triggered by LWFA-driven X-ray and gamma ray sources, (a-c) nuclear excitation by electron capture, (d) nuclear resonance fluorescence, and (e) photoemission. Reprinted from [170].

source is easier to tune than betatron radiation and can have a narrower bandwidth (provided the electron energy spread is small and the source operates in the undulator regime where the scattering laser has a normalized vector potential $a_0 < 1$). The photon source required for isotopes production application must have a high average flux ($10^{13} - 10^{15}$ photons/s), a small relative spectral bandwidth, a small diameter, and the correct energies for the γ -induced reactions in the energy range of 1 – 10 MeV.

Despite the significant research effort currently ongoing on LWFA-based Compton scattering sources, great improvements are necessary to increase the average flux (from $\sim 10^8$ photons/s to 10^{13} photons/s) and decrease the spectral bandwidth (from 50 % to 1 % and less) for these nuclear physics applications.

EXPERIMENTAL RESULTS AND DISCUSSIONS

Building the tunable source of X-ray pulses based on the betatron or Compton radiation using a few-terawatt laser pulse required dividing the task into three stages. For each of these steps it was necessary to introduce new diagnostics and equipment that had to be designed for our experiments from the beginning. This chapter describes all the effort which I did as a part of the work on this dissertation in pursuit of creating the secondary X-ray source. The work included designing plasma accelerator and particle diagnostics, running the experiment and adjusting the parameters based on the performance, and analysing all experimental data.

The first stage consisted of building a stable laser-plasma electron accelerator and performing optimization of the laser and plasma parameters in order to minimize energy spread and divergence of the electron beams, and to stabilize the electron energy via various injection techniques. The second stage included meeting the requirements of the bubble regime for generation of the betatron radiation. The third stage was building the Compton source and has been by far the most challenging experimental part of the three steps due to high demands on the generated electron beam in terms of electron flux. These stages can be build experimentally with some modifications of the setup, employing new sets of diagnostics while improving others that are fundamentally same throughout all experimental campaigns.

In this chapter, experimental results obtained at Ti:Sapphire laboratory at PALS Research Center are presented. Our small lab was used for prototyping the diagnostics and other experimental equipment, which had to be designed from the beginning, and then calibrated and properly tested. First, the Ti:Sapphire laser system is described and the main experimental setup is presented. Special focus is put on the description of the plasma and particle diagnostics, which I designed for the experiments. Second, two sets of Ross filters for hard X-ray spectroscopy are described as an important element of the experimental setup. Third, a specially designed piece of equipment which enables generation of Compton radiation at 10 Hz repetition rate is presented. And last but not least, the obtained experimental results are described and all monitored quantities from the diagnostics are discussed, including generated electron bunches and betatron radiation. Moreover, the first application of the betatron source is presented as the X-ray source size allows phase-contrast imaging.

3.1 Experimental setup at PALS laboratory

The Ti:sapphire laser system at the PALS research center provides laser pulses with a maximum power of 25 TW, duration of 40 fs and central wavelength of 808 nm at maximum repetition rate of 10 Hz. During the experimental campaigns, however, it was mostly operated in the single shot regime, generating laser pulses with a duration of 50 fs and energy of 600 mJ on target. The laser beam on target was linearly polarized at an angle of approximately 20 degrees with respect to the horizontal plane.

The experimental setup, which I designed and built myself as a part of the work on this dissertation, is shown in Fig. 3.1. The laser pulse was focused using an off-axis parabolic (OAP) mirror with an effective focal length $EFL = 326$ mm corresponding to $f/6.5$. The beam has a

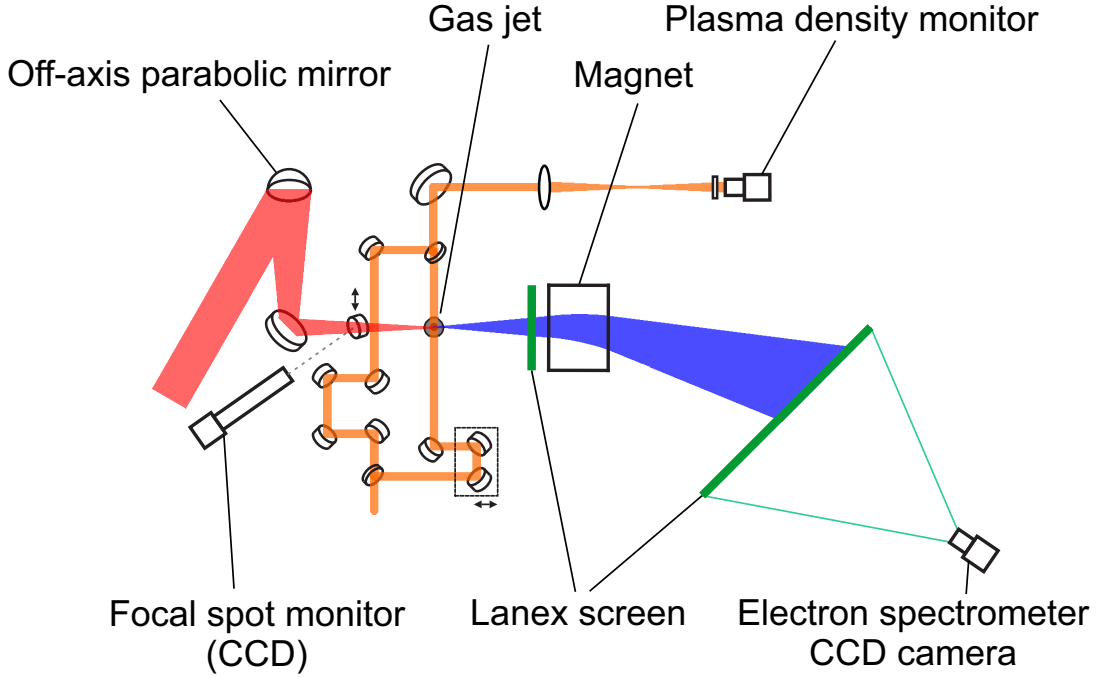


Figure 3.1: The experimental setup of the laser-driven electron accelerator and all used laser, plasma and particle diagnostics. The femtosecond laser pulse (red) is focused onto the gas jet target. A CCD camera is used as an offline diagnostics of the focal spot. The plasma created in the target region is probed by the auxiliary pulse employing the Mach-Zehnder interferometer (orange). Accelerated electrons (blue) are deflected and their energy is measured by the magnetic spectrometer, and the pointing stability is monitored before electrons enter the magnetic field of the spectrometer. Electrons are detected by scintillating Lanex screens (green) imaged by their respective CCD cameras.

supergaussian profile and its diffraction-limited size for this f-number is $\simeq 10 \mu\text{m}$.

3.1.1 Target

The target is represented by a gas jet consisting of a valve mounted with a supersonic de Laval nozzle, and various compressed gases are used as the accelerating medium. During the experiment, dry air, a mixture of helium and argon and eventually a mixture of helium and dry air were used as supersonic gas jet targets, respectively, and in both cases, the backing pressure was set in the range of 3–20 bar. The approach to use dry air was chosen to test the possibility of an inexpensive, widely available gas as the accelerating medium in addition to commonly used noble gases. Helium was mixed with argon and with dry air, respectively, in both cases in a pressure ratio of 99:1 in an attempt to increase the electron bunch charge using the ionization injection mechanism [86] as was theoretically described in chapter 1. In the case of dry air, the electrons were injected into the accelerating phase by self-injection and most probably also by the ionization injection in self-focusing. In the case of admixture of argon in helium, the ionization injection regime was employed as well. Moreover, a razor blade was used with the mixture targets in order to create a step density gradient at the front of the gas jet increasing the injected charge and consequently the number of generated X-ray photons.

3.1.2 Focal spot and laser pointing monitor

Before even starting to use the laser pulse to ionize the gas and accelerate electrons by the wakefield in plasma, the focal spot of the laser is optimized for the experiment using an offline

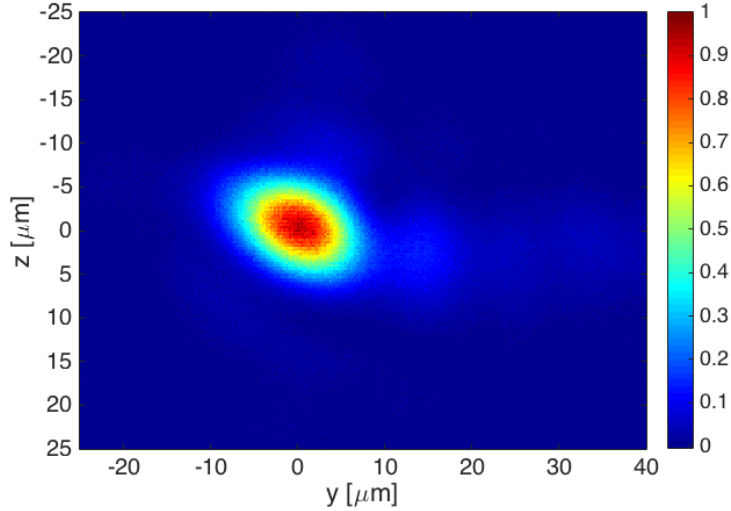


Figure 3.2: A typical focal spot shape shows comatic aberrations. The maximum intensity is normalized to unity and the focal spot size was measured within the $1/e^2$ width.

diagnostics consisting of a CCD camera with a microscopic lens. The optimization process consists of minimizing the focal spot size and maximizing the energy in the spot by means of fine alignment of the parabola.

The focal spot monitor uses a small motorized mirror, which can be moved in front of the target, reflecting the laser beam in the direction of the diagnostics. Neutral density filters are placed in front of the laser pulse compressor in order to reduce the laser beam intensity and prevent damaging the camera during the focal spot optimization and checks. The optimization is performed using the tip and tilt and the rotation of the off-axis parabolic mirror in combination with searching for the focal spot using the XYZ movement of the camera mount.

The optimization process of the focusing allows the laser focal spot size to be near the diffraction-limited size ($\simeq 10 \mu\text{m}$) without using adaptive optics. The focal spot shape was obtained from the image and the energy of the spot within the $1/e^2$ width was calculated. It was determined that the focal spot was elliptical with a diameter of $14 \mu\text{m}$ on the major axis and $11 \mu\text{m}$ on the minor axis (see Fig. 3.2). It was determined that the focal spot contains $(60 \pm 5) \%$ of the energy of the entire laser pulse, which corresponds to an energy of $(360 \pm 30) \text{ mJ}$. The maximum laser intensity in the center of the focal spot was $\simeq 10^{19} \text{ W/cm}^2$, which results in the laser strength parameter $a_0 \approx 2$, and thus the experimental conditions are near the threshold of the bubble regime. Using the same diagnostics as for the laser focal spot measurements, the pointing stability of the laser beam could be monitored. The repetition rate was set to 10 Hz, the camera exposure to 100 ms, and the laser was attenuated to prevent saturation of the camera. Hence, every captured image from the diagnostics contained only one laser pulse. A thousand images of the focal spot were taken, and center points were assigned to each of them by calculating the weighted average of the signal intensity in the images. Subsequently, the center points were taken as input values to calculate a mean value of the pointing (set as the center with zero coordinates) and a standard deviation $\sigma_L = 3 \mu\text{rad}$ from the mean position of the focal center points in the images (see Fig.3.3).

3.1.3 Plasma diagnostics

During the experiments, fundamental parameters of plasma must be monitored in order to understand how the acceleration is achieved and if experimental conditions are stable. As shown,

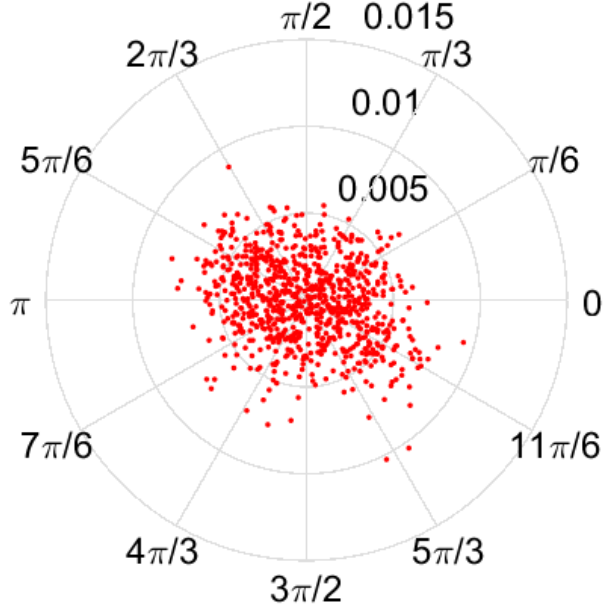


Figure 3.3: A polar plot showing the laser pointing stability. The values of the pointing angle are in milliradians and the point $(0,0)$ corresponds to the mean of all points.

in chapters 1 and 2, one of the most important parameters is the electron plasma density n_e , which defines acceleration conditions, such as the phase velocity of the plasma wave (Eq. 1.38), the dephasing length (Eq. 1.46) and the maximum energy gain of electron (Eq. 1.48), as well as the strength parameter of the betatron motion (Eq. 2.54) and consequently the energy of X-ray photons the betatron radiation and the number of emitted photons (Eqs. 2.57 and 2.59).

It has been chosen to monitor the plasma density using a Mach-Zehnder interferometer, which employs a secondary laser beam for probing the plasma. In our case, the probe laser beam was split from the main beam in the compressor [173]. The auxiliary beam is then split into two using a beamsplitter - one of the beams is the object beam which probes the plasma channel, and the second one is the reference beam, the phase of which remains unchanged. The two beams are then merged on another beam-splitter, and an interference pattern is created and detected by a camera. The interference pattern shows characteristic curved fringes due to a phase shift caused by the propagation of the object beam through plasma. Since the phase shift is proportional to the integral of the index of refraction along the optical path length, it would be necessary to know the index of refraction everywhere in the medium. However, we can assume the cylindrical symmetry, and the radial distribution of the index of refraction can be calculated from the phase shift measurement along one dimension. Abel transform allows the transformation from an axial distribution to the radial one. The variation of the phase shift integrated along the object beam direction and caused by the plasma is given by [174]

$$\Delta\phi(x) = \frac{2\pi}{\lambda_L} \int_{-y_0}^{y_0} [n_e(r) - 1]dy = \frac{4\pi}{\lambda_L} \int_0^{y_0} [n_e(r) - 1]dy, \quad (3.1)$$

where λ_L is the wavelength of the laser photons, n_e is the electron plasma density. When the expression from Eq. 3.1 is converted from the Cartesian to the cylindrical coordinates, we obtain

$$\phi(x) = \frac{4\pi}{\lambda_L} \int_x^{r_0} \frac{[n(r) - 1]rdr}{\sqrt{x^2 - r^2}} + \text{const.} \quad (3.2)$$

and after the inverse Abel transform is used, it gives a formula for the refractive index η

$$\eta(r) = 1 - \frac{\lambda_L}{2\pi^2} \int_r^{+\infty} \frac{\phi'(x)}{\sqrt{x^2 - r^2}} dx, \quad (3.3)$$

where r is the radius from the axis of the plasma channel and $\phi'(x)$ is the first derivative of $\phi(x)$. In order to prevent the neutral gas to contribute to the phase shift, the fringes are oriented along the neutral gas flow (perpendicularly to the laser propagation direction). The plasma density is then derived from the formula in Eq. 1.29 and we obtain

$$n_e = n_c (1 - \eta^2). \quad (3.4)$$

In addition, the interferometer serves as an additional alignment technique based on the position of the channel above the motorized gas jet, and for optimization of the acceleration conditions when the self-focusing technique is of interest.

3.1.4 Particle diagnostics

Beside the conditions of the plasma accelerator itself, the parameters of accelerated electron beams and generated X-ray pulses must be monitored in order to characterize the performance of the accelerator. These parameters, discussed below, include the electron pointing stability and divergence, the electron energy and energy spread, the electron bunch charge, the photon energy of the generated X-ray radiation and the X-ray radiation source size.

The laser-accelerated relativistic electron beams are crucial for our high energy X-ray radiation sources. As seen in chapter 2, the generated X-ray radiation depends primarily on the energy and the number of the generated electrons. For this reason, the electron energy and charge are among the most important quantities that must be monitored. Furthermore, the pointing stability and divergence are measured not only due to their importance for spatial synchronization for the inverse Compton scattering but also in order to ensure the feasibility of the betatron source for applications that typically demand a high source stability.

Electron pointing monitor

The first diagnostics, which detects the accelerated electron beam after the electrons leave the laser-plasma accelerator, is a pointing stability monitor. It consists of a scintillating screen, which is placed on axis at a distance of 135 mm downstream from the electron source (the plasma), and a CCD camera for imaging. Moreover, the detection screen is placed in a region with a negligible magnetic field caused by the dipole magnet of the electron spectrometer. Hence, the magnetic field does not alter the trajectory of the electrons and an undispersed bunch is measured. In front of the scintillating screen, there is a shielding made of an aluminum foil covered with paper in order to stop the driving IR laser beam, which would otherwise cause the scintillating screen to emit photons.

The electron pointing monitor is a multipurpose diagnostics. The electron pointing of each shot is obtained as weighted average value of the signal on the detection screen. A typical image from the electron pointing monitor is shown in Fig. 3.4. The diagnostics shows that a collimated electron bunch is accelerated in the plasma and thus it is possible to estimate the electron beam divergence from the size of the spot at full width at half maximum (FWHM) and the distance of the detection screen from the source. Furthermore, it is important to employ the pointing monitor in order to be able to minimize the pointing, which is important for experiments that subsequently employ the electron bunch, such as the source based on the inverse Compton scattering or user experiments with an end-station further downstream the laser axis.

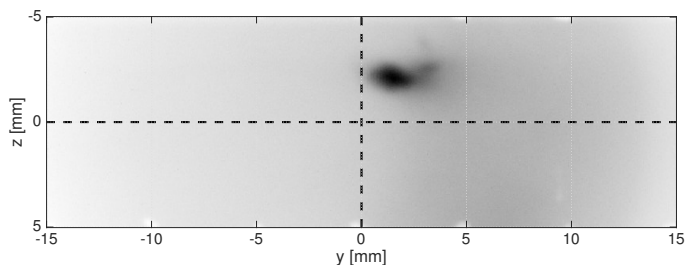


Figure 3.4: A typical image from the electron pointing monitor (inverted colors). The diagnostics consists of a Lanex screen imaged by a CCD camera. For an easier image distortion correction and clear spatial reference, the screen is marked with points spaced by 5 mm on around the edge of the scintillating side. The laser axis is in the center of the axes.

Measurements of the the pointing stability and electron spectrum can be performed simultaneously. For the purpose of the analysis of electron spectrum (described below in the part about the electron spectrometer), the pointing was used either directly - the observed pointing from the electron pointing monitor is used as an incident angle for analysing a corresponding electron spectrum since the angle of electrons, which enter the dipole magnet, alters the energy determination by the magnetic spectrometer. Although the multiple scattering of electrons on the scintillating screen of the pointing monitor can be effectively removed [175], the screen and its shielding are eventually removed when the stable generation of electron beams is achieved in order to improve the signal on the electron spectrometer. For the recorded shots without the pointing monitor in its position, the mean value of the pointing is calculated statistically for all shots made with the same accelerator parameters. These shots for the pointing statistics are usually performed before removing the pointing monitor.

Electron spectrometer

Since the electron spectrum from a tunable laser-plasma accelerator can be generated in a broad energy range (from few MeV to hundreds of MeV), the magnetic spectrometer is ideal for the electron spectroscopy. It consists of a dipole magnet and a particle detector. The dipole magnet deflects electrons, which enter its perpendicular magnetic field, by the Lorentz force (Eq. 1.1)

$$\vec{F} = -e(\vec{E} + \vec{v}_e \times \vec{B}) = -e\vec{v}_e \times \vec{B},$$

where e is the absolute value of the electron charge, \vec{v}_e is the electron velocity, \vec{B} is the magnetic field and \vec{E} is the electric field (which equals zero in the case of a dipole magnet). From the balance between the centrifugal force and the centripetal force (i.e. the Lorentz force) the expression for the radius of the electron trajectory in a magnetic field can be derived as

$$R = \frac{\gamma m_e v_e}{eB} = \frac{\gamma m_e c}{eB} \sqrt{1 - \left(\frac{m_e c^2}{E_e}\right)^2}, \quad (3.5)$$

where m_e is the rest mass of electron and γ is the relativistic Lorentz gamma factor, c is the speed of light in vacuum and E_e is the total energy of the electron. The electron bunch leaving the magnet gap is thus dispersed with respect to its momentum in the dimension perpendicular to the magnetic field of the spectrometer magnet. Then the particle detector, typically a scintillating screen imaged by a CCD camera, detects the position of electrons, which at this point depends on their energy. Therefore, the determination of the energy is reduced to a geometry problem. The electron dispersion $D(E_e)$ can be found for such an experimental setup.

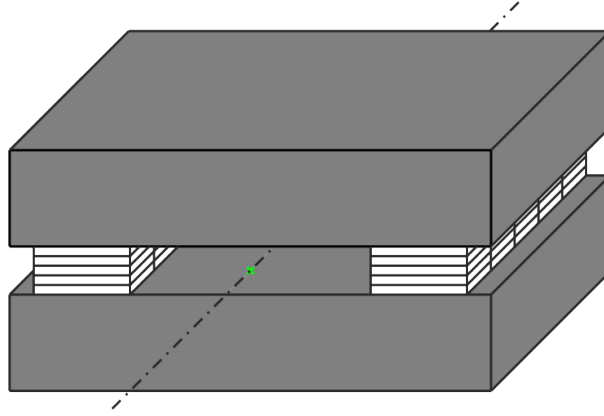


Figure 3.5: A dipole magnet designed for experiments at PALS with a length of 7 cm and the magnet gap of 1 cm. The dipole consists of many small neodymium magnet blocks (white) joined into columns and put on the sides between two iron blocks (grey) parallelly with the vector of the magnetic field pointing in the same direction in order to create a uniform magnetic field in the gap between the plates. The center of the magnet gap is placed on the laser axis.

For the experiments at PALS, a dipole magnet has been designed as a part of the work for this dissertation. Small neodymium magnet blocks are joined together into columns that are placed on both sides between two iron plates and their magnetic field is aligned parallelly with the vector of the field pointing in the same direction in order to create a uniform magnetic field in the gap between the plates (as shown in Fig. 3.5). If the direction of the magnetic field vector of the columns on one side is the opposite than on the other side, the magnetic field would be whirled in the gap and effectively cancelled out on the axis. The resulting designed dipole is 7 cm long and the magnet gap, which is vertically centered on the laser axis, is 1 cm high.

By using this geometry, it is ensured that the magnetic field will be uniform even when many small magnets are used. The magnetic field inside and outside of the gap has been measured with a gaussmeter on a grid in horizontal plane at various heights of the laser axis. The result is a map of magnetic field such as the one shown in Fig. 3.6 and the mean measured value of the magnetic is $B = 0.27$ T with a good level of uniformity. The difference in the magnetic field measured at different heights on the z -axis are within the systematic error of the measurement. Since electrons are most likely to experience the magnetic field in the horizontal plane at the height of the laser axis going through the center of the magnet gap and the differences in the magnetic field in the adjacent planes are negligible. These field values have been used in the analysis of electron spectra. A large Lanex scintillating screen with dimensions of 28×13 cm is placed at a distance of 300 mm from the back side of the dipole magnet at an angle of 42° as shown in Fig. 3.7. The Lanex screen is observed by a CCD camera and the whole detection system is light-tight in order to prevent detecting a false signal created by the laser light scattered inside the vacuum chamber. The shielding includes a thin aluminum foil in front of the Lanex to shield the screen from the driving laser light. Electron scattering of the thin aluminum foil is considered negligible. During the experimental campaigns, the camera is positioned either below the level of the experimental axis or the Lanex screen is imaged by the camera via a reflection on a mirror (with an extra camera shielding) in order to prevent electrons hitting the camera chip and electronics. Note that the dependence of the electron energy and electron detection position on the scintillating screen is not linear (as shown on a reference image in Fig. 3.8).

This detection system also provides a simple charge measurement using a calibrated system consisting of the CCD camera and the scintillating screen. The principle of this method is described in an article by Glinec et al [176]. The Lanex screen is suitable for the use in

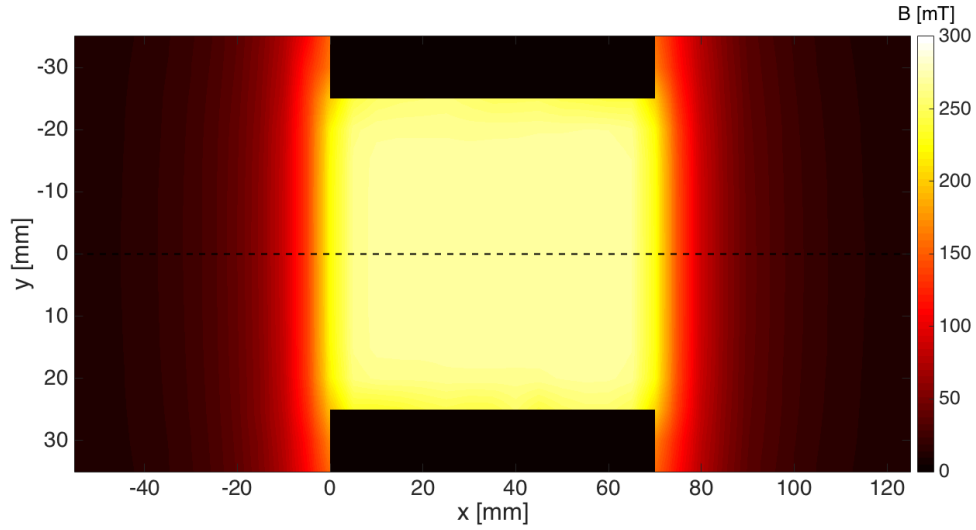


Figure 3.6: A map of the magnetic field measured in the horizontal plane at the height of the laser axis. The columns of neodymium magnet blocks (black rectangles) on the side of the dipole are shown at the top and bottom of the figure with zero values of the magnetic field as it is not possible to measure the magnetic field inside the magnets. The laser is coming along the axis from left to right.

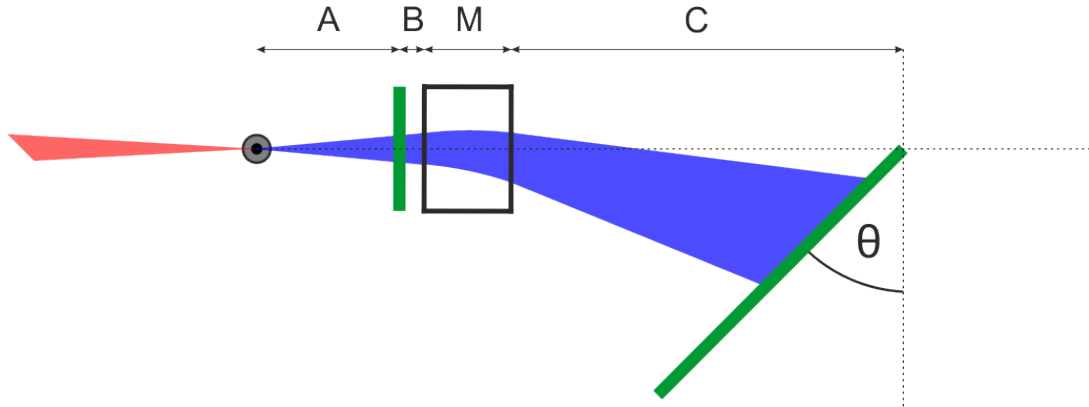


Figure 3.7: The experimental setup of the electron magnetic spectrometer. The small scintillating screen of the pointing monitor (green) is placed in a distance of $A = 135$ mm from the electron source and $B = 30$ mm in front of the dipole magnet of a length $M = 70$ mm creating a magnetic field $B = 0.27$ T within its gap. The large scintillating screen is placed in a distance of $C = 300$ mm at an angle of $\theta = 42^\circ$ and imaged by a CCD camera behind it (not shown in the figure).

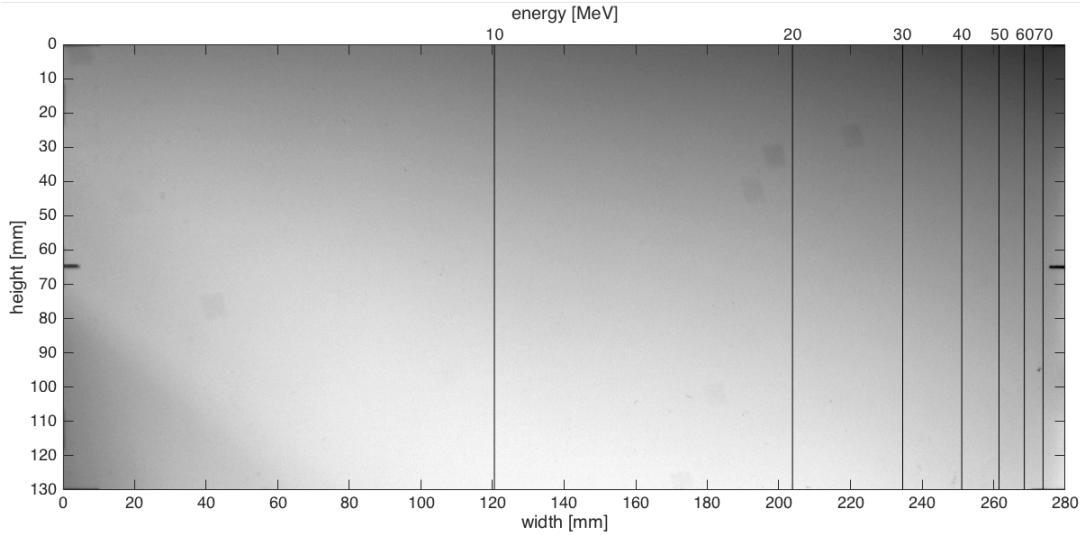


Figure 3.8: A reference image from the electron magnetic spectrometer showing the nonlinear dependence of the electron energy and the position on the scintillating screen. As the electron energy increases, the spectrometer resolution decreases due to high energies being more tightly spaced than lower energies of the same difference.

electron magnetic spectrometers because the deposited energy is constant for electrons above approximately 3 MeV (see Fig. 3.9). This threshold is less than the lower limit of our magnetic spectrometer. The reason behind the shape of the curve of the deposited energy in Fig. 3.9 is as follows: the lowest energy electrons cannot get through the first plastic layer of the screen; for energies beyond the detection threshold, the deposited energy peaks near 500 keV and is constant for the energies, which are achieved in our experiments (a few MeV and higher) since all electrons in this energy range deposit the same amount of energy in the sensitive layer before they escape the screen. The Lanex screen calibration is described in articles from Glinec et al. [176] and Buck et al. [177]. The charge determination using the screen consists of three steps. First, the number of scintillation photons emitted by the screen per one incident electron (or per 1 eV) must be calculated. The number of photons per one incident electron is given by

$$\frac{dN_{\text{emit}}}{dN_e} = \frac{1}{E_\gamma} \varepsilon \frac{dE_e}{dx} \delta x, \quad (3.6)$$

where $E_\gamma = 2.27$ eV is the energy of one photon emitted by the scintillating screen, $\varepsilon dE_e/dx = 1.8 \pm 0.2$ MeV/cm is the yield of the electron kinetic energy that is transformed into visible light [176] and δx is the equivalent of a phosphor in the sensitive layer crossed by an electron. This quantity depends on the phosphor surface loading h_S , which equals $h_S = 0.033$ g/cm² in our case, the density of the phosphor $\rho = 7.44$ g/cm³ and the angle θ_\perp between the normal to the scintillating screen and the electron trajectory as $\delta x = h_S/(\rho \cos(\theta_\perp))$.

Then, the number of photons collected by a single pixel of the CCD camera per one emitted photon is estimated as

$$\frac{dN_{\text{coll}}}{dN_{\text{emit}}} = \xi g(\theta_{\text{cam}}) \delta\Omega \prod_i q_i, \quad (3.7)$$

where $\xi = 0.22$ is the transmission output factor giving the fraction of emitted photons that escape the scintillating screen since the emitted photons undergo multiple scattering in the screen. The fraction of photons that escape the screen is derived in the article of Radcliffe et al. [178]. The function $g(\theta_{\text{cam}}) = \cos(\theta_{\text{cam}})/\pi$ is the angular distribution of the photons that escape

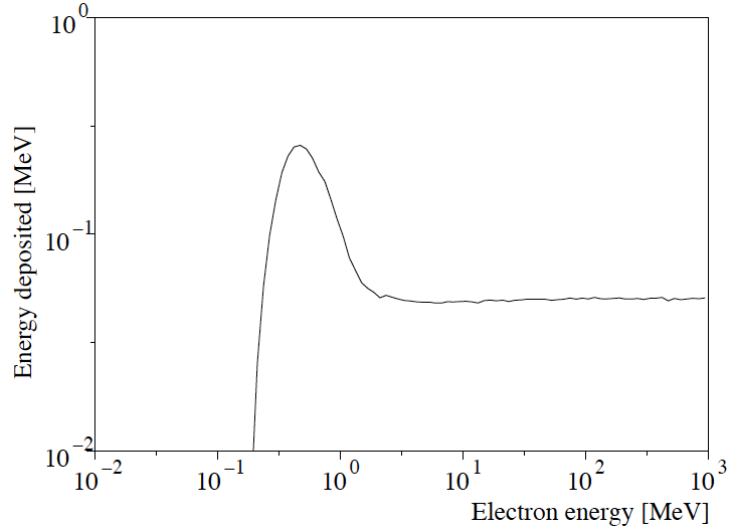


Figure 3.9: Energy deposited in the sensitive layer of Lanex screen with respect to the incident electron energy. Reprinted from [176].

the screen at the angle of the CCD camera with respect to the normal [179], $\delta\Omega$ is the solid angle of the imaging system with respect to the position on the screen where the scintillation photon is emitted, and $\prod_i q_i$ is the product of all transmission and reflectivity coefficients of optical equipment of the imaging system (lenses, mirrors, etc.). And finally, the CCD yield, i.e. the number of counts registered in a pixel per one collected photon is given by

$$\frac{dN_{\text{counts}}}{dN_{\text{coll}}} = \frac{\eta_{\text{quant}}}{(e^-/ADU)}, \quad (3.8)$$

where η_{quant} is the quantum efficiency of the CCD camera and (e^-/ADU) is the number of electron-hole pairs created in the pixel that is needed to create one count.

By determining the derivatives above, the electron spectrum can be calibrated using an expression

$$\frac{dN_e}{dE_e}(E_0) = \frac{dD}{dE_e} \frac{C(E_0)}{\delta a_{\text{pixel}}} \div \left(\frac{dN_{\text{emit}}}{dN_e} \frac{dN_{\text{coll}}}{dN_{\text{emit}}} \frac{dN_{\text{counts}}}{dN_{\text{coll}}} \right), \quad (3.9)$$

where dD/dE_e is the first derivative of the dispersion of electrons D along the Lanex screen with respect to the electron energy E_e , $C(E_0)$ is the number of counts from the CCD pixels integrated along the non-dispersive dimension, δa_{pixel} is the size of the pixel of the CCD projected along the imaged scintillating screen. Since each pixel projected along the screen has an assigned energy value given by the setup geometry, the calibrated electron spectrum is obtained from Eq. 3.9.

Furthermore, a significant effort was spent on the setup of the electron spectrometer in order to successfully reconstruct information on electron spectra. For the data analysis, a code in MATLAB was created as a part of the work on this thesis, which used the equations of motion to simulate electron trajectories in the magnetic field of the dipole. In order to properly verify the correct functionality of the code, a few extra steps were done:

1. First, a code in Matlab was written, which calculates the trajectory in a constant magnetic field of 0.27 T, which was experimentally measured inside the magnet gap, using the geometry of the experiment. This code will be referred in the text as *Spectrometer analysis v1.0* and it works with an assumption of an ideal dipole magnet in a shape of a rectangle, which creates the uniform magnetic field $B = 0.27$ T in its gap and a magnetic field

$B = 0$ T outside this gap. A radius of electron in the perpendicular magnetic field is assigned to every value of the reference electron energy used in the code. The reference electron energy ranges from the lowest energy that leaves the magnet from the back side (8 MeV) to 300 MeV. The trajectories outside the magnet are considered to be straight lines. A point of entry into the magnet gap (and thus the magnetic field) is calculated using the information on the electron pointing for any given shot. The radius of the electron trajectory within the magnet depends on the electron energy. The point where the electron exits the magnet and the exit angle can be calculated using analytic geometry as described by Glinec et al [176]. From the geometry of the experimental setup (i.e. the position of the large scintillating screen with respect to the dipole magnet), the point of detection can be calculated for all energies. The electron dispersion, which is a distance between the electron detection point on the screen and the intersection of the laser axis with the scintillating screen in the (x,y) plane, can be determined (see the blue curve in Fig.3.10). Note that the curve changes with the setup geometry and used dipole magnet as well as with different values of electron pointing. Therefore, the analytic code must not only be adjusted for each experimental setup but for each shot with measured pointing as well and it is necessary that the data obtained from the pointing monitor are used in the code.

2. A new version of the Matlab code was written and named *Spectrometer analysis v2.0*, which used a discrete grid of values of the magnetic field, was written and the magnetic field was set to the value $B = 0.27$ T for all grid points inside of the magnet gap and $B = 0$ T for the grid points outside of the gap. The trajectory of electrons is calculated using equations of motion. This step was done to verify the proper functionality of the code since it must give the same results as v1.0 which uses analytic geometry calculation. The code interpolates values between the grid points and in each time step of numerical calculations solves equations of motions for electron in magnetic field using the value from the closest grid point. The time step was set properly in order to obtain results comparable with the results from Spectrometer analysis v1.0 but to keep a reasonable duration of the numerical calculation.
3. Version *Spectrometer analysis v2.1* was obtained as a modified v2.0 by using the exact values of the magnetic field on the grid obtained from the real measurement (as shown in Fig. 3.6) and the electron dispersion with respect to the electron energy was determined.
4. Due to the sufficient level of uniformity of the magnetic field, it was possible to create *Spectrometer analysis v3.0* based on the code of Spectrometer analysis v1.0 using the approach of the analytical geometry could have been modified in order to give results comparable with Spectrometer analysis 2.1 while significantly decreasing the computation time. This was achieved by calculating an effective magnetic field defined as

$$B_{\text{eff}} = \frac{1}{L_m} \int_{-\infty}^{+\infty} B_z(y) dy, \quad (3.10)$$

where B_z is the magnetic field in the transverse dimension (z -axis) and L_m is the length of the magnet. This value was calculated by integrating over all rows of grid points (with the spacing of 5 mm) along y direction. This method thus used the same approach as the code of Spectrometer analysis v1.0, only the magnet was divided into 5 mm thick regions (slices) that behaved as magnets with different values of magnetic field. For each electron energy, the code calculated the exit point and angle at the end of a region and uses it as an entrance point and angle for the next region. It was possible to use this model due to the fact that the magnetic field is approximately constant along y direction in each

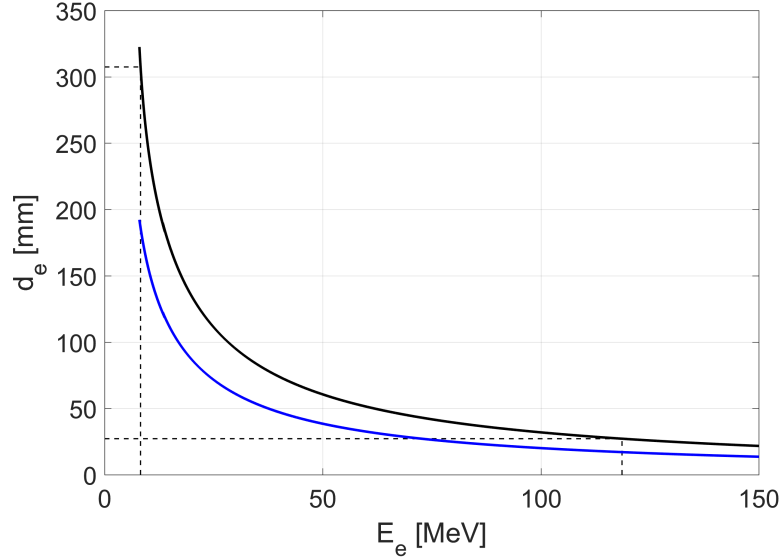


Figure 3.10: A dispersion of electrons with respect to their energy obtained using the simple Matlab code *Spectrometer analysis v1.0* with uniform magnetic field (blue) and the optimized model with the effective magnetic field obtained using the Matlab code *Spectrometer analysis v3.0* (black) are compared, showing the improvement in the energy determination when the real magnetic field is considered in the optimized model.

row. A comparison of the deflections of electrons obtained using the simple model in v1.0 and this optimized approach v3.0 are depicted in Fig. 3.10. In addition, using this model of effective magnetic field calculated in the thin regions decreased the time of calculation by two orders of magnitude, while keeping the precision of calculations between v2.1 and v3.0 within 1 % of difference. This helps making the analysis of electron spectra from hundreds of shots significantly shorter despite the fact that all shots have, in principle, their corresponding value of electron pointing obtained from the pointing monitor, and therefore they require new calculation of the electron dispersion.

X-ray spectrometers

X-ray spectrometers for photon energy ranging up to about 90 keV have been designed and manufactured for the experimental campaigns and are going to be used in future experiments. Two methods of detection in use are both based on detection using a calibrated charged-coupled device (CCD). The CCD can be used as an X-ray spectrometer in either direct or indirect detection mode. In the direct detection mode, X-ray photons with energy of up to 20 keV can be detected directly by the CCD pixels. For higher energy, a scintillator must be used to convert the X-ray photons to photons with a lower energy (typically of visible light). Two methods - one based on the direct detection and one based on the indirect detection - have been employed to design the X-ray spectrometers and are described in details below. Note that the design of the X-ray spectrometers had been done after the first experiment focused solely on electron acceleration. Thus, the approximate experimental conditions and parameters of electron bunches have been already known and could be used for estimations of quantities such as the critical photon energy and the X-ray photon flux.

Single photon counting mode: When the X-ray spectrometer is used in the direct detection mode, it is possible to employ so-called single photon counting mode [180]. In the direct

detection mode, X-ray photons are detected by the CCD. The detection is based on creation of electron-hole pairs in the silicon chip of the CCD. It requires an energy of 3.65 eV to create one electron-hole pair. Therefore, the number of created pairs depends on the energy deposited in the silicon layer by the incident photon. The electrons in the silicon diffuse further from the original point of the electron-hole pair creation and create an electron cloud, which can spread into a diameter of [181]

$$d[\mu m] = 0.017E_\gamma[\text{keV}]^{7/4}, \quad (3.11)$$

where $E_\gamma[\text{keV}]$ is the energy of the incident photon. The expression in Eq. 3.11 is valid for photon energies from 11 eV to 11 keV but we can safely assume that it is possible to extrapolate to higher energies up to about 50–100 keV as well where Compton scattering begins to dominate over photoelectric effect [182].

We assume multipixel detection events from a single photon to be no more than 2x2 pixels in size for all incident photon energies that have a diameter smaller than the pixel size of the CCD of the X-ray spectrometer. The CCD used for our X-ray spectrometer has a pixel size of 13.5 μm , which means that the upper photon energy limit given by this model is 45 keV. However, the CCD cannot be used for direct detection of X-ray photons with an energy higher than the limit of 20 keV due to its thickness and the attenuation length of higher energy photons. Additionally, it was shown in [183] that the probability of creating multipixel events from a single photon is negligible for photon energies up to 5 keV. For the energy of 5–20 keV, the multipixel events are most probably being contained in 2 pixels. In such case, the energy of the incident photon can be obtained by summing the energy deposited in both adjacent events.

Another condition for employing the single photon counting mode is to have low enough photon flux in order to minimize the number of pixels struck by more than one photon and thus appearing as a single photon of a higher energy. It is achieved by a combination of placing the detector on axis far enough from the source (typically a few meters) and attenuating the photon flux by layer of light-tight material (e.g aluminum foil). The total expected number of radiated photons from the source can be estimated using Eq. 2.59 (for a betatron source) or Eq. 2.66 (for a Compton source).

Since the intensity of X-ray photons in the generated beam is normally distributed with respect to the axis, the unattenuated number of photons on the CCD chip in a certain distance can be calculated and the attenuation on the foil can be estimated using the data from the CXRO database for solid filter transmission [184]. The number of photons that we want to get on the CCD chip is given by minimizing the probability of multiphoton events created in a single pixel (with an assumption that a single photon does not create multipixel events). In order to calculate the probability, we need to determine the number of combinations with repetition of N photons being distributed among M pixels of the CCD. This is given by

$$C_{all} = \binom{M+N-1}{M-1} = \binom{M+N-1}{N} = \frac{(M+N-1)!}{N!(M-1)!}. \quad (3.12)$$

Furthermore, we need to know the number of combinations with repetition of k photons striking a given pixel, which is given by

$$C_k = \binom{M+N-1-(k+1)}{N-k} = \frac{(M+N-k-2)!}{(M-2)!(N-k)!}. \quad (3.13)$$

The probability of k -photons striking a single pixel is then

$$p_k = \frac{C_k}{C_{all}} = \frac{(M+N-k-2)!}{(M-2)!(N-k)!} \frac{N!(M-1)!}{(M+N-1)!} = (M-1) \frac{N!}{(N-k)!} \frac{(M+N-k-2)}{(M+N-1)}. \quad (3.14)$$

Instead of investigating the probability for various numbers of incident X-ray photons N , we define a desired flux density of one photon per area of $P \times P$ pixels. The desired number of

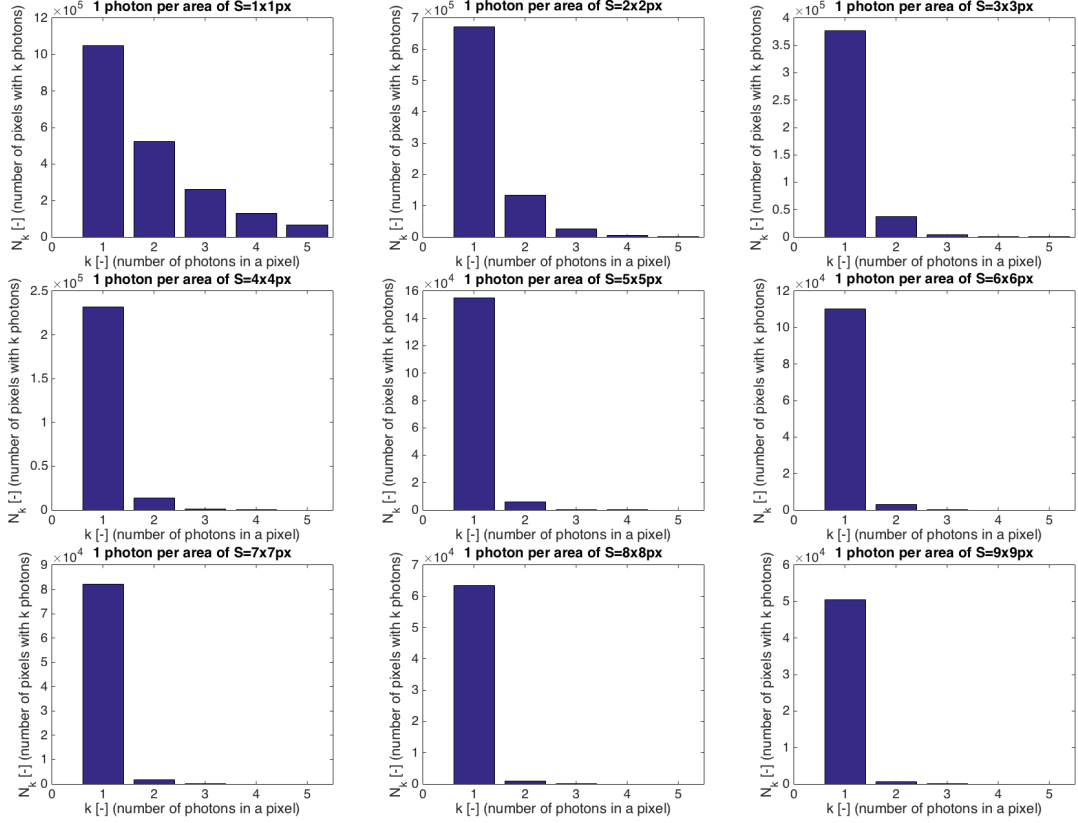


Figure 3.11: Number of pixels of the CCD struck by k photons for various photon flux densities. It was chosen to attenuate the generated X-ray photon flux to a density of 1 photon per area of 5×5 pixels as a compromise between minimizing the probability for multiphoton events in a single pixel and providing a sufficient photon flux on the CCD.

photons is then given by multiplying the flux density by the number of pixels of the CCD chip M . The CCD used in our experiment has a square chip with $M = 2048 \times 2048$ pixels. Figure 3.11 shows numbers of pixels of the CCD struck by k photons for various photon flux densities. Based on these calculations, it was chosen to attenuate the generated X-ray photon flux to a density of 1 photon per area of 5×5 pixels as a compromise between minimizing the probability for multiphoton events in a single pixel and providing a sufficient photon flux on the CCD. For our CCD, it results into a required attenuated photon flux of $N_{\gamma, \text{att}} \simeq \frac{2048 \times 2048}{5 \times 5} = 1.7 \times 10^5$, while the multiphoton events in a single pixel present about 4 % of the total number of detected events.

The expected number of X-ray photons N_{γ} generated by the betatron source can be estimated considering an electron bunch with a bunch charge of $Q_e = 5$ pC accelerated to an average energy of $E_e = 60$ MeV in a plasma with an electron density of $n_e = 3 \times 10^{19} \text{ cm}^{-3}$. Using practical unit formulas defined in Eq. 2.54, Eq. 2.57 and Eq. 2.59, it can be estimated that in these conditions we can expect the betatron strength parameter of $K = 7.9$, the critical energy of the betatron radiation of $E_{\text{crit}} = 2.2$ keV and the total number of photons of $N_{\gamma} = 2.5 \times 10^7$. Typical parameters of the betatron source with a betatron oscillation radius of $r_{\beta} = 1 \text{ } \mu\text{m}$ and 3 periods of betatron oscillations [60] were taken into account.

Therefore, the total number of X-ray photons generated by the betatron source must be attenuated by more than two orders of magnitude. If we assume the divergence of the betatron radiation to be similar to the divergence of the produced electron bunch, which was $\theta \simeq 20$ mrad), we can limit the number of photons on the CCD by increasing the distance between the detector and the photon source beyond the point where the photon beam diameter becomes larger than

the CCD chip. The maximum possible distance due to the available vacuum equipment and space in the laboratory was 310 cm. At this distance, the CCD chip with a square size of 27.65 mm covers an angle of approximately 9 mrad in both dimensions and it can be calculated that approximately 13 % of the total number of generated X-ray photons strike the CCD. Further attenuation is thus required and it is achieved by adding an aluminum filter with a thickness of 6 μm , which has a transmission of about 5 % [184]. The resulting attenuated photon flux on the CCD using this setup is $N_{\gamma,\text{att}} = 1.6 \times 10^5$, which corresponds to the flux density of 1 photon per area of 5×5 pixels as intended.

Therefore, the designed X-ray spectrometer based on the single photon counting mode minimizes the probability of multiple photons striking a single pixel of the CCD by limiting the photon flux to a density of about 1 photon per area of 5×5 pixels. The energy deposited in a pixel by a single photon can be calculated from a number of counts in each pixels using the CCD calibration data (e^-/ADU) and the ionization energy needed to create one electron-hole pair (3.65 eV for the silicon chip).

During the analysis of the experiment, the background noise of the CCD camera is subtracted using a background image, which is obtained without the generated radiation. The reconstruction of the original spectrum calibrated with respect to the number of incident photons consists of deconvolution of the obtained signal with the transmission function of the aluminum attenuator. This method provides absolutely calibrated spectra since the result of this process is the incident number of photons in the generated X-ray pulse. Obtained experimental results will be discussed in Section 3.2.

Note that when the beam size at the distance of the X-ray spectrometer is larger than the size of the CCD (as was our case), an additional step of renormalization must be performed. Moving the CCD camera closer to the source (or alternatively adding a scintillator closer to the source and imaging it by another camera) where the whole beam can be imaged allows measuring the X-ray photon beam divergence and determining the X-ray beam profile. Using the information on the divergence and the photon distribution from the beam profile, it can be estimated how many photons is outside the surface area of the CCD chip of the X-ray spectrometer and thus the total number of generated X-ray photons can be obtained.

Ross filter based spectrometer: Since CCD cameras can be used as X-ray spectrometers only up to a photon energy of about 20 keV, another method must be used for higher radiation energies. It is suitable to use a set of Ross filters [185] designed for a certain X-ray photon energy range, which is expected from a given X-ray source. The number of photons is determined in multiple small energy intervals, which are defined by the physical properties of the chosen filters. The precision of the energy determination is much higher compared to a method with covering the detector with foils of a single element and different thickness. While the method can be used for photon energies from a few keV to a hundred keV, we need to keep in mind the energy limit of 20 keV for direct detection, when a CCD camera is used as the detector behind the Ross filters. For higher energies, the X-ray spectrometer based on Ross filters must be equipped with a scintillator between the filters and the CCD.

The method employs filters of different elements, which are near each other in the periodic table (i.e. similar proton number). They are matched into pairs, each with a precisely selected thickness in order to match transmission functions almost completely excluding the energy interval $\langle E_A; E_B \rangle$ between the absorption edges of the chosen elements A and B (see Fig. 3.12 with an example for Zr and Y). Each filter covers a distinct area of the detector, from which regions struck with a comparable photon flux can be selected. The signal on the detector behind each filter (or its part) is then analysed. The signal on the CCD is represented by a number of counts in each pixel. In this method, it is not important if a pixel of the CCD is struck by one or more photons as we are interested in the radiated energy, and all counts of the selected pixel area are summed during the analysis. The difference of signals $N_A - N_B$ that passed through

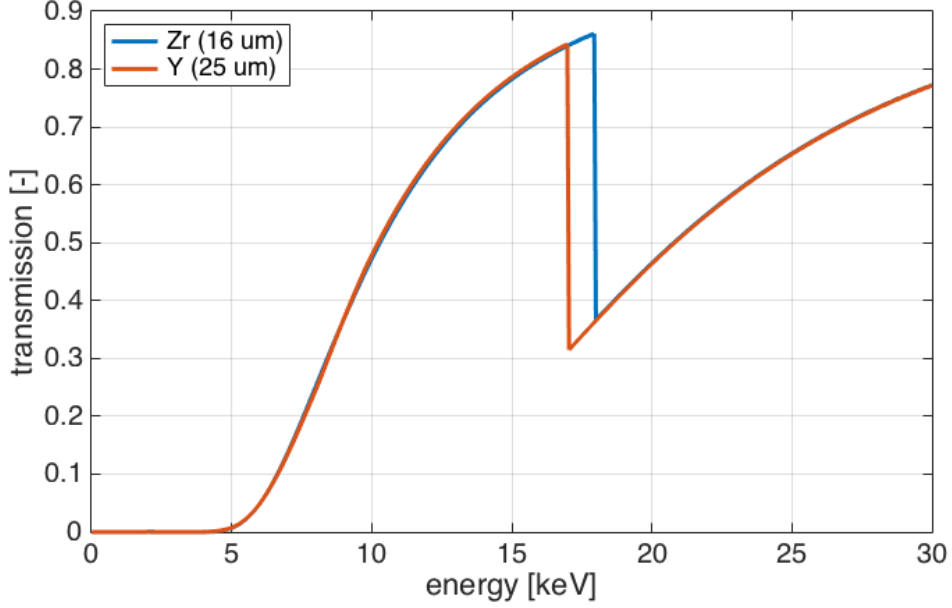


Figure 3.12: An example of transmission for an ideally matched pair of Ross filters. The transmission function with respect to the photon energy for Zr with a thickness of $16 \mu\text{m}$ and Y with a thickness of $25 \mu\text{m}$ differs only in the energy interval between the absorption edges of both elements.

filters A and B, respectively, is proportional to the radiated energy of the source $dI/d\omega$ and depends on the difference in the transmission functions $T_A(E_\gamma)$ and $T_B(E_\gamma)$ (as depicted in Fig. 3.13). Therefore, the incident number of photons in the energy range $\langle E_A; E_B \rangle$ is selected by the absorption edges and can be obtained as

$$N_\gamma = \frac{N_A - N_B}{T_A - T_B}. \quad (3.15)$$

At least three pairs of Ross filters are needed in order to reconstruct the X-ray spectrum since betatron radiation is synchrotron-like and thus the shape of the spectrum can be described by a modified Bessel function of the second kind [93]. This method requires a sufficient photon flux and high energy of X-ray photons as the absorption edges of solids can be effectively employed for a photon energy of 3 keV and higher. Moreover, this detection cannot be combined with the single photon counting mode for obvious reasons.

A set of Ross filters was designed for an energy range from 3 keV to 20 keV since a critical energy of a few keV was expected in our experiments. Using the data on solid foil transmission from the CXRO database [184], 9 filters were chosen from the available metallic foils and combined into pairs. Due to a possibility to pair one filter with more than one other, a total of 6 filter pairs were created (see Tab. 3.1).

The differences of transmission functions for these filter pairs are shown in Fig. 3.14. As can be seen, the transmission differences are negative in small energy intervals, which should ideally be avoided but does not significantly influence the obtained results. It is still possible to use a filter set like this if the negative parts of the transmission function difference have small amplitudes and are in narrow energy intervals.

Due to the limited availability of metallic foils, some filters have been made of multiple layers of a foil of the given element to ensure the matching transmission function with another filter. In order to ensure the same intensity illuminating all filter pairs during an experiment, a pie layout has been designed (as shown in Fig. 3.15). Since a Gaussian spatial distribution of photons is

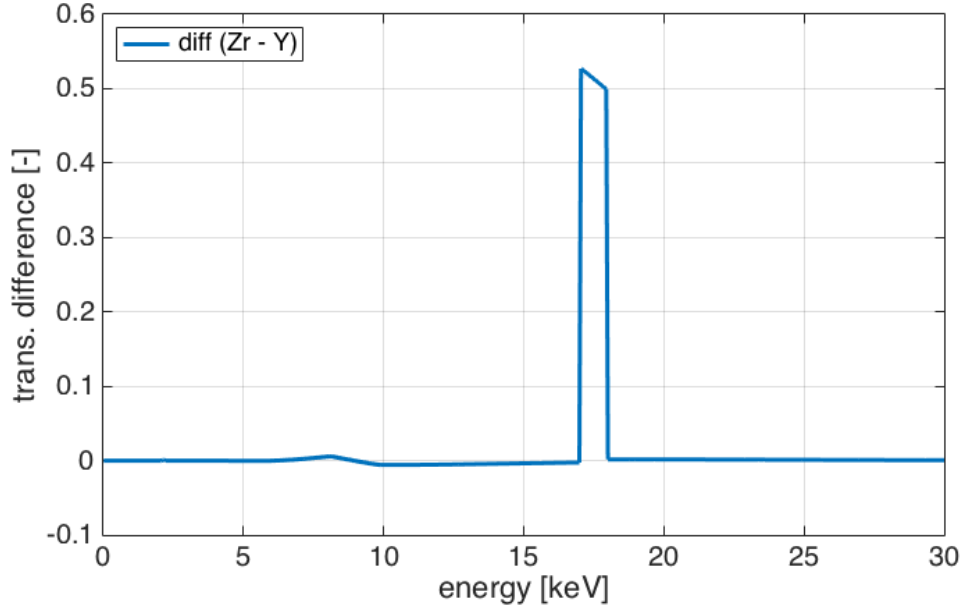


Figure 3.13: An example of transmission difference for an ideally matched pair of Ross filters. When thicknesses of the filters are chosen correctly, the transmission difference is non-zero only in an energy interval between the absorption edges of both elements.

Filter pair	Element A	Thickness d_A	Element B	Thickness d_B	Energy range (keV)
#1	Ti	12.5 μm	Al	100.0 μm	3.5–5.0
#2	Fe	5.0 μm	Ti	12.5 μm	5.0–7.1
#3	Cu	12.5 μm	Fe	20.0 μm	7.5–9.0
#4	Ge	50.0 μm	Cu	37.5 μm	9.0–11.1
#5	Zr	20.0 μm	Ge	50.0 μm	11.1–18.1
#6	Mo	12.5 μm	Zr	20.0 μm	18.1–20.0

Table 3.1: The first prototype of Ross filters for X-ray spectrometer consisting of 6 pairs.

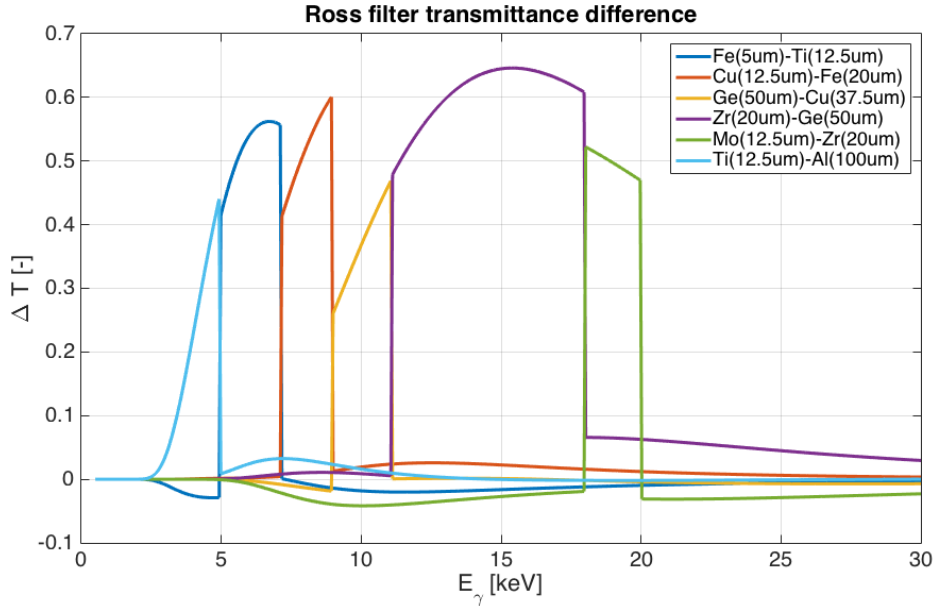


Figure 3.14: The difference in transmission functions for the selected Ross filter pairs consisting of 9 metallic foils.

expected from the betatron source, the center of the cake filter layout can be placed on axis and it is possible to identify the regions that were illuminated by photons with the same intensity. An exception in this layout is a germanium filter, which was available only as a small sheet of 4×4 mm. The different shape and dimensions do not affect the functionality of Ross filter pairs containing the germanium filter. A prototype with the cake layout is shown in Fig. 3.15, the filters are taped to a thin Mylar foil with a thickness of $13 \mu\text{m}$. The comparison of the values of the photon signal behind each Ross filter is possible due to the large distance of the diagnostics from the laser-plasma source, where we assume the photon distribution to be flat over the area of the small CCD chip.

A second set of Ross filters has been designed using the knowledge and experience gained with the first prototype without the strict cost restrictions and with an aim to add coverage for high energy photon range of at least 10–50 keV, which is the most feasible energy range for applications of the betatron radiation (discussed in the next chapter). Contrary to the first prototype, the new set of filters requires a scintillator to be placed between the filters and the detector (CCD camera).

A total number of 10 filter pairs was used to cover a spectral range of 9–88 keV, each pair covering an energy interval of approximately 5 keV in lower energies and 10 keV in higher energies (see Tab. 3.2). The transmission differences of the high energy filter set is shown in Fig. 3.17. These filter pairs consist of 19 foils which are made into the pie layout as in the case of the first prototype (see schematic drawing in Fig. 3.16), with two foils from each pair being placed next to each other in the layout in order to ensure a similar signal illuminating the filters while being able to center the spectrometer on the experimental (laser) axis.

3.1.5 Plasma mirror for the Compton source with high repetition rate

For the first version of the Compton source, the scheme with a plasma mirror has been chosen as it is simpler to set up and is not difficult to synchronize spatially and temporally. In this scheme, a thin solid foil is inserted into the path of the driving laser beam of LWFA as

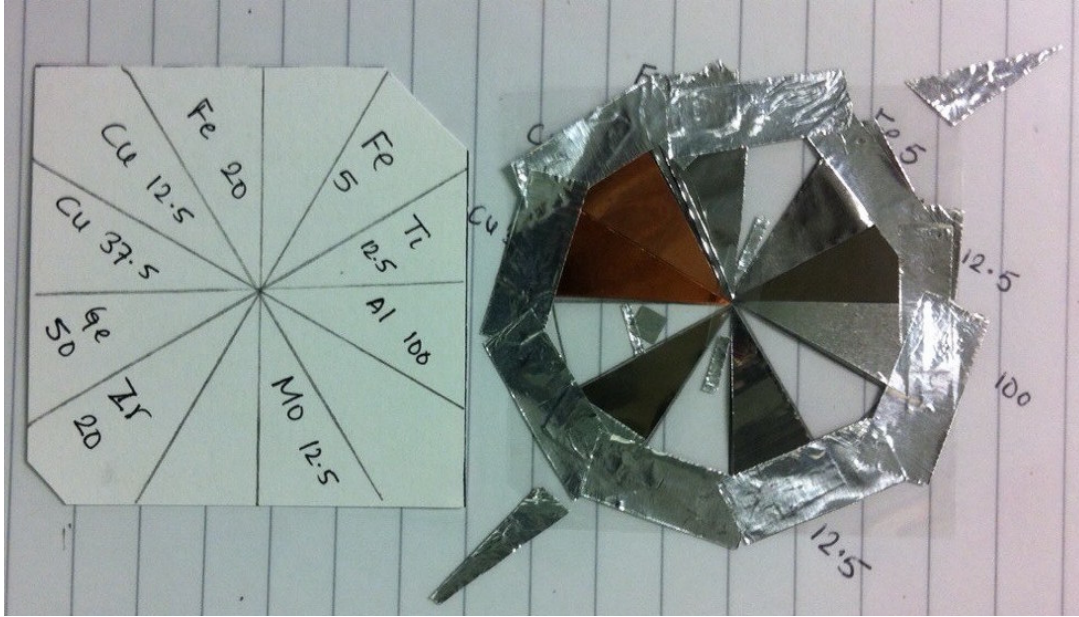


Figure 3.15: A cake layout of Ross filters prepared for an energy range from ~ 3 keV to 20 keV. Nine filters is combined into 7 pairs in total. The filters are taped to a thin Mylar foil with a thickness of $13 \mu\text{m}$. The numbers with the filter element mark the thickness in μm .

Filter pair	Element A	Thickness d_A	Element B	Thickness d_B	Energy range (keV)
#1	Ge	50.0 μm	Cu	37.5 μm	9.0–11.1
#2	Zr	45.0 μm	Ge	100.0 μm	11.1–18.0
#3	Mo	50.0 μm	Zr	90.0 μm	18.0–20.0
#4	Ag	70.0 μm	Mo	100.0 μm	20.0–25.5
#5	Sn	93.0 μm	Ag	75.0 μm	25.5–29.2
#6	Nd	100.0 μm	Sn	150.0 μm	29.2–43.6
#7	Dy	50.0 μm	Nd	75.0 μm	43.6–53.8
#8	Ta	40.0 μm	Dy	100.0 μm	53.8–67.2
#9	Au	55.0 μm	Ta	80.0 μm	67.4–80.7
#10	Pb	85.0 μm	Au	55.0 μm	80.7–88.0

Table 3.2: Design of Ross filters for X-ray spectrometer for high energy photons consisting of 10 pairs.

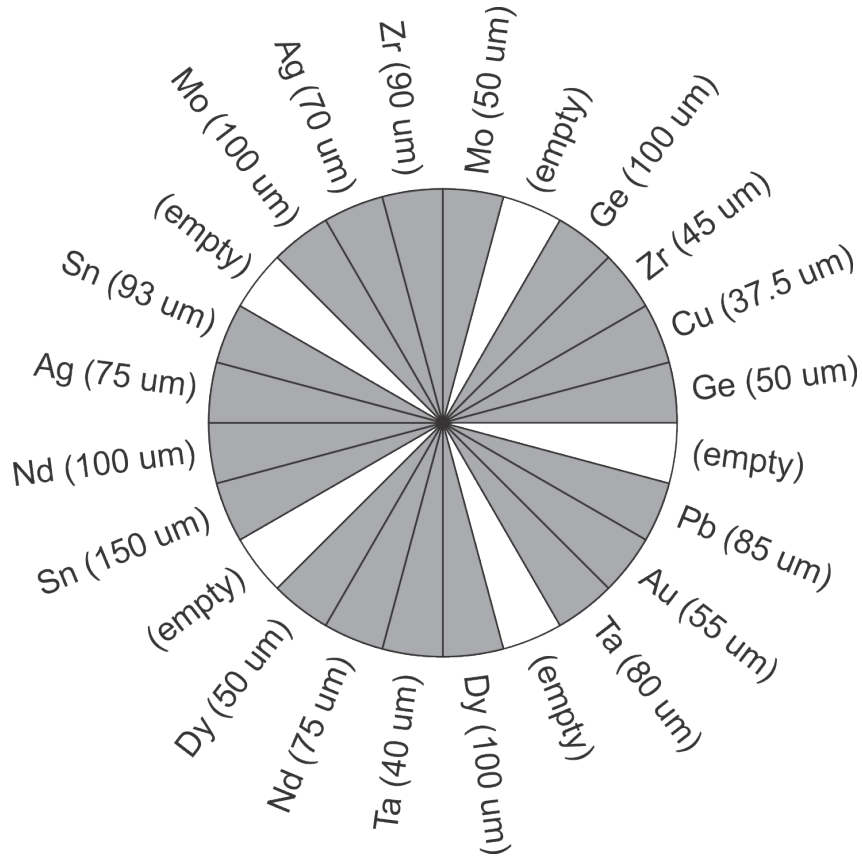


Figure 3.16: Cake layout schematics of Ross filters for the high energy range from 9 keV to 89 keV. In this case, 10 filter pairs consists of 19 foils.

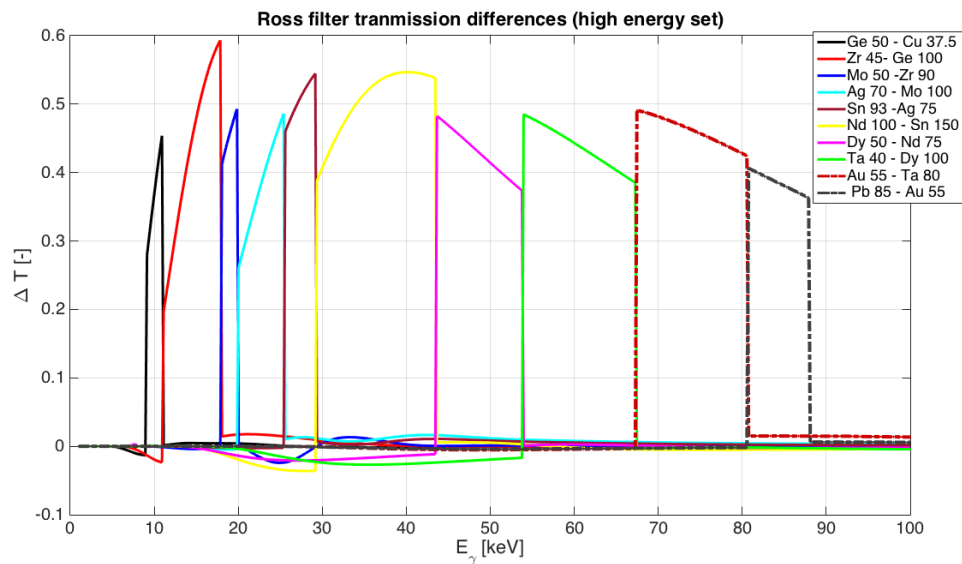


Figure 3.17: Differences of transmission functions for the high-energy X-ray spectrometer prototype based on Ross filters, covering the energy range from 9 keV to 88 keV.

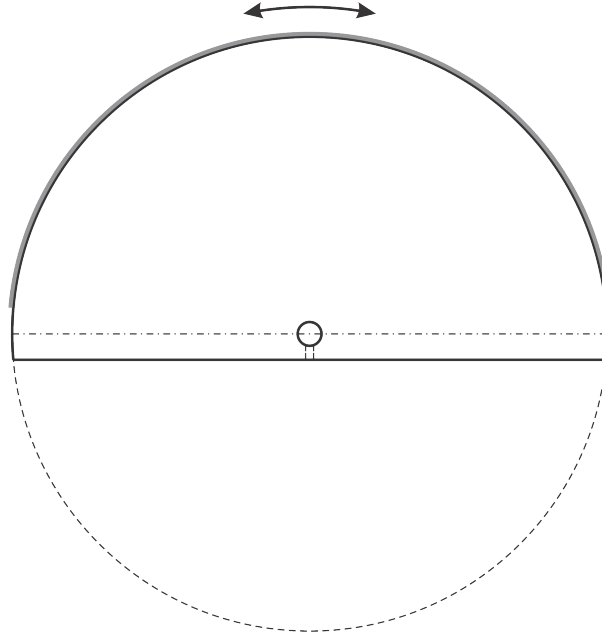


Figure 3.18: A drawing of the motorized rotating stage. An aluminum circle with a diameter of 15 cm is partly cut and a hole for the stepper motor is drilled in the center. An aluminum foil (grey) with a thickness of $9\ \mu\text{m}$ is hanging from the edge of the aluminum circle.

close to its exit from plasma as possible in order to maintain high intensity of the backreflecting laser pulse. An overdense plasma is created by the interaction of the laser pulse and solid foil which backreflects the pulse towards the electrons accelerated in the wake of the driving laser. The driving laser pulse is thus used also as the counter-propagating pulse for inverse Compton scattering.

A dedicated motorized rotating stage was designed for this purpose as a part of work on this thesis. A strip of thin aluminum foil of $9\ \mu\text{m}$ is attached to an edge of a half-circle aluminum plate with a diameter of 15 cm, which was mounted to a stepper motor rotation axis (see Fig. 3.18). The thickness of the aluminum foil was chosen in order to support itself without an additional frame but thin enough for the generated Compton radiation and accelerated electrons to pass through without undesired scattering and in the direction of their respective diagnostics.

The stepper motor allows operation with both continuous and stepping rotation (1 step equals an angle of 1.8°). In order to reduce vibrations of the setup, the continuous mode was selected with a speed of about $0.3\ \text{rad/s}$, which is equal to the movement of about 2 mm between shots with the high repetition rate of 10 Hz and thus allows the driving laser to hit a fresh spot on the aluminium foil with every shot. The thin foil was placed about 1 mm from the end of plasma. This results in a maximum laser intensity in the order of magnitude of $10^{17}\ \text{W/cm}^2$, which should allow a sufficient number of scattering events even considering the low cross-section of inverse Compton scattering.

3.2 Obtained experimental results with a few-terawatt laser

The set of diagnostics, which were designed as a part of the work on this thesis and which are described in the previous section, were used in the experimental campaigns to obtain results. The diagnostics were employed for monitoring and finely tuning the experimental conditions, and achieving stable electron bunch acceleration and X-ray pulse generation. There were three

experimental campaigns in total performed at the Ti:sapphire laboratory at PALS, during which only minor changes, which do not alter the functionality, were done to the diagnostics, e.g. dimensions, angles, distances, positions, different optical system magnification, etc. The first experimental campaign was focused solely on the laser wakefield acceleration of electrons, while the purpose of the other two was to generate betatron radiation as well. This allowed focusing the effort on optimizing the diagnostics. When results were obtained during one of the experimental campaigns with certain settings of the system, which were different from the standard used in the other experiments, it is clearly mentioned in the text. Otherwise, the conditions remain the same throughout the experiments.

Two more experiments were performed at Laboratoire d'Optique Appliquée (LOA), where the betatron source is well-defined and generates stable X-ray pulses with a sufficient photon flux. The two experiments at LOA were focused on testing the prototype of the X-ray spectrometer based on Ross filters and phase-contrast imaging as an application of the betatron source.

3.2.1 Accelerated electron beams

Electron beam pointing stability

The Lanex screen for the electron pointing measurement was placed 30 mm in front of the dipole magnet of the electron spectrometer. However, even at this distance from the magnet and in the region between the laser-plasma source and the Lanex screen, there is a non-zero magnetic field. In order to determine the effect of this field on the electron pointing measurement, the dispersion of low-energy electrons was calculated using the minimum electron energy (~ 8 MeV), which passes through the magnet (electrons of other energies are stopped inside the magnet and are thus not relevant for us). The lowest energy electrons were chosen because they are dispersed most by the magnetic field from the whole electron bunch. The magnetic field taken into account is the maximum value in the described region. It was found out from the magnetic field map shown in Fig. 3.6 that it is 25.1 mT. The distance, on which we assume the magnetic field deflects the electrons in front of the detection screen, equals the length on which we observed a magnetic field larger than the measurement error (~ 2 mT) in the region in front of the pointing monitor, which equals 25 mm.

The Lorentz force causes the electron to follow a circular trajectory in the perpendicular magnetic field as described by Eq. 3.5. For the given values, the electron radius is $R = 1.06$ m. It can be further calculated using analytic geometry that on the length of 25 mm the maximum electron deflection is about 0.3 mm, which presents an error of 2 mrad in the measurement. Therefore, this value was added to the error of the electron beam pointing and further considered in the analysis of the electron spectrometer data.

The electron beam pointing monitor shows not only the presence of collimated electron beams (see Fig. 3.19) but also the dependence on the linear polarization of the laser pulse (an example for the helium-argon target is shown in Fig. 3.20). The former shows that electrons are accelerated through laser wakefield acceleration rather than direct laser acceleration. The latter is caused by the laser pulse linear polarization at an angle of approximately 20° (with respect to the horizontal plane). The generated electron bunches detected in the pointing stability measurements are normally distributed (in 2D) along the polarization plane. The pointing stability of electron beams is defined as one standard deviation from the mean and is equal to 20 mrad.

The measurement of the laser pointing stability using the focal spot monitor showed the standard deviation to be $3 \mu\text{rad}$. It was investigated whether there is a connection between pointing stability of the laser pulse and generated electron beams. The pointing stability of the laser is four orders of magnitude lower than the pointing stability of the electron beams. This suggests that the electron bunch pointing instability is not caused by the instability of the

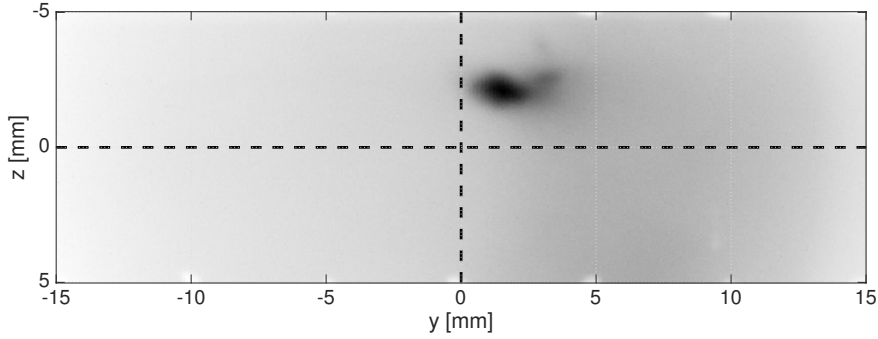


Figure 3.19: Electron beam pointing diagnostics consisting of a dedicated screen shows the profile of electron beams before entering the magnetic spectrometer. A collimated electron beam (dark grey) is detected proving the laser wakefield acceleration takes place.

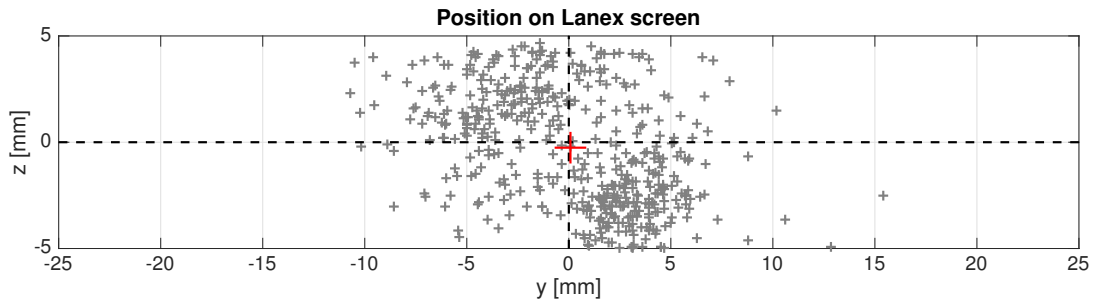


Figure 3.20: Measured positions of collimated electron beams generated from a helium target with an admixture of argon (99:1). Each data point represents a weighted position of an electron beam. The electron beams are normally distributed (in 2D) along the polarization plane of the driving linearly polarized laser pulse.

laser pulse, but most likely by the transverse betatron oscillations in the accelerating bubble structure and oscillations of electrons that reach the laser pulse. Furthermore, the information about electron pointing was used to make corrections on the electron energy assigned to each position on the Lanex screen used in the magnetic spectrometer.

Electron beam divergence

The divergence of the electron beam was measured using two diagnostics. The first detector allowing to monitor the divergence is the electron beam pointing diagnostics. The spot size on the Lanex screen can be used directly for estimation of the divergence using the measured distance of the screen from the plasma source, although with a limited precision due to a small distance of the screen from the source.

The divergence is measured by the electron spectrometer as well. It is assumed that the divergence is not affected by the dipole magnet in the non-dispersive dimension and the divergence is approximately the same as the divergence in the other dimension had the beam not been dispersed. The electron spectrometer imaging provides a comparable resolution as the pointing monitor and thus higher precision of the divergence measurement due to much larger distance between the screen of the spectrometer and the plasma source.

Since the pointing monitor causes multiple scattering of electrons, the divergence measured by the large scintillating screen of the electron spectrometer might detect greater divergence than the pointing monitor. The additional divergence is proportional $\theta_e \sim 1/E_e$ and presents an issue for electrons up to a hundred MeV [175]. Therefore the measurement performed by the pointing diagnostics cannot be entirely considered a non-perturbative method and it is preferable to eventually remove the scintillating screen of the pointing monitor and depend solely on the electron spectrometer for the divergence measurement. Removing the screen from the path of electrons improves the electron spectrometer resolution due to the decreased divergence.

Accelerated electron beams are detected as spots on the scintillating screen with a diameter of (280 ± 60) μm corresponding to a divergence of (21 ± 4) mrad (full opening angle of the divergence cone). Thus an elliptically shaped spot is created on the spectrometer scintillating screen with the size of about 1 cm in the nondispersive dimension.

Electron energy spectra and bunch charge

Various targets have been used for the laser wakefield acceleration. Compressed synthetic air has been tested as a novel approach to stabilize the energy and energy spread of electron spectra for a few terawatt laser pulse. It has been compared with the standard approach to create an electron plasma accelerator using a mixture of helium and argon (in a pressure ratio of 99:1), and a target of helium with an admixture of synthetic air has been used as well.

The electron accelerator which uses the compressed synthetic air as the target shows remarkable energy stability with a peak electron energy of $E = (17.4 \pm 1.1)$ MeV and an energy spread $\delta = (13.5 \pm 1.5)$ MeV (FWHM). In the optimum condition, which includes a plasma density increased to approximately $4.0 \times 10^{19} \text{ cm}^{-3}$, the electron beams of these properties were generated in 85 % of shots.

The typical electron spectra generated with synthetic air are depicted in Fig. 3.21. These results show an excellent stability given the properties of laser-driven electron accelerator. The shot-to-shot variation of the peak energy of 1.1 MeV is satisfactory for the possible applications of the generated electrons. The charge or electron bunches has been measured using the properties of the calibrated scintillating screen, which provides a linear response with respect to the charge of detected particles (as described above). Using the charge measurement method described in the previous section, it has been possible to determine that the mean electron bunch charge is approximately $Q = 3.1$ pC and the relative fluctuations (σ) of the charge are within 21 %.

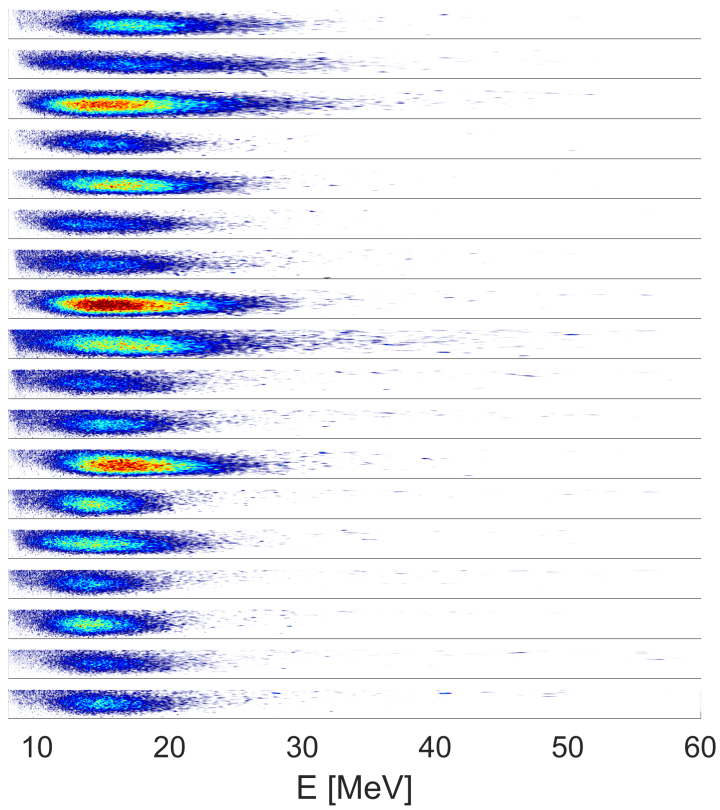


Figure 3.21: Typical electron spectra corrected on the beam pointing and obtained using the supersonic air jet target showing high stability in energy and energy spread with a peak electron energy of $E = (17.4 \pm 1.1)$ MeV and an energy spread $\delta = (13.5 \pm 1.5)$ MeV (FWHM).

Table 3.3 shows the reason behind the stability of electron spectra with the synthetic air target. The values of the laser intensity, which is required to ionize atoms, in Tab. ?? are obtained considering ionization via the Coulomb barrier suppression. This simple theoretical model which assumes that ionization occurs when the peak electric field of the laser pulse is above the threshold given by the critical electric field strength $\epsilon = E_{\text{ion}}^4 / (16e^6 Z^2)$. The required laser intensity in practical units is thus [21]

$$I[\text{W}/\text{cm}^2] = 4 \times 10^9 E_{\text{ion}}^4 [\text{eV}] Z^{-2}, \quad (3.16)$$

where Z is the charge state of the resulting ion and E_{ion} is the ionization potential. The values of the ionization potentials for various elements can be found in [85].

There are, in principle, two possible injection mechanisms when using the synthetic air target: self-injection due to plasma wave breaking [186] and ionization injection [86]. In the case of a few-terawatt laser system, the typical vacuum intensity of laser pulse is in the order of magnitude of $10^{18} \text{ W}/\text{cm}^2$ (as was the case in our experiments), and thus it does not allow complete ionization of nitrogen and oxygen atoms (the required laser intensity to ionize K-shells of these elements is more than $10^{19} \text{ W}/\text{cm}^2$), while electrons from L-shells are fully depleted by the rising edge of the pulse. Nevertheless, the K-shell electrons can be ionized when intensity higher than $10^{19} \text{ W}/\text{cm}^2$ is achieved due to relativistic self-focusing of the laser beam in plasma. When it happens, electrons can be trapped in the acceleration phase also due to the ionization injection mechanism.

The self-focusing in plasma occurs for a laser power P exceeding the critical power P_{crit} , which can be calculated for a collimated Gaussian beam using Eq. 1.32

$$P_{\text{crit}}[\text{PW}] = 16.2 \left(\frac{\omega_L}{\omega_p} \right)^2 = 16.2 \frac{n_{\text{crit}}}{n_e}.$$

This equation shows an important property of plasma: the value of the critical power P_{crit} decreases when the plasma density n_e is increased, which results in stronger self-focusing. The laser pulse reaches a higher normalized vector potential due to self-focusing given by Eq. 1.36

$$a_{\text{SF}} = 2 \left(\frac{P}{P_{\text{crit}}} \right)^{1/3}$$

with the focal spot radius (as defined by Eq. 1.37)

$$R_{\text{SF}} = \frac{\lambda_L}{\pi} \left(a_{\text{SF}} \frac{n_{\text{crit}}}{n_e} \right)^{1/2}.$$

Therefore, by setting the plasma density accordingly, the focal spot in self-focusing can be tailored to reach the laser intensity required for complete ionization of the target atoms in a relatively small region of space within the plasma.

The experimental results obtained with the synthetic air target providing stable conditions for electron acceleration with a few-terawatt laser were published in an article *Stable electron beams from laser wakefield acceleration with few-terawatt driver using a supersonic air jet* [187].

The additional ionization injection is, of course, possible also in commonly used helium targets with admixture of heavier atoms, e.g. argon. The disadvantage of using argon is obvious when laser intensity necessary for ionization of atoms is considered again. The laser pulse intensity necessary for ionization of the L-shell of argon ranges from $1.5 \times 10^{18} \text{ W}/\text{cm}^2$ to $1 \times 10^{19} \text{ W}/\text{cm}^2$, which in our case results in gradual injection of electrons along the laser propagation in the plasma as the intensity of a self-channeling few-terawatt laser pulse fluctuates between these values, and thus the energy spread of accelerated electron bunch is broadened as

L-shell								K-shell		
X	IX	VIII	VII	VI	V	IV	III	II	I	Gas
									1.36×10^{14}	H
								1.45×10^{15}	8.77×10^{15}	He
			1.78×10^{14}	–			1.47×10^{16}	1.03×10^{19}	1.6×10^{19}	N
			1.38×10^{14}	–			4.04×10^{16}	2.44×10^{19}	3.6×10^{19}	O
			1.57×10^{18}	–			1.11×10^{19}	3.99×10^{21}	4.74×10^{21}	Ar

Table 3.3: Laser intensity thresholds required to ionize electrons in atomic shells obtained considering ionization via the Coulomb barrier suppression.

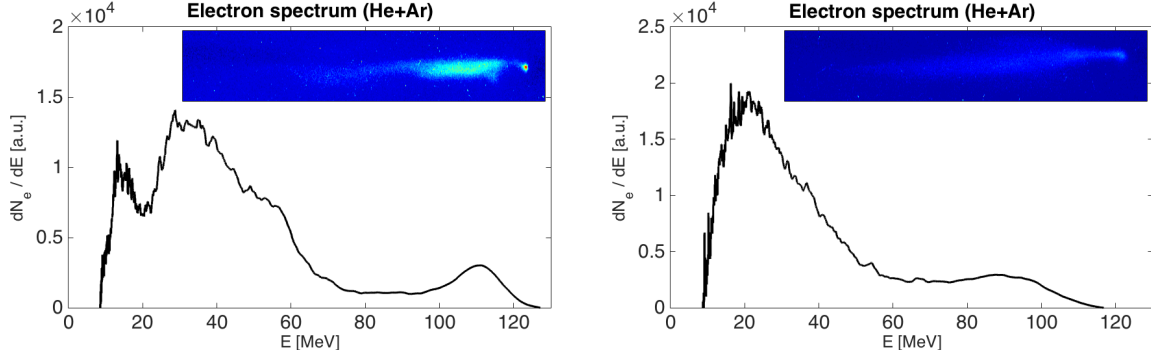


Figure 3.22: Typical electron spectra corrected on the beam pointing and obtained using the mixture of helium and argon (in a pressure ratio of 99:1). On left, the maximum obtained energy of electron bunch $E = 110$ MeV. On right, an electron spectrum from a consecutive shot showing a peak around 90 MeV. Previews of the spectrometer images are included, although not rescaled to the energy on the horizontal axis of the plot.

a consequence of unequal acceleration lengths. This might be avoided when the synthetic air target is used, and consequently electron bunches with a stable peak energy and energy spread can be obtained. The expected energy of accelerated electrons is lower than compared to an ideal bubble regime with an ion cavity which is completely evacuated of electrons.

In order to verify this theory, the mixture of helium and argon in a pressure ratio of 99:1 has been tested as a gas jet target. Furthermore, a razor blade is placed on top of the gas jet nozzle. The reason is twofold: first, to create a steep density gradient with a shock wave on the front end of the target, and thus increase the electron charge; and second, to alter the plasma length. The maximum achieved energy of the accelerated electron bunch is $E_e = 110$ MeV (see Fig. 3.22 (left)). However, the electron energy is fluctuating shot-to-shot, usually containing a high-energy peak above 50 MeV (as shown in Fig. 3.22 (right)). Each electron spectrum also includes additional peaks in lower energy. This is most probably due to multiple injection schemes employed in the laser-plasma accelerator.

The steep density gradient created by the razor blade is probably causing the peak of the highest energy since its position in the spectra strongly depended on the shape and the position of the created shock wave. The electrons injected due to the sudden density difference are accelerated in the full length of the plasma, and thus gained the highest energy. The broad part in the middle of electron spectrum corresponds to our knowledge on the gradual ionization injection from argon in self-focusing, which is expected with the used laser power as stated above (see the laser intensities for ionization in Tab.3.3). The electrons from the low energy peak are trapped in self-injection, judging by the shape of this part of the spectrum.

Furthermore, a combination of both targets has been tested - a mixture of helium with synthetic air in a pressure ratio of 99:1. The idea is to keep the advantages of the He-Ar

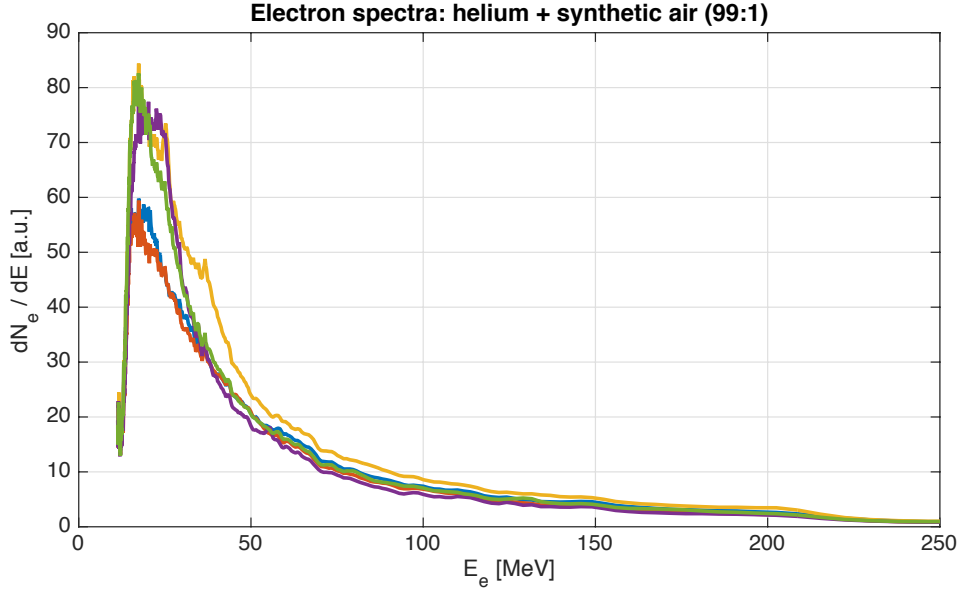


Figure 3.23: Typical electron spectra corrected on the beam pointing and obtained using a mixture of helium with dry air in a pressure ratio of 99:1. The spectra show high stability in energy and energy spread with a mean electron energy $E_{mean} = (34.1 \pm 1.5)$ MeV, a peak energy $E_e = (22.7 \pm 1.7)$ MeV and an energy spread at FWHM $\delta_e = (21.8 \pm 3.9)$ MeV. The charge of the accelerated electron bunches was estimated using the linear signal from the scintillating screen as $Q = (1.5 \pm 0.2)$ pC.

target but avoid the large energy spread in electron spectrum caused by the gradual injection from argon. The generated electron spectra (shown in Fig. 3.23) has a mean electron energy $E_{mean} = (34.1 \pm 1.5)$ MeV, a peak energy $E_e = (22.7 \pm 1.7)$ MeV and an energy spread at FWHM $\delta_e = (21.8 \pm 3.9)$ MeV. The charge of the accelerated electron bunches has been estimated using the signal from the scintillating screen as $Q = (1.5 \pm 0.2)$ pC.

In conclusion, the results obtained with the synthetic air target show an excellent stability with the shot-to-shot variation of the peak energy of only 1.1 MeV. The obtained electron bunch charge was 3.1 pC with a satisfactory shot-to-shot fluctuations of 21 %. The energy of the electrons generated with the mixture of helium and synthetic air in the pressure ratio of 99:1 is higher compared to the synthetic air target with a similar energy fluctuations and relative energy spread but the advantages of the electron spectra obtained with the helium-argon target with their high energy peaks have not been recreated. The higher plasma density, which is needed to stabilize the obtained electron energy, negatively affects the density gradient injection and prevents the creation of the high energy peak. However, using synthetic air instead of argon partly has worked as intended since the broad part of spectrum caused by the gradual injection from argon has been eliminated. The stable peak in electron spectrum is probably consisting of both contributions from self-injection and localized ionization injection as in the case of compressed dry air.

3.2.2 Generated betatron radiation

Betatron radiation generated by electron oscillations has been produced in the plasma with the LWFA scheme using the He-Ar and He-air targets. The photon energy is monitored by the single photon counting X-ray spectrometer (described in section 3.1.4) and the source size is measured using a knife-edge technique. Spectra of similar properties are obtained with both respective targets, varying slightly in the photon energy.

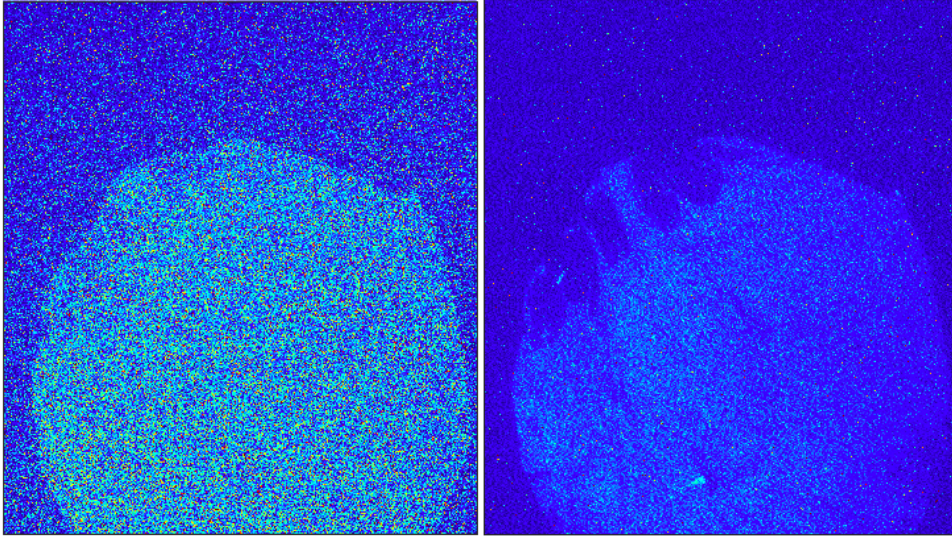


Figure 3.24: Images obtained by the CCD camera using a knife edge technique. The area with more photons in the center is covered by a thin aluminum foil, while the area at the edges is covered by a thick aluminum foil. The betatron source size is calculated by the size of the shadow of the sharp edges on the CCD chip.

X-ray source size

The size of the source is given mainly by the radius of the betatron oscillations of electrons in the plasma. While the source size is one of the biggest advantages of the betatron X-ray source due to its micron size, decreasing the source size can limit the performance of the source since the undulator parameter of the plasma wiggler (Eq. 2.53) is proportional to the betatron radius. This restricts the number of photons emitted by the electron bunch. Moreover, the photon energy is proportional to the radius of the oscillations as well. Therefore, it is important to monitor the source size as one of the crucial parameters of the source to verify the energy measurement and the number of photons, as well as due to its importance for some applications (e.g. phase-contrast microtomography).

The betatron source size has been determined using a knife-edge technique. In our case, the knife edge is a transition between a thick aluminum foil with a hole in the center and a thin aluminum foil (2.3 μm) that covers this hole. In addition, this setup makes the detection system with the CCD detector light-tight. The detector is placed at a distance of 1 m from the source of radiation for this measurement, which is closer than for the single photon counting, for obvious reasons.

From the profile of the signal on the edge between the thin and thick aluminum foils, the size of the source is determined from the size (length) of the drop between the plateau of the uncovered part of the image (behind the thin foil) and the part covered by the "knife" (behind the thicker foil), taking into account the distances between the source, the knife edge and the CCD detector in order to include magnification (see Fig. 3.24). It has been calculated that the betatron source size is $D_S = (6.0 \pm 2.6) \mu\text{m}$. The error is caused mainly by the pixel size of the CCD camera (13.5 μm), which limits the precision of the measurement.

Betatron radiation energy spectrum

Since the photon energy of the betatron radiation depends mainly on the energy of oscillating electrons, the plasma density and the radius of the betatron oscillations (Eq. 2.57), it is possible to estimate the expected critical energy of the betatron radiation. This has been done for both

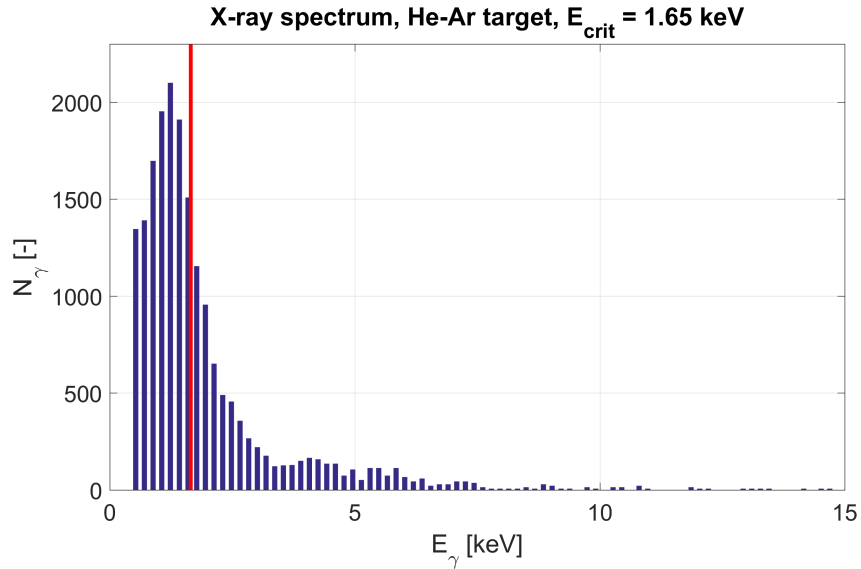


Figure 3.25: A typical betatron X-ray spectrum from the He-Ar target. The critical energy of the synchrotron-like radiation is $E_\gamma = 1.65$ keV.

types of targets. However, for the mixture of helium and argon, it has been done as a verification after the experimental campaign. For the target of helium with the admixture of synthetic air, all the necessary parameters have been measured and determined, and thus this estimation could be done impartially before the betatron radiation measurement.

The first obtained betatron radiation on the source at PALS has been done with the helium target with the admixture of argon. For this case, the supporting PIC simulations [152] has shown a radius of the betatron oscillations $r_\beta = 2$ μm . The mean electron energy is between 40 MeV and 50 MeV and the plasma density is $n_e = 2 \times 10^{19}$ cm^{-3} . Using Eq. 2.57, it could be estimated that the expected critical energy is between $E_\beta = 1.3$ keV and $E_\beta = 2.0$ keV.

The experimental data from X-ray spectrometer operated in the single photon counting mode shows a good agreement with this estimation as energy spectra with a critical energy of $E_{\beta, \text{He+Ar}} = 1.65$ keV have been obtained (see Fig. 3.26).

For the target of helium with the admixture of synthetic air, the plasma density is set to $n_e = 3 \times 10^{19}$ cm^{-3} , the mean measured electron energy is $E_e = 34.1$ MeV, and the radius of betatron oscillations has been estimated again by the supporting PIC simulations as $r_\beta = 3$ μm . Equation 2.57 gives the expected betatron critical energy $E_{crit} = 2.1$ keV.

This is in an excellent agreement with the experimentally obtained energy spectra of the betatron X-ray radiation as the critical energy is found to be approximately $E_{crit} = 2.3$ keV.

3.2.3 X-ray spectrum from Ross filter based spectrometer

As it has been soon found out, the number of photons per shot is low during the experiments at PALS and it is not possible to obtain results from the X-ray spectrometer based on Ross filters due to the low signal-to-noise ratio. For this reason, the Ross filters have been tested at an experiment with betatron radiation at Laboratoire d'Optique Appliquée (LOA), where the betatron source is well-defined and generates stable X-ray pulses with a sufficient photon number. The Ti:sapphire laser in Salle Jeune produces pulses with a maximum energy of 2 J and a duration of 30 fs. During an experiment, the Ross filters have been used in combination with a scintillating screen. A typical image from the CCD camera of the X-ray spectrometer obtained by combining images from 20 shots is shown in Fig. 3.27.

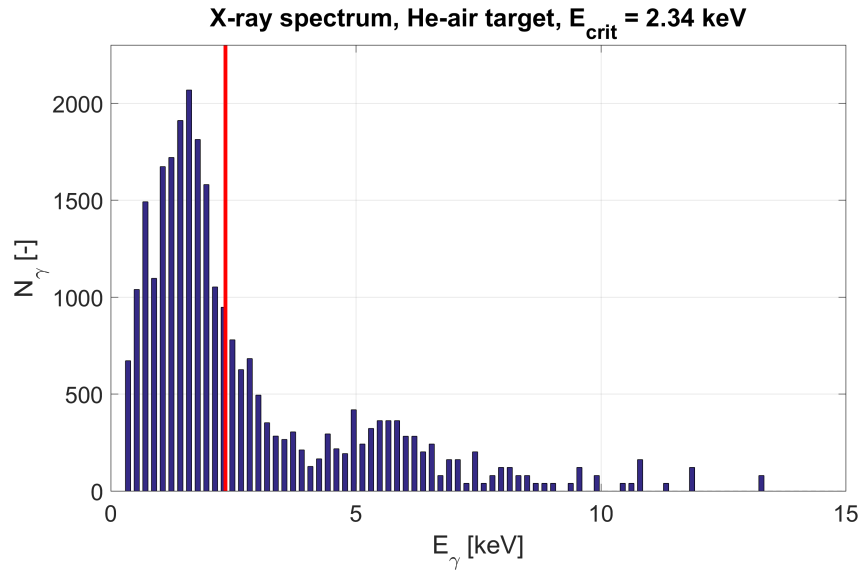


Figure 3.26: A typical betatron X-ray spectrum from the He-air target. The critical energy of the synchrotron-like radiation is $E_{\gamma} = 2.34$ keV.

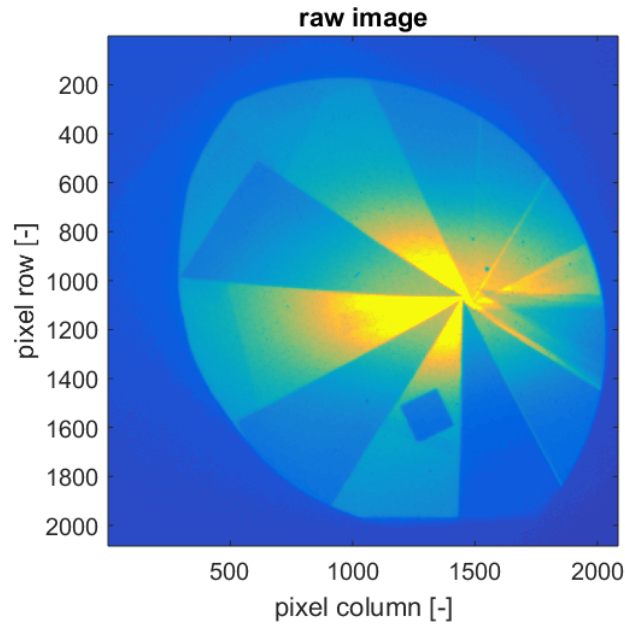


Figure 3.27: A typical image from the CCD camera of the X-ray spectrometer obtained by combining images from 20 shots.

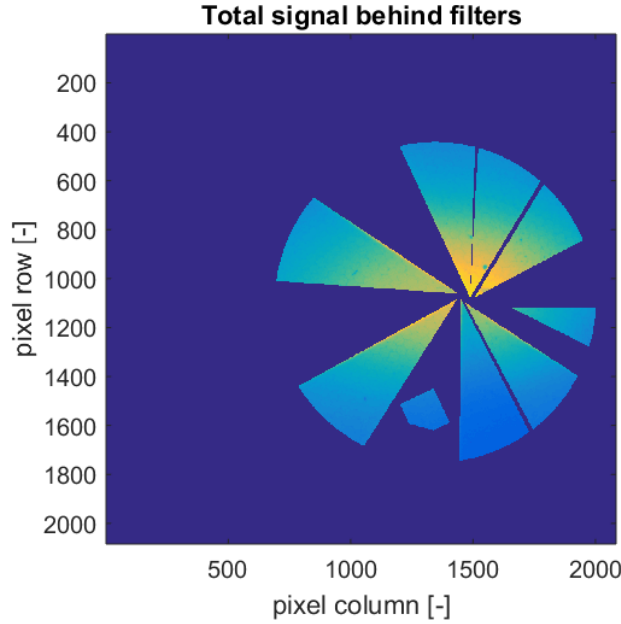


Figure 3.28: Selected areas of all filters. Largest possible regions of the filter without additional obstacles have been selected from the image.

In the analytic code, which has been written in Matlab software as a part of the work on this thesis, the edges of all filters are carefully defined and the areas of filters are saved separately. Largest possible regions of the filter without additional obstacles have been selected. The result of the filter selection is depicted in Fig. 3.28. In the same manner, the areas without filters (covered only by the supporting Mylar foil) were selected separately for the purpose of fitting as described below.

In order to correctly select areas of filters that are illuminated with the same photon intensity, the signal behind all filters and behind the unfiltered regions is approximately renormalized to the same levels and fitted with a two-dimensional function. This auxiliary modified image, which is used in the analysis only for the purpose of fitting, is depicted in Fig. 3.30. As the spatial distribution of photons illuminating the Ross filters is normally distributed, a general 2D gaussian function has been chosen as the best candidate for the fit function, providing seven parameters (amplitude, width in x-dimension, width in y-dimension, $[x,y]$ coordinates of the center, angle of rotation and an additional constant in the z-dimension). The resulting fit is shown in Fig. 3.31. The change of amplitude due to the renormalization of signal behind filters does not affect the analysed data as only the relative position with respect to the maximum of the fit function is used later in the analysis.

The areas for the comparison of the signal behind the Ross filters are selected as circles of a defined radius placed on intersections of the 2D gaussian fit and axes of the filters at a height of $1/e$. Each filter axis is defined as a line pointing from the center of the cake layout through the middle of the filter.

The comparison of signals for the Ross filter analysis then uses the signal from the selected circular areas. The signal N_{sig} (number of counts) in each region is summed and is divided by the number of pixels N_{pix} to obtain an average signal value $n_{sig} = \langle N_{sig} \rangle$ (the density of the signal). The differences of the density values are calculated for each filter pair. It is possible, in general, to select the circular regions for some filters around intersections at different relative height (e.g. $1/2$ or $1/e^2$) than others. However, the height has to be the same for both filters from the pair and a renormalization to the spatial distribution is necessary in order to obtain

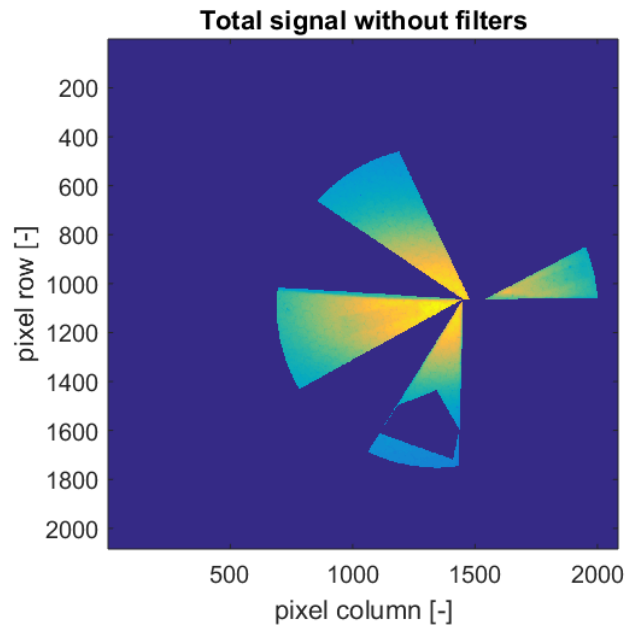


Figure 3.29: Selected areas without filters (covered only by the supporting Mylar foil).

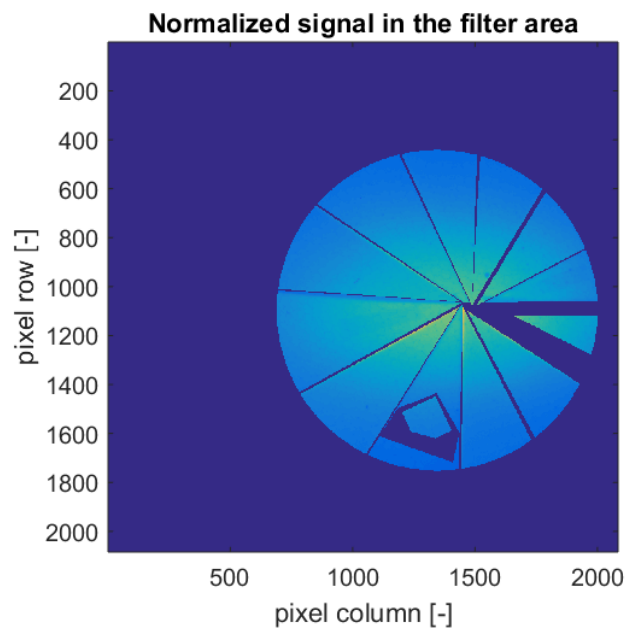


Figure 3.30: An auxiliary modified image with the signal in all selected regions (behind filters and without filters) approximately renormalized to the same levels for the purpose of fitting.

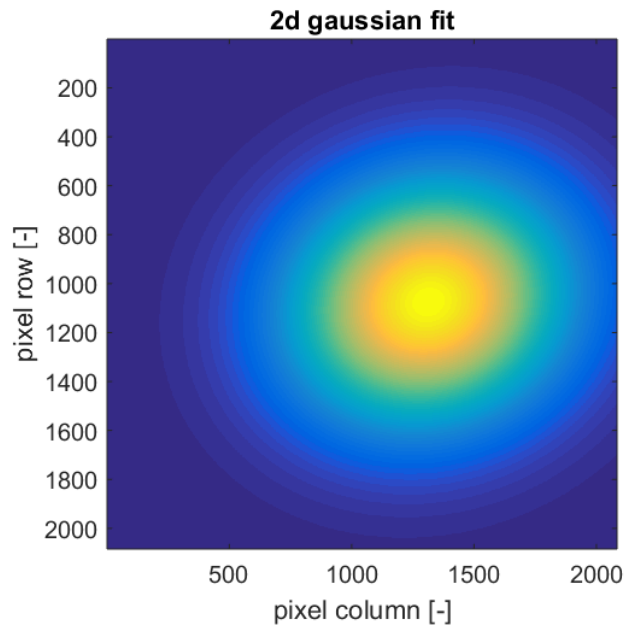


Figure 3.31: A general 2D gaussian fit of the signal in all selected regions renormalized to the same levels.

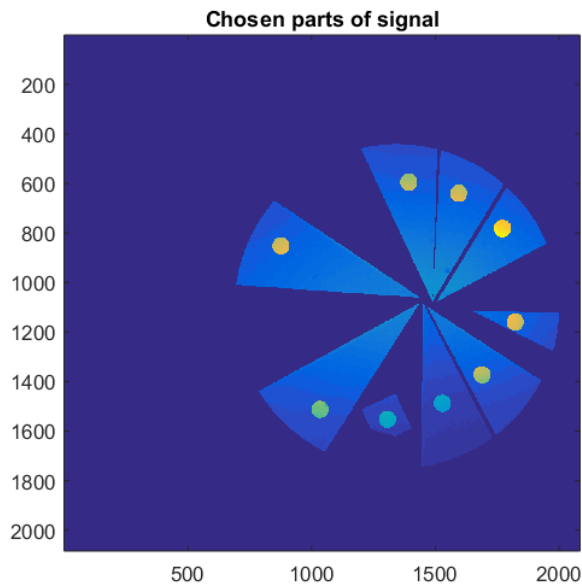


Figure 3.32: The chosen circular areas for the comparison of the signal behind the Ross filters (highlighted $5x$ for the purpose of plotting). The circles of a defined radius are placed on intersections of the 2D gaussian fit and axes of the filters (pointing from the center of the cake layout through the middle of each respective filter) at the height of $1/e$.

comparable results for the energy spectrum reconstruction.

Differences in the transmission functions are determined for each filter pair as well. Since a narrow energy range $\langle E_{min}; E_{max} \rangle$ defined by the absorption edges of two filters in a pair is of a finite width, a mean energy needs to be assigned to the pair instead of the energy range. The width of the energy interval projects into the final obtained X-ray spectrum as a horizontal errorbar. The mean energy is calculated as a weighted average

$$\langle E_\gamma \rangle = \frac{\int_{E_{min}}^{E_{max}} E_\gamma \Delta T dT}{\int_{E_{min}}^{E_{max}} \Delta T dT}, \quad (3.17)$$

where E_γ is the photon energy and ΔT is the difference of transmission functions for any given filter. In a similar manner, a mean value of the transmission difference is calculated as a weighted average

$$\langle \Delta T \rangle = \frac{\int_{T_{min}}^{T_{max}} \Delta T E_\gamma dE_\gamma}{\int_{T_{min}}^{T_{max}} E_\gamma dE_\gamma}, \quad (3.18)$$

where $T_{min} = \Delta T(E_{min})$ and $T_{max} = \Delta T(E_{max})$. The errors can be calculated as one standard deviation. The radiated energy is then obtained as

$$dI/d\omega = \frac{n_{sig}}{\langle \Delta T \rangle} \frac{1}{E_{max} - E_{min}}, \quad (3.19)$$

which already includes a normalization to the energy interval width. The obtained data points (one for each filter) are then fitted by a Bessel function of the second kind, which describes the shape of the synchrotron-like spectrum, and the critical energy of the betatron radiation is calculated. A typical spectrum obtained from the data from LOA by the analysis described above is shown in 3.33 with a critical energy of $E_{crit} = 5.87$ keV. The data point obtained from the filter pair no.3 have had to be discarded as it has a negative value of the radiated energy. This is due to a partly damaged Fe (20 μm) filter, which consists of 4 layers of Fe foil with a thickness of 5 μm . One of the middle foils has been partly crumpled, which has been discovered after the experiment.

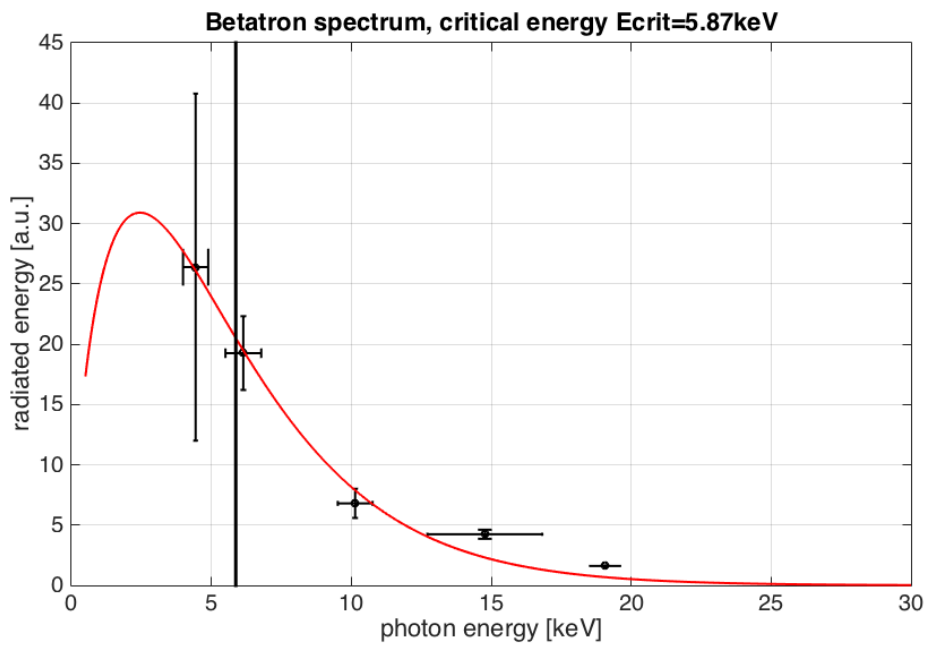


Figure 3.33: A typical betatron spectrum obtained using Ross filters. The critical energy is 5.87 keV. Each data point corresponds to one filter pair. The error bars are given by the uncertainties in calculation of the mean difference of transmissions of given filters in a pair.

BETATRON AND COMPTON SOURCES AT ELI BEAMLINES

This chapter describes the conceptual design of the betatron and Compton source at ELI Beamlines, to which the author significantly contributed in design development. The experimental setup based on the previous experiments and prototyping of equipment is presented and the expected parameters of the source are highlighted. Design of a modular electron magnetic spectrometer for broad electron energy range and the measurement of its magnetic field are shown and it is explained how the electron spectrometer can be improved with focusing of electron beams by the dipole magnet of the spectrometer and how it can be utilized in a Compton source in order to obtain a monoenergetic X-ray/gamma beam.

4.1 ELI Beamlines facility

ELI Beamlines is a modern state-of-the-art European research facility in Dolní Břežany, Czech Republic, which is focused on the laser-driven sources of secondary particles. The betatron and Compton source are among these sources being built. ELI Beamlines is equipped with three main laser systems of distinct parameters and performance, which are transported into five experimental halls, each containing one or more laser-driven sources of photons, electrons or ions [188].

The L1 laser is designed in-house by ELI Beamlines to generate laser pulses of about 100 mJ and with a duration of 20 fs with a high repetition rate of 1 kHz. Frequency chirped picosecond pulses are amplified by seven amplifier based on the optical parametric chirped pulse amplification (OPCPA) technique.

The L3 HAPLS laser (The High-Repetition-Rate Advanced Petawatt Laser System) developed at the Lawrence Livermore National Laboratory is a petawatt-class system delivering pulses with an energy of up to 30 J and a duration of < 30 fs with repetition rate of 10 Hz.

The L4 laser is a kJ laser system designed to generate an extremely high peak pulse power of 10 PW with a duration of about 130 fs. The uncompressed laser pulses reach an energy of about 2 kJ and are generated once per minute, bringing a major improvement in the kJ-class laser systems. The L4 laser can provide pulses of a duration of various orders of magnitude. There will be L4n (nanosecond), L4p (picosecond) and L4f (femtosecond) beams available.

The *E1 experimental hall* contains laser-driven secondary sources for applications in material and biomolecular scientific fields, which produce photon beams from the UV to X-ray spectral range. *Plasma X-ray Source* (PXS) uses laser pulses from the high-repetition L1 laser focused on continuously restoring solid-density metal targets in order to generate ultrashort, high-brightness X-ray pulses in the spectral range of 4–30 keV at the ultra high repetition rate of 1 kHz. *High-order Harmonic Generation* (HHG) beamline employs the mechanism of EUV radiation (10–100 eV) generated from a gas target at the kHz repetition rate in a beam with a low divergence. *Multi-purpose chamber* (MAC), which will be used for atomic and molecular physics and optics (AMO) and for coherent diffractive imaging (CDI) is one of special purpose end-stations in E1 placed at the direct beam line of the HHG source. The MAC chamber can be equipped with various types of targets and diagnostics and enables pump-probe experiments

with two HHG beams. The *ELI instrument for sub-ps VUV ellipsometry* (ELIps) is a VUV ellipsometer at the HHG beamline, which provides femtosecond magneto-optical ellipsometry in the energy range between 1 eV and 40 eV. A modular station for *Time Resolved Experiments with X-rays* (TRES) is available in E1 as well, providing the sub-picosecond X-ray pulses and perfectly synchronized UV-VIS-IR pump pulses to other X-ray end-stations for X-ray scattering and diffraction (XRD), X-ray absorption spectroscopy (XAS) and phase contrast imaging (PCI).

The *E2 experimental hall* is dedicated to tunable hard X-ray sources and houses the betatron and Compton beamlines (joined into a single setup under a name *gammatron*) for user experiments. The L3 PW laser will be focused onto a gas jet target and electrons within the resulting plasma are accelerated to relativistic energies. In the case of betatron source, the electrons are forced to wiggle in a plasma bubble, which serves as a plasma undulator/wiggler, and emit photons of up to 100 keV. The Compton sources uses the accelerated electrons for scattering on a secondary laser pulse. A double Doppler shift in the photon energy results in generation of hard X-ray beams of up to 1 MeV. Both sources may operate at the repetition rate of 10 Hz of the driving L3 laser and are perfectly synchronized with its laser pulse. The full description of the betatron and Compton sources is available in the section 4.2.

The *E3 experimental hall* houses a multi-functional experimental infrastructure dedicated to laser-matter interaction research on warm dense matter (WDM), high energy density physics (HEDP), laboratory astrophysics, plasma optics and ultra-high intensity interaction. The interaction area utilizes L2, L3 and L4 lasers with a flexible energy partition between L4n, L4p and L4f laser beams.

The *E4 experimental hall* contains the *ELI Multidisciplinary Applications of laser-Ion Acceleration* (ELIMAIA) beamline. The L3 and L4 lasers (both at the PW power) will be available for the ion accelerator and ELI-Beamlines MEDical and multidisciplinary applications (ELIMED) beamline. An auxiliary beam L3-aux with an energy of 0.1-1 J will be split from L3 and available for pump-probe experiments.

The *E5 experimental hall* contains two sperate beamlines dedicated to laser-driven electron acceleration and undulator x-ray source, respectively. *The High-energy Electron Laser Light* (HELL) beamline consists of two parts: electron accelerator driven by the L3 and L4 lasers (both at the PW power level), and laser beam transport and monitoring. HELL is designed as a flexible platform for user experiments and allows temporal synchronization between pulses below 10 fs due to splitting of the L3 beam. On the other side of the E5 experimental hall is *the Laser-driven Undulator X-ray source* (LUX), which will provide X-ray pulses with a duration of a few femtoseconds and an energy in the water window spectral region. Additionally, laser pulses of < 30 fs and < 7 fs synchronized with the generated X-ray pulses with a precision of a few femtoseconds will allow pump and probe user experiments.

4.2 Conceptual design of the betatron and Compton source at ELI Beamlines

Using the experience in working with laser-driven sources of electrons and secondary particles, setup of the Gammatron beamline (containing both betatron and Compton sources) in the E2 experimental hall has been created. An overview of the E2 experimental hall is shown in Figs. 4.1 and 4.2. A beam transport line supplies the L3 laser beam into an experimental chamber unit (ECU) and the laser beam is focused by an off-axis parabolic mirror with a dielectric coating in a focusing cylindrical chamber. The Compton source uses an additional cylindrical chamber containing a focusing mirror for the secondary laser beam, which is split in the last small chamber of the beam transport. A concrete beam dump is built on one side of the ECU chamber to absorb the energy of the deviated electron beam and provide a high level of radiation

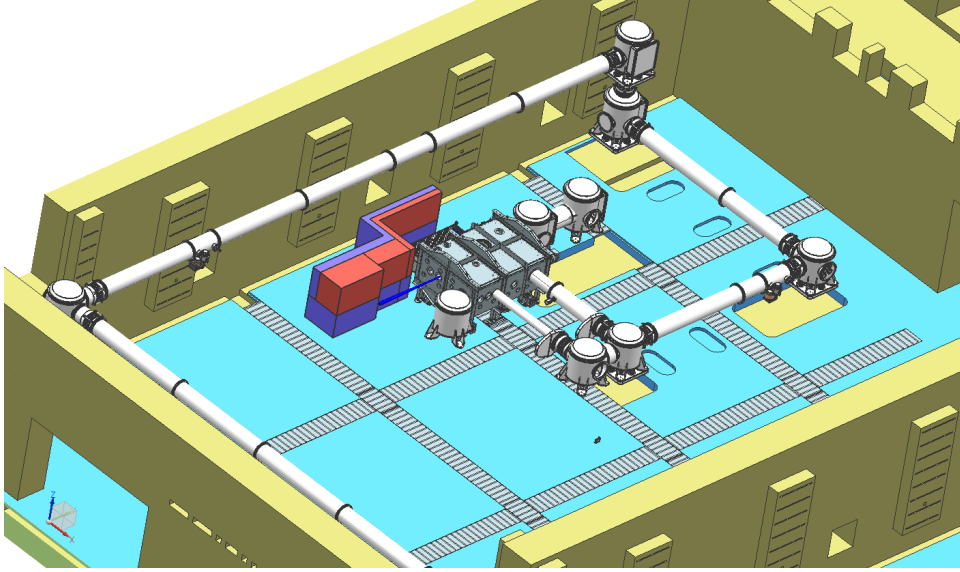


Figure 4.1: An overview of the experimental hall E2 at ELI Beamlines with the experimental setup of the betatron and Compton source in the ECU chamber in the center of the image. The laser pulse of the laser L3 is brought to the chamber via the beam transport vacuum pipes and chambers from the edge of the room in order to ensure the direction of the accelerated electrons and generated X-rays away from the local control room (behind the wall in the top right corner of the image).

safety.

For the betatron source, the experimental setup can be much simplified, using only the ECU chamber and one small focusing chamber with a variable distance as shown in Fig. 4.3. The ECU chamber can house most of the setup while all necessary systems of diagnostics are placed outside on an optical table. In the same manner as the experiments at PALS, the set of diagnostics includes an electron pointing monitor, an electron spectrometer, an X-ray spectrometer, an interferometer, a topview camera and a focal spot monitor. Furthermore, scattered beam diagnostics and a Raman spectroscope are used.

An overview of the model of the experimental setup is shown in Fig. 4.4 and the schematic drawing in Fig. 4.5. The L3 laser beam comes into the chamber and is reflected by a plane dielectric mirror onto the off-axis parabolic mirror with an effective focal length of 2 m (short) or 4 m (long), respectively. The beam is focused onto a gas jet target with a length of 2–8 mm. The range of the length values is calculated for electron plasma densities of $3 \times 10^{18} - 1 \times 10^{19} \text{ cm}^{-3}$ and approximated by Eq. 1.45 and the laser pulse depletion length $L_{\text{dep}} \sim a_0 \lambda_p^3 / \lambda_L^2$ [5]. The pulse depletion length is similar to the dephasing length in the nonlinear regime ($a_0 > 1$) Electrons of up to 1.5 GeV are planned to be accelerated with these parameters and they are expected to generate betatron X-ray radiation with an energy of up to hundreds of keV.

The accelerated electron bunch will be analysed in a similar manner as in the prototyping phase: the pointing of electrons is monitored by a scintillating screen imaged by a CCD camera. Then the electron beam is deviated and analyzed by a magnetic spectrometer with the magnetic field $\sim 1 \text{ T}$ in the gap. The electron pointing monitor is motorized in order to remove it from the trajectory of the generated betatron X-ray radiation, which continues along the laser axis towards the X-ray spectrometer - a CCD camera with Ross filters and a scintillating screen (as described in Section 3.1.4). Simultaneously, the setup allows the laser beam to be analysed after the laser-plasma interaction. The plasma density is obtained using interferometry. For this purpose, a Mach-Zehnder interferometer or Michelson interferometer or Wollaston interferometer may be used.

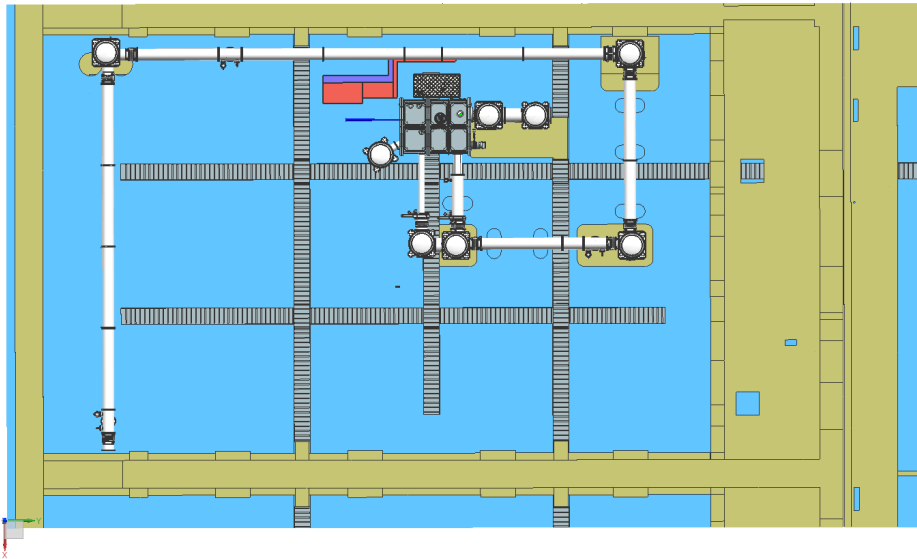


Figure 4.2: A top view of the experimental hall E2 at ELI beamlines with the experimental setup of the betatron and Compton source in the ECU chamber. A user end-station will be located in the area downstream of the experimental setup (top left corner of the image).

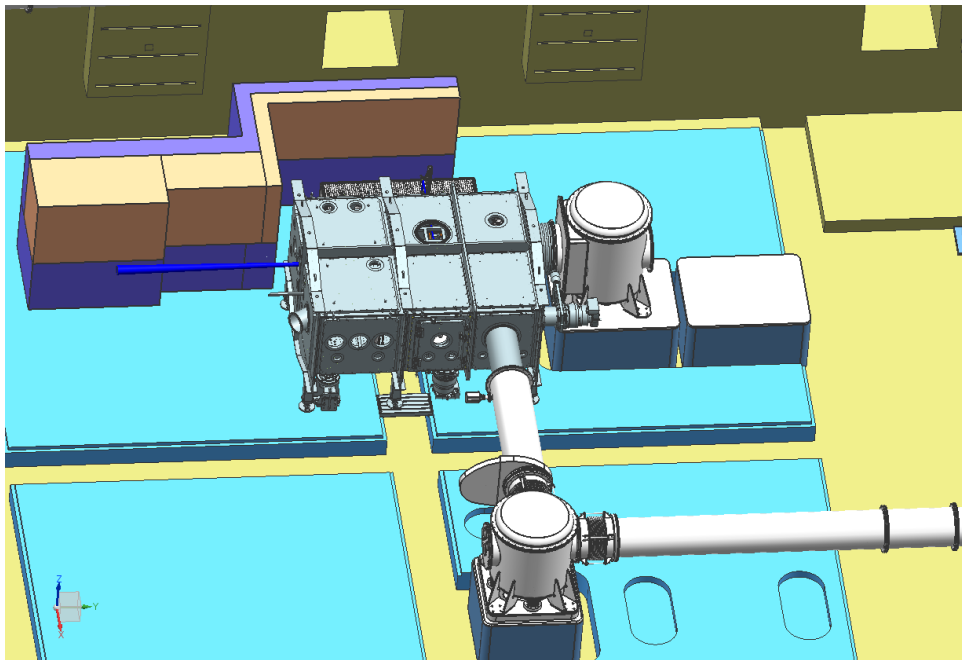


Figure 4.3: The interaction chamber of the betatron and Compton source in the E2 hall at ELI Beamlines. The small cylindrical vacuum chamber to the right of the interaction contains the focusing optics for the L3 laser beam. The focal length is variable and can be switched between 2 m (shown in the image) and 4 m (in this case, the cylindrical chamber is moved further to the right onto the second concrete block).

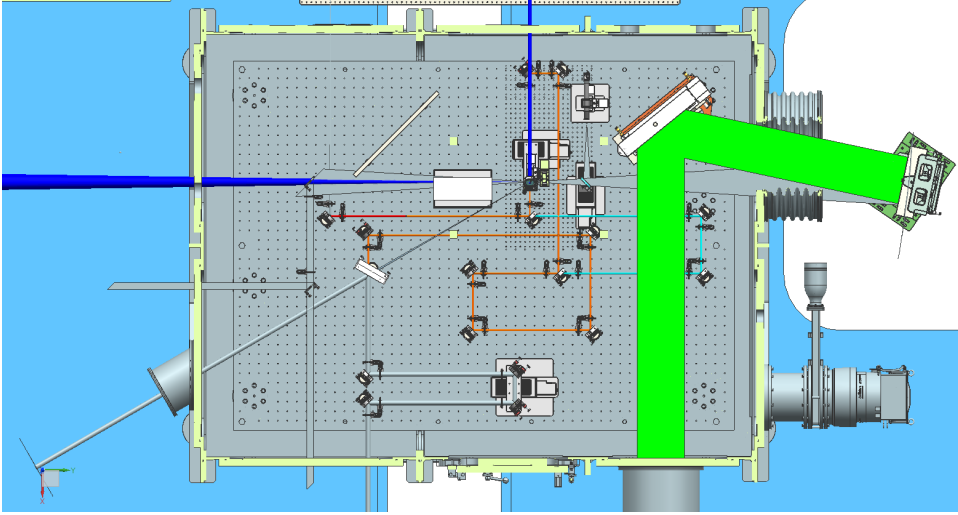


Figure 4.4: A top view of the experimental setup of the betatron and Compton source in the E2 hall. The incoming laser beam of the L3 laser (green beam) is focused by an off-axis parabolic mirror onto a gas jet target. Electrons are produced and used for X-ray pulse generation (blue beam). An auxiliary laser pulse (orange) is used for the interferometry and as the secondary pulse for inverse Compton scattering.

Source	Betatron (phase A)	Betatron (phase B)	Compton source
Energy range	1–10 keV	1–100 keV	100 keV–5 MeV
Photon number	10^8	$> 10^8$	10^8
Spectrum	Broadband	Broadband	Monochromatic/Broadband
Pulse duration	10 fs	10 fs	10 fs
Divergence	< 40 mrad	< 20 mrad	< 20 mrad
Source size	< 5 μm	< 5 μm	< 5 μm

Table 4.1: Betatron and Compton beamline parameters requirements.

It is expected that in the first phase, when the L3 laser is operated with a power of a few hundreds of terawatt, the betatron source produces X-ray pulses with a critical energy of up to 10 keV and a pulse duration of about 10 fs. In the second phase, after the upgrade to the full laser power of 1 PW, the betatron source should be capable to generate broadband X-ray radiation with an energy of up to 100 keV. A set of parameters of the betatron source is described in Tab. 4.1, divided into *phase A* intended for the period before the L3 laser is operated with full power and *phase B* for the period when the L3 laser is capable of 1 PW operation.

An experimental setup for the Compton source requires only a few modifications compared to the betatron source. An auxiliary beam is split in the last cylindrical chamber of the beam transport and used for the interferometry and inverse Compton scattering on the accelerated electrons. Another option is to use a foil mounted to the prototype holder as a plasma mirror near the exit point of electrons from the plasma as described in previous chapters. With the foil at a distance of 1 cm from the focal spot of the laser, the laser intensity for scattering is about three orders of magnitude lower than in the focal spot. With a laser intensity of more than 10^{21} W/cm² in focus, it is thus possible to reach intensities of more than 10^{18} W/cm² for inverse Compton scattering, which enables the wiggler regime of the Compton source and reaching the maximum energy of 5 MeV as specified in the planned parameters in Tab. 4.1. The Compton source consists of a single phase as it will be operational only once the L3 laser is capable of 1 PW operation. Moreover, it will be operational at the challenging high repetition rate of 10 Hz.

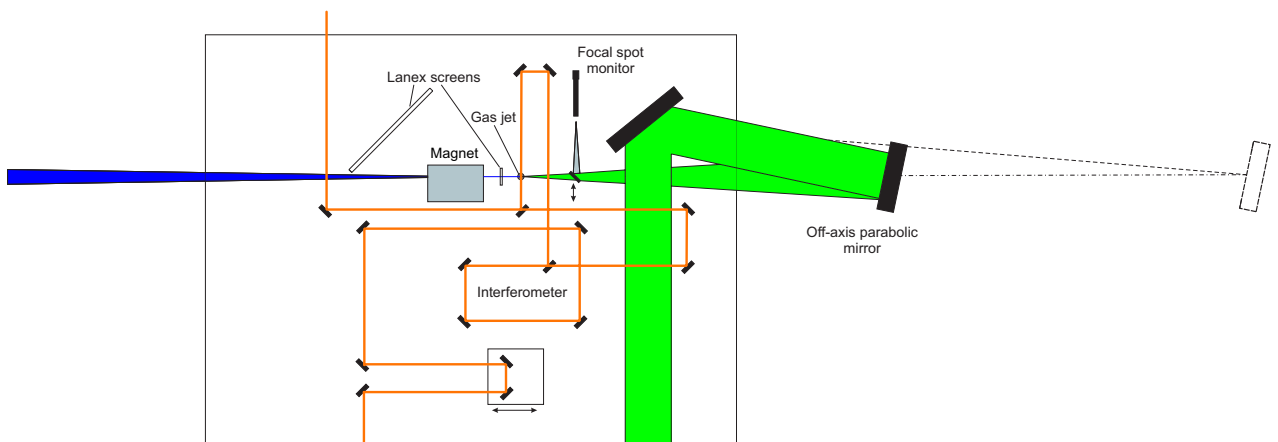


Figure 4.5: A schematic drawing of the experimental setup of the betatron source in the E2 experimental hall. The L3 laser pulse (green) is focused by an off-axis parabolic mirror with a focal length 2 m (or alternatively 4 m) onto a gas jet target. An offline focal spot monitor is used to optimize the focus of the laser. An auxiliary beam (orange) is used for interferometry (Mach-Zehnder interferometer is depicted) in order to obtain the plasma density. Accelerated electrons are monitored via electron pointing diagnostics and the electron magnetic spectrometer consisting of the dipole magnet and Lanex screens imaged by CCD cameras. The generated X-ray pulses are eventually allowed to leave the ECU chamber (shown as the outside rectangular border) and continue to the user end-station.

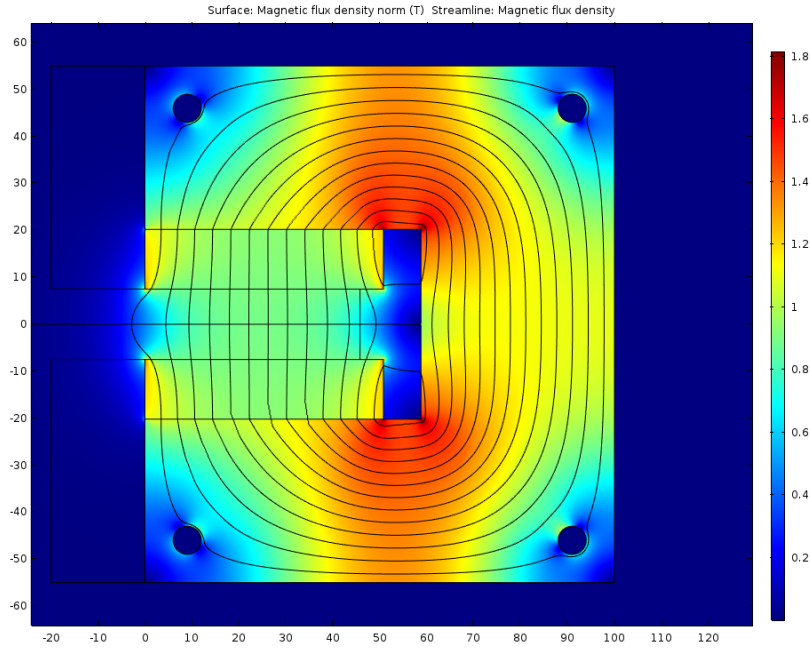


Figure 4.6: The result of magnetic flux density simulations for the smaller version of the dipole magnet designed for experiments in the laboratory at Lund University, Sweden. Figure courtesy of Jonas Svensson, Lund University, Sweden.

4.3 Modular magnetic spectrometer for high-energy electrons

For the purpose of the electron spectrometry, a modular electron magnetic spectrometer was designed and manufactured as a part of the work on this disertation. Each module of the spectrometer is comprised of a C-shaped magnetic steel yoke with a length of 4 inches and the first prototypes are going to be equipped with two large N52 neodymium dipole magnets with dimensions of $4 \times 2 \times 2$ inches in each module. There are aluminum inner spacers that prevents magnetic saturation in the inner edges of the yoke and aluminum outer spacers preventing damage to the magnets while manipulating with other magnetic objects (e.g. tools) near it.

The design was prepared in a collaboration with the laboratory at Lund University, Sweden. Fig. 4.6 shows the magnetic flux density in the dipole magnet cross-section in a smaller dipole magnet intended for use in a lab at Lund (planned with magnets with a height of 0.5 inch instead of our magnets with a height of 2 inch). The primary purpose of the simulation is the estimation of the magnetic flux in the inner edges of the yoke. Since the dimensions of our design and the Lund design are the same in this region, comparable results are expected. The material for the magnet yoke is a magnetic steel, type DD13 (EN10111:2008), which has a value of magnetic flux saturation more than 2 T. This is sufficient given the simulations showed a maximum expected magnetic flux density of 1.8 T around the inner edges inside the yoke.

The separate modules and outer spacers are held together using rods (for better description, see Fig. 4.7). It is intended that up to three of these modules will be connected together into a large dipole magnet (see Fig. 4.8) in order to provide a sufficient resolution for spectrometry of electrons with energies up to 1.5 GeV.

The magnetic field inside the gap with a height of 1.5 cm was measured using a gaussmeter. The resulting magnetic field map of the horizontal plane in the middle of the magnet gap is shown in Fig. 4.9 and the magnetic field on the axis (vertically centered in the magnet gap) is depicted in Fig. 4.10. The maximum measured field was found to be equal to 1.06 T and the

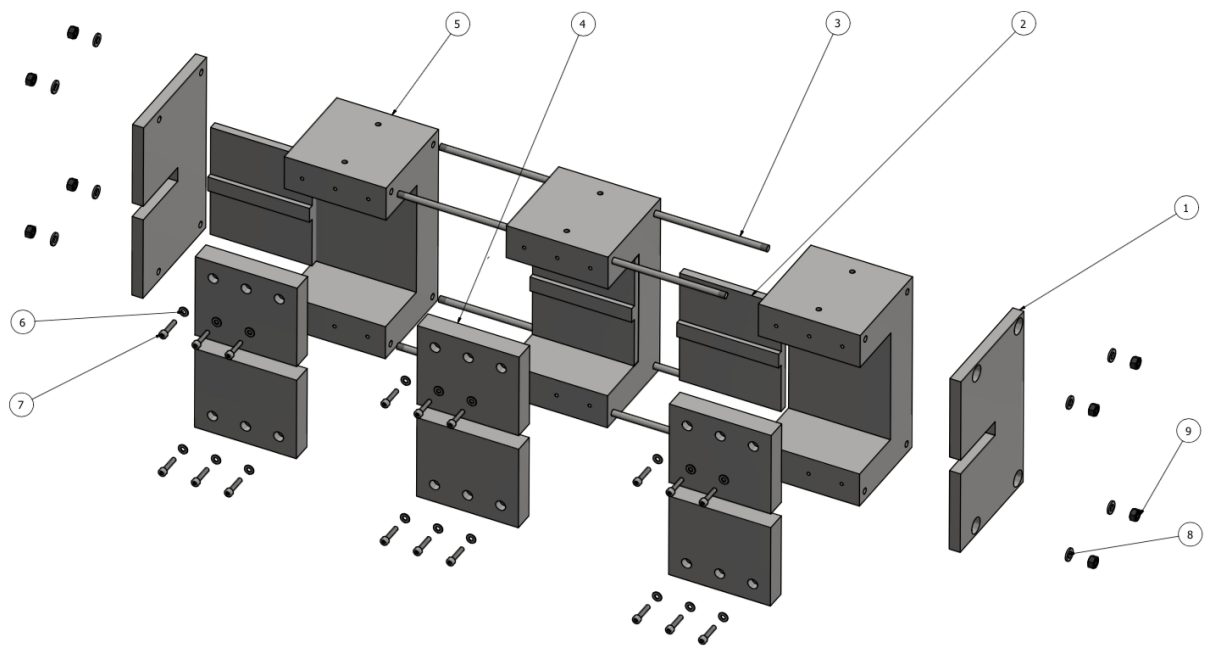


Figure 4.7: The yoke of the dipole magnet of the electron spectrometer for the betatron and Compton source in E2. The outer aluminum spacers (1) and (4) serve as a protection for the neodymium magnets placed inside the designed steel yoke (5) and the inner spacers (2) prevent magnetic saturation in the inner edges of the yoke. The modules are connected together with rods (3), which are screwed into their places with bolts (9) and washers (8).

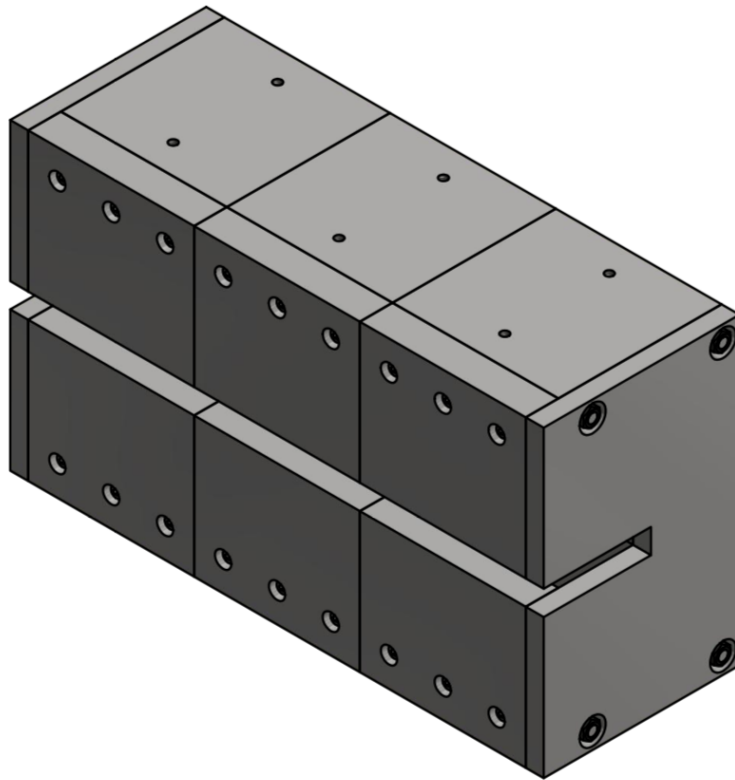


Figure 4.8: The dipole magnet of the electron spectrometer for the betatron and Compton source in E2 comprised of three separate modules.

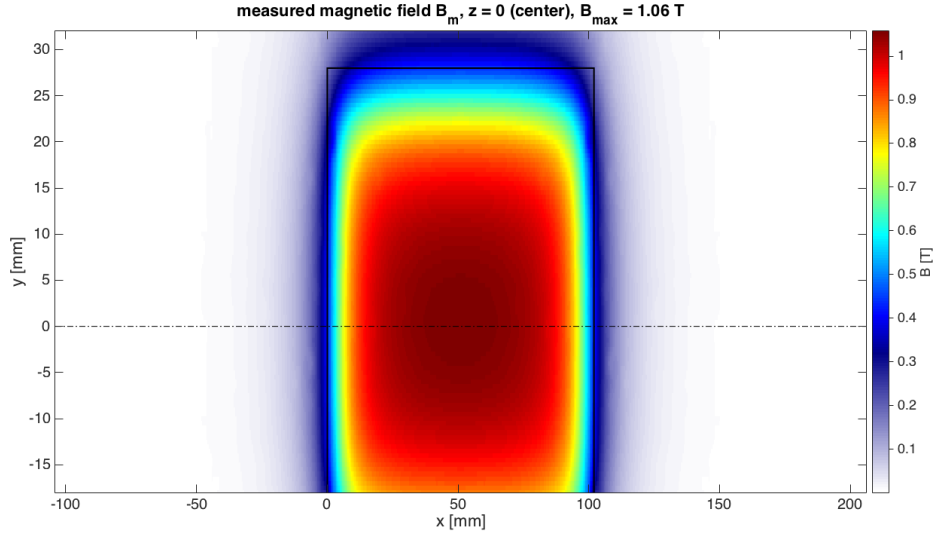


Figure 4.9: The map of the magnetic field of a single module of the dipole magnet of the electron spectrometer for the betatron and Compton source in E2 measured on the middle horizontal plane in the magnet gap. The maximum measured magnetic field equals 1.06 T.

level of uniformity is sufficient for the electron spectrometry.

The number of magnet modules which is planned to be used depends on the energy of the accelerated electrons in an experiment. If we consider that only electrons leaving the magnet gap from the back are detected, it is beneficial to use more modules in order to achieve a greater dispersion along the detector (and thus better energy resolution) for high energy electrons. On the other hand, the more magnet modules in use means the higher the minimum electron energy that exits the magnet from the back. A comparison of the dispersion of electrons along the detector as a function of the electron energy is shown in Fig. 4.11 for the magnetic spectrometer consisting of one, two and three magnet modules, respectively. The distance and angle of the scintillating screen is kept at the same position with respect to the back of the dipole magnet.

4.4 Electron spectrometer for tunable Compton source

During the simulations of the magnetic electron spectrometer with a C-shaped steel yoke, which has one side of the magnet gap open (as described in the previous section), it was found out that it might be advantageous to let all electrons from the beam leave the magnet gap through the open side rather than trying to ensure they leave through the back.

It is shown in this section that naturally divergent electron beams can be focused in the dispersive dimension using the dipole magnet with the open side, and thus the energy uncertainty in the magnetic spectrometer can be improved. Since the resolution of the magnetic spectrometer depends on the dispersion of electrons across the particle detector, which is directly related to the beam divergence, this method can be beneficial for spectroscopy of quasi-monoenergetic beams as it effectively suppresses the effect of the divergence around a certain value of the electron energy. This energy is given by a combination of the magnetic field and the magnet geometry.

4.4.1 Electron focusing with dipole magnet

The investigation of this phenomenon leads to a general condition under which the focusing occurs. For the monoenergetic electron bunch with an energy E_e , the Larmor electron radius in

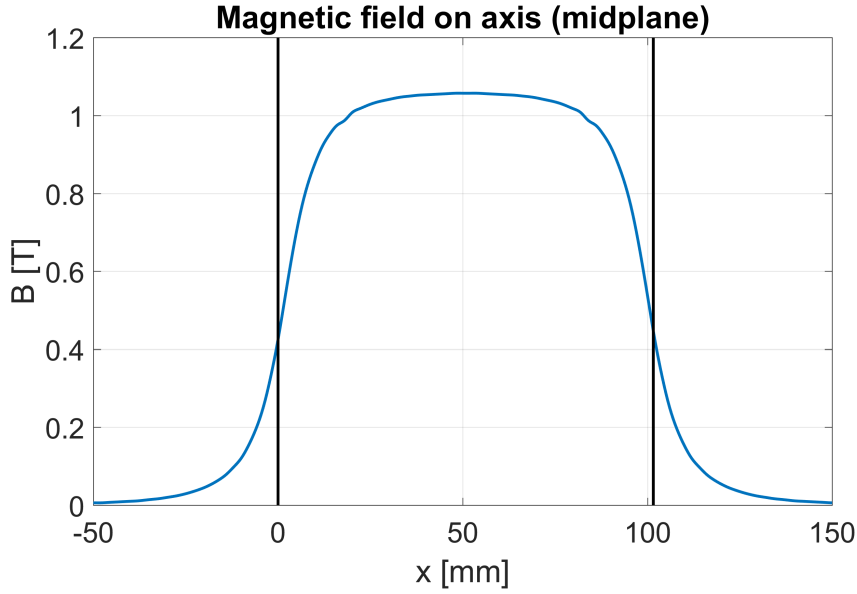


Figure 4.10: The magnetic field of a single module of the dipole magnet of the electron spectrometer for the betatron and Compton source in E2 measured on axis on the middle horizontal plane in the magnet gap.

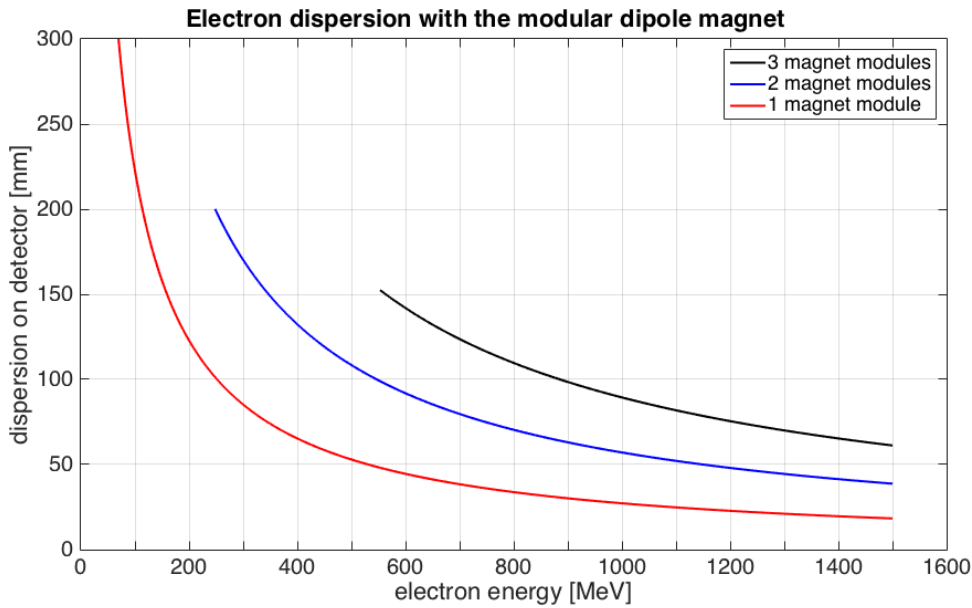


Figure 4.11: The dispersion of electrons along the detector as a function of the electron energy for the magnetic spectrometer consisting of one, two and three magnet modules, respectively. The lowest energy is given by the length of the magnet since only electrons leaving the magnet gap from the back side are considered in this plot. The higher the dispersion for a given electron energy, the better the energy resolution of the spectrometer. Thus, the number of modules in use must depend on the energy of the accelerated electrons during an experiment.

a uniform magnetic field is given by Eq. 3.5 for all electrons. In the text, we mostly refer to three electron beams that define the electron bunch with a half-angle divergence θ . First, the "zero" electron beam is the center beam on the axis of the electron bunch, which enters the magnet gap at an angle $\alpha_0 = \alpha$. Furthermore, "-" and "+" electron beams are the envelope beams of the bunch in the dispersion dimension of the electron magnetic spectrometer, where "-" and "+" beams enter the magnet gap at an angle of $\alpha_- = \alpha - \theta$ and $\alpha_+ = \alpha + \theta$, respectively (see Fig. ??). The incident angles of the center beam and the envelope beams meet the following inequation:

$$\begin{aligned}\alpha_- &< \alpha_0 < \alpha_+ \\ \alpha - \theta &< \alpha < \alpha + \theta.\end{aligned}$$

Focusing of such an electron bunch occurs when the exit angle β_+ is larger than the exit angle β_- . Both angles β_- and β_+ are measured counterclockwise from the magnet axis. Therefore, the obvious focusing condition can be written as

$$\beta_+ - \beta_- > 0. \quad (4.1)$$

In order to focus the divergent electron beam by the magnetic field, a sufficient difference between the trajectory lengths of the envelope beams must occur. Therefore, the condition 4.1 can be rewritten in terms of trajectory lengths instead of angles. For our case of a rectangular magnet, the difference between the exit angle and the incident angle defines the length of the circular arc in the magnet gap as

$$L_i = R[\beta_i - (\pi/2 - \alpha_i)], \quad (4.2)$$

where $i \in \{-, 0, +\}$. The trajectory length difference can be thus expressed as

$$\begin{aligned}L_+ - L_- &= R[\beta_+ - \pi/2 + \alpha_+ - \beta_- + \pi/2 - \alpha_-] \\ L_+ - L_- &= R[\beta_+ - \pi/2 + \alpha + \theta - \beta_- + \pi/2 - \alpha + \theta] \\ L_+ - L_- &= R[\beta_+ - \beta_- + 2\theta].\end{aligned}$$

When including the focusing condition from Eq. 4.1, the equation above can be translated into a condition on the difference between the trajectory lengths

$$L_+ - L_- > 2R\theta. \quad (4.3)$$

This condition is independent of the incident angle α , under which the electron bunch enters the magnet gap and depends only on the electron bunch divergence and radius (which is a function of the electron energy E_e and the magnetic field B). By substituting the expression for the relativistic Larmor radius (3.5), we may rewrite the condition for the monoenergetic electron beam focusing as

$$\Delta L = L_+ - L_- > 2\beta\gamma \frac{m_e c}{eB} \theta, \quad (4.4)$$

where β is the velocity of electron normalized to the speed of light c , γ is the relativistic (Lorentz) factor, m_e is the mass of electron, e is the electron charge and B is the magnetic field in the gap. In practical units, the condition can be rewritten as

$$\Delta L[\text{mm}] = 6.67 \times 10^{-3} \frac{E_e[\text{MeV}]}{B[\text{T}]} \theta[\text{mrad}]. \quad (4.5)$$

Real differences between the trajectory lengths within an electron beam in magnetic field must satisfy the condition derived above in order to obtain focused electron beams and are given by the magnet geometry. Rather than focusing electrons by making them exit the magnet gap

from the open side of the rectangular magnet, it is considered to use a trapezoidal shape of the dipole magnet, which would create the same focusing effect with tilted front and back. This allows avoiding limitation of the maximum electron energy due to the magnet length as it is the case for the rectangular dipole magnet with electrons leaving from the open side.

However, since trapezoidal magnets with a uniform magnetic field are difficult to manufacture, it has been decided to use a tilted magnet with the rectangular gap with one of the sides open, which results in a similar geometry (in fact, it is virtually same as a trapezoidal geometry with the front and back at an angle of 90 degrees). Using this approach, electrons of higher energies, which would normally exit the rectangular magnet gap from the back (and thus would not be focused), can benefit from the advantage of this method as well.

For the rectangular shape of the magnet, the geometry is simplified to the length of the magnet L_m and the incident angle α , at which the electron beams enter the magnet. The differences in the lengths of electron trajectories for a given geometry were calculated using a modified Matlab code described in the previous chapter in section 3.1.3 in the part about the electron spectrometer. The code calculates the trajectory lengths of the envelope beams in the magnet gap and compares it with the minimum trajectory length difference from the Eq. 4.3.

Various geometries and experimental conditions were investigated. It was studied for which electron energy values the electrons are focused for a given magnetic field B . Fig. 4.12 shows the calculated differences in the trajectory lengths of envelope beams ΔL with respect to the electron energy E_e for a divergence of $\theta = 5$ mrad and various angles α . While the difference in trajectory lengths necessary for focusing ΔL_{foc} is same for all cases as it does not depend on the incident angle but only on the electron energy and the divergence, the calculated differences ΔL change significantly. Electron beams are focused only for the energy range, where the calculated differences are larger than the necessary differences ($\Delta L > \Delta L_{\text{foc}}$). The boundary case where the differences are equal ($\Delta L = \Delta L_{\text{foc}}$) results in a collimated electron beam.

Furthermore, Fig. 4.12 shows that for angles $\alpha < 90^\circ$ (Fig. 4.12a - 4.13d) the electron beams are focused only up to a certain energy, at which the beam becomes collimated and subsequently divergent for higher energies. This energy limit increases as the incident angle α approaches 90° and the limit vanishes for $\alpha \geq 90^\circ$ and above. For these angle values, however, other constraints take place. For $\alpha = 90^\circ$ (Fig. 4.12c) the length of the magnet is the limiting factor as electrons only up to a certain energy E_{side} leave the magnetic field through the side of the magnet and all electron energies $E_e > E_{\text{side}}$ leave the magnet gap through the back. For a constant magnetic field B , the limiting energy E_{side} depends on the magnet length.

The effect is apparent in Fig. 4.11 describing the electron dispersion in the modular magnet, where only electrons leaving through the back of the magnet were considered (i.e. electrons with a lower energy than the minimum energy plotted in the figure leave the magnetic field through the side; for the magnet consisting of three 4-inch modules, it means $E_{\text{side}} \simeq 550$ MeV). A similar constraint is present for angles $\alpha > 90^\circ$ (Fig. 4.12d - 4.12f), where not only the length of the magnet but also the width of the magnet gap are limiting factors since the high energy electrons significantly penetrate into the magnet gap laterally.

Due to the reasons mentioned above, the trapezoid-like geometry using the rectangular magnet rotated at an angle of $\alpha < 90^\circ$ has been chosen in order to prevent building a dipole magnet, which is large in length or width, since the uniformity of the magnetic field is easier to achieve with small dimensions. Moreover, due to the divergence of the electron beam and a finite size of the beam at the exit, which increases as α approaches 90° , an angle $\alpha = 85^\circ$ has been chosen as ideal for real experimental application despite the energy limit on focusing.

In addition, it was studied if the electron divergence for the selected angle $\alpha = 85^\circ$ affects the value of the maximum focused electron beam energy given by the boundary condition $\Delta L = \Delta L_{\text{foc}}$. The results are shown in Fig. 4.13. It has been concluded that the energy limit on focusing does not vary with the divergence. Both the difference of electron trajectory lengths

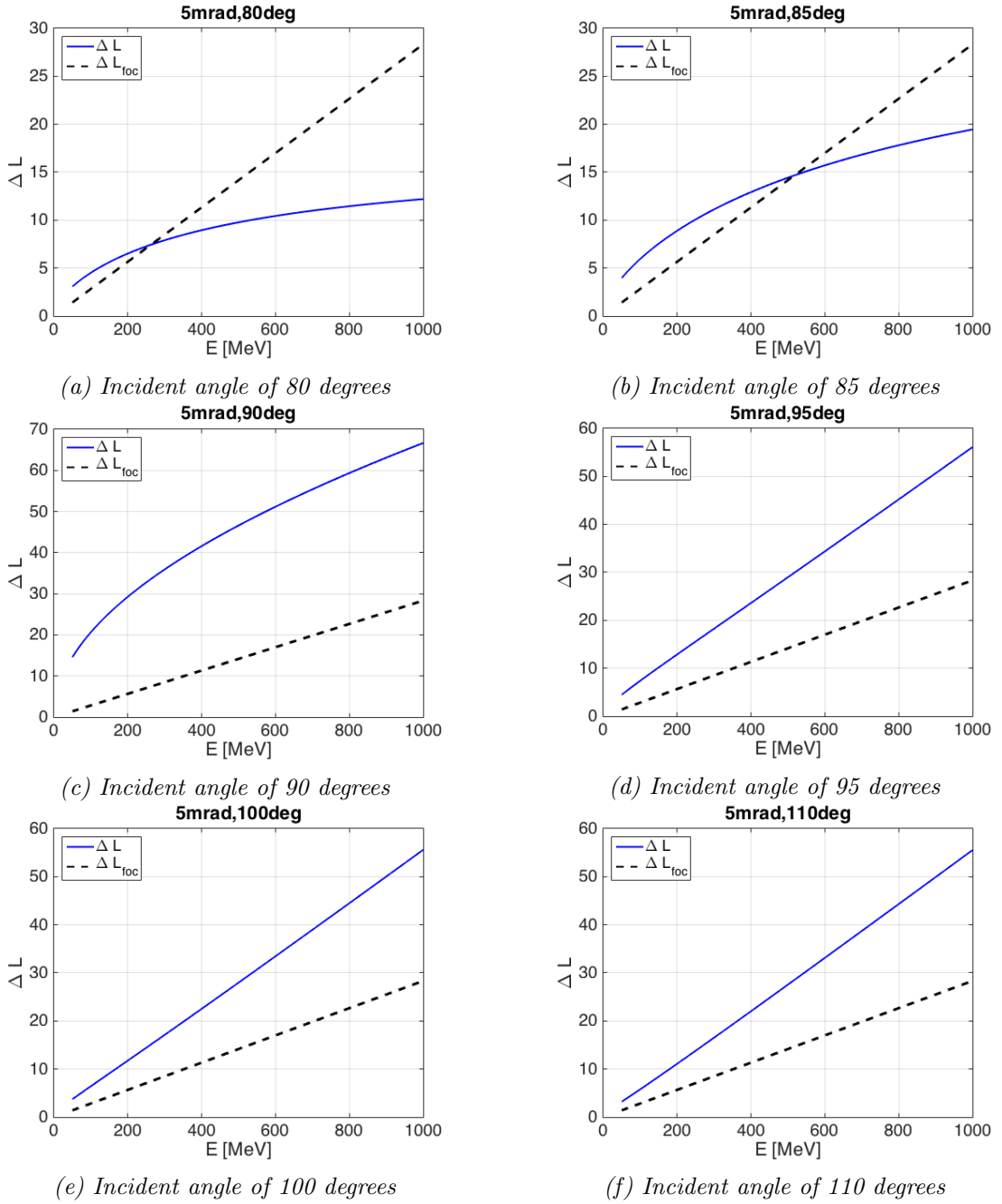


Figure 4.12: Differences in electron trajectory lengths created by a dipole magnet for various values of the incident angle α . The simulated difference in electron trajectory lengths of envelope beams ΔL (blue) created for a given entrance angle, divergence and electron energies must be larger than the difference in trajectory lengths ΔL_{foc} , which is necessary to obtain focused electron beams and which is given by the magnet geometry.

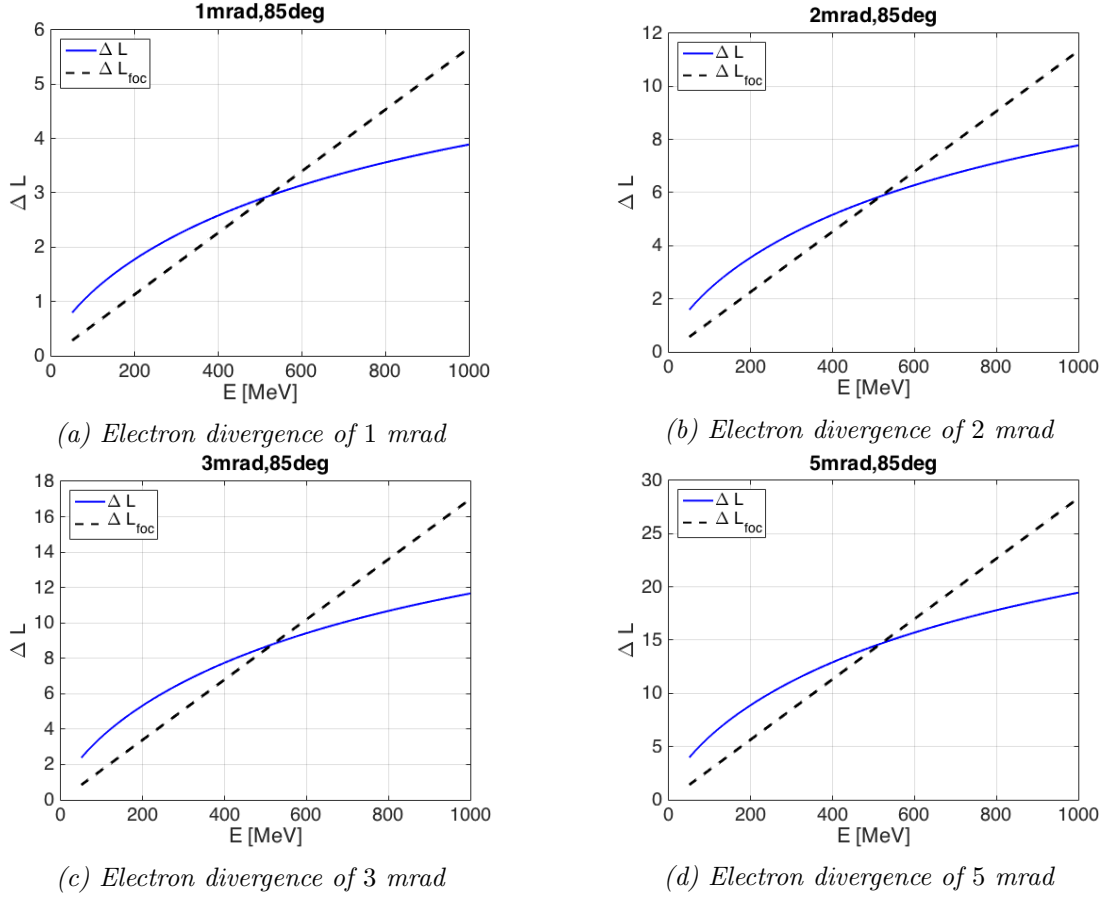


Figure 4.13: Differences in electron trajectory lengths created by a dipole magnet for various values of divergence θ . The calculated difference in electron trajectory lengths of envelope beams ΔL created by a given geometry (blue) must be larger than the necessary difference in trajectory lengths ΔL_{foc} in order to obtain focused electron beams. As the divergence increases, the maximum energy for which a focused beam is obtained remains the same.

ΔL and the difference of electron trajectory lengths necessary for focusing ΔL_{foc} increase proportionally with the electron divergence, which was expected according to Eq. 4.4. This is an important property of the focusing method as monoenergetic electron beams with fluctuating divergence are focused into a focus with the same coordinates.

The method of focusing electron beams using a dipole magnet, which has an open side and is rotated in the plane of the experiment, can be used to improve the energy uncertainty of the magnetic spectrometer for a quasi-monoenergetic electron beams since the resolution of a standard rectangular spectrometer depends mainly on the divergence of the beam.

A divergent monoenergetic beam with an energy E_0 is dispersed by such spectrometer in the dipole magnet and the trace of electrons creates an elongated spot in the detector, which is defined by three values of deflection (i.e. the distance of the detection point on the scintillating screen and the laser axis) that are of importance: the deflection of the central (on-axis) electron beam and the deflection values of the two envelope beams in the horizontal plane. Each part of the scintillating screen has a value of the electron energy assigned to it depending on the setup geometry and the magnetic field of the dipole. The energy values are assigned to the positions on the screen using a reference nondivergent electron beam.

Therefore, if the central electron beam with the energy E_0 is detected on the screen in a position that corresponds to a deflection $D_0 = D(E_0)$, the envelope beams are detected on the screen with deflections $D_- = D(E_1)$ and $D_+ = D(E_2)$, respectively (see Fig. 4.14), where E_1

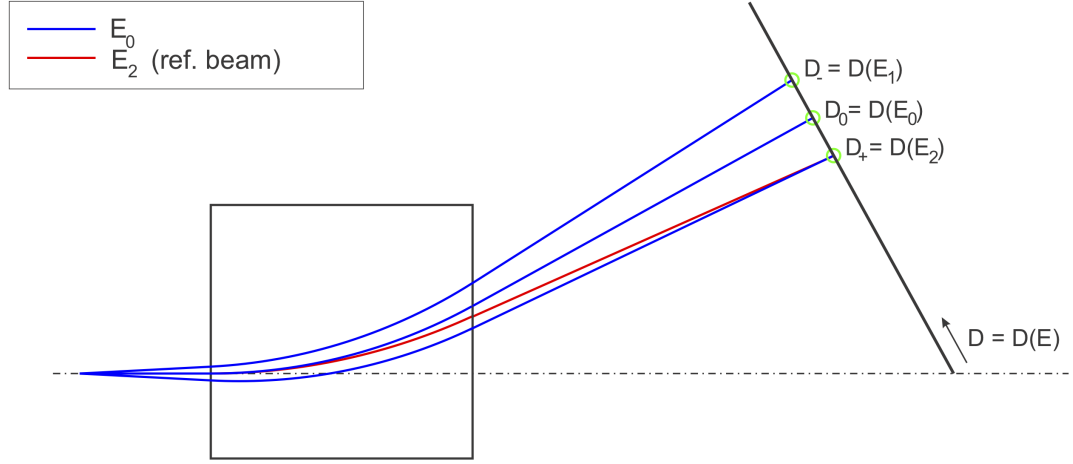


Figure 4.14: The explanation of the uncertainty in the energy measurement of a divergent monoenergetic electron beam with magnetic spectrometer. The divergent electron beam with an energy E_0 (blue) is dispersed on the detector over an area corresponding to the dispersion values $D_- = D(E_1)$ and $D_+ = D(E_2)$, where E_1 and E_2 are electron energy values ($E_1 < E_0 < E_2$) assigned to the positions on the scintillating screen using the reference nondivergent electron beams. A reference beam of the energy E_2 is shown (red).

and E_2 are electron energy values of the reference nondivergent electron beam. Therefore, the energy uncertainty of the magnetic spectrometer is given by an expression

$$\frac{\Delta E}{E} = \frac{E_2 - E_1}{E_0}, \quad (4.6)$$

where the energy values E_1 and E_2 vary with the electron beam divergence due to their dependence on the deflection caused by the magnetic field.

The size of the spot on the screen (given by the difference of the deflections D_+ and D_-) for the monoenergetic beam with the energy E_0 creates an uncertainty in the energy determination, which can reach large values and eventually even go to infinity for high energy electron beams, for which some electrons from the beam cross the experimental axis to the opposite side with respect to the direction of deflection. Since it is not possible to assign energy to these electrons as they appear in the region beyond a position of a hypothetical particle with an infinite energy, which would follow the laser axis, the energy uncertainty becomes infinite as well.

However, using the proposed method of focusing the electron beam, the spot in the detector becomes smaller if the detector position is chosen correctly for the electron energy, and thus the uncertainty in the energy measurement is improved as well. In order to correctly describe the improvement in the energy uncertainty, a method for comparing a typical divergent electron beam dispersed by a commonly used rectangular dipole magnet and a similar setup with a rotated dipole magnet had to be developed. In both approaches of the comparison, a rectangular magnet is considered with a magnetic field of 1 T, which is a magnetic field typically used in the electron magnetic spectrometer on a laser-plasma accelerator based on a PW-class driving laser system.

First, the rotated rectangular magnet is considered. As the ideal angle of the dipole rotation for focusing of electrons was explained above, the magnet is rotated by 5° , and thus an electron beam enters the magnetic field at an angle of $\alpha = 85^\circ$ in the center of the magnet gap. A divergent electron beam with an energy E_0 enters the magnet, different parts of the beam follow a different trajectory length in the magnetic field and leave the magnet gap. The electron beam is focused if the condition from Eq. 4.3 is met. The electron trajectories were found using

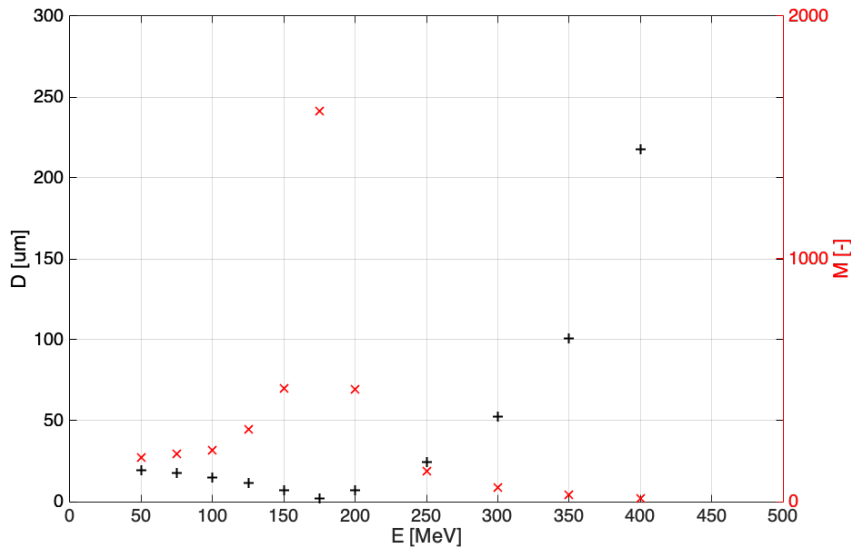


Figure 4.15: The focal spot size of electron beams D (black points and y -axis) and the factor of improvement M of the focused electron beam over the divergent beam (red points with y -axis) are shown with respect to the electron energy for electrons focused by a dipole magnet rotated by 5° and a magnetic field of 1 T. It is obvious that the chosen geometry and the magnetic field favor an energy of about 175 MeV.

SIMION software for numerical simulations of charged particles in static electromagnetic fields. Two quantities are of interest for later use: a coordinate of the average exit point $x_{\text{exit},0}$ on the longitudinal axis (x -axis), and the average exit angle $\beta_{\text{exit},0}$. The electron focus is found using a Matlab code, which was written as a part of the scope of this dissertation. The focus is found in a plane perpendicular to the propagation direction of the electron beam $\beta_{\text{exit},0}$ downstream of the rotated magnet. The position of the focal plane is numerically found as a position where the electron spot size (FWHM) is the smallest and it is saved as an ideal position of the electron detector.

For a proper comparison, a rectangular dipole magnet was chosen with a length of $L_m = x_{\text{exit},0}$ and the coordinates of the electron detector were kept from the previous (ideal) case. This way the size of the focused beam and the divergent beam can be directly compared and the improvement in the energy uncertainty can be calculated.

Electron energy was chosen from the range of $\langle 50; 400 \rangle$ MeV and the energy uncertainty was calculated for both spectrometer cases. For higher electron energies, the electron focal length obtained with the 1 T would be too long already. Therefore, only electron beams with an energy of up to 400 MeV were considered. However, it is possible with a different magnetic field to design a focusing dipole magnet for higher energies as well. The size of the focal spot with respect to the electron energy is plotted in Fig. 4.15. It is obvious that the given magnet geometry with the fixed magnetic field favor a single energy value which is focused better than any other - in this case it is about 175 MeV. The factor of improvement of the focused beam over the divergent beam is also shown in Fig. 4.15 and it is simply obtained as $M = D_{\text{foc}}/D_{\text{div}}$, where D_{foc} is a focal spot size (FWHM) of the focused electron beam and D_{div} is a spot size (FWHM) of the divergent beam in the detector at the same position.

Moreover, the electron focal spot size with respect to the electron beam divergence has been studied as well for the electron energy of 100 MeV. Logically, the focal spot size of the electron beam in the detector increases with increasing beam divergence as depicted in Fig. 4.16. On the other hand, the size is always significantly smaller when compared to an unfocused beam using the same detector geometry.

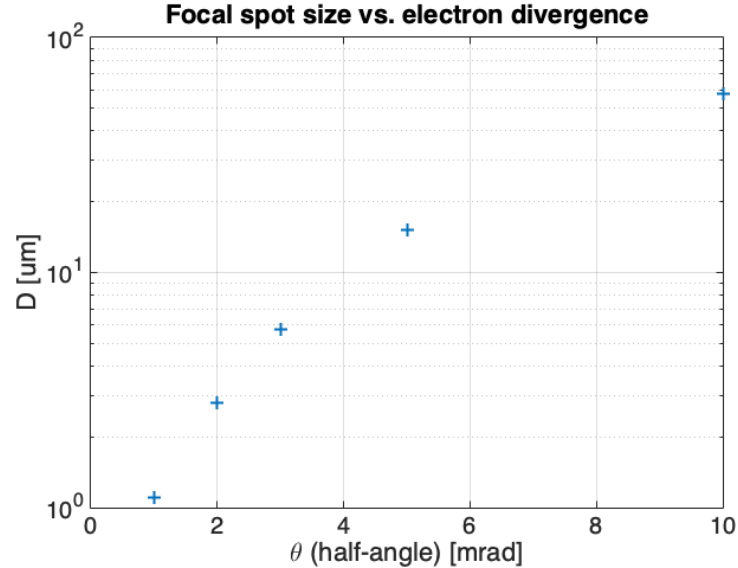


Figure 4.16: The electron focal spot size with respect to the electron beam divergence for the electron energy of 100 MeV.

Finally, electron energy uncertainties are shown for divergent (unfocused) electron beams and focused electron beams in Figs. 4.17 and 4.18, respectively. The difference in the energy uncertainty between both methods is clear when comparing these two figures. The relative energy uncertainty in the measurement of the unfocused beam is $\Delta E/E \simeq 4\%$ for 50 MeV (i.e. $\Delta E = 2$ MeV) and steadily grows to $\Delta E/E \simeq 7\%$ for 175 MeV (i.e. $\Delta E \simeq 12$ MeV) and reaches up to $\Delta E/E = 11\%$ for 400 MeV (i.e. $\Delta E = 44$ MeV). In the case of the focused beam, we observe a similar dependence to the one previously depicted in Fig. 4.15. For 50 MeV electrons, the energy uncertainty is only $\Delta E/E = 0.02\%$ (i.e. $\Delta E \simeq 10$ keV), it reaches the minimum of $\Delta E/E = 0.005\%$ for 175 MeV (i.e. $\Delta E = 8$ keV) and then increases up to 0.8% for 400 MeV (i.e. $\Delta E \simeq 3$ MeV). Therefore, the improvement in the energy uncertainty measurement is up to three orders of magnitude.

4.4.2 Dipole magnet for electron selection for Compton source

Furthermore, the focusing dipole magnet can be used not only as a mean to improve the uncertainty in the energy measurement of quasi-monoenergetic electron beams but also as a selector of electrons for a monochromatic Compton source, which utilizes inverse Compton scattering of accelerated electrons on a secondary laser pulse. The technique allows using a broadband electron source as long as the electron bunch charge is sufficiently high. Then a part of the electron spectrum can be selected by the focusing dipole magnet in combination with a simple collimator placed at the electron focus.

Numerical simulations were performed using a Monte Carlo method in order to determine the improvement in the generated hard X-ray radiation. The positions for the inverse Compton scattering were chosen by the position of the focal spot of the electron energy of interest as described in the previous section. Electron bunch with a peak energy of 100 MeV was chosen as an example for these numerical calculations. The energy spread was defined as a full width at half maximum of a normal distribution and the electron energy was chosen randomly from this distribution centered around the peak energy. The divergence was defined as a full width at half maximum of a normal distribution as well and chosen randomly for each electron. The simulation calculated trajectories of 10^7 electrons and the spectra were renormalized to the

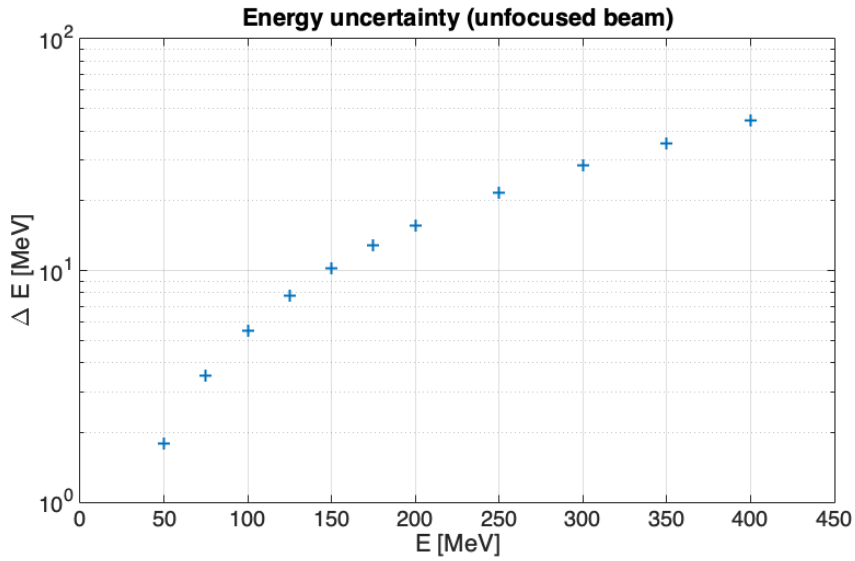


Figure 4.17: The energy uncertainty in the measurement of electron energy using a rectangular magnetic spectrometer placed perpendicularly to the electron beam propagation direction. It has been calculated that the relative energy uncertainty in the measurement of the unfocused beam is $\Delta E/E \simeq 4\%$ for 50 MeV and steadily grows to $\Delta E/E \simeq 7\%$ for 175 MeV and reaches up to $\Delta E/E = 11\%$ for 400 MeV.

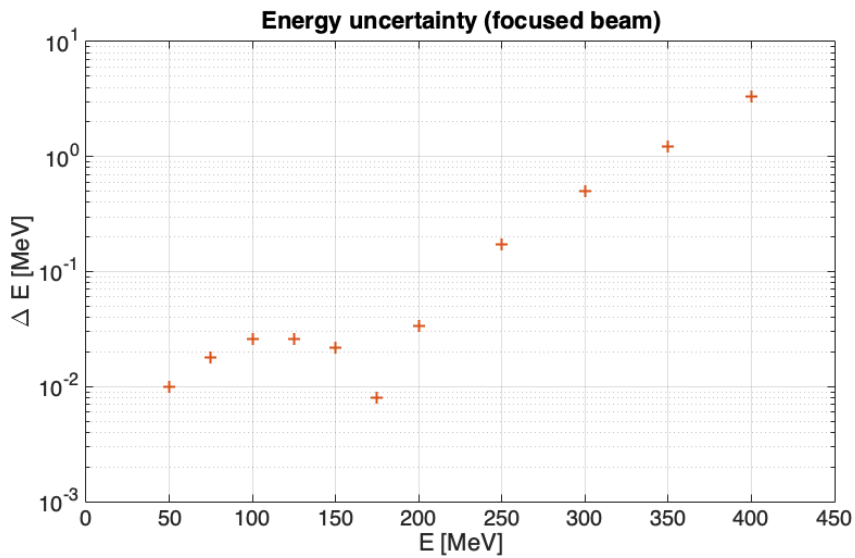


Figure 4.18: The energy uncertainty in the measurement of electron energy using a rectangular magnetic spectrometer rotated by an angle of 5° (electrons enter the dipole magnet gap at an angle of 85°). For 50 MeV electrons, the energy uncertainty is only $\Delta E/E = 0.02\%$, it reaches the minimum of $\Delta E/E = 0.005\%$ for 175 MeV and then increases up to 0.8% for 400 MeV. The improvement in the energy uncertainty measurement is up to three orders of magnitude.

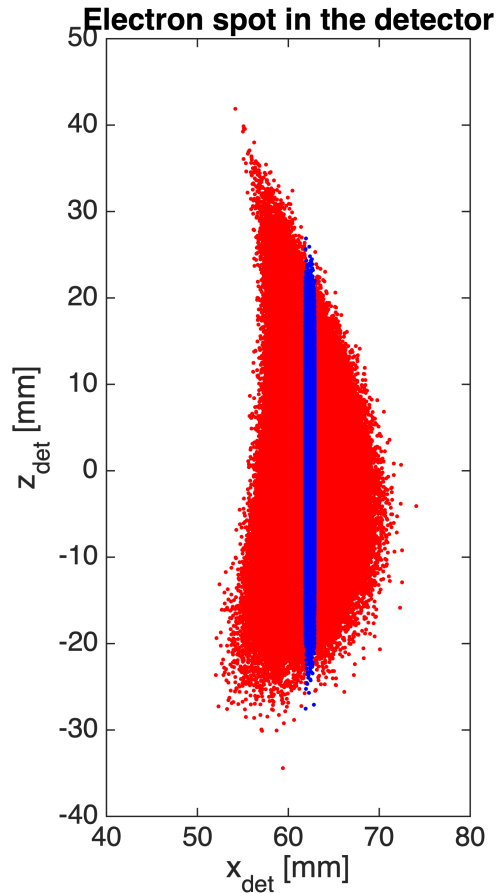


Figure 4.19: A shape of the spot created by the electron beam with a peak energy of 100 MeV and an energy spread of 10 % in the detector obtained using the Monte Carlo simulation code. The electrons which pass through the collimator centered around the dispersion position of the mean electron energy of 100 MeV are highlighted in blue while all other electrons are in red. The blue region contains about 22 % of all electrons.

desired electron number.

A collimator with a width of 0.5 mm was considered to be placed at the position of the electron focus in order to decrease the width of the electron spectrum. Due to the electron focusing performed by the rotated dipole magnet, this approach does not drastically limit the number of electrons but simply cuts off the electrons that deviate too much from the peak energy. Fig. ?? shows the shape of the electron focus on an ideally placed detector with a highlighted part of the electron bunch which passes through the collimator. This approach thus distinguishes between two electron beams and their spectra: (I) the full electron beam with an energy spread centered around the peak energy as it leaves the laser-plasma accelerator – this beam will be referred to as *full electron beam*, and (II) the part of the focused electron beam which passed through the collimator – this beam will be referred to as *optimized electron beam*. Energy spectra of the full and optimized beam, respectively, are shown in Fig. 4.20. Note that the shape of the energy spectrum of the optimized beam is not symmetrical around the mean electron energy due to the nonlinear dispersion with respect to the electron energy.

For the purpose of the Compton source simulations, it was assumed that the optimized electrons undergo head-on inverse Compton scattering on the secondary laser pulse with an intensity of $I_L = 1 \times 10^{18} \text{ W/cm}^2$ concentrated in an elliptically shaped focus resembling the shape of the electron spot. This laser intensity corresponds to a laser strength parameter of

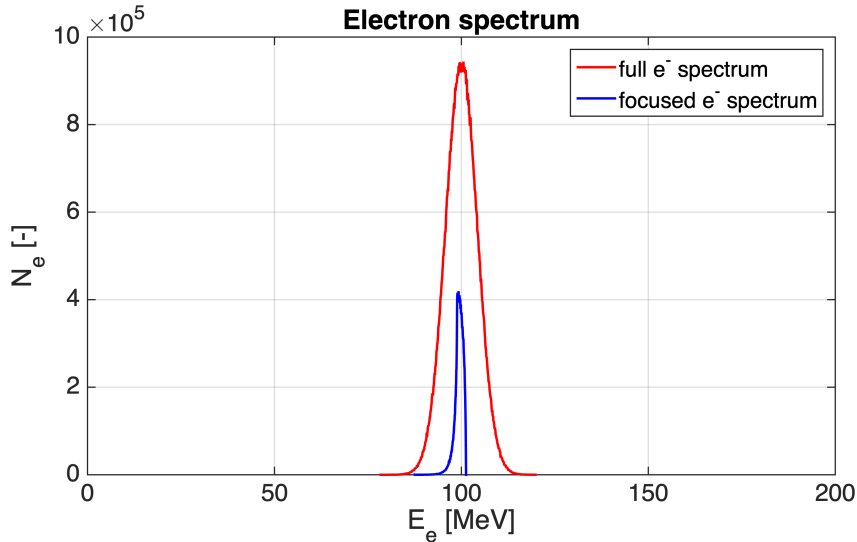


Figure 4.20: A comparison of the full electron spectrum as it leaves the laser-plasma accelerator (red) and the spectrum of the optimized (focused and selected) electron beam (blue).

approximately $a_0 = 0.7$ for a Ti:sapphire laser with a wavelength around 800 nm. It is thus in the undulator regime of the Compton source, which is able to generate monochromatic X-ray radiation near the propagation axis instead of the broadband radiation in the wiggler case.

The X-ray radiation generated by scattering on the optimized electrons is compared in the calculations with an X-ray spectrum generated by scattering on the full electron beam. The latter could be experimentally done by focusing the secondary laser pulse near the exit from the plasma if the electron spectrum is stable and was well characterized so the electron spectrometer can be omitted from the setup. The laser intensity of the secondary pulse taken into account is the same in both cases. Advantages and disadvantages of both methods are discussed below.

In the following text, quantities related to the full electron beam and the photons scattered on it are marked with index 1, quantities related to the optimized electron beam and the X-ray photons scattered on it are marked with index 2 in the remaining part of the chapter. The practical unit formulas from chapter 2 are used within the calculations. The main assumption is that the near-axis limit is valid for the generated X-ray radiation, i.e. we assume scattering of all electrons of an energy E_e generates quasimonochromatic X-ray photons with an energy spectrum centered around the energy E_γ as the generated radiation is highly collimated and our detectors would be far from the Compton source (i.e. from the electron focus) on the axis of the X-ray beam propagation.

For the full electron beam with the peak energy of 100 MeV, a laser pulse with a wavelength of 800 nm and a number of electrons in the bunch $N_{e,1} = 10^8$, the peak X-ray photon energy is $E_\gamma \simeq 240$ keV (estimated using Eq. 2.64) and the number of X-ray photons generated by the full electron beam is $N_{\gamma,1} = 7.9 \times 10^6$ (obtained from Eq. 2.66). These are values that the results from the proposed method are compared to.

In order to make the summary of obtained results clearer, we must first investigate how divergence affects the method of generating X-ray photons from inverse Compton scattering on the focused electron beam. For each value of the electron energy spread $\Delta E/E$, a few typical values of the divergence θ have been considered. Table 4.2 shows calculated numbers of focused electrons $N_{e,2}$ for the peak electron energy $E = 100$ MeV and values of the energy spread $\Delta E/E$ of the full electron beam between 1 % and 40 %. The numbers of X-ray photons generated by the optimized electron beam are mentioned. A comparison of an X-ray peak width $\text{FWHM}_{\gamma,1}$

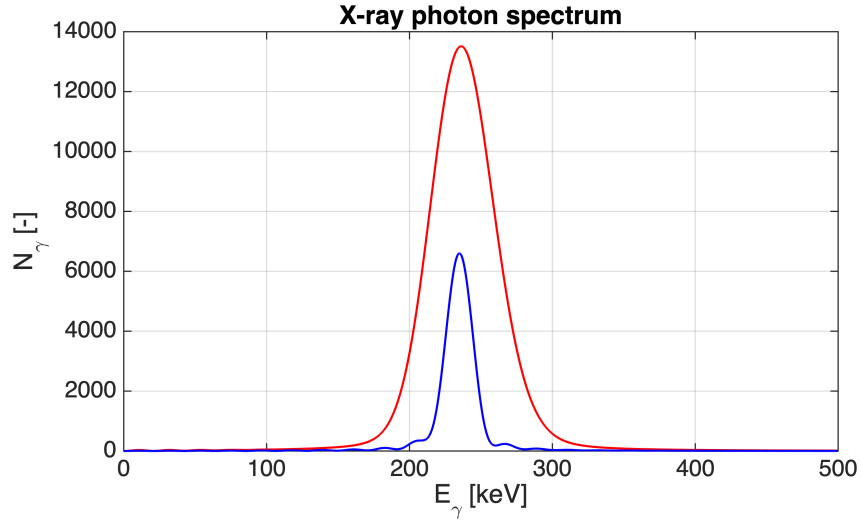


Figure 4.21: A comparison of the X-ray photon spectrum obtained from inverse Compton scattering on the full electron spectrum (red) and the X-ray spectrum scattered on the optimized (focused and selected) electron beam (blue).

of the "full" X-ray beam and a peak width $\text{FWHM}_{\gamma,2}$ of the "optimized" X-ray pulse is made.

The most obvious result is that the electron divergence of 10 mrad and lower does not play any role in the resulting width of the X-ray photon spectrum. This can be understood from Fig. 4.16 in the previous section which shows that the focal spot size (FWHM) for the divergence values of up to 10 mrad is less than a few tens of μm , which is an order of magnitude smaller than the collimator size of 0.5 mm.

For this reason a test was done with an energy spread of $\Delta E/E = 10\%$ and a divergence of 30 mrad and 50 mrad (shown in the table 4.2 as well). With these values of divergence, we barely start to notice a decrease in the number of the optimized electron beam $N_{e,2}$ that passed through the collimator (and, as a result, in the number of photons $N_{\gamma,2}$ generated by these electrons), and the width of the optimized X-ray peak $\text{FWHM}_{\gamma,2}$. The values of the electron divergence are, however, not common in the LWFA experiments as they are too large and do not have to be considered further.

We can thus remove the divergence from the list of quantities on which the "optimized" X-ray photon spectrum depends. Table 4.3 simplifies the data shown in Table 4.2 and only the data for the divergence of $\theta = 5$ mrad are shown. A ratio of the number of X-ray photons $N_{\gamma,2}/N_{\gamma,1}$ of the "optimized" X-ray pulse and the "full" X-ray photon beam. Furthermore, an improvement in the FWHM of the X-ray photon peak is calculated and shown in Table 4.3.

As the energy spread $\Delta E/E$ of the electron beam increases, logically the number of electrons $N_{e,2}$ focused through the collimator decreases. Moreover, the collimator with the width of 0.5 mm maintains the $\text{FWHM}_{\gamma,2}$ approximately constant as the energy spread increases. For example, for the energy spread $\Delta E/E = 30\%$, the width of the "full" X-ray spectrum is $\text{FWHM}_{\gamma,1} = 145.4$ keV, more than 60% of the peak X-ray photon energy.

For the same energy spread, the proposed method limits the width of the generated spectrum to $\text{FWHM}_{\gamma,2} = 20.3$ keV, which corresponds to less than 9% of the peak energy. This is done at the cost of the photon count, which is reduced to 7.3% of the number of X-ray photons that would be generated by the full electron spectrum. However, if the electron bunch is produced by the LWFA accelerator with a sufficiently high charge but with a broad energy spread (similar to what was experimentally obtained in our experiments at PALS as described in chapter 3), the proposed method with the focusing dipole magnet and the collimator offer a solution for

$\Delta E/E[\%]$	$\theta[\text{mrad}]$	$N_{e,2}[-]$	$\text{FWHM}_{\gamma,1}[\text{keV}]$	$N_{\gamma,2}[-]$	$\text{FWHM}_{\gamma,2}[\text{keV}]$
1	1	9.94×10^7	19.6	7.83×10^6	19.5
	2	9.94×10^7	19.6	7.83×10^6	19.5
	5	9.94×10^7	19.6	7.83×10^6	19.5
	10	9.94×10^7	19.6	7.83×10^6	19.5
2	1	8.33×10^7	20.9	6.56×10^6	20.0
	2	8.33×10^7	20.9	6.56×10^6	20.0
	5	8.33×10^7	20.9	6.56×10^6	20.0
	10	8.33×10^7	20.9	6.56×10^6	20.0
5	1	4.20×10^7	30.0	3.30×10^6	20.3
	2	4.20×10^7	30.0	3.31×10^6	20.3
	5	4.19×10^7	30.0	3.30×10^6	20.3
	10	4.20×10^7	30.0	3.31×10^6	20.3
10	1	2.18×10^7	52.2	1.72×10^6	20.3
	2	2.18×10^7	52.3	1.72×10^6	20.3
	5	2.18×10^7	52.3	1.71×10^6	20.3
	10	2.18×10^7	52.2	1.72×10^6	20.3
	30	2.17×10^7	52.3	1.71×10^6	20.6
	50	2.09×10^7	52.2	1.65×10^6	21.5
20	1	1.10×10^7	98.9	8.67×10^5	20.3
	2	1.10×10^7	99.1	8.65×10^5	20.3
	5	1.10×10^7	98.8	8.67×10^5	20.3
	10	1.10×10^7	99.0	8.66×10^5	20.3
30	1	7.36×10^6	145.4	5.79×10^5	20.3
	2	7.33×10^6	145.4	5.77×10^5	20.3
	5	7.34×10^6	145.4	5.78×10^5	20.3
	10	7.35×10^6	145.5	5.79×10^5	20.3
40	1	5.49×10^6	191.0	4.32×10^5	20.3
	2	5.51×10^6	191.1	4.34×10^5	20.3
	5	5.51×10^6	190.9	4.34×10^5	20.3
	10	5.52×10^6	191.1	4.34×10^5	20.3

Table 4.2: The comparison of X-ray photon beams generated by the full electron beams with the peak energy of 100 MeV and X-ray photon beams generated by the optimized electron beams for various values of the energy spread $\Delta E/E$ and for different values of electron divergence. The number of electrons in the optimized beam $N_{e,2}$ is shown and the peak width $\text{FWHM}_{\gamma,2}$ of the X-ray photons generated by them is compared with the X-ray peak width $\text{FWHM}_{\gamma,1}$ of the photons generated by the full electron beam in order to estimate the importance of the electron divergence on the performance of the Compton source that uses the electron beam focusing.

$\Delta E/E[\%]$	$N_{e,2}[-]$	$\text{FWHM}_{\gamma,1}[\text{keV}]$	$N_{\gamma,2}[-]$	$\text{FWHM}_{\gamma,2}[\text{keV}]$	$N_{\gamma,2}/N_{\gamma,1}[-]$	M
1	9.94×10^7	19.6	7.83×10^6	19.5	99.4%	1.0
2	8.33×10^7	20.9	6.56×10^6	20.0	83.3%	1.0
5	4.20×10^7	30.0	3.30×10^6	20.3	42.0%	1.5
10	2.18×10^7	52.2	1.72×10^6	20.3	21.8%	2.6
20	1.10×10^7	99.0	8.66×10^5	20.3	11.0%	4.9
30	7.35×10^6	145.4	5.78×10^5	20.3	7.3%	7.2
40	5.51×10^6	191.0	4.34×10^5	20.3	5.5%	9.4

Table 4.3: The comparison of the "full" X-ray photon beams and the "optimized" X-ray photon beams for various values of the energy spread $\Delta E/E$ for the electron divergence of 5 mrad. The number of electrons in the optimized electron beam $N_{e,2}$ is shown and the peak width $\text{FWHM}_{\gamma,2}$ of the "optimized" X-ray photon pulse containing $N_{\gamma,2}$ photons is compared with the peak width $\text{FWHM}_{\gamma,1}$ of the "full" X-ray photon spectrum directly and through the improvement factor $M = \text{FWHM}_{\gamma,1}/\text{FWHM}_{\gamma,2}$.

creating a quasimonochromatic Compton source under these conditions.

Nevertheless, the X-ray pulse duration is slightly increased by this technique due to the trajectory difference of electrons within a bunch caused by the dipole magnet (as described in section 4.4), which results in an electron bunch duration to be prolonged by one order of magnitude from tens of femtoseconds to hundreds of femtoseconds (for the assumed divergence and magnetic field). This is still sufficient for a Compton source to be of use for its novel applications. For the reason of increasing the electron bunch duration, only head-on collisions were considered for the Compton source in this chapter in order not to decrease the photon count further by a introducing an acute collision angle.

It is obvious that the proposed method is capable of significantly decreasing the energy spread of the generated X-ray photons, which is done at the cost of lowering the number of photons. Therefore, even an electron source producing electrons with large energy spread can be used for generating monochromatic X-ray radiation via inverse Compton scattering if the electron charge in the energy range of interest is sufficiently high. The technique can be improved by creating magnets for dedicated electron energies and with a special shape for the purpose. Moreover, electromagnets can be used to create a variable magnetic field with a possible extension to a stronger field than considered in this work, which would allow extension to GeV electron energy resulting in photon energies in the MeV range.

Conclusion

The goal of this thesis was to design an all-optical type of X-ray source employing a few-terawatt laser system. Such approach has had an advantage over sources based on conventional accelerators due to its compactness, lower costs and the properties of the generated X-ray pulses. Laser-plasma X-ray sources based on the betatron radiation and inverse Compton scattering are modern ways of generating X-ray pulses with high brightness, low divergence, ultrashort duration and tunable energy in the keV range and higher.

Parameters of X-ray photons produced by these types of sources strongly depend on parameters of the relativistic electrons which generate the X-ray radiation, such as their energy and energy spread, and the electron energy itself is proportional to the power of the driving laser pulse. Therefore using a few-terawatt Ti:sapphire laser system at PALS Research Centre in Prague, Czech Republic, presented a challenging task in building a stable X-ray source with a sufficient photon energy stability.

In the first chapter, the theory of the laser wakefield acceleration of electrons was explained in order to understand the processes occurring in the laser-plasma accelerator and the behaviour of electrons that serve as the source of X-ray radiation, starting with how a laser pulse interacts with a single electron and explaining the ionization of matter with laser. Fundamental phenomena of the laser-plasma interaction and the most important physical quantities describing the plasma were discussed. Furthermore, nonlinear relativistic effects and creation of plasma waves were introduced including the bubble regime, which is the paramount technique behind the most effective acceleration of electrons in the plasma and the betatron X-ray pulse generation. Electron trapping in plasma waves and the limits on the electron acceleration were described along the means of electron injection into the acceleration phase of the plasma waves since localized injection is crucial for achieving stable acceleration of electrons.

In the second chapter, the properties of radiation from relativistic electrons were described and synchrotron radiation generated in bending magnets and periodic magnetic structures was covered due to the betatron and Compton sources generating specific types of this radiation. Subsequently, the theory of betatron and Compton radiation could have been described by explaining the connection between the conventional undulators and wigglers, and the betatron oscillations in plasma and electron oscillations in the electric field of a laser pulse known as inverse Compton scattering, respectively. Fundamental parameters were derived in the theory and it was identified how their variations provide the tunability of the betatron and Compton sources. Formulas in practical units were derived for the fundamental parameters, which is of use for experimental physicists in order to quickly and conveniently predict the requirements for the source and its resulting performance. Possible applications of ultrashort X-ray pulses in the keV range for various research fields were mentioned in this chapter as well.

The third chapter contains the principal work of this thesis – the thorough design and development process of the experimental setup of the stable betatron and Compton source of X-ray pulses using the few-terawatt laser pulse. This major effort required dividing the task into three stages. For each of these steps it was necessary to introduce new diagnostics and equipment that had to be designed specifically for our experiments. In the first step the laser-plasma electron accelerator based on the laser wakefield acceleration (LWFA) was designed for

the few-terawatt laser system, the gaseous target was developed and the set of diagnostics was prepared in order to monitor the fundamental parameters of the plasma accelerator as well as the parameters of the electron beams. The second step consisted of building the betatron source by modifying the LWFA electron source, and developing diagnostics of X-ray pulses. The third step included improving the betatron source and experimental testing of equipment for the tunable Compton source.

The most important plasma parameters identified in the theory were monitored. The information on the laser focal spot allowed calculation of the laser pulse intensity on the target which was important for understanding the ionization of the gas mixture target. Mach-Zehner interferometer was included in the experimental setup to determine the electron plasma density – one of the crucial parameters for the energy tuning of the electron accelerator and consequently the betatron and Compton X-ray source.

The information on both the plasma density and the laser intensity helped tailoring the gas jet target for the ionization injection and thus stabilizing the acceleration process and obtaining electron beams stable in energy. It was proven that the commonly used gas jet target consisting of a mixture of helium and argon employed as the accelerating medium is not ideal for the few-terawatt driving laser due to the available laser intensity in the focal spot and consequently in the self-guided propagation in the plasma. Although high-energy electrons were present in the energy spectra obtained with the helium-argon target as a consequence of the density ramp injection on the shock wave created by a razor blade, the spectra were very broad in general because of other means of electron injection.

Using the knowledge on the behaviour of the plasma accelerator with the helium-argon target, it was proposed to employ synthetic air as the gas jet target in order to stabilize the accelerator performance and obtain quasi-monoenergetic electrons. The properties of the synthetic air allowed reaching higher laser intensity in self-focusing which resulted in the localized ionization injection using the few-terawatt laser pulse. The result were stable electron beams with the peak energy of 17.4 MeV and the shot-to-shot variation of the peak energy of only 1.1 MeV. This is considered sufficient for applications of the electron beam.

A combination of both targets was tested in a form of the mixture of helium and synthetic air in a pressure ratio of 99:1 and it was investigated whether the high-energy peak obtained with the helium-argon target prevails while the stability of the synthetic air target is preserved. However, due to the localized ionization injection and the density ramp injection being distinct mechanisms, it was not possible to take advantage of the best properties of the previous targets.

Stable betatron X-ray radiation was detected using a CCD in the single-photon counting mode. This absolutely calibrated X-ray spectrometer was used to successfully reconstruct the X-ray spectra with the critical energy of about 2 keV generated with the helium-argon and the helium-air target, respectively. The betatron source size was measured using knife-edge technique. The diameter of the X-ray source was found to be less than 6.0 μm , where the obtained result was limited by the pixel size of the CCD.

For higher X-ray photon energy range, the Ross filter based X-ray spectrometer was designed and tested at LOA, France. The data from the signal in the detector behind the filters allowed to reconstruct the X-ray energy spectrum of the well characterized betatron source with the critical energy of about 6 keV. The analysis of the experimental data obtained using the Ross filters was not trivial due to the gaussian beam profile of the generated X-rays being slightly misaligned with respect to the center of the cake layout. Hence, the complete analytical code is described in Appendix B.

The fourth chapter describes the ELI Beamlines facility and focuses on the betatron and Compton source in E2 hall. The experiences in the plasma and particle diagnostics were used to design the experimental setup and diagnostics for the source, which will be driven by a PW-class laser system and thus much improved, scaled-up results can be expected. An improved

electron spectrometer based on the analytical code from the previous experiments was designed and developed for energies up to 1.5 GeV. The purpose of the dipole magnet of the electron spectrometer was found to be twofold in the Compton source. It was discovered that the divergent electron beam can be focused in the dispersion dimension of the magnet when certain conditions are met. When the magnet is used with a quasi-monoenergetic electron beam, the energy uncertainty in the detector can be significantly decreased. Not only does this technique improve the resolution of the spectrometer around the selected energy value but the focused electron beam can be used in the Compton source to generate monochromatic X-ray pulses by forcing the accelerated focused electrons to oscillate in a secondary laser pulse with a low intensity ($a_0 < 1$) in head-on collisions. For the use in the Compton source, the technique allows using a broadband electron source as long as the number of electrons that pass through a collimator, which would be placed at the location of the electron focus, is sufficiently high to generate the desired number of photons from inverse Compton scattering.

The numerical results showed it is possible to improve the energy uncertainty in the magnetic electron spectrometer by up to three orders of magnitude from a few tens of MeV to only tens of keV. The effect of the focused electron beam was studied from the point of view of the Compton source performance. It was showed that the width of the X-ray photon peak in the energy spectra can be up to one order of magnitude narrower than the width of the peak in the spectra obtained with the full electron beam. It is done at the cost of the total number of X-ray photons. Nevertheless, this method can be of critical importance in applications where the X-ray photon pulse must be truly quasi-monoenergetic.

In conclusion, the tasks set for the PhD thesis were completed. The stable laser-plasma based electron and X-ray source was developed for few-terawatt laser systems and its performance was experimentally proven and characterized. Such source is readily feasible for usage in Compton sources due to its low shot-to-shot peak energy fluctuations. The tunability of the laser-plasma based X-ray sources based on radiation of relativistic electron was described and numerically proven. The method for generating quasi-monoenergetic X-ray photon beams was discovered for the Compton source, which was shown to be highly tunable in energy. Such quasi-monoenergetic tunable X-ray sources can be utilized in many novel applications in the medical diagnostics, material science and biochemistry and can open new possibilities in industry as well as in studying processes in the nuclear domain. An effort of increasing the number of generated photons must be done and the overall conversion efficiency must be improved in order to make the source feasible for some of the envisioned applications.

PRACTICAL UNIT FORMULAS

It is often necessary to perform quick calculations of important physical quantities and parameters of the laser-plasma electron accelerator or the related X-ray radiation source, either for the purpose of an experimental setup and adjustments, or simply as an estimation for different purposes. Since the formulas typically include constants, simpler expressions of the theoretical and empirical formulas can be derived by plain substitution of the constant values and converting the remaining variables into the units of preference. For this reason, expressions in practical units can be found using the standard formulas mentioned throughout this thesis. For future reference and readers' convenience, these useful expressions are also summarized in this appendix.

Please note that usage of the practical unit formulas typically has its limitations that are explained in the respective parts of the thesis.

Electron plasma frequency (Eq. 1.23)

$$\omega_e[\text{Hz}] = 5.64 \times 10^4 \sqrt{n_e[\text{cm}^{-3}]}$$

Plasma wavelength (Eq. 1.25)

$$\lambda_p[\mu\text{m}] = \frac{3.34 \times 10^{10}}{\sqrt{n_e[\text{cm}^{-3}]}}$$

Critical plasma density (Eq. 1.27)

$$n_c[\text{cm}^{-3}] = \frac{1.1 \times 10^{21}}{\lambda_L^2[\mu\text{m}]}$$

Critical power for self-focusing (Eq. 1.32)

$$P_c[\text{GW}] = 16.2 \frac{n_c}{n_e}$$

Plasma density for which plasma waves are effectively created (Eq. 1.39)

$$n_e[\text{cm}^{-3}] \simeq \frac{1.6 \times 10^{21}}{\tau_L^2[\text{fs}]}$$

Longitudinal electric field in plasma (Eq. 1.41)

$$E_0[\text{V/cm}] \simeq 0.96 \sqrt{n_e[\text{cm}^{-3}]}$$

Dephasing length (Eq. 1.46)

$$L_d = 0.3 \lambda_L (n_{\text{crit}}/n_e)^{4/3} P[\text{TW}]^{1/6}$$

Maximum energy gain of electron accelerated in plasma (Eq. 1.48)

$$\Delta E[\text{GeV}] \simeq 1.7 \left(\frac{P[\text{TW}]}{100} \right)^{1/3} \left(\frac{10^{18}}{n_e[\text{cm}^{-3}]} \right)^{2/3} \left(\frac{0.8}{\lambda_L[\mu\text{m}]} \right)^{4/3}$$

Critical photon energy of bending magnet radiation (Eq. 2.17)

$$E_c[\text{keV}] = 6.650 \times 10^{-7} B[\text{T}] (E_e[\text{MeV}])^2$$

Photon energy (on axis) of undulator radiation (Eq. 2.27)

$$E_{\gamma,\text{max}}[\text{keV}] = 9.5 \times 10^{-7} \frac{(E_e[\text{MeV}])^2}{\lambda_u[\text{cm}]}$$

Betatron source strength parameter (Eq. 2.54)

$$K = 1.33 \times 10^{-10} \sqrt{\gamma n_e[\text{cm}^{-3}]} r_\beta[\mu\text{m}]$$

Betatron source photon energy (on axis) in undulator regime (Eq. 2.57)

$$E_\gamma[\text{keV}] = 5.25 \times 10^{-14} \gamma^{3/2} \sqrt{n_e[\text{cm}^{-3}]} \quad \text{for } K < 1$$

Betatron source critical photon energy in wiggler regime (Eq. 2.57)

$$E_c[\text{keV}] = 5.24 \times 10^{-24} \gamma^2 r_\beta[\mu\text{m}] n_e[\text{cm}^{-3}] \quad \text{for } K > 1$$

Betatron source number of photons per period of oscillation per one electron (undulator regime) (Eq. 2.59)

$$N_\gamma = 1.53 \times 10^{-2} K^2 \quad \text{for } K < 1$$

Betatron source number of photons per period of oscillation per one electron (wiggler regime) (Eq. 2.59)

$$N_\gamma = 3.31 \times 10^{-2} K \quad \text{for } K > 1$$

Compton source strength parameter

$$K = a_0 = 0.855 \sqrt{I[10^{18} \text{ W/cm}^2]} \lambda_L^2[\mu\text{m}]$$

Compton source photon energy (on axis) in undulator regime (Eq. 2.65)

$$E_\gamma[\text{keV}] = 4.96 \times 10^{-3} \frac{\gamma^2}{\lambda_L[\mu\text{m}]} \quad \text{for } K < 1$$

Compton source critical photon energy in wiggler regime (Eq. 2.65)

$$E_c[\text{keV}] = 3.18 \times 10^{-3} \gamma^2 \sqrt{I[10^{18} \text{ W/cm}^2]} \quad \text{for } K > 1$$

Number of photons generated by Compton source per period of oscillation per one electron (undulator regime) (Eq. 2.66)

$$N_\gamma = 1.53 \times 10^{-2} K^2 \quad \text{for } K < 1$$

Number of photons generated by Compton source per period of oscillation per one electron (wiggler regime) (Eq. 2.66)

$$N_\gamma = 3.31 \times 10^{-2} K \quad \text{for } K > 1$$

Diameter of electron cloud in a CCD chip (Eq. 3.11)

$$d[\mu\text{m}] = 0.017 E_\gamma[\text{keV}]^{7/4}$$

Laser intensity required to ionize an atom/ion (Eq. 3.16)

$$I[\text{W}/\text{cm}^2] = 4 \times 10^9 E_{\text{ion}}^4[\text{eV}] Z^{-2}$$

Trajectory difference for electrons in divergent beam required for focusing by a dipole magnet (Eq. 4.5)

$$\Delta L[\text{mm}] = 6.67 \times 10^{-3} \frac{E_e[\text{MeV}]}{B[\text{T}]} \theta[\text{mrad}]$$

ROSS FILTER ANALYSIS CODE

The X-ray photon spectrometer based on Ross filters is described in details in Chapter 3. This appendix contains a description of the Matlab code used for analysis of the experimental data obtained using the set of Ross filters and a CCD camera since it is not trivial compared to the other sources described in this thesis. The code is optimized for the use with a beam with the Gaussian profile.

In the text, only parts of the code, which are important for the analysis, are described. At the beginning, the code loads the CCD image containing the signal which passed through the set of Ross filters. As the code was used both on Windows and Mac platforms, a simple "if" switch is used throughout the code to simplify the differences related mostly to the path directions. If multiple files is loaded, the code combine them together into a `combined` matrix. Median filtering using an area of 4x4 pixels around each pixel is used on each loaded image in order to remove hot pixels of the CCD.

```
for ii = 1:N_files
    fileNumber = files(ii);
    ross_file = fullfile(strcat(file_directory, 'SUM_tir_228.tif'));
    ross = double(imread(ross_file));
    ross = medfilt2(ross,[4 4]);
    combined = combined + ross;
end
```

In order to verify that the CCD images were properly loaded, `combined` is plotted as an image using the `imagesc()` function (Fig. 3.27). All negative values, which might appear due to the background subtraction in the camera software, are thrown away as they do not bring any value to the analysis.

```
combined(combined<0) = 0;
figure;
imagesc(combined)
title('raw image');
axis image
```

Then, the maximum of the signal is found since it is needed later.

```
[signal_cent_ver, signal_cent_hor] = ...
    find(combined==max(max(combined)));
```

The data on the photon transmission with respect to the photon energy is loaded from files and positions of all filters are defined manually. The tedious process is beneficial over simple selection using `ginput()` function as it provides better precision in selection of the filter areas. Moreover, due to blurry edges of the filters in the image, it has been found that selecting inner edges of the filters (for filter selection) and outer edges of the filters (for selection of the uncovered areas) is necessary. Fortunately, the process of identifying filter edges is usually needed to be done

only once per experimental campaign. Each filter is selected using three points (with exception of the germanium filter, more about it below): "center" corner which is closest to the center of the pie layout of the filters, and "left" and "right" corners which are close to the outside edges of the filters (the "right" corner is defined as the one in the clockwise direction from the "left" corner).

```
% filter (1) Fe 5um
filter1 = load('Fe_5um_500-30000eV.txt ');

Ox(1) = 1506;    % x-coordinate of the "center" corner (inside edge)
Oy(1) = 1078;    % y-coordinate of the "center" corner (inside edge)
Lx(1) = 1805;    % x-coordinate of the "left" corner (inside edge)
Ly(1) = 590;    % y-coordinate of the "left" corner (inside edge)
Rx(1) = 1950;    % x-coordinate of the "right" corner (inside edge)
Ry(1) = 843;    % y-coordinate of the "right" corner (inside edge)
Oxout(1) = 1485; % x-coordinate of the "center" corner (outside edge)
Oyout(1) = 1093; % y-coordinate of the "center" corner (outside edge)
Lxout(1) = 1799; % x-coordinate of the "left" corner (outside edge)
Lyout(1) = 578;  % y-coordinate of the "left" corner (outside edge)
Rxout(1) = 1955; % x-coordinate of the "right" corner (outside edge)
Ryout(1) = 848;  % y-coordinate of the "right" corner (outside edge)
```

In a similar manner, all other triangle-shaped filters are loaded.

```
% filter (2) Fe 20um
filter2 = load('Fe_20um_500-30000eV.txt ');

Ox(2) = 1652;
Oy(2) = 1116;
Lx(2) = 2022;
Ly(2) = 1120;
Rx(2) = 2028;
Ry(2) = 1305;
Oxout(2) = 1451;
Oyout(2) = 1064;
Lxout(2) = 2011;
Lyout(2) = 1059;
Rxout(2) = 2014;
Ryout(2) = 1438;

% filter (3) Cu 12.5um
filter3 = load('Cu_12.5um_500-30000eV.txt ');

Ox(3) = 1468;
Oy(3) = 1098;
Lx(3) = 2011;
Ly(3) = 1451;
Rx(3) = 1858;
Ry(3) = 1828;
Oxout(3) = 1451;
```

```
Oyout(3) = 1064;
Lxout(3) = 2014;
Lyout(3) = 1438;
Rxout(3) = 1852;
Ryout(3) = 1836;

% filter (4) Cu 37.5um
filter4 = load('Cu_37.5um_500-30000eV.txt');

Ox(4) = 1452;
Oy(4) = 1086;
Lx(4) = 1842;
Ly(4) = 1844;
Rx(4) = 1441;
Ry(4) = 1963;
Oxout(4) = 1451;
Oyout(4) = 1064;
Lxout(4) = 1852;
Lyout(4) = 1836;
Rxout(4) = 1429;
Ryout(4) = 1963;

% filter (5) Zr 20um
filter5 = load('Zr_20um_500-30000eV.txt');

Ox(5) = 1436;
Oy(5) = 1084;
Lx(5) = 906;
Ly(5) = 1919;
Rx(5) = 532;
Ry(5) = 1579;
Oxout(5) = 1451;
Oyout(5) = 1064;
Lxout(5) = 917;
Lyout(5) = 1921;
Rxout(5) = 526;
Ryout(5) = 1572;

% filter (6) Mo 12.5um
filter6 = load('Mo_12.5um_500-30000eV.txt');

Ox(6) = 1441;
Oy(6) = 1062;
Lx(6) = 304;
Ly(6) = 983;
Rx(6) = 614;
Ry(6) = 512;
Oxout(6) = 1451;
Oyout(6) = 1064;
Lxout(6) = 297;
```

```
Lyout(6) = 991;
Rxout(6) = 614;
Ryout(6) = 499;

% filter (7) Al 100um
filter7 = load('Al_100um_500-30000eV.txt');

Ox(7) = 1489;
Oy(7) = 1079;
Lx(7) = 1069;
Ly(7) = 179;
Rx(7) = 1513;
Ry(7) = 327;
Oxout(7) = 1489;
Oyout(7) = 1086;
Lxout(7) = 1060;
Lyout(7) = 190;
Rxout(7) = 1522;
Ryout(7) = 346;

% filter (8) Ti 12.5um
filter8 = load('Ti_12.5um_500-30000eV.txt');

Ox(8) = 1489;
Oy(8) = 1078;
Lx(8) = 1528;
Ly(8) = 339;
Rx(8) = 1793;
Ry(8) = 575;
Oxout(8) = 1485;
Oyout(8) = 1093;
Lxout(8) = 1522;
Lyout(8) = 346;
Rxout(8) = 1799;
Ryout(8) = 578;

The germanium filter is the only one in the layout that is not triangle-shaped. Furthermore, in order to attach the filter onto the mylar foil, a stripe of aluminum tape covers one of the corners of the 4 × 4 mm square filter (the corner closest to the outside edge of the cake layout). Therefore, selection of the filter area uses five points starting from 0 closest to the pie layout center and going clockwise as A, B, C and D. In the same way as for the other filters, inside and outside edges of the filter were selected.

% filter (9) Ge 50um
filter9 = load('Ge_50um_500-30000eV.txt');

Ox_Ge = 1339;
Oy_Ge = 1449;
Ax_Ge = 1405;
Ay_Ge = 1588;
```

```

Bx_Ge = 1339;
By_Ge = 1621;
Cx_Ge = 1240;
Cy_Ge = 1593;
Dx_Ge = 1203;
Dy_Ge = 1514;
Ox_Ge_out = 1343;
Oy_Ge_out = 1436;
Ax_Ge_out = 1437;
Ay_Ge_out = 1597;
Bx_Ge_out = 1410;
By_Ge_out = 1719;
Cx_Ge_out = 1109;
Cy_Ge_out = 1611;
Dx_Ge_out = 1184;
Dy_Ge_out = 1498;

```

The left and right sides (**OA** and **OB** edges) of all filters are identified and an axis going through the center of each filter is defined as a line with a slope **aC** and a y-intercept **bC** for all filters respectively. For each filter, auxiliary signs for the left and right edges must be introduced in order to define correctly whether the filter in question is above or below an edge line.

```

ori_sign_L = [+1, +1, +1, +1, -1, -1, -1, +1];
ori_sign_R = [-1, -1, -1, +1, +1, +1, -1, -1];

```

For coordinates **xxC** corresponding to the horizontal pixels of the CCD, coordinates **yyC** of all axes are calculated and restricted to those that fit onto the CCD chip. Finally, an area of each filter is selected as all pixels which satisfy all the following conditions:

1. are between the left and right edge,
2. are out of a circle with a radius **radius_min** with a center [**signal_cent_hor**,**signal_cent_ver**],
3. are in a circle with a radius **radius_max** with a center [**signal_cent_hor**,**signal_cent_ver**].

The result is saved into a 3D matrix **signal**, in which each level is a matrix containing the signal from one filter. In a similar manner, the areas that are not covered by any filter are progressively selected into a 3D matrix **invsignal**, in which the last level contains all uncovered parts.

```

for jj = 1:8

    xxC = 1:2084;
    yyC(jj,1:2084) = aC(jj)*xxC + bC(jj);
    yyC2(jj,1:2084) = round(yyC(jj,1:2084));
    onchip_index_yy = find(1 <= yyC2(jj,:) & yyC2(jj,:) <= 2084);
    yy_index_min(jj) = min(onchip_index_yy);
    yy_index_max(jj) = max(onchip_index_yy);

    for xx = 1:2084
        for yy = 1:2084

            if (ori_sign_R(jj)*yy) > ori_sign_R(jj)*(aR(jj)*xx ...

```

```

+ bR(jj)) && (ori_sign_L(jj)*yy) >...
ori_sign_L(jj)*(aL(jj)*xx + bL(jj)) &&...
((xx-signal_cent_hor)^2 + (yy-signal_cent_ver)^2)...
< radius_max^2 && ((xx-signal_cent_hor)^2...
+ (yy-signal_cent_ver)^2) > radius_min^2

signal(yy,xx,jj) = combined(yy,xx);
N_pixels(jj) = N_pixels(jj)+1;

end

if (ori_sign_R(jj)*yy) > ori_sign_R(jj)*(aRout(jj)*xx...
+ bRout(jj)) && (ori_sign_L(jj)*yy) >...
ori_sign_L(jj)*(aLout(jj)*xx + bLout(jj)) &&...
((xx-signal_cent_hor)^2 + (yy-signal_cent_ver)^2)...
< radius_max^2 && ((xx-signal_cent_hor)^2 + ...
(yy-signal_cent_ver)^2) > radius_min^2

    continue

else
    if ((xx-signal_cent_hor)^2 + ...
        (yy-signal_cent_ver)^2) < radius_max^2 &&...
        ((xx-signal_cent_hor)^2 + (yy-signal_cent_ver)^2)...
        > radius_min^2

        if jj == 1
            invsignal(yy,xx,jj) = combined(yy,xx);
        elseif jj > 1
            invsignal(yy,xx,jj) = invsignal(yy,xx,jj-1);
        end

    end

end

end

end

end
end
end

```

Separately, the area of the germanium filter is selected again using definition of the edge lines and selecting all pixels between them.

```

aOA = (Oy_Ge - Ay_Ge)/(Ox_Ge - Ax_Ge);
bOA = Ay_Ge - Ax_Ge*aOA;
aAB = (By_Ge - Ay_Ge)/(Bx_Ge - Ax_Ge);
bAB = Ay_Ge - Ax_Ge*aAB;
aBC = (Cy_Ge - By_Ge)/(Cx_Ge - Bx_Ge);
bBC = By_Ge - Bx_Ge*aBC;
aCD = (Dy_Ge - Cy_Ge)/(Dx_Ge - Cx_Ge);
bCD = Cy_Ge - Cx_Ge*aCD;
aDO = (Dy_Ge - Oy_Ge)/(Dx_Ge - Ox_Ge);

```

```

bDO = Oy_Ge - Ox_Ge*aDO;

aOA_out = (Oy_Ge_out - Ay_Ge_out)/(Ox_Ge_out - Ax_Ge_out);
bOA_out = Ay_Ge_out - Ax_Ge_out*aOA_out;
aAB_out = (By_Ge_out - Ay_Ge_out)/(Bx_Ge_out - Ax_Ge_out);
bAB_out = Ay_Ge_out - Ax_Ge_out*aAB_out;
aBC_out = (Cy_Ge_out - By_Ge_out)/(Cx_Ge_out - Bx_Ge_out);
bBC_out = By_Ge_out - Bx_Ge_out*aBC_out;
aCD_out = (Dy_Ge_out - Cy_Ge_out)/(Dx_Ge_out - Cx_Ge_out);
bCD_out = Cy_Ge_out - Cx_Ge_out*aCD_out;
aDO_out = (Dy_Ge_out - Oy_Ge_out)/(Dx_Ge_out - Ox_Ge_out);
bDO_out = Oy_Ge_out - Ox_Ge_out*aDO_out;

for xx = 1:2084
    for yy = 1:2084

        if yy > (aOA*xx + bOA) &&...
            yy < (aAB*xx + bAB) && yy <...
                (aBC*xx + bBC) && yy <...
                    (aCD*xx + bCD) && yy > (aDO*xx + bDO)

                signal(yy,xx,9) = combined(yy,xx);
                N_pixels(9) = N_pixels(9)+1;

            end

            if yy > (aOA_out*xx + bOA_out) &&...
                yy < (aAB_out*xx + bAB_out) &&...
                    yy < (aBC_out*xx + bBC_out) &&...
                        yy > (aCD_out*xx + bCD_out)...
                            && yy > (aDO_out*xx + bDO_out)

                continue

            else

                invsignal(yy,xx,9) = invsignal(yy,xx,8);

            end

        end

    end

end

```

For plotting purposes, a matrix `signal_total` is made as a sum of all levels of the `signal` matrix containing all filters (Fig. 3.28). In order to verify the selection, the uncovered area was plotted as well (Fig. 3.29).

```

signal_total = signal(:,:,1)+signal(:,:,2)+signal(:,:,3)+...
signal(:,:,4)+signal(:,:,5)+signal(:,:,6)+signal(:,:,7)+...
signal(:,:,8)+signal(:,:,9);

```

```

figure ;
imagesc(signal_total);
title('Total signal behind filters ');
axis image

```

```

figure ;
imagesc(invsignal(:,:,9));
title('Total signal without filters ');
axis image

```

An average signal density in each filter is calculated and saved as a variable `signal_level`. An auxiliary signal matrix is then created for the purpose of fitting the signal. The level of the signal behind each filter and the level of the signal obtained from the uncovered areas are approximately renormalized in order to be of the similar amplitude and to create a smooth signal shape, which resembles the shape of the original signal that irradiated the Ross filters. The matrix is then plotted for verification (Fig. 3.30).

```

signal_norm = 1.2*signal(:,:,1)/signal_level(1) +...
signal(:,:,2)/signal_level(2) + signal(:,:,3)/signal_level(3)...
+ signal(:,:,4)/signal_level(4) + 1.5*signal(:,:,5)/signal_level(5)...
+ 1.5*signal(:,:,6)/signal_level(6) + signal(:,:,7)/signal_level(7)...
+ signal(:,:,8)/signal_level(8) + signal(:,:,9)/signal_level(9);

```

```

signal_norm2 = signal_norm + 2*invsignal(:,:,9)/signal_level(10);
signal_smooth = smooth2a(signal_norm2,20);

```

```

figure ;
imagesc(signal_norm2)
title('Normalized signal in the filter area ');
axis image

```

```

figure ;
surf(XxS,YyS,signal_smooth)
shading interp

```

The resulting shape is then fitted with a 2D gaussian function using a function `fmgaussfit`, which returns necessary parameters of the 2D gaussian function. The resulted fit is then plotted (Fig. 3.31). The fit results are then saved into variables, where `gA` is the amplitude, `gPhi` is the rotation angle, `gSigx` and `gSigy` are the sigma widths of the 2D gaussian function in x - and y -dimension, respectively, `gBx` and `gBy` are the coordinates of the center and `gC` is the additional constant. Value `gAint` is defined to calculate the intersection of the filter axes with the gaussian signal fit, where `gAint` is the height in the z -dimension at which the axis should be positioned. In case that we want to define a different height for a pair, alternative values can be set in variable `gAintalt`.

```

[fitresult, zfit, fiterr, zerr, resnorm, rr]=...
fmgaussfit(xxS,yyS,signal_smooth);

```

```

[max_ver,max_hor]=find(zfit==max(max(zfit)));
figure;imagesc(zfit)
title('2d gaussian fit ')
axis image

```

```

gA = fitresult(1);
gPhi = fitresult(2);
gSigx = fitresult(3);
gSigy = fitresult(4);
gBx = fitresult(5);
gBy = fitresult(6);
gC = fitresult(7);

```

```

% universal value for intersection
gAint = gA/exp(1);

```

```

% alternative value for intersection for each filter pair
% gAint = [gA/exp(1), gA/exp(1), gA/exp(1), gA/exp(1), ...
% gA/1.2, gA/1.2, gA/exp(1), gA/exp(1), gA/exp(1)];

```

The 2D gaussian function is defined using the obtained parameters.

```

f_gauss = gC + gA*exp(-(((XxS-gBx).* cosd(gPhi)+(YyS-gBy)...
.* sind(gPhi))./ gSigx).^2 - (((-XxS-gBx).* sind(gPhi)+(YyS-gBy)...
.* cosd(gPhi))./ gSigy).^2);

```

Position of each filter with respect to the center of the pie layout is defined

```

filter_pos_cent_x = [+1, +1, +1, +1, -1, -1, -1, +1, -1];
filter_pos_cent_y = [-1, +1, +1, +1, +1, -1, -1, -1, +1];

```

and the intersections of all filter axes with the gaussian fit function are calculated (including the alternative values). Rather complicated explicit expressions obtained using the Maple software are used as the calculation of the intersections can be rather tedious in Matlab. The correct intersections in the filter areas are then selected using the filter position signs `filter_pos_cent_x` and `filter_pos_cent_y`.

```

for gg=1:9

```

```

    xint1 = (-gSigx + gSigy) * ((-gBy + bC(gg))...
    .* aC(gg) + gBx) * (gSigx - gSigy) * cos(gPhi) ^ 2...
    - sin(gPhi) * (gSigx - gSigy) * (gSigx + gSigy)...
    .* (gBx * aC(gg) + gBy - bC(gg)) * cos(gPhi)...
    + gBx * gSigx ^ 2 + (gBy - bC(gg)) * gSigy ^ 2...
    .* aC(gg) - sqrt(-gSigx ^ 2 * (((gSigx ^ 2 -...
    gSigy ^ 2) * aC(gg) .^ 2 - gSigx ^ 2 + gSigy ^ 2)...
    * cos(gPhi) ^ 2 - 0.2e1 * sin(gPhi) .* aC(gg)...
    * (gSigx - gSigy) * (gSigx + gSigy) * cos(gPhi)...
    + aC(gg) .^ 2 * gSigy ^ 2 + gSigx ^ 2)...
    * log(gAint / gA) + (gBx * aC(gg) - gBy +...
    bC(gg)) .^ 2) * gSigy ^ 2)) ./ (((gSigx ^ 2...
    - gSigy ^ 2) .* aC(gg) .^ 2 - gSigx ^ 2...
    + gSigy ^ 2) * cos(gPhi) ^ 2 - 0.2e1 * sin(gPhi)...
    .* aC(gg) * (gSigx - gSigy) * (gSigx + gSigy)...
    * cos(gPhi) + aC(gg) .^ 2 * gSigy ^ 2 + gSigx ^ 2);

```

```

xint2      = (-gSigx + gSigy) * ((-gBy + bC(gg))...
.* aC(gg) + gBx) * (gSigx - gSigy) * cos(gPhi) ^ 2...
- sin(gPhi) * (gSigx - gSigy) * (gSigx + gSigy)...
.* (gBx * aC(gg) + gBy - bC(gg)) * cos(gPhi)...
+ gBx * gSigx ^ 2 + (gBy - bC(gg)) * gSigy ^ 2...
.* aC(gg) + sqrt(-gSigx ^ 2 * (((gSigx ^ 2 -...
gSigy ^ 2) * aC(gg) .^ 2 - gSigx ^ 2 + gSigy ^ 2)...
* cos(gPhi) ^ 2 - 0.2e1 * sin(gPhi) .* aC(gg)...
* (gSigx - gSigy) * (gSigx + gSigy) * cos(gPhi)...
+ aC(gg) .^ 2 * gSigy ^ 2 + gSigx ^ 2)...
* log(gAint / gA) + (gBx * aC(gg) - gBy...
+ bC(gg)) .^ 2) * gSigy ^ 2) ./ (((gSigx ^ 2...
- gSigy ^ 2) .* aC(gg) .^ 2 - gSigx ^ 2...
+ gSigy ^ 2) * cos(gPhi) ^ 2 - 0.2e1 * sin(gPhi)...
.* aC(gg) * (gSigx - gSigy) * (gSigx + gSigy)...
* cos(gPhi) + aC(gg) .^ 2 * gSigy ^ 2 + gSigx ^ 2);

yint1      = aC(gg).*xint1 + bC(gg);

yint2      = aC(gg).*xint2 + bC(gg);

if filter_pos_cent_x(gg)*xint1 > filter_pos_cent_x(gg)*Ox(gg)
    xint(gg) = round(xint1);
elseif filter_pos_cent_x(gg)*xint2 > filter_pos_cent_x(gg)*Ox(gg)
    xint(gg) = round(xint2);
else
    xint(gg) = NaN;
end

if filter_pos_cent_y(gg)*yint1 > filter_pos_cent_y(gg)*Oy(gg)
    yint(gg) = round(yint1);
elseif filter_pos_cent_y(gg)*yint2 > filter_pos_cent_y(gg)*Oy(gg)
    yint(gg) = round(yint2);
else
    yint(gg) = NaN;
end
end
end

```

A pixel radius of the area which is selected around each intersection is defined and pixels within the circle with a radius `signal_area_radius` centered at each intersection is selected and the number of pixels is calculated (in our case it is the same for all areas but in general the radius can be defined differently for each filter pair).

```

signal_gauss = zeros(2084,2084,8);
signal_pixels = zeros(9,1);
signal_gauss_alt = zeros(2084,2084,8);
signal_pixels_alt = zeros(9,1);
signal_area_radius = 35;

```

```

for hh = 1:9
    for xx = 1:2084
        for yy = 1:2084
            if (xx-xint(hh))^2 + (yy-yint(hh))^2 < signal_area_radius^2
                signal_gauss(yy,xx,hh) = signal(yy,xx,hh);
                signal_pixels(hh) = signal_pixels(hh)+1;
            end
        end
    end

    density_select(hh) = sum(sum(signal_gauss(:, :, hh)))...
    /signal_pixels(hh);

```

```
end
```

The selected circles of the signal from all filters are then plotted (Fig. 3.32) with the selected areas enhanced five times in their amplitude only for the plotting purpose.

```

figure;
imagesc(signal_total+5*(signal_gauss(:, :, 1)+signal_gauss(:, :, 2)...
+signal_gauss(:, :, 3)+signal_gauss(:, :, 4)+signal_gauss(:, :, 5)...
+signal_gauss(:, :, 6)+signal_gauss(:, :, 7)+signal_gauss(:, :, 8)...
+signal_gauss(:, :, 9)));

title('Chosen parts of signal')
axis image

```

In case an alternative value of the intersection height was used for a filter pair, renormalization using `density_norm_factor` must be used. Otherwise, it is set to be equal to one.

```

% density_norm_factor = density_select./density_select;
density_norm_factor = 1;

```

The density values of the signals are then subtracted for each filter pair.

```

density_pair18 = (density_select(1) - density_select(8))...
/((density_norm_factor(1)+density_norm_factor(5))/2);

density_pair32 = (density_select(3) - density_select(2))...
/((density_norm_factor(2)+density_norm_factor(3))/2);

density_pair94 = (density_select(9) - density_select(4))...
/((density_norm_factor(4)+density_norm_factor(9))/2);

density_pair59 = (density_select(5) - density_select(9))...
/((density_norm_factor(5)+density_norm_factor(9))/2);

density_pair65 = (density_select(6) - density_select(5))...
/((density_norm_factor(5)+density_norm_factor(6))/2);

density_pair87 = (density_select(8) - density_select(7))...

```

```
/((density_norm_factor(7)+density_norm_factor(8))/2);
```

An array of the photon energy is then defined using the X-ray energy from the file with the filter transmission. Additional transmission values of filters that were placed in front of all filters or in front of the whole CCD chip are then loaded.

```
energy = filter1(1:501,1);
% energy array for the filter transmittances
```

```
filter_Be = load('Be_500um_500-30000eV.txt');
filter_Mylar = load('Mylar_13um_500-30000eV.txt');
filter_Mylar2 = load('Mylar_75um_500-30000eV.txt');
```

Transmission values are calculated for all filter pairs using the transmission data. At the same time, the data are deconvoluted with the additional filter transmission values.

```
transmit_pair18 = (filter1(1:501,2) - filter8(1:501,2))...
.*filter_Be(1:501,2).*filter_Mylar2(1:501,2).*filter_Mylar(1:501,2);
```

```
transmit_pair32 = (filter3(1:501,2) - filter2(1:501,2))...
.*filter_Be(1:501,2).*filter_Mylar2(1:501,2).*filter_Mylar(1:501,2);
```

```
transmit_pair94 = (filter9(1:501,2) - filter4(1:501,2))...
.*filter_Be(1:501,2).*filter_Mylar2(1:501,2).*filter_Mylar(1:501,2);
```

```
transmit_pair59 = (filter5(1:501,2) - filter9(1:501,2))...
.*filter_Be(1:501,2).*filter_Mylar2(1:501,2).*filter_Mylar(1:501,2);
```

```
transmit_pair65 = (filter6(1:501,2) - filter5(1:501,2))...
.*filter_Be(1:501,2).*filter_Mylar2(1:501,2).*filter_Mylar(1:501,2);
```

```
transmit_pair87 = (filter8(1:501,2) - filter7(1:501,2))...
.*filter_Be(1:501,2).*filter_Mylar2(1:501,2).*filter_Mylar(1:501,2);
```

Indices of the energy values corresponding to the minimum and maximum energy, in which each filter pair works, are then defined.

```
E_pair6_min = 51;
E_pair6_max = 76;
E_pair1_min = 77;
E_pair1_max = 113;
E_pair2_min = 119;
E_pair2_max = 150;
E_pair3_min = 145;
E_pair3_max = 180;
E_pair4_min = 181;
E_pair4_max = 300;
E_pair5_min = 301;
E_pair5_max = 331;
```

A mean energy value, mean transmission (difference of transmission) value and a standard deviation of the transmission difference are calculated for each filter pair as a weighted average.

```

E_mean(1) = sum(energy(E_pair1_min:E_pair1_max)...
.*transmit_pair18(E_pair1_min:E_pair1_max))...
/sum(transmit_pair18(E_pair1_min:E_pair1_max));

T_mean(1) = sum(energy(E_pair1_min:E_pair1_max)...
.*transmit_pair18(E_pair1_min:E_pair1_max))...
/sum(energy(E_pair1_min:E_pair1_max));

T_std(1) = std(transmit_pair18(E_pair1_min:E_pair1_max));

E_mean(2) = sum(energy(E_pair2_min:E_pair2_max)...
.*transmit_pair32(E_pair2_min:E_pair2_max))...
/sum(transmit_pair32(E_pair2_min:E_pair2_max));

T_mean(2) = sum(energy(E_pair2_min:E_pair2_max)...
.*transmit_pair32(E_pair2_min:E_pair2_max))...
/sum(energy(E_pair2_min:E_pair2_max));

T_std(2) = std(transmit_pair32(E_pair2_min:E_pair2_max));

E_mean(3) = sum(energy(E_pair3_min:E_pair3_max)...
.*transmit_pair94(E_pair3_min:E_pair3_max))...
/sum(transmit_pair94(E_pair3_min:E_pair3_max));

T_mean(3) = sum(energy(E_pair3_min:E_pair3_max)...
.*transmit_pair94(E_pair3_min:E_pair3_max))...
/sum(energy(E_pair3_min:E_pair3_max));

T_std(3) = std(transmit_pair94(E_pair3_min:E_pair3_max));

E_mean(4) = sum(energy(E_pair4_min:E_pair4_max)...
.*transmit_pair59(E_pair4_min:E_pair4_max))...
/sum(transmit_pair59(E_pair4_min:E_pair4_max));

T_mean(4) = sum(energy(E_pair4_min:E_pair4_max)...
.*transmit_pair59(E_pair4_min:E_pair4_max))...
/sum(energy(E_pair4_min:E_pair4_max));

T_std(4) = std(transmit_pair59(E_pair4_min:E_pair4_max));

E_mean(5) = sum(energy(E_pair5_min:E_pair5_max)...
.*transmit_pair65(E_pair5_min:E_pair5_max))...
/sum(transmit_pair65(E_pair5_min:E_pair5_max));

T_mean(5) = sum(energy(E_pair5_min:E_pair5_max)...
.*transmit_pair65(E_pair5_min:E_pair5_max))...
/sum(energy(E_pair5_min:E_pair5_max));

T_std(5) = std(transmit_pair65(E_pair5_min:E_pair5_max));

```

```

E_mean(6) = sum(energy(E_pair6_min:E_pair6_max)...
.*transmit_pair87(E_pair6_min:E_pair6_max))...
/sum(transmit_pair87(E_pair6_min:E_pair6_max));

```

```

T_mean(6) = sum(energy(E_pair6_min:E_pair6_max)...
.*transmit_pair87(E_pair6_min:E_pair6_max))...
/sum(energy(E_pair6_min:E_pair6_max));

```

```

T_std(6) = std(transmit_pair87(E_pair6_min:E_pair6_max));

```

Radiated energy of X-ray photons detected in the narrow energy intervals defined by the filter pairs is determined and renormalized to the energy range widths. Furthermore, the uncertainty in the radiated energy estimation is obtained in a similar manner using the standard deviation of the transmission values.

```

% radiated energy

```

```

N_photons(1) = density_pair18./T_mean(1)/(energy(E_pair1_max)...
-energy(E_pair1_min));

```

```

N_photons(2) = density_pair32./T_mean(2)/(energy(E_pair2_max)...
-energy(E_pair2_min));

```

```

N_photons(3) = density_pair94./T_mean(3)/(energy(E_pair3_max)...
-energy(E_pair3_min));

```

```

N_photons(4) = density_pair59./T_mean(4)/(energy(E_pair4_max)...
-energy(E_pair4_min));

```

```

N_photons(5) = density_pair65./T_mean(5)/(energy(E_pair5_max)...
-energy(E_pair5_min));

```

```

N_photons(6) = density_pair87./T_mean(6)/(energy(E_pair6_max)...
-energy(E_pair6_min));

```

```

% radiated energy error

```

```

N_phot_err(1) = sqrt((density_pair18^2)/((T_mean(1))^4)...
*((T_std(1))^2))/(energy(E_pair1_max)-energy(E_pair1_min));

```

```

N_phot_err(2) = sqrt((density_pair32^2)/((T_mean(2))^4)...
*((T_std(2))^2))/(energy(E_pair2_max)-energy(E_pair2_min));

```

```

N_phot_err(3) = sqrt((density_pair94^2)/((T_mean(3))^4)...
*((T_std(3))^2))/(energy(E_pair3_max)-energy(E_pair3_min));

```

```

N_phot_err(4) = sqrt((density_pair59^2)/((T_mean(4))^4)...
*((T_std(4))^2))/(energy(E_pair4_max)-energy(E_pair4_min));

```

```

N_phot_err(5) = sqrt((density_pair65^2)/((T_mean(5))^4)...
*((T_std(5))^2))/(energy(E_pair5_max)-energy(E_pair5_min));

```

```
N_phot_err(6) = sqrt((density_pair87^2)/((T_mean(6))^4)...  
*((T_std(6))^2))/(energy(E_pair6_max)-energy(E_pair6_min));
```

The data are then prepared for the energy spectrum fitting and plotting.

```
rr = 1;  
for pp = 1:6  
    photon_energy(rr) = E_mean(pp);  
    photon_number(rr) = N_photons(pp);  
    photon_number_err(rr) = N_phot_err(pp);  
    rr = rr + 1;  
end  
photon_err_weight = 1./photon_number_err.^2;
```

The obtained data points with errorbars are then fitted with a Bessel function of the second kind (Fig. 3.33) and the process of determining the X-ray photon spectrum is complete.

Bibliography

- [1] D. H. Bilderback, P. Elleaume, and E. Weckert. *Review of third and next generation synchrotron light sources*. Journal of Physics B: Atomic, molecular and optical physics, 38(9):S773, 2005.
- [2] P. Suortti and W. Thomlinson. *Medical applications of synchrotron radiation*. Physics in Medicine & Biology, 48(13):R1, 2003.
- [3] P. Emma et al. *First lasing and operation of an ångstrom-wavelength free-electron laser*. Nature Photonics, 4(9):641, 2010.
- [4] S. Dobert. *Rf breakdown in high frequency accelerators*. Technical report, SLAC National Accelerator Lab., Menlo Park, CA (United States), 2018.
- [5] E. Esarey, C. B. Schroeder, and W. P. Leemans. *Physics of laser-driven plasma-based electron accelerators*. Reviews of Modern Physics, 81(3):1229, 2009.
- [6] W. P. Leemans et al. *Multi-GeV electron beams from capillary-discharge-guided subpetawatt laser pulses in the self-trapping regime*. Physical Review Letters, 113(24):245002, 2014.
- [7] O. Lundh et al. *Few femtosecond, few kiloampere electron bunch produced by a laser-plasma accelerator*. Nature Physics, 7(3):219, 2011.
- [8] A. J. DeMaria et al. *Self mode-locking of lasers with saturable absorbers*. Applied Physics Letters, 8(7):174–176, 1966.
- [9] D. Strickland and G. Mourou. *Compression of amplified chirped optical pulses*. Optics Communications, 55(6):447–449, 1985.
- [10] NobelPrize.org. *The Nobel Prize in Physics 2018*. URL: <https://www.nobelprize.org/prizes/physics/2018/summary/>, 2018.
- [11] S. Kiselev, A. Pukhov, and I. Kostyukov. *X-ray generation in strongly nonlinear plasma waves*. Physical Review Letters, 93(13):135004, 2004.
- [12] A. Rousse et al. *Production of a keV X-ray beam from synchrotron radiation in relativistic laser-plasma interaction*. Physical Review Letters, 93(13):135005, 2004.
- [13] P. Gibbon. *Short Pulse Laser Interactions with Matter: An Introduction*. Imperial College Press, 2005.
- [14] K. Bohacek. *Design and optimization of gamma photon beam production using inverse Compton scattering of femtosecond electron beam and femtosecond laser pulse*. FNSPE, CTU (Master’s thesis), 2013.
- [15] B. Quesnel and P. Mora. *Theory and simulation of the interaction of ultraintense laser pulses with electrons in vacuum*. Physical Review E, 57, 1998.

-
- [16] W. L. Kruer. *The Physics of Laser Plasma Interaction*. Addison-Wesley, 1988.
- [17] Y. Raizer. *Laser-Induced Discharge Phenomena (Studies in Soviet Science)*. Springer, 1978.
- [18] L. V. Keldysh et al. *Ionization in the field of a strong electromagnetic wave*. *Sov. Phys. JETP*, 20(5):1307–1314, 1965.
- [19] J. L. Bobin. *Laser Plasma Interaction*. *Physica Scripta T30*, T30:77.
- [20] C. I. Moore et al. *Measurements of energetic electrons from the high-intensity laser ionization of gases*. *Physics of plasmas*, 8.
- [21] S. Augst et al. *Tunneling Ionization of Noble Gases in a High-Intensity Laser Field*. *Physical Review Letters*, 63(20):2212–2215, 1989.
- [22] W. Becker et al. *Above-threshold ionization: From classical features to quantum effects*. *Advances in atomic, molecular, and optical physics*, 45:35, 2002.
- [23] F. F. Chen. *Introduction to plasma physics and controlled fusion*. Los Angeles: Plenum Press, 1984.
- [24] O. Svelto and D. C. Hanna. *Principles of lasers*, volume 4. Springer, 1998.
- [25] G.-Z. Sun et al. *Self-focusing of short intense pulses in plasmas*. *Physics of Fluids*, 30(2):526–532, 1987.
- [26] A. B. Borisov et al. *Observation of relativistic and charge-displacement self-channeling of intense subpicosecond ultraviolet (248 nm) radiation in plasmas*. *Physical Review Letters*, 68(15):2309, 1992.
- [27] C. Ren et al. *Compressing and focusing a short laser pulse by a thin plasma lens*. *Physical Review E*, 63(2):026411, 2001.
- [28] A. G. R. Thomas et al. *Effect of laser-focusing conditions on propagation and monoenergetic electron production in laser-wakefield accelerators*. *Physical Review Letters*, 98(9):095004, 2007.
- [29] S. Kneip et al. *Near-GeV acceleration of electrons by a nonlinear plasma wave driven by a self-guided laser pulse*. *Physical Review Letters*, 103(3):035002, 2009.
- [30] D. F. Gordon et al. *Asymmetric self-phase modulation and compression of short laser pulses in plasma channels*. *Physical Review Letters*, 90(21):215001, 2003.
- [31] J. Faure et al. *Observation of laser-pulse shortening in nonlinear plasma waves*. *Physical Review Letters*, 95(20):205003, 2005.
- [32] W. B. Mori. *The physics of the nonlinear optics of plasmas at relativistic intensities for short-pulse lasers*. *IEEE Journal of Quantum Electronics*, 33(11):1942–1953, 1997.
- [33] I. Watts et al. *Measurements of relativistic self-phase-modulation in plasma*. *Physical Review E*, 66(3):036409, 2002.
- [34] A. G. Litvak. *Finite-amplitude wave beams in a magnetoactive plasma*. *Sov. Phys. JETP*, 30(344):166, 1970.

-
- [35] C. E. Max et al. *Self-modulation and self-focusing of electromagnetic waves in plasmas*. Physical Review Letters, 33(4):209, 1974.
- [36] P. Sprangle. *Propagation and guiding of intense laser pulses in plasmas*. Physical Review Letters, 69(15):2200, 1992.
- [37] N. E. Andreev et al. *Resonant excitation of wakefields by a laser pulse*. JETP Letters, 55, 1992.
- [38] W. P. Leemans et al. *GeV electron beams from a centimetre-scale accelerator*. Nature Physics, 2(10):696, 2006.
- [39] S. Y. Kalmykov et al. *Electron self-injection and trapping into an evolving plasma bubble*. Physical Review Letters, 103(13):135004, 2009.
- [40] P. Monot et al. *Experimental demonstration of relativistic self-channeling of a multiterawatt laser pulse in an underdense plasma*. Physical Review Letters, 74(15):2953, 1995.
- [41] P. E. Young et al. *Fast ion production by laser filamentation in laser-produced plasmas*. Physical Review Letters, 76(17):3128, 1996.
- [42] K. Krushelnick et al. *Plasma channel formation and guiding during high intensity short pulse laser plasma experiments*. Physical Review Letters, 78(21):4047, 1997.
- [43] C. E. Clayton et al. *Plasma wave generation in a self-focused channel of a relativistically intense laser pulse*. Physical Review Letters, 81(1):100, 1998.
- [44] K. Krushelnick et al. *Multi-mev ion production from high-intensity laser interactions with underdense plasmas*. Physical Review Letters, 83(4):737, 1999.
- [45] G. S. Sarkisov et al. *Self-focusing, channel formation, and high-energy ion generation in interaction of an intense short laser pulse with a He jet*. Physical Review E, 59(6):7042, 1999.
- [46] T. Hosokai et al. *Effect of a laser prepulse on a narrow-cone ejection of MeV electrons from a gas jet irradiated by an ultrashort laser pulse*. Physical Review E, 67(3):036407, 2003.
- [47] S. Y. Kalmykov et al. *Laser wakefield electron acceleration on Texas petawatt facility: Towards multi-GeV electron energy in a single self-guided stage*. High Energy Density Physics, 6(2):200–206, 2010.
- [48] I. Kostyukov et al. *Electron self-injection in multidimensional relativistic-plasma wake fields*. Physical Review Letters, 103(17):175003, 2009.
- [49] V. Malka et al. *Staged concept of laser-plasma acceleration toward multi-GeV electron beams*. Physical Review Special Topics-Accelerators and Beams, 9(9):091301, 2006.
- [50] T. Tajima and J. M. Dawson. *Laser electron accelerator*. Physical Review Letters, 43(4):267, 1979.
- [51] J. M. Dawson. *Nonlinear electron oscillations in a cold plasma*. Physical Review, 113(2):383, 1959.
- [52] S. V. Bulanov et al. *Excitation of ultrarelativistic plasma waves by pulse of electromagnetic radiation*. JETP Letters, 50(0):4–25, 1989.

-
- [53] V. I. Berezhiani and I. G. Murusidze. *Relativistic wake-field generation by an intense laser pulse in a plasma*. Physics Letters A, 148(6-7):338–340, 1990.
- [54] P. Sprangle, E. Esarey, and A. Ting. *Nonlinear interaction of intense laser pulses in plasmas*. Physical Review A, 41(8):4463, 1990.
- [55] P. Sprangle, E. Esarey, and A. Ting. *Nonlinear theory of intense laser-plasma interactions*. Physical Review Letters, 64(17):2011, 1990.
- [56] A. Ting and P. Sprangle E. Esarey. *Nonlinear wake-field generation and relativistic focusing of intense laser pulses in plasmas*. Physics of Fluids B: Plasma Physics, 2(6):1390–1394, 1990.
- [57] W. P. Leemans et al. *Laser guiding for GeV laser-plasma accelerators*. Philosophical Transactions of the Royal Society of London A: Mathematical, Physical and Engineering Sciences, 364(1840):585–600, 2006.
- [58] A. Pukhov and J. Meyer ter Vehn. *Laser wake field acceleration: the highly non-linear broken-wave regime*. Applied Physics B, 74(4-5):355–361, 2002.
- [59] W. Lu et al. *Generating multi-GeV electron bunches using single stage laser wakefield acceleration in a 3D nonlinear regime*. Physical Review Special Topics-Accelerators and Beams, 10(6):061301, 2007.
- [60] S. Corde et al. *Femtosecond X-rays from Laser-Plasma Accelerators*. Reviews of Modern Physics, 85(1):1, 2013.
- [61] W. Lu et al. *A nonlinear theory for multidimensional relativistic plasma wave wakefields*. Physics of Plasmas, 13(5):056709, 2006.
- [62] F. S. Tsung et al. *Near-GeV-energy laser-wakefield acceleration of self-injected electrons in a centimeter-scale plasma channel*. Physical Review Letters, 93(18):185002, 2004.
- [63] W. Lu et al. *Nonlinear theory for relativistic plasma wakefields in the blowout regime*. Physical Review Letters, 96(16):165002, 2006.
- [64] M. Tzoufras et al. *Beam loading in the nonlinear regime of plasma-based acceleration*. Physical Review Letters, 101(14):145002, 2008.
- [65] T. Katsouleas and W. B. Mori. *Wave-breaking amplitude of relativistic oscillations in a thermal plasma*. Physical Review Letters, 61(1):90, 1988.
- [66] J. B. Rosenzweig. *Trapping, thermal effects, and wave breaking in the nonlinear plasma wake-field accelerator*. Physical Review A, 38(7):3634, 1988.
- [67] W. M. Wang and Z. M. Sheng. *Effect of laser parameters on electron injection into laser wakefields in plasma with a counterpropagating additional laser pulse*. Physics of Plasmas, 15(1):013101, 2008.
- [68] S. Humphries Jr. *Principles of charged particle acceleration*. Courier Corporation, 2013.
- [69] C. G. R. Geddes et al. *High-quality electron beams from a laser wakefield accelerator using plasma-channel guiding*. Nature, 431(7008):538, 2004.
- [70] E. Esarey et al. *Trapping and acceleration in self-modulated laser wakefields*. Physical Review Letters, 80(25):5552, 1998.

-
- [71] S. P. D. Mangles. *Monoenergetic beams of relativistic electrons from intense laser-plasma interactions*. Nature, 431(7008):535, 2004.
- [72] J. Faure et al. *A laser-plasma accelerator producing monoenergetic electron beams*. Nature, 431(7008):541, 2004.
- [73] S. V. Bulanov et al. *Two-dimensional regimes of self-focusing, wake field generation, and induced focusing of a short intense laser pulse in an underdense plasma*. Physical Review Letters, 74(5):710, 1995.
- [74] S. V. Bulanov et al. *Particle injection into the wave acceleration phase due to nonlinear wake wave breaking*. Physical Review E, 58(5):R5257, 1998.
- [75] T. Hosokai et al. *Refraction effects on the cavity formation and interaction of an intense ultra-short laser pulse with a gas jet*. Physics of Plasmas, 11(10):L57–L60, 2004.
- [76] T. Hosokai et al. *Observation of strong correlation between quasimonoenergetic electron beam generation by laser wakefield and laser guiding inside a preplasma cavity*. Physical Review E, 73(3):036407, 2006.
- [77] D. H. Froula et al. *Measurements of the critical power for self-injection of electrons in a laser wakefield accelerator*. Physical Review Letters, 103(21):215006, 2009.
- [78] S. P. D. Mangles et al. *Self-injection threshold in self-guided laser wakefield accelerators*. Physical Review Special Topics-Accelerators and Beams, 15(1):011302, 2012.
- [79] S. V. Bulanov et al. *Transverse-wake wave breaking*. Physical Review Letters, 78(22):4205, 1997.
- [80] S. V. Bulanov. *Variety of nonlinear wave-breaking*. Nuclear Instruments and Methods in Physics Research Section A: Accelerators, Spectrometers, Detectors and Associated Equipment, 410(3):477–487, 1998.
- [81] S. V. Bulanov et al. *Relativistic interaction of laser pulses with plasmas*. In Reviews of Plasma Physics, pages 227–335. Springer, 2001.
- [82] R. G. Hemker et al. *Computer simulations of a single-laser double-gas-jet wakefield accelerator concept*. Physical Review Special Topics-Accelerators and Beams, 5(4):041301, 2002.
- [83] P. Tomassini et al. *Production of high-quality electron beams in numerical experiments of laser wakefield acceleration with longitudinal wave breaking*. Physical Review Special Topics-Accelerators and Beams, 6(12):121301, 2003.
- [84] N. M. Hafz et al. *Dependence of the electron beam parameters on the stability of laser propagation in a laser wakefield accelerator*. Applied Physics Letters, 90(15):151501, 2007.
- [85] D. R. Lide. *CRC Handbook of Chemistry and Physics, 84th Edition*. CRC Press, 2003.
- [86] C. McGuffey et al. *Ionization induced trapping in a laser wakefield accelerator*. Physical Review Letters, 104(2):025004, 2010.
- [87] J. Faure et al. *Injection and acceleration of quasimonoenergetic relativistic electron beams using density gradients at the edges of a plasma channel*. Physics of Plasmas, 17(8):083107, 2010.

-
- [88] K. Schmid et al. *Density-transition based electron injector for laser driven wakefield accelerators*. Physical Review Special Topics-Accelerators and Beams, 13(9):091301, 2010.
- [89] M. Burza et al. *Laser wakefield acceleration using wire produced double density ramps*. Physical Review Special Topics-Accelerators and Beams, 16(1):011301, 2013.
- [90] M. Hansson et al. *Down-ramp injection and independently controlled acceleration of electrons in a tailored laser wakefield accelerator*. Physical Review Special Topics-Accelerators and Beams, 18(7):071303, 2015.
- [91] J. D. Jackson. *Classical Electrodynamics*. Wiley, New York, 2001.
- [92] H. Wiedemann. *Particle accelerator physics*, volume 314. Springer, 2007.
- [93] D. Attwood and A. Sakdinawat. *X-rays and Extreme Ultraviolet Radiation: Principles and Applications*. Cambridge University Press, 2017.
- [94] A. Hofmann. *Quasi-monochromatic synchrotron radiation from undulators*. Nuclear Instruments and Methods, 152(1):17–21, 1978.
- [95] K. J. Kim. *Physics of particle accelerators*. In *AIP Conf. Proc.*, volume 184, page 565, 1989.
- [96] G. K. Green. *Spectra and optics of synchrotron radiation*. Technical report, Brookhaven National Lab., Upton, NY (USA), 1976.
- [97] P. Michel et al. *Radiative damping and electron beam dynamics in plasma-based accelerators*. Physical Review E, 74(2):026501, 2006.
- [98] A. H. Compton. *A quantum theory of the scattering of X-rays by light elements*. Physical Review, 21(5):483, 1923.
- [99] R. W. Schoenlein et al. *Femtosecond X-ray pulses at 0.4 Å generated by 90 Thomson scattering: a tool for probing the structural dynamics of materials*. Science, 274(5285):236–238, 1996.
- [100] F. Albert et al. *Characterization and applications of a tunable, laser-based, MeV-class Compton-scattering γ -ray source*. Physical Review Special Topics-Accelerators and Beams, 13(7):070704, 2010.
- [101] K. Ta Phuoc et al. *All-optical Compton gamma-ray source*. Nature Photonics, 6(5):308, 2012.
- [102] H. C. Kapteyn et al. *Prepulse energy suppression for high-energy ultrashort pulses using self-induced plasma shuttering*. Optics Letters, 16(7):490–492, 1991.
- [103] S. Chen et al. *MeV-energy X rays from inverse Compton scattering with laser-wakefield accelerated electrons*. Physical Review Letters, 110(15):155003, 2013.
- [104] A. Paz et al. *Thomson backscattering from laser-generated, relativistically moving high-density electron layers*. New Journal of Physics, 14(9):093018, 2012.
- [105] N. D. Powers et al. *Quasi-monoenergetic and tunable X-rays from a laser-driven Compton light source*. Nature Photonics, 8(1):28, 2014.

- [106] Nathan D Powers, I Ghebregziabher, G Golovin, Cheng Liu, Shouyuan Chen, Sudeep Banerjee, Jun Zhang, and Donald P Umstadter. *Quasi-monoenergetic and tunable X-rays from a laser-driven Compton light source*. Nature Photonics, 8(1):28, 2014.
- [107] J. Drenth. *Principles of protein X-ray crystallography*. Springer Science & Business Media, 2007.
- [108] A. Rousse, C. Rischel, and J. C. Gauthier. *Femtosecond x-ray crystallography*. Reviews of Modern Physics, 73(1):17, 2001.
- [109] E. Roessl and R. Proksa. *K-edge imaging in x-ray computed tomography using multi-bin photon counting detectors*. Physics in Medicine & Biology, volume=52, number=15, pages=4679, year=2007.
- [110] F. Zernike. *How I discovered phase contrast*. Science, 121(3141):345–349, 1955.
- [111] S. Kneip et al. *X-ray phase contrast imaging of biological specimens with femtosecond pulses of betatron radiation from a compact laser plasma wakefield accelerator*. Applied Physics Letters, 99(9):093701, 2011.
- [112] J. Wenz et al. *Quantitative X-ray phase-contrast microtomography from a compact laser-driven betatron source*. Nature Communications, 6:7568, 2015.
- [113] G. Materlik and Th. Tschentscher. *The X-ray free electron laser*. URL: http://tesla.desy.de/new_pages/TDR_CD/PartV/xfel.pdf, 2001.
- [114] URL: <http://www-ssrl.slac.stanford.edu/lcls/>.
- [115] E. C. Schreiber et al. *First measurement of the near-threshold $^2\text{H}(\vec{\gamma},n)p$ analyzing power using a free-electron laser based γ -ray source*. Physical Review C, 61(6):061604, 2000.
- [116] E. Kwan et al. *Discrete deexcitations in ^{235}U below 3 MeV from nuclear resonance fluorescence*. Physical Review C, 83(4):041601, 2011.
- [117] F. Albert et al. *Isotope-specific detection of low-density materials with laser-based monoenergetic gamma-rays*. Optics letters, 35(3):354–356, 2010.
- [118] D. Habs et al. *Vision of nuclear physics with photo-nuclear reactions by laser-driven gamma beams*. The European Physical Journal D, 55(2):279, 2009.
- [119] H. A. Weidenmuller. *Nuclear excitation by a zeptosecond multi-mev laser pulse*. Physical Review Letters, 106(12):122502, 2011.
- [120] B. Girolami et al. *Photon beams for radiosurgery produced by laser Compton backscattering from relativistic electrons*. Physics in Medicine & Biology, 41(9):1581, 1996.
- [121] K. J. Weeks. *Radiation therapy potential of intense backscattered Compton photon beams*. Nuclear Instruments and Methods in Physics Research Section A: Accelerators, Spectrometers, Detectors and Associated Equipment, 393(1-3):544–547, 1997.
- [122] S. Lacombe et al. *Spatio-temporal radiation biology: new insights and biomedical perspectives*. Cell Death Dis.
- [123] J. B. Gronberg et al. *Lasers and optics for a gamma-gamma collider*. Proc. Part. Acc. Conf., 5, 2001.

-
- [124] Y. Zhang. *Design Concept of a $\gamma - \gamma$ Higgs Factory Driven by Thin Laser Targets and Energy Recovery Linacs*. Proc. Int. Part. Acc. Conf, 4, 2013.
- [125] T. J. Davis et al. *Phase-contrast imaging of weakly absorbing materials using hard X-rays*. Nature, 373(6515):595, 1995.
- [126] A. Momose. *Phase-sensitive imaging and phase tomography using X-ray interferometers*. Optics Express, 11(19):2303–2314, 2003.
- [127] A. Momose. *Recent advances in X-ray phase imaging*. Japanese Journal of Applied Physics, 44(9R):6355, 2005.
- [128] J. M. Cole et al. *Laser-wakefield accelerators as hard x-ray sources for 3D medical imaging of human bone*. Scientific Reports, 5:13244, 2015.
- [129] E. Eggl et al. *X-ray phase-contrast tomosynthesis of a human ex vivo breast slice with an inverse Compton x-ray source*. Europhysics Letters, 116(6):68003, 2017.
- [130] U. Chaulagain et al. *X-ray phase contrast imaging of biological samples using a betatron x-ray source generated in a laser wakefield accelerator*. In Proceedings SPIE, volume 10240, page 1024014, 2017.
- [131] J. Rizzi et al. *X-ray phase contrast imaging using a broadband X-ray beam and a single phase grating used in its achromatic and propagation-invariant regime*. In Journal of Physics: Conference Series, volume 425, page 192002, 2013.
- [132] A. Dopp et al. *Quick x-ray microtomography using a laser-driven betatron source*. Optica, 5(2):199–203, 2018.
- [133] A. Pogany, D. Gao, and S. W. Wilkins. *Contrast and resolution in imaging with a micro-focus x-ray source*. Review of Scientific Instruments, 68(7):2774–2782, 1997.
- [134] F. Pfeiffer et al. *Phase retrieval and differential phase-contrast imaging with low-brilliance X-ray sources*. Nature Physics, 2(4):258, 2006.
- [135] R. Toth et al. *In-line phase-contrast imaging with a laser-based hard x-ray source*. Review of Scientific Instruments, 76(8):083701, 2005.
- [136] S. Pikuz et al. *Phase-contrast x-ray radiography using the X pinch radiation*. In Proceedings SPIE, volume 4504, pages 234–240, 2001.
- [137] R. Shah et al. *Coherence-based transverse measurement of synchrotron x-ray radiation from relativistic laser-plasma interaction and laser-accelerated electrons*. Physical Review E, 74(4):045401, 2006.
- [138] S. Kneip et al. *Bright spatially coherent synchrotron X-rays from a table-top source*. Nature Physics, 6(12):980, 2010.
- [139] K. Ta Phuoc et al. *Demonstration of the ultrafast nature of laser produced betatron radiation*. Physics of Plasmas, 14(8):080701, 2007.
- [140] S. W. Wilkins et al. *Phase-contrast imaging using polychromatic hard X-rays*. Nature, 384(6607):335, 1996.
- [141] E. Hecht. *Optics, 4th Edition*. Addison-Wesley, San Francisco, 2002.

-
- [142] J. C. Wood et al. *Ultrafast imaging of laser driven shock waves using betatron x-rays from a laser wakefield accelerator*. Scientific Reports, 8(1):11010, 2018.
- [143] S. Fourmaux et al. *Single shot phase contrast imaging using laser-produced Betatron x-ray beams*. Optics Letters, 36(13):2426–2428, 2011.
- [144] Y. Ping et al. *Solid iron compressed up to 560 GPa*. Physical Review Letters, 111(6):065501, 2013.
- [145] A. Levy et al. *X-ray diagnosis of the pressure induced mott nonmetal-metal transition*. Physical Review Letters, 108(5):055002, 2012.
- [146] A. Benuzzi-Mounaix et al. *Electronic structure investigation of highly compressed aluminum with K edge absorption spectroscopy*. Physical Review Letters, 107(16):165006, 2011.
- [147] J. Gaudin et al. *Towards simultaneous measurements of electronic and structural properties in ultra-fast x-ray free electron laser absorption spectroscopy experiments*. Scientific Reports, 4:4724, 2014.
- [148] M. Harmand et al. *X-ray absorption spectroscopy of iron at multimegabar pressures in laser shock experiments*. Physical Review B, 92(2):024108, 2015.
- [149] B. Mahieu et al. *Femtosecond X-ray absorption spectroscopy in warm dense matter*. arXiv preprint arXiv:1711.09144, 2017.
- [150] G. C. O’Neil et al. *Ultrafast time-resolved X-ray absorption spectroscopy of ferrioxalate photolysis with a laser plasma X-ray source and microcalorimeter array*. The Journal of Physical Chemistry Letters, 8(5):1099–1104, 2017.
- [151] S. N. Luo et al. *Gas gun shock experiments with single-pulse x-ray phase contrast imaging and diffraction at the Advanced Photon Source*. Review of Scientific Instruments, 83(7):073903, 2012.
- [152] V. Horny et al. *Temporal profile of betatron radiation from laser-driven electron accelerators*. Physics of Plasmas, 24(6):063107, 2017.
- [153] J. Edwards and S. J. Rose. *Ionization time scales in hot dense plasma*. Journal of Physics B: Atomic, Molecular and Optical Physics, 26(16):L523, 1993.
- [154] S. M. Vinko et al. *Creation and diagnosis of a solid-density plasma with an X-ray free-electron laser*. Nature, 482(7383):59, 2012.
- [155] D. Arnlund et al. *Visualizing a protein quake with time-resolved X-ray scattering at a free-electron laser*. Nature Methods, 11(9):923, 2014.
- [156] A. Cavalleri et al. *Femtosecond structural dynamics in VO₂ during an ultrafast solid-solid phase transition*. Physical Review Letters, 87(23):237401, 2001.
- [157] M. C. Newton et al. *Time-resolved coherent diffraction of ultrafast structural dynamics in a single nanowire*. Nano Letters, 14(5):2413–2418, 2014.
- [158] P. Shearing et al. *In situ X-ray spectroscopy and imaging of battery materials*. The Electrochemical Society Interface, 20(3):43–47, 2011.
- [159] A. Barty et al. *Self-terminating diffraction gates femtosecond X-ray nanocrystallography measurements*. Nature Photonics, 6(1):35, 2012.

-
- [160] H. N. Chapman, C. Caleman, and N. Timneanu. *Diffraction before destruction*. Philosophical Transactions of the Royal Society B, 369(1647):20130313, 2014.
- [161] F. R. Metzger. *Progress in Nuclear Physics*. Pergamon Press, Inc., New York, 1959.
- [162] N. Pietralla et al. *Parity measurements of nuclear levels using a free-electron-laser generated γ -ray beam*. Physical Review Letters, 88(1):012502, 2001.
- [163] G. Zentai. *X-ray imaging for homeland security*. In 2008 IEEE International Workshop on Imaging Systems and Techniques, pages 1–6, 2008.
- [164] H. Kuwabara, Y. Mori, and Y. Kitagawa. *Standoff detection of hidden objects using backscattered ultra-intense laser-produced x-rays*. Journal of applied Physics, 114(8):083103, 2013.
- [165] R. Takashima et al. *Numerical evaluation of nuclide analysis of I 129, Sr 90, and Cs 137 using bremsstrahlung high energy x ray generated by ultrashort pulse laser*. Journal of Applied Physics, 100(6):064906, 2006.
- [166] J. Silano et al. *Selective activation with all-laser-driven Thomson γ -rays*. In 2013 IEEE International Conference on Technologies for Homeland Security (HST), pages 429–434, 2013.
- [167] G. Zentai. *X-ray imaging for homeland security*. International Journal of Signal and Imaging Systems Engineering, 3(1):13–20, 2010.
- [168] P. Reimers et al. *Some aspects of industrial non-destructive evaluation by X- and γ -ray computed tomography*. Nuclear Instruments and Methods in Physics Research, 221(1):201–206, 1984.
- [169] A. G. Davies et al. *Terahertz spectroscopy of explosives and drugs*. Materials Today, 11(3):18–26, 2008.
- [170] F. Albert and A. G .R. Thomas. *Applications of laser wakefield accelerator-based light sources*. Plasma Physics and Controlled Fusion, 58(10):103001, 2016.
- [171] S. Banerjee et al. *Compact source of narrowband and tunable X-rays for radiography*. Nuclear Instruments and Methods in Physics Research Section B: Beam Interactions with Materials and Atoms, 350:106–111, 2015.
- [172] G. Sarri et al. *Ultra-high brilliance multi-MeV γ -ray beams from nonlinear relativistic Thomson scattering*. Physical Review Letters, 113(22):224801, 2014.
- [173] J. Hrebicek et al. *25TW Ti:sapphire laser chain at PALS*. In *Proceedings SPIE*, volume 8080, page 80800U, 2011.
- [174] V. Malka et al. *Characterization of neutral density profile in a wide range of pressure of cylindrical pulsed gas jets*. Review of Scientific Instruments, 71(6):2329–2333, 2000.
- [175] M. Krus et al. *Quadrupole lens-free multiple-profile diagnostics for emittance measurement of laser wakefield accelerated electron beams*. Nuclear Instruments and Methods in Physics Research Section A: Accelerators, Spectrometers, Detectors and Associated Equipment, 810:32–36, 2016.
- [176] Y. Glinec et al. *Absolute calibration for a broad range single shot electron spectrometer*. Review of Scientific Instruments, 77(10):103301, 2006.

-
- [177] A. Buck et al. *Absolute charge calibration of scintillating screens for relativistic electron detection*. Review of Scientific Instruments, 81(3):033301, 2010.
- [178] T Radcliffe, G Barnea, B Wowk, R Rajapakshe, and S Shalev. *Monte Carlo optimization of metal/phosphor screens at megavoltage energies*. Medical Physics, 20(4):1161–1169, 1993.
- [179] G. E. Giakoumakis and D. M. Miliotis. *Light angular distribution of fluorescent screens excited by x-rays*. Physics in Medicine & Biology, 30(1):21, 1985.
- [180] W. Fullagar et al. *The use and characterization of a backilluminated charge-coupled device in investigations of pulsed X-ray and radiation sources*. Review of Scientific Instruments, 79(10):103302, 2008.
- [181] Andor Instruments. *Direct detection CCDs*. URL: <http://www.andor.com/learning-academy/direct-detection-understand-direct-detection-ccds>, 2018.
- [182] V. Vorobel. *Interakce jaderného záření s látkou*. FNSPE, CTU (University textbook), 2009.
- [183] J. Vancura. *Laser-produced femtosecond sources of high energy radiation*. FNSPE, CTU (Bachelor’s project), 2016.
- [184] B. L. Henke, E. M. Gullikson, and J. C. Davis. *X-ray interactions: photoabsorption, scattering, transmission and reflection $E= 50\text{-}30,000\text{ eV}$, $Z= 1\text{-}92$* . 1993.
- [185] P. Kirkpatrick. *On the theory and use of Ross filters*. Review of Scientific Instruments, 10(6):186–191, 1939.
- [186] S. Y. Kalmykov et al. *Electron self-injection into an evolving plasma bubble: Quasi-monoenergetic laser-plasma acceleration in the blowout regime*. Physics of Plasmas, 18(5):056704, 2011.
- [187] K. Bohacek et al. *Stable electron beams from laser wakefield acceleration with few-terawatt driver using a supersonic air jet*. Nuclear Instruments and Methods in Physics Research Section A: Accelerators, Spectrometers, Detectors and Associated Equipment, 883:24–28, 2018.
- [188] B. Rus et al. *Outline of the ELI-Beamlines facility*. In *Proceedings SPIE*, volume 8080, page 808010, 2011.